

ABSTRACT

BLUMENSCHNEIN, NICHOLAS ANTHONY. Development of Gallium Oxide for High-Power Semiconductor Device Applications. (Under the direction of Dr. John. F Muth and Dr. Tania Paskova).

Pulsed laser deposition was used for growing heteroepitaxial and homoepitaxial thin films on c-plane sapphire substrates and native single-crystalline Ga₂O₃ substrates, respectively. N-type doping was accomplished by implementing low concentrations of SnO₂ and SiO₂ into the Ga₂O₃ ablation source material, and a doping concentration ranging from 7×10^{16} to 2×10^{20} cm⁻³ was realized in the homoepitaxial thin films.

The 3ω measurement technique was used to evaluate and extract the thermal conductivity along different crystallographic orientations of bulk Ga₂O₃. A maximum thermal conductivity of 29.5 W/m-K was identified along [010] at 300 K, whereas the thermal conductivity ranged from 16.1 to 18.4 W/m-K along other crystallographic directions.

The high-frequency dielectric properties of Ga₂O₃ were investigated using time-domain terahertz spectroscopy. The dielectric spectra contained a non-monotonic temperature dependence which was described using a dual harmonic oscillator model. The dependence was found to be an effect of charge carrier localization caused by thermal activation of unintentional dopants at 50 K.

Ga₂O₃-based deep-UV photodetectors, thin-channel MOSFETs, and Schottky barrier diodes were also studied. Photodetector performance was evaluated by varying the oxygen partial pressure during Ga₂O₃ thin film growth. The devices had excellent responsivity and $I_{\text{photo}}/I_{\text{dark}}$ ratio values of 30.45 A/W and 90X, respectively. Self-heating effects of Ga₂O₃ thin-channel MOSFETs were evaluated using pulsed I-V and Raman nanothermography characterization techniques, which resulted in thermal resistance values of 73 °C-mm/W and 60 °C-mm/W, respectively. Schottky barrier diodes were fabricated using undoped and Sn-doped Ga₂O₃ drift layers grown on highly-

doped Ga₂O₃ substrates. A maximum breakdown voltage of -186 volts was observed. Trapping effects were evaluated using transient voltage measurements and frequency-dependent equivalent parallel conductance measurements, and a trap state was identified at an energy of $E_C - 0.485$ eV.

© Copyright 2020 by Nicholas Anthony Blumenschein

All Rights Reserved

Development of Gallium Oxide for High-Power Semiconductor Device Applications

by
Nicholas Anthony Blumenschein

A dissertation submitted to the Graduate Faculty of
North Carolina State University
in partial fulfillment of the
requirements for the degree of
Doctor of Philosophy

Electrical Engineering

Raleigh, North Carolina
2020

APPROVED BY:

Dr. John F. Muth
Committee Co-Chair

Dr. Tania Paskova
Committee Co-Chair

Dr. Albena Ivanisevic

Dr. Spyridon Pavlidis

DEDICATION

In loving memory of my mother, Ameena S. Yaktin.

BIOGRAPHY

Nicholas Anthony Blumenschein was born on June 29, 1991 to Tony Blumenschein and Ameena Yaktin in Marysville, OH. Nicholas was raised with two brothers, Lucas and Andrew, and a sister, Alyssa. Nicholas earned a Bachelor of Science degree in Electrical and Computer Engineering with minors in Mathematics and Biomedical Electronics from the University of Cincinnati in 2015. Interested in semiconductor research, Nicholas then began his graduate career at North Carolina State University in August of 2015. He received his Master of Science degree in Electrical Engineering in December of 2017. He received his Doctorate of Philosophy in Electrical Engineering while minoring in Materials Science and Engineering in 2020 under the direction of Dr. John F. Muth and Dr. Tania Paskova.

ACKNOWLEDGMENTS

I would like to thank Dr. John Muth and Dr. Tania Paskova for all of the guidance and support they have provided to me during my graduate studies. I would also like to thank Dr. Albena Ivanisevic and Dr. Spyros Pavlidis for serving as faculty members of my Ph.D. committee, as well as Dr. Robert Kolbas for providing research-related guidance.

During the time I have spent at NC State, I have been lucky to have had the opportunity to work with many of the research faculty and staff members in the Monteith Research Center. I would like to thank Ching-Chang ‘BB’ Chung for his help in the AIF XRD Laboratory, as well as Dr. Bill Kiether, Nicole Hedges, Marcio Cerullo, Greg Allion, Jeff Ricker-Hagler, and Jim Mitchell for their assistance in the NNF Cleanroom.

During my graduate studies I was fortunate to have been given the opportunity to study abroad at the Institute of Physics – Czech Academy of Sciences and to work as an intern for the Air Force Research Laboratory – Sensor Directorate. While at the Institute of Physics, I am thankful for the excellent mentorship provided by Filip Kadlec, Christelle Kadlec, Alice Hospodkova, and Oleksandr Romanyuk. While at AFRL, I received excellent mentorship provided by Kelson Chabak, Kevin Leedy, Neil Moser, Andy Green, and Eric Heller.

I would like to thank Dr. Andrew Steckl for being an excellent advisor to me during my undergraduate career at the University of Cincinnati. I am grateful for the opportunities you gave me to explore my research interests. These experiences helped me develop a passion for the work that I have pursued ever since. During my time as an undergraduate researcher, I am grateful for the mentorship provided to me by Dr. Daewoo Han and Dr. Han ‘Jerry’ You.

To Karly and my family, I am grateful for the encouragement you provided over the years.

TABLE OF CONTENTS

LIST OF TABLES	vii
LIST OF FIGURES	ix
Chapter 1: Ga₂O₃ Introduction and Material Properties	1
1.1 Motivation for Ga ₂ O ₃ Development	1
1.2 Gallium Oxide Properties	7
1.2.1 Crystalline Properties	7
1.2.2 Electronic Properties	9
1.2.3 Thermal Properties	15
1.3 Challenges	17
1.4 References	20
Chapter 2: Material Growth and Device Accomplishments	23
2.1 Bulk Crystal Growth Capability	23
2.2 Thin Film Growth	27
2.2.1 Overview	27
2.2.2 Molecular Beam Epitaxy	29
2.2.3 Metal Organic Vapor Phase Epitaxy	32
2.2.4 Pulsed Laser Deposition	34
2.3 Ga ₂ O ₃ Device Types	38
2.3.1 Overview	38
2.3.2 Ultraviolet Photodetectors	38
2.3.3 Schottky Barrier Diodes	42
2.3.4 Field-Effect Transistors	44
2.3.5 Challenges to Explore	48
2.4 References	50
Chapter 3: Growth	56
3.1 Gallium Oxide Crystal Structure	56
3.2 Gallium Oxide Thin Film Growth	57
3.2.1 Target Fabrication and Substrate Preparation	57
3.2.2 Heteroepitaxial Growth	58
3.2.3 Homoepitaxial Growth	73
3.3 Conclusions	79
3.4 References	81
Chapter 4: Thermal Conductivity	84
4.1 3 ω Technique	84
4.1.1 Heat Source	86
4.1.2 Heat Sensor	88
4.1.3 Device Fabrication	91
4.2 Single-Crystal Ga ₂ O ₃	93
4.3 Thin Film Ga ₂ O ₃	102
4.4 Conclusions	110
4.5 References	112
Chapter 5: Time-Domain Terahertz Spectroscopy	114
5.1 TDTS Fundamental Description	114
5.2 Characterization	120

5.2.1 Bulk Ga ₂ O ₃	122
5.2.2 Thin Film Ga ₂ O ₃	129
5.3 Conclusions.....	134
5.4 References.....	135
Chapter 6: Deep-Ultraviolet Photodetectors	137
6.1 Photodetector Device Physics.....	137
6.2 Device Fabrication	138
6.3 Photodetector Performance.....	140
6.4 Conclusions.....	146
6.5 References.....	147
Chapter 7: Metal-Oxide-Semiconductor Field-Effect Transistors.....	148
7.1 Device Fabrication.....	148
7.2 MOSFET Device Physics	149
7.3 DC Performance.....	151
7.4 Pulsed I-V Measurement Technique.....	152
7.5 Self-Heating Characterization.....	153
7.6 Raman Nanothermography and Thermal Simulations.....	156
7.7 Conclusions.....	163
7.8 References.....	164
Chapter 8: Schottky Barrier Diodes	166
8.1 SBD Device Physics	166
8.2 Device Fabrication.....	168
8.3 Device Performance.....	171
8.3.1 Electrical Characterization.....	171
8.3.2 Trap Characterization.....	183
8.3.3 Electric Field Simulations.....	187
8.4 Conclusions.....	189
8.5 References.....	191
Chapter 9: Summary and Conclusions	193
Appendices.....	197
A. Sentaurus TCAD SDE Command File.....	198
B. Sentaurus TCAD SDevice I-V Command File	200
C. Sentaurus TCAD SDevice B-V Command File.....	203
D. Sentaurus TCAD Ga ₂ O ₃ Parameter File	206
List of Publications	213

LIST OF TABLES

Table 1.1	Relevant material properties of Si, GaAs, 4H-SiC, GaN, β -Ga ₂ O ₃ , Diamond, and AlN for determining high-power device capability	3
Table 1.2	Figures-of-merit (relative to Si) calculated for Si, GaAs, 4H-SiC, GaN, β -Ga ₂ O ₃ , Diamond, and AlN used for determining high-power device capability	5
Table 1.3	Five polymorphs of Ga ₂ O ₃ and their crystal properties	8
Table 2.1	Commercially available Ga ₂ O ₃ substrates from Tamura Corporation	25
Table 2.2	Film dopants and substrate orientation of films shown in Figure 2.3 grown by varying growth techniques	29
Table 3.1	Molar mass and density of powders used for fabricating PLD targets	58
Table 3.2	Interplanar spacing and lattice mismatch between the epitaxial crystallographic directions of ($\bar{2}01$)-oriented Ga ₂ O ₃ grown on c-plane sapphire.....	61
Table 3.3	Growth conditions for films of Figure 3.3	61
Table 3.4	XRD reflection planes calculated for α -Al ₂ O ₃ and β -Ga ₂ O ₃ . Calculated and measured values of reflection angles are shown for comparison.....	63
Table 3.5	Optimized PLD growth recipe for β -Ga ₂ O ₃	71
Table 4.1	Sample set used for analyzing anisotropic thermal conductivity as a function of Ga ₂ O ₃ orientation and doping.....	96
Table 4.2	Room temperature anisotropic thermal conductivity of undoped, Sn-doped, and Fe-doped Ga ₂ O ₃ samples.....	98
Table 4.3	Power slope values obtained by fitting the temperature-dependent thermal conductivity of Ga ₂ O ₃ samples with different dopants and crystal orientations	101
Table 4.4	Undoped and Sn-doped Ga ₂ O ₃ thin films grown on c-plane sapphire with varying film thicknesses used for thermal conductivity experiments	105
Table 4.5	Fitting constants for κ -d _F data of Figure 4.10.....	108
Table 4.6	Fitting constants for σ -d _F data of Figure 4.11	109
Table 5.1	Bulk and thin film Ga ₂ O ₃ samples analyzed by TDTS. Thin film samples were grown on 430 μ m thick c-plane sapphire substrates	121

Table 6.1	Dimensional properties of fabricated devices	140
Table 6.2	Rise and decay time constants gathered by fitting the transient response curves of Figure 6.4 using Equation 6.2	144
Table 7.3	Comparison of Ga ₂ O ₃ MOSFET R _{TH} values and corresponding device fabrication properties.....	162
Table 8.1	Schottky barrier diode sample details	176
Table 8.2	Device parameters extracted from J-V and C-V profiles	176

LIST OF FIGURES

Figure 1.1	Theoretical on-resistance versus breakdown voltage for various semiconductor materials	2
Figure 1.2	Power-frequency diagram showing the application space of various semiconductor materials	7
Figure 1.3	Unit cell of β -Ga ₂ O ₃	9
Figure 1.4	(a) Band structure of β -Ga ₂ O ₃ with valence band maxima aligned to zero energy and (b) high-resolution view of Γ point	10
Figure 1.5	Relaxed atomic configurations and isosurfaces of the squared wave functions for the STHs on various oxygen sites in Ga ₂ O ₃	12
Figure 1.6	Electron mobility of β -Ga ₂ O ₃ versus donor concentration for varying temperatures	14
Figure 1.7	Calculated Schottky barrier heights versus metal work function for Schottky barrier diodes fabricated on ($\bar{2}01$) bulk and (010) epitaxial Ga ₂ O ₃	15
Figure 1.8	(a) Temperature-dependent thermal conductivity of β -Ga ₂ O ₃ and (b) tabulated results for 300 K and 500 K. (c) Anisotropic phonon velocity	16
Figure 1.9	Number of publications on gallium oxide per year since 1950.....	19
Figure 2.1	Images of bulk β -Ga ₂ O ₃ crystals produced by EFG.....	24
Figure 2.2	Modeled costs for manufacturing 6" Ga ₂ O ₃ and SiC wafers. Additional price reduction avenues are shown for Ga ₂ O ₃ , reducing the price/wafer cost to \$195	26
Figure 2.3	Mobility versus carrier concentration of homoepitaxial β -Ga ₂ O ₃ thin films grown by MBE, MOVPE, HVPE, MOCVD, Mist-CVD, and PLD.....	28
Figure 2.4	(a) Schematic diagram of an MBE used for growing Sn-doped Ga ₂ O ₃ and (b) an optical image showing an MBE growth chamber	30
Figure 2.5	Ga ₂ O ₃ growth rate as a function of substrate temperature when using a TEGa precursor for various chamber pressures and TEGa molar flow rates	33
Figure 2.6	(a) Optical image showing the inside of the PLD chamber used in this work during growth and (b) schematic drawing of the PLD growth technique	35
Figure 2.7	Si concentration of Si:Ga ₂ O ₃ homoepitaxial thin films as a function of SiO ₂ wt.% in PLD targets. Films were evaluated by SIMS.....	36

Figure 2.8	Carrier concentration, mobility, and conductivity values of homoepitaxial Ga ₂ O ₃ thin films grown by different growth methods.....	37
Figure 2.9	Schematic diagram of a MSM UV Photodetector fabricated using Au/Ni/Ga ₂ O ₃ /Ni/Au on a sapphire substrate. Inset shows an optical image of the device surface	39
Figure 2.10	(a) Responsivity and response time of UV PDs fabricated using Ga ₂ O ₃ . (b)-(d) Schematic diagram of various Ga ₂ O ₃ -based devices.....	41
Figure 2.11	State-of-the-art Schottky barrier diodes	44
Figure 2.12	Device schematics and I-V characteristics for field-plated depletion-mode Ga ₂ O ₃ MOSFETs with a 750 V breakdown voltage	46
Figure 2.13	(a) Device schematic and (b) false-colored SEM image of enhancement-mode FinFET device. (c) I _{DS} -V _{DS} characteristic showing V _{BR} of 612 V.....	47
Figure 2.14	(a) Schematic drawing of delta-doped Ga ₂ O ₃ MOSFET and corresponding (b) energy band diagram, 2DEG charge profile, and (c) transfer characteristic	48
Figure 3.1	β-Ga ₂ O ₃ unit cell with (010), (001), and ($\bar{2}$ 01) crystallographic planes shown with green, blue, and red planes, respectively.....	56
Figure 3.2	In-plane epitaxial relationships which can occur for ($\bar{2}$ 01)-oriented β-Ga ₂ O ₃ on c-plane Al ₂ O ₃ . Sapphire oxygen atom locations are shown using red circles.....	60
Figure 3.3	θ-2θ XRD data gathered from β-Ga ₂ O ₃ thin films grown at varying substrate temperatures	62
Figure 3.4	θ-2θ intensity of (a) ($\bar{2}$ 01) and (b) (110) reflections normalized to the (0006) sapphire reflection. (c) ($\bar{2}$ 01)/(110) ratio versus substrate temperature	65
Figure 3.5	Formation energy – fermi level relationship of (a) oxygen vacancies and (b) hydrogen impurities in β-Ga ₂ O ₃	66
Figure 3.6	(a) θ-2θ, (b) ω, and (c) φ XRD data gathered for β-Ga ₂ O ₃ thin films with varying P _{O2}	67
Figure 3.7	SEM images taken at 100 kX for samples with P _{O2} of (a) 0.1 mT, (b) 0.5 mT, (c) 1 mT, (d) 5 mT, and (e) 10 mT	68
Figure 3.8	AFM images samples with P _{O2} of (a) 0.1 mT, (b) 0.5 mT, (c) 1 mT, (d) 5 mT, and (e) 10 mT	69

Figure 3.9	Transmission spectra of Ga ₂ O ₃ thin films. Inset shows an estimation of bandgap energy for the three samples.....	70
Figure 3.10	(a) Conductivity of Sn-doped β-Ga ₂ O ₃ thin films with grown on c-plane Al ₂ O ₃ . (b) Carrier concentration of the films as a function of ablation target Sn content ...	72
Figure 3.11	SIMS profiles of Sn-doped Ga ₂ O ₃ thin films grown using ablation targets containing (a) 1 mol% Sn and (b) 10 mol% Sn.....	73
Figure 3.12	θ-2θ XRD profiles for single-crystalline β-Ga ₂ O ₃ substrates with different orientations	74
Figure 3.13	θ-2θ and ω XRD profiles of (a, b) (001) Sn-doped, (c, d) (010) Sn-doped, and (e, f) (010) Si-doped homoepitaxial β-Ga ₂ O ₃ thin films	75
Figure 3.14	FWHM values obtained by ω measurements grown using NCSU- and KJL-fabricated ablation targets	77
Figure 3.15	Mobility and carrier concentration of homoepitaxial Sn- and Si-doped Ga ₂ O ₃ thin films. The Ga ₂ O ₃ mobility approximation is shown using a dashed line.....	78
Figure 3.16	Mobility, carrier concentration, and conductivity of Si-doped Ga ₂ O ₃ thin film as a function of temperature	79
Figure 4.1	Side-view representation on the basis of the 3ω technique depicting radial diffusion of thermal waves through the material from the metal heat source	85
Figure 4.2	Schematic of metal heat source/thermometer layout on sample surface.....	87
Figure 4.3	Penetration depth versus frequency. Frequency limitations to achieve a measurement error of less than 1% is shown for Ga ₂ O ₃ with 650 μm thickness	90
Figure 4.4	Example V _{3ω} measurements as a function of frequency for validation of the 3ω slope method. Data was gathered for an undoped (010) Ga ₂ O ₃ sample.....	94
Figure 4.5	Example of 3ω heat source and sensor configuration.....	95
Figure 4.6	Temperature-dependent thermal conductivity along various crystallographic directions in (a) undoped, (b) Sn-doped, and (c) Fe-doped Ga ₂ O ₃	100
Figure 4.7	Effect of Sn and Fe doping on the thermal conductivity of Ga ₂ O ₃ along the (a) [010], (b) [201], (c) ⊥[201], and (d) ⊥(-201) crystallographic directions.....	101
Figure 4.8	(a) Side-view and (b) top-side-view schematic drawings of Ga ₂ O ₃ /Al ₂ O ₃ structures	104

Figure 4.9	Example measurement of an undoped Ga ₂ O ₃ film showing linear dependencies of (a) $\ln(\omega/2\pi)-V_{3\omega}$ and (b) $\Delta T/P$. (c) Extracted value of $\Delta T_F/P$	106
Figure 4.10	Thermal conductivity of undoped and Sn-doped heteroepitaxial Ga ₂ O ₃ thin films grown on c-plane sapphire	108
Figure 4.11	Electrical conductivity of undoped and Sn-doped heteroepitaxial Ga ₂ O ₃ thin films grown on c-plane sapphire	109
Figure 4.12	(a) Cross-sectional TEM image of an undoped Ga ₂ O ₃ thin film (b) High-resolution image shows ordered atomic arrangement. (c) Overlaid unit cell.....	110
Figure 5.1	Schematic diagram of the TDTS experimental setup.....	115
Figure 5.2	(a) Example THz waveforms. Free-space reference and measured waveforms are shown with black and red curves, respectively	118
Figure 5.3	Ga ₂ O ₃ unit cell and orientation of the bulk samples cut along the ($\bar{2}01$) plane. The inset shows a top-side schematic view of the sample	122
Figure 5.4	Dielectric properties of the bulk Ga ₂ O ₃ sample showing the (a) n , (b) k , (c) ϵ' , (d) ϵ'' , (e) σ' , and (f) σ'' . The modeled fits are shown with dotted lines	123
Figure 5.5	Fitting results for ϵ' and σ' obtained by the double harmonic oscillator model and Drude model for data measured at 70 K.....	126
Figure 5.6	Temperature dependence of f_1 , γ_1 , and $\Delta\epsilon_1$ fitting parameters obtained when applying the double harmonic oscillator model to $\epsilon'(T)$ and $\sigma'(T)$ data	128
Figure 5.7	Dielectric properties of the thin film Ga ₂ O ₃ sample showing (a) n , (b) k , (c) ϵ' , (d) ϵ'' , (e) σ' , and (f) σ'' . Drude-Smith fits are shown using lines.....	130
Figure 5.8	(a) c , (b) N_c , and (c) τ fitting parameters obtained using the Drude-Smith model to fit ϵ' and σ' measured for the Sn-doped thin film sample.....	132
Figure 5.9	Top-view AFM images of the Sn-doped Ga ₂ O ₃ (a) thin film and (b) bulk crystal. Three-dimensional images of the (c) thin film and (d) bulk crystal.....	133
Figure 6.1	Band diagram of MSM photodetector under (a) zero bias and (b) forward bias ...	138
Figure 6.2	Schematic drawing and optical image of MSM PD structure. Physical dimensions shown here are for sample A.....	140
Figure 6.3	I-V characteristic of PD devices containing (a) films grown with varying P _{O2} and (b) grown at a P _{O2} of 1 mT with varying device geometrical properties.....	142

Figure 6.4	Transient response of MSM PDs for devices containing (a) films grown with varying P_{O_2} and (b) 1 mT with varying device geometrical properties.....	144
Figure 6.5	Spectral responsivity of MSM PDs containing Ga_2O_3 thin films grown with varying P_{O_2} . The inset plot contains the spectral responsivity on a log scale	145
Figure 7.1	Schematic drawing of the β - Ga_2O_3 thin-channel MOSFET used in this work	149
Figure 7.2	I-V characteristic of depletion-mode MOSFET	150
Figure 7.3	(a) DC I_D - V_{DS} characteristic while varying V_G from -16 to 0 V. (b) Transfer characteristic for a V_D of 10 V. The inset shows a -17.5 V turn-off voltage	151
Figure 7.4	Depiction of $V_{DS}(t)$ waveforms used during the pulsed I-V characterization.....	153
Figure 7.5	I-V characteristic for varying (a) pulsewidths. I-V characteristic for varying $T_{baseplate}$ using (b) 200 μs and (c) 200 ns PW. (d) R_{ON} and $I_{D,max}$ versus T_{CH}	155
Figure 7.6	(a) Pulsed I_D - V_{DS} characteristic obtained when varying V_{DSQ} from 2 to 15 V. (b) R_{ON} and $I_{D,max}$ plotted as a function of dissipated power.....	155
Figure 7.7	T_{CH} - P_D approximations obtained using R_{ON} and $I_{D,max}$. The estimated R_{TH} was obtained using the slope of T_{CH} - P_D and found to be 73 $^{\circ}C$ -mm/W.....	156
Figure 7.8	(a) TiO_2 nanoparticle locations on the device. (b) T_{CH} measured using Raman thermography for four amounts of P_D . (c) T_{CH} - P_D obtained at TiO_2 location.....	158
Figure 7.9	(a)-(c) MOSFET thermal simulation images while applying $P_D = 0.9$ W/mm. (d) Channel length and (e) gate width profiles are shown	159
Figure 7.10	T_{CH} - P_D obtained by pulsed I-V and Raman nanothermography. Simulated gate width and channel length profiles are shown for $P_D = 0.9$ W/mm.....	160
Figure 8.1	Band diagram of metal- Ga_2O_3 junction (a) before and (b) after equilibrium. Band bending due to (c) forward, (d) reverse, and (e) high reverse biasing	167
Figure 8.2	Schematic drawing of fabricated Ga_2O_3 Schottky barrier diodes	171
Figure 8.3	Effect of Schottky cap diameter on (a) I-V and (b) C-V characteristics	172
Figure 8.4	(a) $E_C - E_F$ and W_D versus N_D for Ga_2O_3 when using Ni and Pt Schottky contacts. Energy band diagrams for (b) Ni/ Ga_2O_3 and (c) Pt/ Ga_2O_3 junctions.....	174
Figure 8.5	C-V and $(A/C)^2$ profiles for (a) sample A, (b) sample B, and (c) sample C	177

Figure 8.6	J-V characteristic of samples A, B, and C on (a) log and (b)-(d) linear scale. (e) Natural log of J_F used to extract ideality factor and saturation current density	178
Figure 8.7	Reverse breakdown voltage measurements for the three samples	180
Figure 8.8	(a) Image force barrier lowering at the Schottky-Ga ₂ O ₃ interface. Leakage current fits for samples (a) A, (b) B, and (c) C	182
Figure 8.9	Transient voltage measured while forcing constant stress and release currents for approximately 300 seconds each	184
Figure 8.10	(a) C-V profiles for frequencies ranging from 2 – 200 kHz. (b) G/ω - ω profiles for $V_A = 0.3-0.8$ V and the extracted (c) τ and (d) N_{it} versus trap energy level.....	186
Figure 8.11	Electric field simulations of (a) sample C and a Ga ₂ O ₃ SBD with a field plate when biased at -186 V. (c) Electric field profiles at the Pt/Ga ₂ O ₃ interface	188

CHAPTER 1 – Ga₂O₃ INTRODUCTION AND MATERIAL PROPERTIES

1.1 Motivation of Ga₂O₃ Development

Gallium oxide shows promise for future high-power and high-frequency device applications because of its high critical electric field strength, reasonable mobility, and bulk growth capability. Silicon is the most commonly used material for fabricating devices such as diodes and transistors for low power and integrated circuit applications, respectively. The performance of silicon devices has reached a ceiling because of its low critical electrical field strength (E_C). For power switching applications, a low E_C limits operating voltage capability. The maximum power capable of silicon RF devices is limited by the power frequency product because of its low bandgap energy and breakdown voltage. These property limitations cannot be overcome through traditional engineering approaches, and have provoked extensive research efforts on other semiconductors such as silicon carbide and gallium nitride that resulted in massive improvements to the high-power electronics market in terms of device capability and energy efficiency.

Semiconductor device efficiency is incredibly important when considering economic and environmental impacts. Increasing energy efficiency results in devices that are able to deliver the power needed for a particular application by using less current. Current amplitude corresponds to temperature elevations within the device and any external cabling, and therefore, the increased energy efficiency reduces thermal dissipation and mitigates the need for high gauge wiring. This is incredibly important in military and space applications where the system performance is dependent upon its mass. It is also beneficial for the environment since reducing the amount of poly-based materials needed for cable insulation eliminates pollution. Materials with a higher critical electric field strength can also be used in RF devices for operating at higher frequencies.

High frequency operation results in size reduction of passive components like capacitors and inductors. This leads to electrical systems with less volume and mass and helps with materials cost.

The relationship between on-resistance (R_{ON}) and off-state breakdown voltage (V_{BR}) in transistors provides a common basis for analyzing the potential merits of different semiconductor materials. **Figure 1.1** shows the theoretical limit of on-resistance versus breakdown voltage for silicon (Si), gallium arsenide (GaAs), silicon carbide (SiC), gallium nitride (GaN), beta gallium oxide (β -Ga₂O₃), aluminum nitride (AlN), and diamond. The theoretical R_{ON} can be calculated using **Equation 1.1**, where ϵ is the dielectric constant, μ_n is the electron mobility, E_C is the critical electric field strength, W_D is drift region width, q is electron charge, and N_D is drift region doping concentration [1]. The R_{ON} - V_{BR} relationship can be used to identify transistor materials with low theoretical power switching losses.

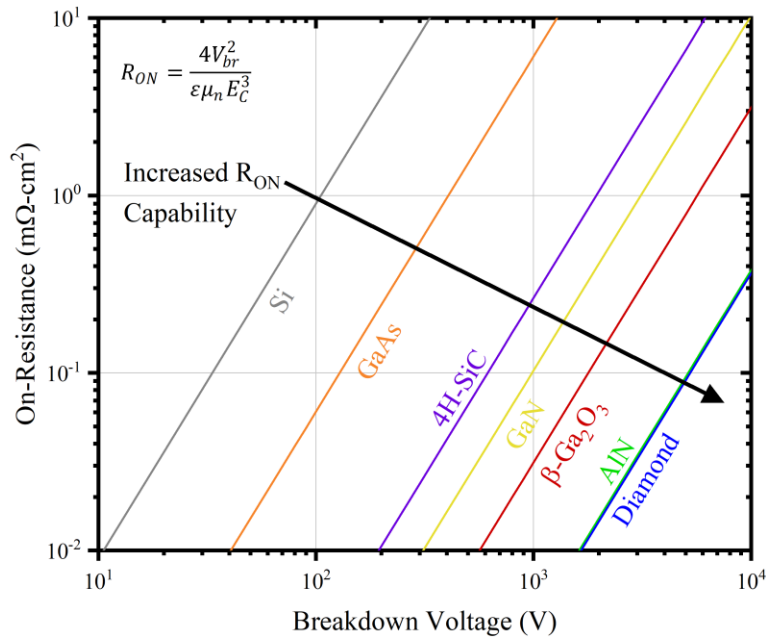


Figure 1.1 Theoretical on-resistance versus breakdown voltage for various semiconductor materials.

$$R_{ON-sp}(ideal) = \frac{4V_{br}^2}{\epsilon\mu_n E_C^3} = \frac{W_D}{q\mu_n N_D} \quad [m\Omega \cdot cm^2] \quad (1.1)$$

Ga₂O₃ offers promise particularly for high-power applications due to a combination of its material properties and the ability to grow high-quality epitaxial material using low-cost native substrates. Its relatively wide 4.9 eV bandgap energy (E_g) and theoretical critical electrical field strength (E_c) of 8 MV/cm are crucially important for its use in devices operating at high-power conditions. A wide bandgap is required for operating at high temperatures to reduce leakage current and a large critical electric field strength is needed for operating devices at a high voltage while maintaining appropriate feature dimensions [1]. These parameters, as well as other key material properties, such as dielectric constant (ϵ), mobility (μ), saturation velocity (v_s), and thermal conductivity (κ) of β -Ga₂O₃ are shown in **Table 1.1** and compared with the previously mentioned semiconductor materials.

Table 1.1 Relevant material properties of Si, GaAs, 4H-SiC, GaN, β -Ga₂O₃, Diamond, and AlN for determining high-power device capability.

Material Property	Si	GaAs	4H-SiC	GaN	β-Ga₂O₃	Diamond	AlN
Bandgap, E_g (eV)	1.1	1.4	3.3	3.4	4.9	5.5	6.2
Dielectric Const., ϵ	11.8	12.9	9.7	9.0	10.0	5.5	8.5
Critical E-Field, E_C (MV/cm)	0.3	0.4	2.5	3.3	8.0	10.0	15.4
Electron Mobility, μ (cm ² /V-s)	1400	8000	1000	1200	250	2000	850
Sat. Velocity, v_s (10 ⁷ cm/s)	1.0	1.2	2.0	2.5	1.1	1.0	2.0
Thermal Cond., κ (W/m-K)	150	50	370	230	10 – 30	2000	340

Table 1.2 shows the most commonly used figures-of-merit for determining material suitability for high-power applications. The Baliga figure-of-merit ($BFOM = \epsilon\mu E_c^3$) is perhaps the most important metric when considering high-power applications, as it describes the theoretical specific on-resistance ($R_{on,sp}$) of the material within the vertical drift region of field-effect transistors which determines the material's on-state conductivity for a given breakdown voltage. In 1982, Baliga showed that the power handling capability of FETs can be expected to increase linearly with electron mobility and increase to the third power with energy band gap [2]. In 1989, Baliga expanded on these findings when he introduced the Baliga high-frequency figure-of-merit ($BHFFOM = \mu E_c^2$) [3]. The BHFFOM is used as a measure of switching losses and determining the efficiency of a material and its suitability for high-frequency applications. The Johnson figure-of-merit ($JFOM = E_c^2 v_s^2 / 4\pi^2$) was first proposed in 1965, and has since been used to provide a measure of a semiconductors suitability in applications where both high-frequency and high-power are of importance [4]. The JFOM is informative because it defines a maximum bias voltage and cut-off frequency for the material, and allows for cross-material comparison for signal amplification applications. In 1972, the Keyes figure-of-merit ($KFOM = \kappa \sqrt{c v_s / 4\pi \epsilon}$) was derived and has provided a useful metric that includes thermal conductivity to help better describe a materials' thermal capability for power density and switching speed in FET applications [5]. In 2004, Huang proposed three new figures-of-merit for unipolar switching power devices which included Huang's material figure-of-merit ($HMFOM = \sqrt{\mu} E_c$), Huang's chip-area figure-of-merit ($HCAFOM = \epsilon \sqrt{\mu} E_c^2$), and Huang's thermal figure-of-merit ($HTFOM = \kappa / \epsilon E_c$) [6]. The HMFOM specifies the total conduction and switch power losses of the material by considering gate charge. The HCAFOM is used for comparing the minimum required chip area dimensions of various semiconductor materials when designed to meet similar specifications. The HTFOM

describes the expected temperature rise of a particular material given optimal chip area dimensions and minimal power dissipation conditions are used.

These seven FOMs have been used to describe the potential of Ga₂O₃ for future semiconductor device applications. According to BFOM, BHFFOM, JFOM, and HMFOM, Ga₂O₃ has potential to out-scale some of the competing semiconductor materials such as SiC and GaN in terms of performance in both high-power and high-frequency applications. The HCAFOM also predicts that Ga₂O₃ is superior with regards to manufacturing because of its high E_c which enables high energy density within the unipolar switching devices. Critical electric field strength is a

Table 1.2 Figures-of-merit (relative to Si) calculated for Si, GaAs, 4H-SiC, GaN, β -Ga₂O₃, Diamond, and AlN used for determining high-power device capability.

Figures-of-Merit (relative to Si)	Si	GaAs	4H-SiC	GaN	β -Ga ₂ O ₃	Diamond	AlN
Baliga ($\epsilon\mu E_c^3$)	1	15	340	870	2870	24661	59160
Baliga High-Freq. (μE_c^2)	1	10	50	104	127	1587	1600
Johnson ($E_c^2 v_s^2 / 4\pi^2$)	1	2	17	28	29	33	103
Keyes ($\kappa\sqrt{cv_s / 4\pi\epsilon}$)	1	0.3	3.8	27.8	0.2	19.5	3.8
Huang Chip Area ($\epsilon\mu^{0.5} E_c^2$)	1	5	48	85	255	619	1479
Huang Material ($\mu^{0.5} E_c$)	1	3	7	10	11	40	40
Huang Thermal ($\kappa / \epsilon E_c$)	1	0.23	0.36	1.83	0.01	0.86	0.06

common parameter used for calculating each of these FOMs. The E_c of Ga_2O_3 is likely its most important material property and a driving factor for material development. At the present time, the theoretical E_c of 8 MV/cm is still unproven. In 2016, A.J. Green experimentally demonstrated an E_c of 3.8 MV/cm using a Ga_2O_3 MOSFET [7]. This was a huge breakthrough not only because it surpassed that of SiC and GaN, but it was the highest E_c value ever reported for any semiconductor material. This Ga_2O_3 milestone was later confirmed by Konishi *et al.*, who demonstrated a maximum electric field of 5.1 MV/cm was reached in a Schottky barrier diode drift layer just before breakdown occurred [8]. One drawback characteristic of Ga_2O_3 is its low thermal conductivity, which results in the relatively low KFOM and HTFOM values. Ga_2O_3 has a lower thermal conductivity than any of the other semiconductor materials under discussion, and this will certainly pose a challenge in designing future high-power devices.

The application space for a variety of materials is shown in **Figure 1.2** [1]. The application of each semiconductor can generally be broken down into two distinct categories: high-frequency or high-power. The application space of each semiconductor can be estimated in part using the one-sided abrupt junction approximation of **Equation 1.2**, as demonstrated by Chabak *et al.* [9]. The approximation was used for comparing the depletion width formed in Si, 4H-SiC, GaN, and Ga_2O_3 unipolar two-terminal devices with the assumption that each was doped n-type to achieve an identical breakdown voltage. As the approximation suggests, depletion width scales inversely with critical electric field strength, meaning that when using Ga_2O_3 the metal contacts can be placed much closer together than with the other materials. This is beneficial because it removes a large portion of device resistance which lowers any resulting RC time constants in frequency applications.

$$W_D = \frac{2V_{br}}{E_C} \quad [cm] \quad (1.2)$$

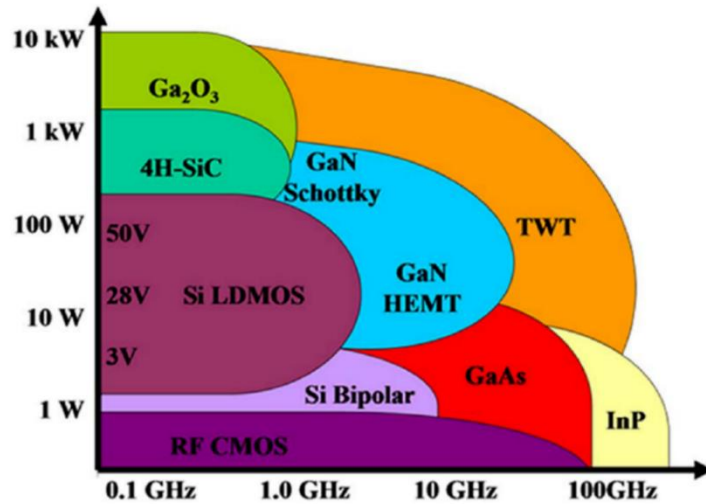


Figure 1.2 Power-frequency diagram showing the application space of various semiconductor materials. Copyright (2017) Electrochemical Society [1].

1.2 Gallium Oxide Properties

1.2.1 Crystalline Properties

Gallium oxide has five distinct polymorphs (α , β , γ , δ , and ϵ) that each have their own unique crystal structure, material properties, and processing requirements. The monoclinic β polymorph is the most commonly studied because it remains thermally stable up to its melting point of 1900°C, while the remaining polymorphs will transition into β -Ga₂O₃ when subject to temperatures greater than 750°C [10], [11]. β -Ga₂O₃ is the main focus of this work, but the four other polymorphs still require discussion since they possess properties which vary from the β phase. The rhombohedral phase α -Ga₂O₃ has been the second most studied polymorph of gallium oxide because of its ease in growing heteroepitaxial films on sapphire substrates. Interestingly, the bandgap of α -Ga₂O₃ (5.03 eV) is larger than that of the beta phase (4.9 eV). A β -to- α transition has been reported when subject to high pressure conditions of 9.5 GPa [12]. γ - and δ -Ga₂O₃ have not generated nearly as much interest as the other three polymorphs despite having cubic and body-centered cubic lattices, respectively [13], [14]. There have been reports of using γ -Ga₂O₃ for

fabricating quantum dots with visible blue-green light emission. ϵ -Ga₂O₃ was reported to possess a unique internal polarization property that could be used in two-dimensional electron gas (2DEG) applications by forming (AlGa)₂O₃/Ga₂O₃ heterostructures in a similar fashion to what has been demonstrated with AlGaN/GaN [10]. These four polymorphs all have unique processing requirements but can generally be synthesized by low-temperature heteroepitaxial growth. **Table 1.3** outlines the crystal structure and lattice parameters of each polymorph.

Table 1.3 Five polymorphs of Ga₂O₃ and their crystal properties.

Polymorph	Crystal Structure	Lattice Parameters (Å, °)	Ref.
α	Rhombohedral	a, b = 5.04, c = 13.56	[12]
β	Monoclinic	a = 12.23, b = 3.04, c = 5.80 $\beta = 103.87$	[15]
γ	Cubic	a, b, c = 8.22	[13]
δ	Body-centered cubic	a, b, c = 9.70	[14]
ϵ	Orthorhombic	a = 5.12, b = 8.79, c = 9.41	[16]

Currently, β -Ga₂O₃ has the most promise among all of the gallium oxide polymorphs despite it having the most complicated monoclinic crystal structure, as shown in **Figure 1.3**. The [010] direction and ($\bar{2}01$) plane are shown here because these are the two most common orientations of bulk and thin film growth. The ($\bar{2}01$) surface is the preferred heteroepitaxial growth plane on α -Al₂O₃ substrates, while the Ga₂O₃ [010] direction has the highest thermal conductivity in the crystal (due to monoclinic-related anisotropy) which makes it the preferred orientation for high-power devices. A detailed explanation for this will be given in the following

section. The unit cell is comprised of 12 gallium and 18 oxygen ions, hence the compound notation of Ga_2O_3 .

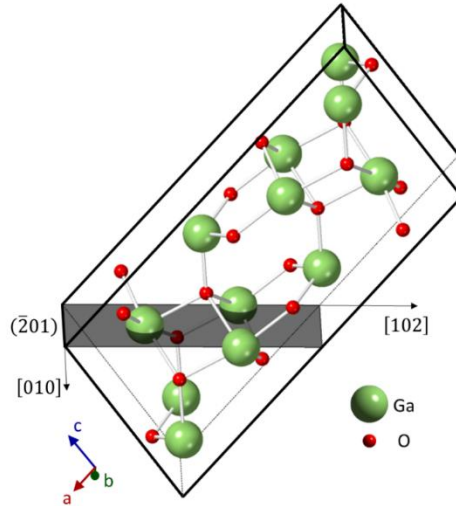


Figure 1.3 Unit cell of $\beta\text{-Ga}_2\text{O}_3$.

1.2.2 Electronic Properties

Similarly to other transparent conducting oxides such as ZnO and In_2O_3 , the $\beta\text{-Ga}_2\text{O}_3$ electronic structure is complex and dependent upon material composition. The $\beta\text{-Ga}_2\text{O}_3$ structure contains both tetrahedral and octahedral coordinated metal ions, which are generated from a strong interaction between the ns metal and $2p$ oxygen orbitals [17]. The $\beta\text{-Ga}_2\text{O}_3$ bandgap, conduction band energy dispersion, and resulting effective electron mass and mobility is produced from these $Ms\text{-}Op$ interactions. **Figure 1.4** shows the energy band structure of $\beta\text{-Ga}_2\text{O}_3$ with the valence band maxima aligned to zero energy [18]. The conduction band minima and valence band maxima are located at the Γ and M points, respectively. By definition, $\beta\text{-Ga}_2\text{O}_3$ is an indirect bandgap semiconductor with an $E_C\text{-}E_V$ of 4.89 eV. The material also contains a direct bandgap of 4.92 eV located at the Γ point. The Heyd-Scuseria-Ernzerhof hybrid functional modeling approach has shown $\beta\text{-Ga}_2\text{O}_3$ to have an electron effective mass of $0.27m_0$ [18], while a similar value of 0.28

was observed experimentally using high-resolution angle-resolved photoelectron spectroscopy [19].

The n-type conductivity of gallium oxide can be controlled over a very wide range ($10^{-12} - 10^3 \Omega^{-1}\text{cm}^{-1}$). Unlike other conducting oxide materials, oxygen vacancies are not responsible for this behavior. Using density functional theory (DFT), Varley *et al.* showed that the oxygen vacancies create deep donors with ionization energies of greater than 1 eV [20]. Varley then

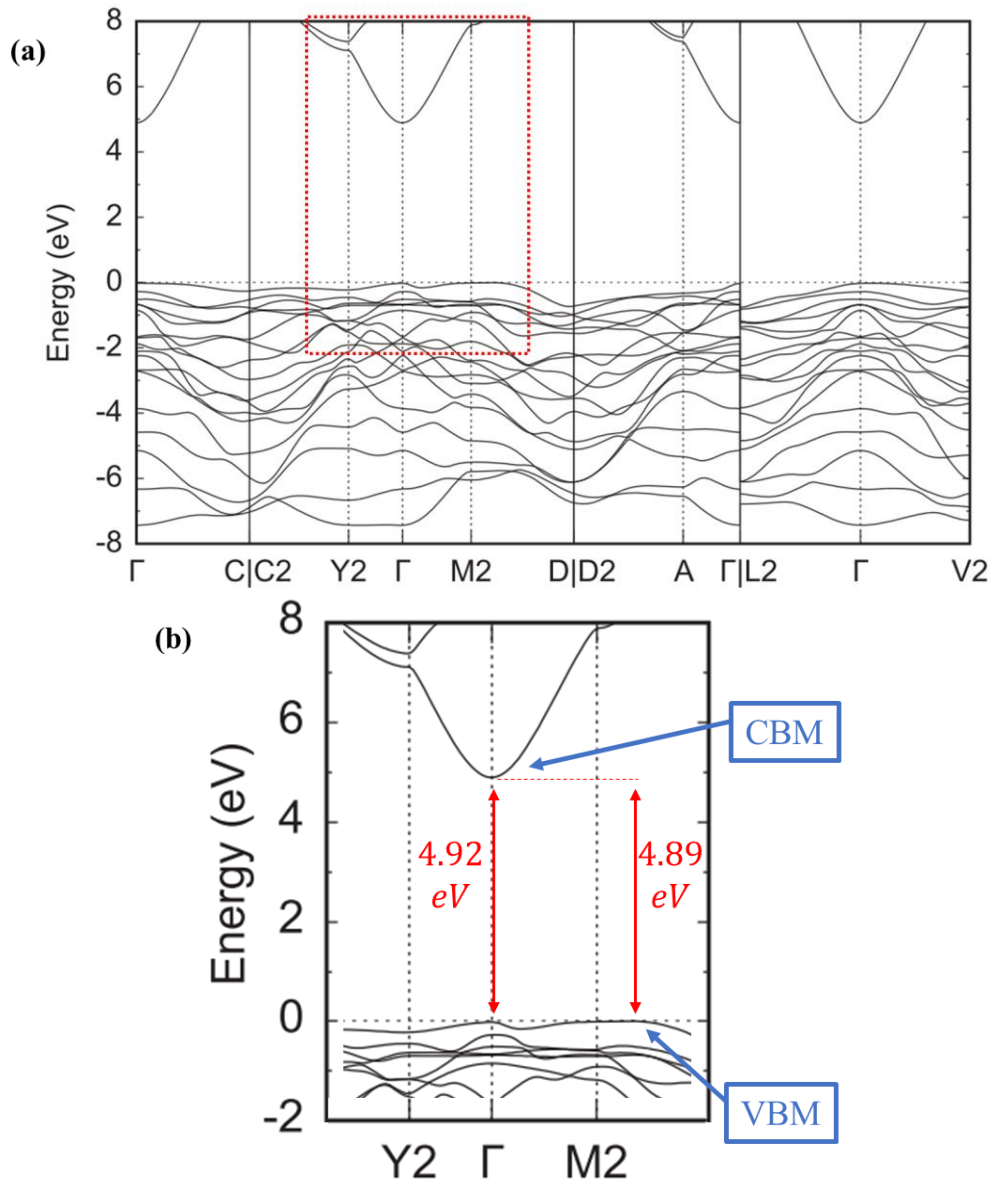


Figure 1.4 (a) Band structure of $\beta\text{-Ga}_2\text{O}_3$ with valence band maxima aligned to zero energy and (b) high-resolution view of Γ point. Copyright (2019) American Physical Society [18].

then proposed that this conductive behavior was due to unintentional shallow donors, such as hydrogen, forming by occupying either interstitial or substitutional sites. The scope of the work also included intentional Si, Sn, and Ge n-type dopants. These group IV elements substitute onto Ga sites, where Si and Ge prefer the tetrahedral coordination of the Ga(I) site while Sn prefers substitution into the octahedral coordination of the Ga(II) site [21]. Other atoms such as F and Cl were shown to substitute onto O(I) sites because of a preference for threefold coordination. However, the donor coordination topic has been somewhat controversial. A more recent DFT modelling report by Lany *et al.* showed that while Si is a shallow donor, Sn and Ge are not, but rather have delocalized impurity states near the conduction band minima but are close enough for ionization at 300 K [22]. Regardless, all three dopants function similarly as shallow donors in Ga₂O₃ and have been shown capable of being precisely controlled for doping in the range of 10¹⁶ – 10²⁰ cm⁻³ using various growth methods [9].

It appears that p-type conductivity is not possible in Ga₂O₃ because of small dispersion in the valence band maxima. This results in a large effective electron mass of 0.27m₀ and causes holes to form localized polarons, or self-trapped holes (STHs), rather than mobile free holes in the valence band [18]. The STHs are an intrinsic defect within the Ga₂O₃ structure, where a hole localizes on an O atom or two O atoms with an atomic displacement as shown in **Figure 1.5** [18]. **Figure 1.5 (a), (d), and (e)** depict the relaxed atomic configurations possible in α-, δ-, and ε-Ga₂O₃, respectively. **Figure 1.5 (b) and (c)** show two situations in β-Ga₂O₃ where the STH is localized on the O1 and O3 sites, respectively. When a hole becomes trapped on the O1 site, it is distributed amongst two distinct O sites which are relaxed by 0.25 and 0.27 Å. On the O3 site the hole is trapped on an oxygen atom and experiences an outward relaxation from the neighboring Ga atoms of ~ 0.16 Å. Gake *et al.* found that for β-Ga₂O₃ the STHs in either situation had high self-trapping

energies of about 0.58 eV, meaning that obtaining hole mobility in β - Ga_2O_3 would be extremely difficult.

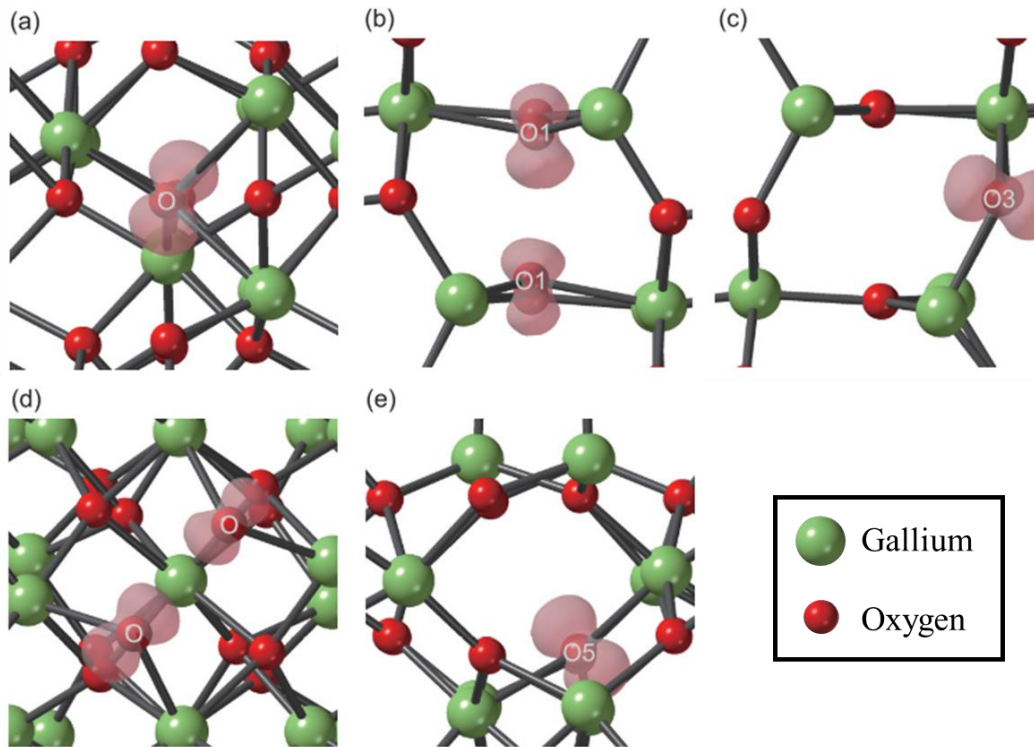


Figure 1.5 Relaxed atomic configurations and isosurfaces of the squared wave functions for the STHs on (a) the O site in α - Ga_2O_3 , (b) the O1 site and (c) the O3 site in β - Ga_2O_3 , (d) the O site in δ - Ga_2O_3 , and (e) the O5 site in ϵ - Ga_2O_3 . Green and red balls indicate Ga and O atoms, respectively. The isosurfaces correspond to 10% of the maximum value. Copyright (2019) American Physical Society [18].

Mg, Fe, N, and Zn deep-level compensating acceptors have been used for p-type doping, but this has only served as an enhancement of insulating properties rather than p-type conduction. Forming p-n junctions in Ga_2O_3 will not be possible unless p-type conduction is somehow realized. This is one of the major limiting factors of the technology in its current stage of development. The absence of p-type conduction in Ga_2O_3 means that all devices will be controlled by majority carriers, effectively limiting the material's application space to unipolar-type devices.

The electron mobility of β - Ga_2O_3 has been studied thoroughly using different experimental and theoretical approaches, and currently the upper limit for intrinsic material is estimated to be

250 cm²/V-s. Ma *et al.* reported on the intrinsic mobility of β -Ga₂O₃ by comparing temperature-dependent Hall measurements with a model derived from fundamental $\mathbf{k} \cdot \mathbf{p}$ theory [23]. As expected, it was found that the electron mobility decreased as a power function with increased carrier concentration. The $\mu(N_D, T)$ relationship of **Equation 1.3** was obtained, where N_D (cm⁻³) is the donor concentration and T (K) is temperature (valid for $300 \leq T \leq 500$ K). **Figure 1.6** shows the electron mobility plotted as a function of donor concentration for temperature ranging from 300 – 500 K. It was found that the room temperature mobility was dominated by polar optical (PO) phonon scattering at doping concentrations below 2.76×10^{18} cm⁻³ (denoted as the critical doping density, N_{cr}) as determined by the $\mu_{PO} \approx (\mu_H^{-1} + \mu_{NI}^{-1})^{-1}$ crossover condition where μ_H is Hall mobility and μ_{NI} is neutral impurity mobility. The mobility was significantly degraded once $N_D > N_{cr}$. Ma *et al.* concluded that, while difficult, it is possible that the PO scattering energy of Ga₂O₃ could be altered by applying strain. If a higher mobility is required for a particular application, one alternative approach could be using (AlGa)₂O₃/Ga₂O₃ heterostructures to form a two-dimensional electron gas (2DEG). As seen in other semiconductors where forming a 2DEG is possible, the electron mobility in a (AlGa)₂O₃/Ga₂O₃ 2DEG should theoretically be higher than that of the bulk material because of momentum conservation relaxation in the interface perpendicular direction during electron–PO scattering processes, eliminating the neutral impurity potential, and significant ionized impurity scattering reduction.

$$\mu(N_D, T) = \frac{56 \left[e^{\frac{508}{T}} - 1 \right]}{\left[1 + \frac{N_D}{2.8 \times 10^{16} (T - 278)} \right]^{0.68}} \quad \left[\frac{cm^2}{V s} \right] \quad (1.3)$$

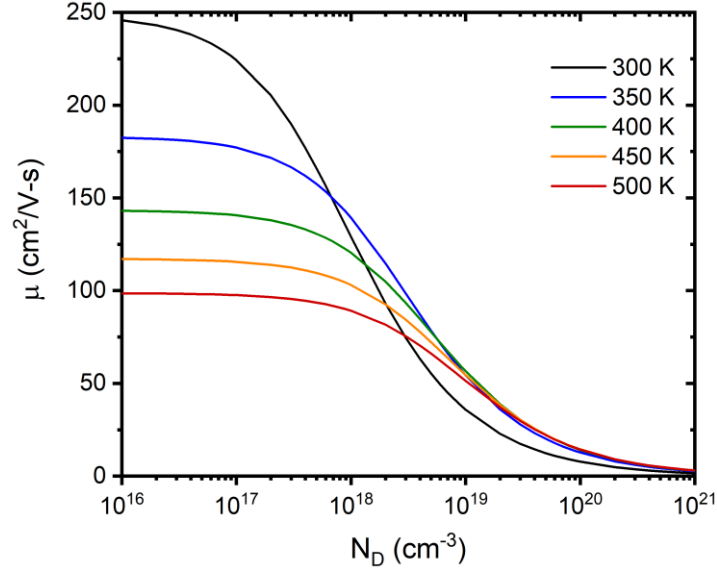


Figure 1.6 Electron mobility of $\beta\text{-Ga}_2\text{O}_3$ versus donor concentration for varying temperatures.

The development of both ohmic and Schottky contacts is important for utilizing these electrical properties in semiconductor device applications. Yao *et al.* investigated Ti, In, Ag, Sn, W, Mo, Sc, Zn, and Zr as electrical contacts onto Ga_2O_3 [24]. Similarly to GaN, it was found that the best performing ohmic contact was achieved when using a Ti contact with an Au capping layer. More advanced metal stacks (Ti/Ni/Al/Au) have also been reported, and their deposition is commonly followed by a 60 second 470 °C rapid thermal anneal (RTA) in an N_2 atmosphere [25], [26]. The Ti/Al/Ni/Au ohmic metal stack results in a contact resistance (R_C) that ranges from 10 – 80 $\Omega\cdot\text{mm}$ for Sn-doped films with carrier concentrations around $1 \times 10^{18} \text{ cm}^{-3}$ [25]. Using photoelectron emission spectroscopy (PES), Mohamed *et al.* reported the electron affinity ($\chi_{\text{Ga}_2\text{O}_3}$) and work function ($\Phi_{\text{Ga}_2\text{O}_3}$) of Ga_2O_3 to be 4.00 eV and 4.11 eV, respectively [27]. The Au barrier height (Φ_{Bn}^{S-m}) was then estimated to be 1.23 eV using the Schottky-Mott rule, $\Phi_B^{S-m} = \Phi_{Au} - \chi_{\text{Ga}_2\text{O}_3} = \Phi_{Au} - \Phi_{\text{Ga}_2\text{O}_3} + (E_C - E_F)$ [28], [29]. The most commonly used metals for forming a Schottky contact are Ni and Pt, however, others have also been evaluated. Yao *et al.* reported on the electrical behavior of five different Ga_2O_3 Schottky barrier diodes when using different

Schottky metals (W, Cu, Ni, Ir, Pt), and a small dependence of Schottky barrier height on the metal work function was observed [30]. A plot of Schottky barrier height versus metal work function is shown in **Figure 1.7** [30].

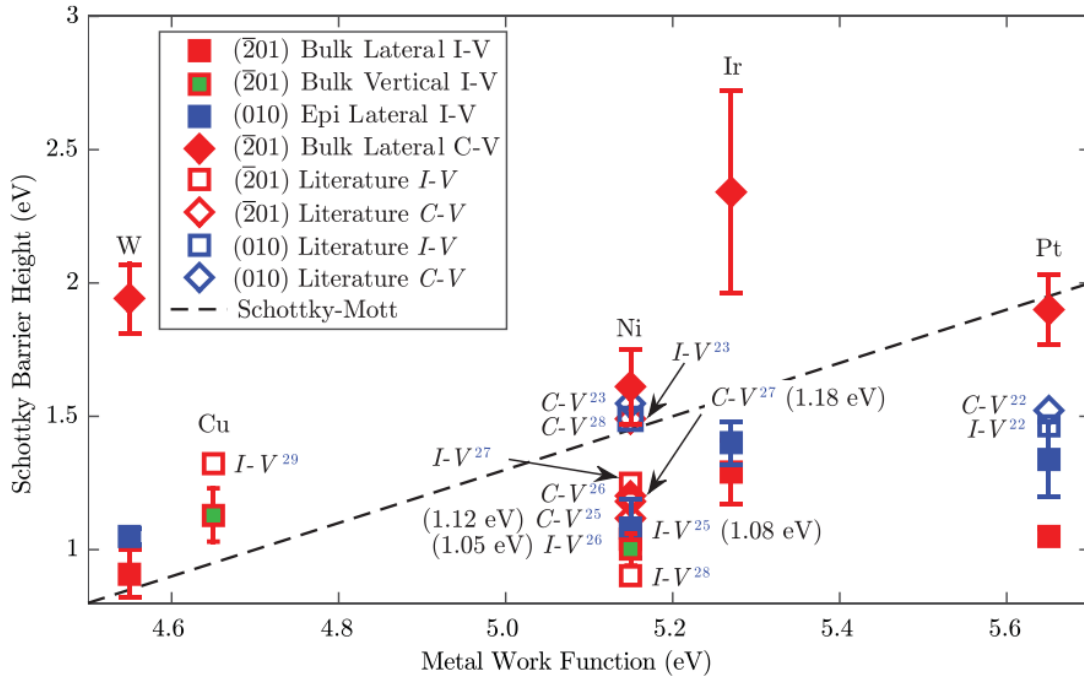


Figure 1.7 Calculated Schottky barrier heights versus metal work function for Schottky barrier diodes fabricated on $(\bar{2}01)$ bulk and (010) epitaxial Ga_2O_3 . The referenced values on the plot are from 22 [31], 23 [32], 25 [33], 26 [34], 27 [35], 28 [36], and 29 [37]. Copyright (2017) AIP Publishing.

1.2.3 Thermal Properties

$\beta\text{-Ga}_2\text{O}_3$ is expected to be used in a variety of high-power semiconductor device applications in the future. These devices will inherently generate large amount of heat because of the dissipated power. The heat dissipation issues in wide bandgap materials like SiC, GaN, and AlN can be mitigated by their high thermal conductivities (**Table 1.1**). This is not the case for Ga_2O_3 , which has a room-temperature anisotropic thermal conductivity that varies between 10 – 30 W/m-K depending on crystal direction [38], [39]. The crystal has a maximum thermal conductivity in the $[010]$ direction, but it is significantly lower in all other crystallographic

orientations. The other crystal directions where thermal conductivity has been analyzed in β - Ga_2O_3 are $[102]$, $\perp [102]$, $[\bar{2}01]$, $\perp (\bar{2}01)$, $[001]$, and $[100]$. Temperature-dependent thermal conductivity data is shown in **Figure 1.8(a)**, where measurements were made using time-domain thermoreflectance [38]. The thermal conductivity values for 300 K and 500 K are shown in **Figure 1.8(b)** for the four crystallographic directions that were measured. The thermal conductivity in each crystal direction followed a linear $1/T$ relationship, which is an indication of phonon-dominated thermal transport. Guo *et al.* extracted the phonon group velocity in each crystal direction experimentally and by first-principle calculations as shown in **Figure 1.8(c)** [38]. The velocities shown are normalized to that in the $[001]$ direction, which had an LA mode group velocity of 7.1×10^5 cm/s. We have also investigated the effect of doping on thermal conductivity using undoped, Sn-doped, and Fe-doped Ga_2O_3 samples and will discuss the methodology used and obtained results in Chapter 4 of this work.

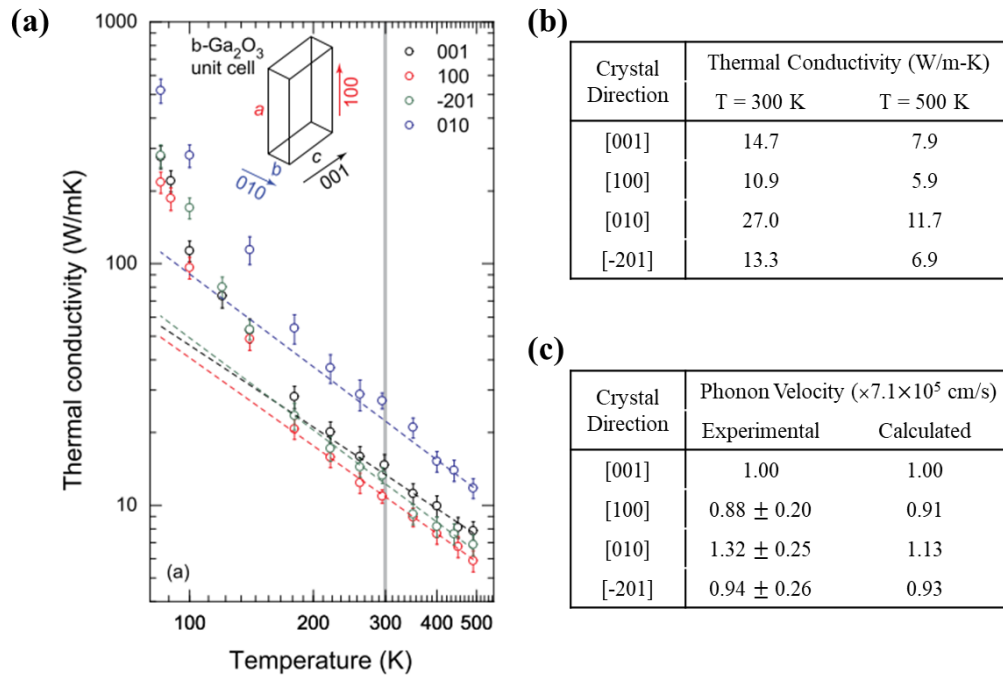


Figure 1.8 (a) Temperature-dependent anisotropic thermal conductivity of β - Ga_2O_3 for four unique crystal directions TDTR. (b) Results for 300 K and 500 K are tabulated. (c) Crystal direction dependent phonon velocity determined experimentally and through first-principle calculations. Copyright (2017) AIP Publishing [38].

1.3 Challenges

The development of gallium oxide is similar to other wide bandgap materials in its early stages of development. There are some material challenges that will need to be investigated in detail as the material matures. The two main challenges identified so far include low thermal conductivity and the inability to fabricate p-type material that exhibits hole conduction rather than just higher insulating properties.

It appears that the thermal conductivity in Ga_2O_3 reaches a maximum of 30 W/m-K along the [010] direction, but one cannot exclude the possibility of other crystallographic directions having higher thermal conductivity which have yet to be studied. The low thermal conductivity will certainly pose challenges in the development of future high-power electronics, but it is possible that new ways of packaging and heat extraction can be developed to accommodate. Top-side heat dissipation can be taken advantage of in (010)-oriented Ga_2O_3 crystals. Increased heat dissipation might be achievable by using thinned substrates. The Ga_2O_3 substrates currently being manufactured have a thickness of 650 μm . Reducing the thickness to 300 μm is achievable by polishing techniques, and would likely increase the heat dissipation. Back-side solutions such as wafer bonding will need to be investigate as well [10]. Thin film transfer of Ga_2O_3 drift layers to compatible materials with higher thermal conductivities are likely to aid in heat dissipation in vertical high-power devices. This was demonstrated by Chatterjee *et al*, where a Ga_2O_3 substrate was thinned to 10 μm and bonded to an AlN/diamond carrier wafer using an epoxy underfill material to fabricate a high-power MOSFET [40]. The thermal resistance in the structure was reduced by a factor of six in comparison to a similar device fabricated on a standalone Ga_2O_3 substrate.

P-type Ga₂O₃ material has been achieved using Mg, Fe, N, and Zn as deep-level compensating acceptors, but so far enhanced p-type conductivity has not been realized. This is common in oxide-based semiconductors, but none of the previously examined oxide materials exhibit the same properties as Ga₂O₃ which make it viable for high-power electronics applications. The 8 MV/cm critical electric field strength provides a pathway for Ga₂O₃ development in unipolar device applications. PN junctions will not be attained without conductive p-type material, but this is not problematic for unipolar devices such as Schottky barrier diodes, MOSFETs, and UV photodetectors.

Some abstract device structures have been reported using Zn-doped Ga₂O₃ in an effort to obtain p-type conduction. Feng *et al.* grew Zn-doped Ga₂O₃ nanowires on an undoped n-type Ga₂O₃ thin film [41]. A PN homojunction was fabricated by depositing Ti/Au contacts on the film and clamping ITO glass onto the top of the nanowire mesh. Electrical measurements showed the device had a rectifying I-V characteristic. Tao *et al.* grew amorphous Zn-doped Ga₂O₃ layers using atomic layer deposition (ALD) [42]. The 20-nm-thick film was grown by depositing ZnO and Ga₂O₃ layers in alternating cycles on a (100) p-type Si wafer. Film composition was varied by the ratio of ZnO and Ga₂O₃ cycles. The films grown by different cycles (3, 5, and 7) of Ga₂O₃ and 1 cycle of ZnO were investigated using optical transmittance measurements. The Tauc method was utilized to determine the optical bandgap of the films. Films containing Ga₂O₃, 7:1 Ga₂O₃:ZnO, 5:1 Ga₂O₃:ZnO, 3:1 Ga₂O₃:ZnO, and ZnO have been reported with bandgaps of 4.65, 4.9, 5.2, 5.25 eV, and 3.25, respectively. Hall measurements confirmed an increased film electrical conductivity when increasing ZnO content, where films with Ga₂O₃, 7:1 Ga₂O₃:ZnO, 5:1 Ga₂O₃:ZnO, 3:1 Ga₂O₃:ZnO, and ZnO had resistivities of 1.80x10⁴, 8.35x10³, 3.54x10³, 1.42x10³, and 1.25x10⁻² Ω-cm, respectively.

Regardless of these material limitations, the interest in Ga₂O₃ has continually increased since the early 2000's. **Figure 1.9** shows the number of publications on gallium oxide per year since 1950. All indications point towards a continued effort in the development of Ga₂O₃ for high-power applications. The following chapter will discuss the progress made in Ga₂O₃ bulk crystal growth, epitaxial thin film growth by molecular beam epitaxy (MBE), metalorganic vapor phase epitaxy (MOVPE), and pulsed laser deposition (PLD) techniques, as well as the device performance of Schottky barrier diodes, MOSFETs, and solar-blind UV photodetectors that have been reported to-date.

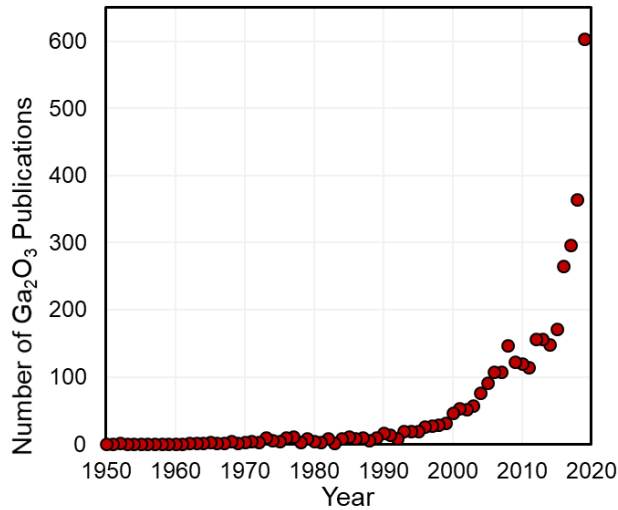


Figure 1.9 Number of publications on gallium oxide per year since 1950.

1.4 References

- [1] M. A. Mastro, A. Kuramata, J. Calkins, J. Kim, F. Ren, and S. J. Pearton, “Opportunities and Future Directions for Ga₂O₃,” *ECS J. Solid State Sci. Technol.*, vol. 6, no. 5, pp. 356–359, 2017.
- [2] B. J. Baliga, “Semiconductors for high-voltage , vertical channel field-effect transistors,” *J. Appl. Phys.*, vol. 53, no. 1759, 1982.
- [3] B. J. Baliga, “Power Semiconductor Device Figure of Merit for High-Frequency Applications,” *IEEE Electron Device Lett.*, vol. 10, no. 10, pp. 455–457, 1989.
- [4] E. O. Johnson, “Physical limitations on frequency and power parameters of transistors,” *RCA Rev.*, vol. 26, pp. 163–177, 1965.
- [5] R. W. Keyes, “Figures of Merit for Semiconductors for High-Speed Switches,” *Proc. IEEE*, vol. February, p. 225, 1972.
- [6] A. Q. Huang, “New unipolar switching power device figures of merit,” *IEEE Electron Device Lett.*, vol. 25, no. 5, pp. 298–301, 2004.
- [7] A. J. Green et al., “3.8-MV/cm Breakdown Strength of MOVPE-Grown Sn-Doped β -Ga₂O₃ MOSFETs,” *IEEE Electron Device Lett.*, vol. 37, no. 7, pp. 902–905, 2016.
- [8] K. Konishi, K. Goto, H. Murakami, A. Kuramata, S. Yamakoshi, and M. Higashiwaki, “1-kV vertical Ga₂O₃ field-plated Schottky barrier diodes,” *Appl. Phys. Lett.*, vol. 111, no. 22, p. 222104, 2017.
- [9] K. D. Chabak et al., “Lateral β -Ga₂O₃ field effect transistors,” *Semicond. Sci. Technol.*, vol. 35, no. 013002, p. 22, 2020.
- [10] M. Higashiwaki and G. H. Jessen, “Guest Editorial: The dawn of gallium oxide microelectronics,” *Appl. Phys. Lett.*, vol. 112, no. 6, p. 060401, 2018.
- [11] S. I. Stepanov Nikolaev, V.I., Bougrov, V.E., Romanov, A.E., “Gallium Oxide: Properties and Applications - A Review,” *Rev. Adv. Mater. Sci.*, vol. 44, pp. 63–86, 2016.
- [12] H. He et al., “First-principles study of the structural, electronic, and optical properties of Ga₂O₃ in its monoclinic and hexagonal phases,” *Phys. Rev. B - Condens. Matter Mater. Phys.*, vol. 74, no. 19, pp. 1–8, 2006.
- [13] T. Chen and K. Tang, “ γ -Ga₂O₃ quantum dots with visible blue-green light emission property,” *Appl. Phys. Lett.*, vol. 90, no. 5, pp. 3–6, 2007.
- [14] R. Roy, V. G. Hill, and E. F. Osborn, “Polymorphism of Ga₂O₃ and the System Ga₂O₃–H₂O,” *J. Am. Chem. Soc.*, vol. 74, no. 3, pp. 719–722, 1952.
- [15] H. He, M. A. Blanco, and R. Pandey, “Electronic and thermodynamic properties β -Ga₂O₃,” *Appl. Phys. Lett.*, vol. 88, no. 26, pp. 2–5, 2006.

- [16] S. Yoshioka, H. Hayashi, A. Kuwabara, F. Oba, K. Matsunaga, and I. Tanaka, “Structures and energetics of Ga₂O₃ polymorphs,” *J. Phys. Condens. Matter*, vol. 19, no. 34, 2007.
- [17] J. E. Medvedeva and C. L. Hettiarachchi, “Tuning the properties of complex transparent conducting oxides: Role of crystal symmetry, chemical composition, and carrier generation,” *Phys. Rev. B - Condens. Matter Mater. Phys.*, vol. 81, no. 12, 2010.
- [18] T. Gake, Y. Kumagai, and F. Oba, “First-principles study of self-trapped holes and acceptor impurities in Ga₂O₃ polymorphs,” *Phys. Rev. Mater.*, vol. 3, no. 4, p. 044603, Apr. 2019.
- [19] M. Mohamed et al., “The electronic structure of β -Ga₂O₃,” *Appl. Phys. Lett.*, vol. 97, no. 21, pp. 2–5, 2010.
- [20] J. B. Varley, J. R. Weber, A. Janotti, and C. G. Van De Walle, “Oxygen vacancies and donor impurities in β -Ga₂O₃,” *Appl. Phys. Lett.*, vol. 97, no. 14, pp. 10–13, 2010.
- [21] V. I. Nikolaev, S. I. Stepanov, A. E. Romanov, and V. E. Bougrov, *Gallium oxide*. Elsevier Ltd, 2019.
- [22] S. Lany, “Defect phase diagram for doping of Ga₂O₃,” *APL Mater.*, vol. 6, no. 4, 2018.
- [23] N. Ma et al., “Intrinsic electron mobility limits in β -Ga₂O₃,” *Appl. Phys. Lett.*, vol. 109, no. 21, pp. 1–6, 2016.
- [24] Y. Yao, R. F. Davis, and L. M. Porter, “Investigation of Different Metals as Ohmic Contacts to β -Ga₂O₃: Comparison and Analysis of Electrical Behavior, Morphology, and Other Physical Properties,” *J. Electron. Mater.*, vol. 46, no. 4, pp. 2053–2060, 2017.
- [25] N. A. Moser et al., “High pulsed current density β -Ga₂O₃ MOSFETs verified by an analytical model corrected for interface charge,” *Appl. Phys. Lett.*, vol. 110, no. 14, pp. 0–5, 2017.
- [26] N. Moser et al., “Ge-doped β -Ga₂O₃ MOSFETs,” *IEEE Electron Device Lett.*, vol. 38, no. 6, pp. 775–778, 2017.
- [27] M. Mohamed, K. Irscher, C. Janowitz, Z. Galazka, R. Manzke, and R. Fornari, “Schottky barrier height of Au on the transparent semiconducting oxide β -Ga₂O₃,” *Appl. Phys. Lett.*, vol. 101, no. 13, p. 132106, 2012.
- [28] W. Mönch, *Electronic Properties of Semiconductor Interfaces*. Springer Berlin, 2004.
- [29] S. M. Sze and K. K. Ng, *Physics of Semiconductor Devices*, 3rd ed. John Wiley and Sons Inc., 2007.
- [30] D. Khan, D. Gajula, S. Okur, G. S. Tompa, and G. Koley, “ β -Ga₂O₃ thin film based lateral and vertical Schottky barrier diode,” *ECS J. Solid State Sci. Technol.*, vol. 8, no. 6, pp. Q106–Q110, 2019.

- [31] K. Sasaki, M. Higashiwaki, A. Kuramata, T. Masui, and S. Yamakoshi, "Ga₂O₃ Schottky Barrier Diodes Fabricated by Using Single-Crystal B-Ga₂O₃ (010) Substrates," *IEEE Electron Device Lett.*, vol. 34, no. 4, pp. 493–495, 2013.
- [32] Z. Zhang, E. Farzana, A. R. Arehart, and S. A. Ringel, "Deep level defects throughout the bandgap of (010) β -Ga₂O₃ detected by optically and thermally stimulated defect spectroscopy," *Appl. Phys. Lett.*, vol. 108, no. 5, pp. 2–7, 2016.
- [33] A. Jayawardena, A. C. Ahyi, and S. Dhar, "Analysis of temperature dependent forward characteristics of Ni/(201) β -Ga₂O₃ Schottky diodes," *Semicond. Sci. Technol.*, vol. 31, no. 11, 2016.
- [34] A. M. Armstrong, M. H. Crawford, A. Jayawardena, A. Ahyi, and S. Dhar, "Role of self-trapped holes in the photoconductive gain of β -gallium oxide Schottky diodes," *J. Appl. Phys.*, vol. 119, no. 10, pp. 1–7, 2016.
- [35] T. Oishi, Y. Koga, K. Harada, and M. Kasu, "High-mobility β -Ga₂O₃(201) single crystals grown by edge-defined film-fed growth method and their Schottky barrier diodes with Ni contact," *Appl. Phys. Express*, vol. 8, no. 3, 2015.
- [36] T. Oishi, K. Harada, Y. Koga, and M. Kasu, "Conduction mechanism in highly doped Ga₂O₃ 201 single crystals grown by edge-defined film-fed growth method and their Schottky barrier diodes," *Jpn. J. Appl. Phys.*, vol. 55, no. 3, 2016.
- [37] D. Splith et al., "Determination of the mean and the homogeneous barrier height of Cu Schottky contacts on heteroepitaxial β -Ga₂O₃ thin films grown by pulsed laser deposition," *Phys. Status Solidi Appl. Mater. Sci.*, vol. 211, no. 1, pp. 40–47, 2014.
- [38] Z. Guo et al., "Anisotropic thermal conductivity in single crystal β -gallium oxide," *Appl. Phys. Lett.*, vol. 106, no. 11, pp. 1–6, 2015.
- [39] M. Slomski, N. Blumenschein, P. P. Paskov, J. F. Muth, and T. Paskova, "Anisotropic thermal conductivity of β -Ga₂O₃ at elevated temperatures: Effect of Sn and Fe dopants," *J. Appl. Phys.*, vol. 121, no. 23, p. 235104, Jun. 2017.
- [40] B. Chatterjee, K. Zeng, C. D. Nordquist, U. Singiseti, and S. Choi, "Device-Level Thermal Management of Gallium Oxide Field-Effect Transistors," *IEEE Trans. Components, Packag. Manuf. Technol.*, vol. 9, no. 12, pp. 1–1, 2019.
- [41] Q. Feng et al., "Catalytic growth and characterization of single crystalline Zn doped p-type β -Ga₂O₃ nanowires," *J. Alloys Compd.*, vol. 687, pp. 964–968, 2016.
- [42] J. Tao et al., "Investigation of growth characteristics, compositions, and properties of atomic layer deposited amorphous Zn-doped Ga₂O₃ films," *Appl. Surf. Sci.*, vol. 476, no. January, pp. 733–740, 2019.

CHAPTER 2 – MATERIAL GROWTH AND DEVICE ACCOMPLISHMENTS

2.1 Bulk Crystal Growth Capability

One motivating factor for developing gallium oxide based devices is the availability of high-quality native substrates that can be produced using traditional melt-based crystal growth methods such as Floating Zone (FZ) [1], [2], Czochralski (CZ) [3], [4], and Edge-Defined Film-Fed Growth (EFG) [5]. The primary benefit of using such techniques is that bulk crystals can be manufactured at lower costs than those associated with sublimation techniques like what is used for growing SiC substrates [6]. To date, EFG is the most commonly used technique in industry for manufacturing native Ga₂O₃ substrates. This is likely because EFG is so widely used for growing bulk sapphire crystals, and there are many similarities between Al₂O₃ and Ga₂O₃ that have made the transition relatively straightforward.

A schematic diagram of the EFG process is shown in **Figure 2.1(a)** [5]. The EFG method uses high-purity Ga₂O₃ powder which is melted in an Ir crucible under an atmospheric pressure containing 98%-N₂ /2%-O₂ and initiated using a β-Ga₂O₃ seed crystal. The melting temperature of 1900 °C is achieved using an RF induction coil. Once the melt reaches temperature, capillary force causes it to rise upward through a slit in an Ir die that is placed in the crucible. After reaching the top of the die, the melt makes contact with the seed crystal which determines the orientation of the resulting bulk crystal. Kuramata *et al.* reported a growth rate of 15 mm/hour when producing rectangular-shaped bulk crystals with dimensions of 2.4 x 60, 18 x 60, and 6 x 100 mm² shown in **Figure 2.1(b)** [5]. SiO₂ and SnO₂ powders can be added to the Ga₂O₃ source material to achieve n-type doping of Si and Sn, respectively. Fe and Mg powders have been added to Ga₂O₃ melt to create a more insulating material, but p-type conductivity has yet to be achieved in Ga₂O₃. Prior

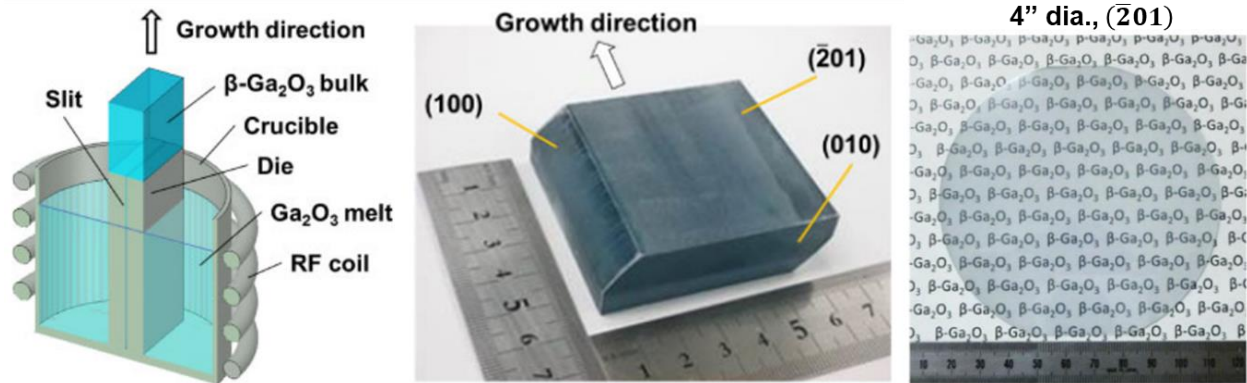


Figure 2.1 Images of bulk β - Ga_2O_3 crystals produced by EFG. Copyright (2016) The Japan Society of Applied Physics [5].

to any additional processing, the bulk crystals were annealed at 1450 °C for 6 hours in a N_2 ambient to reduce stress and fully activate donors. The crystals were processed into substrates using various saws (blade saw, multiple wire saw, and an electrical discharge wire saw), grinders, polishers, and a chemical mechanical polishing (CMP) machine. The fully processed substrates had a thickness of 650 μm and were cut along three different crystallographic planes, including $(\bar{2}01)$, (010), and (001). An image of a 4" diameter Ga_2O_3 substrate is shown in **Figure 2.1(c)** [5]. **Table 2.1** shows a list of the commercially available Ga_2O_3 substrates from Tamura Corporation [7] which are processed using the described method.

The reported EFG recipe results in bulk crystals with defect densities on the order of $1 \times 10^3 \text{ cm}^{-2}$ and without any detectable twin boundaries, as estimated using TEM. Impurity element concentrations were analyzed in the crystals using glow discharge mass spectroscopy (GDMS). The major residual unintentional impurity elements found in the Sn-doped Ga_2O_3 crystals containing 36 wt. ppm of Sn impurities were Al (0.9 wt. ppm), Si (1.6 wt. ppm), and Ir (2.9 wt. ppm). It was speculated that the Ir impurities originated from the growth crucible while the Si impurities were from the melt powder which contained 1.7 wt. ppm of Si impurities itself. No

explanation was provided on the origin of Al impurities. It is possible that the EFG equipment contained contaminants from prior AlN or Al₂O₃ crystal growths.

Substrate manufacturers are currently selling 10x15 mm² and 2” crystal Ga₂O₃ crystals for approximately \$740 (\$4.93/mm²) and \$1,250 (\$2.47/mm²), respectively. Making a direct cost comparison to GaN single crystal wafers can be difficult because of the vast number of vendors and wafer specifications, but some available (0001)-oriented Si-doped single crystals sold by MSE Supplies LLC include 10x10 mm² for \$419 (\$4.19/mm²), 2” LED-grade for \$2,795 (\$1.38/mm²), and 2” Laser-diode grade for \$3,895 (\$1.92/mm²). Meanwhile, the same manufacturer is charging only \$919 (\$0.05/mm²) for a 6” 4H-SiC wafer. The comparative cost of Ga₂O₃ single crystals is to be somewhat expected given that it’s a relatively new material.

Table 2.1 Commercially-available Ga₂O₃ substrates from Tamura Corporation [7].

10x15 mm² Substrates

Orientations	(001), (010), (-201)		
Dopant	Sn	UID	Fe
Conductivity	n-type	n-type	Insulating (>10 ¹⁰ Ω-cm)
N _d -N _a (cm ⁻³)	1x10 ¹⁸ – 2x10 ¹⁹	< 9x10 ¹⁷	-
Thickness (mm)	0.65		
FWHM (sec ⁻¹)	< 150		

2 Inch Substrates

Orientations	(-201)			(001)
Dopant	Sn	UID	Fe	Sn
Conductivity	n-type	n-type	Insulating (>10 ¹⁰ Ω-cm)	n-type
N _d -N _a (cm ⁻³)	1x10 ¹⁸ – 9x10 ¹⁸	< 9x10 ¹⁷	-	1x10 ¹⁸ – 2x10 ¹⁹
Thickness (mm)	0.68			0.65
FWHM (sec ⁻¹)	< 150			< 350

Reese *et al.* recently reported cost analysis data for manufacturing 6” Ga₂O₃ single crystal wafers and compared the finding to the total cost of manufacturing an individual SiC wafer [8]. The model used in their study included the costs associated with materials, energy, utilities, facilities, equipment, maintenance, and labor. Product yield was considered in all cost variables. The model also included the following assumptions: ingot dimensions of 1 meter in length and 6” diameter (similar to commercial SiC), manufacturing throughput of 5,000 wafers/month (determined by full equipment utilization), the Ir crucibles for growth could be used 10 times, 7-year equipment depreciation time, and 20-year building depreciation time. As shown in **Figure 2.2**, they estimate the total cost of manufacturing each 6” Ga₂O₃ wafer will be \$283, which is less than 31% of the SiC wafer cost found by the same model and is consistent with market pricing. They claim that Ga₂O₃ wafer production costs will likely be reduced further. The model predicts that it is possible to reduce the price/wafer to \$195 by doubling the crucible life to 20 growths, doubling the ingot length to 2 meters, and optimizing wafer polishing processes. Additional analysis estimates that the Ga₂O₃ wafer cost savings compared to SiC will lead to high-power devices that are 50% less expensive [8].

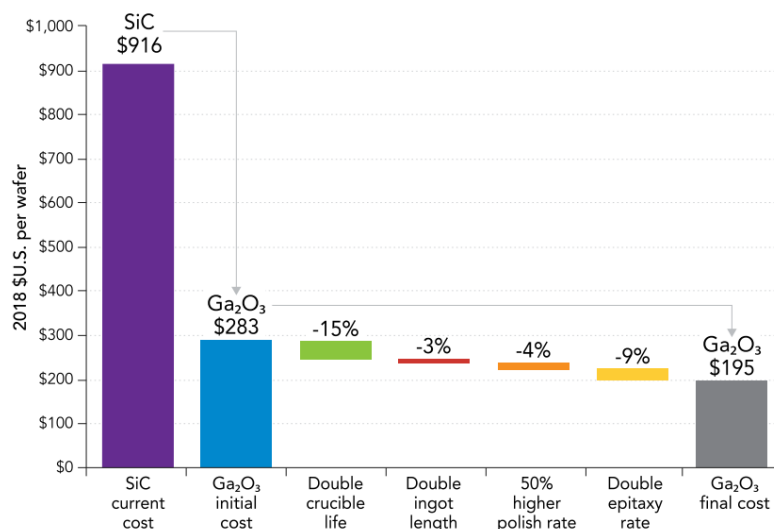


Figure 2.2 Modeled costs to manufacture 6” Ga₂O₃ and SiC wafers. Price reduction avenues are shown for Ga₂O₃, reducing the price/wafer cost to \$195. Copyright (2019) Elsevier [8].

2.2 Thin Film Growth

2.2.1 Overview

Ga_2O_3 thin film growth is not a new area of research. Because of its optical transparency, polycrystalline/amorphous Ga_2O_3 has been used for decades as a charge dissipation layer in optical applications [9]. Single-crystalline Ga_2O_3 was first being reported in 2000, where it was grown on c-plane sapphire using pulsed laser deposition [10]. Since that time, a wide variety of substrates have been explored for Ga_2O_3 thin film growth, such as Al_2O_3 , MgO , and Si , as well as native Ga_2O_3 substrates with various orientations and miscut angles. Currently, the four most commonly used Ga_2O_3 thin film growth techniques are metal-organic vapor phase epitaxy (MOVPE), halide vapor phase epitaxy (HVPE), pulsed laser deposition (PLD), and molecular beam epitaxy (MBE), but there have also been a fair number of reports on films grown by MOCVD and mist chemical vapor deposition (Mist-CVD). **Figure 2.3** shows a plot of carrier concentration versus mobility for homoepitaxial β - Ga_2O_3 films grown using MBE [11]–[14], MOVPE [15]–[17], HVPE [18], MOCVD [19], [20], Mist-CVD [21], and PLD [22], [23]. Additional details for each film can be seen in **Table 2.2**. The dotted line shows the β - Ga_2O_3 N_D -dependent mobility approximation of **Equation 1.3** at 300 K [24].

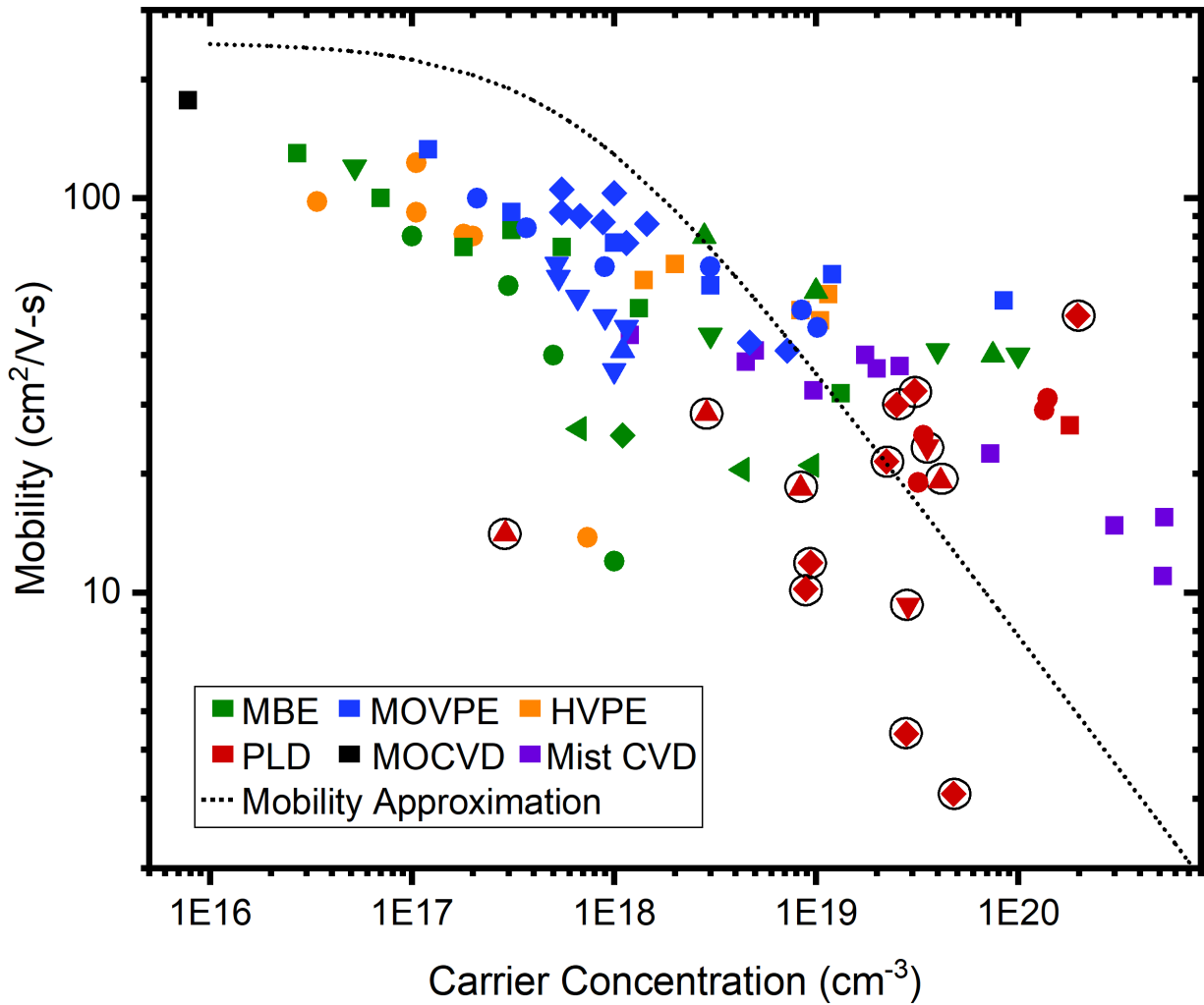


Figure 2.3 Mobility versus carrier concentration of homoepitaxial β -Ga₂O₃ thin films grown by MBE [11]–[14], MOVPE [15]–[17], HVPE [18], MOCVD [19], [20], Mist-CVD [21], and PLD [22], [23]. The dotted line shows the mobility approximation at 300 K as shown in **Equation 1.3** [24]. Copyright (2019) IOP Publishing [25].

Table 2.2 Film dopants and substrate orientation of films shown in **Figure 2.3** grown by varying growth techniques.

Growth Method	Film Dopant	Substrate Orientation	Symbol	Reference
HVPE	Si	(010)	■	[18]
	UID	(010)	●	[18]
MBE	Sn	(010)	■	[11]
	Sn	(010)	●	[12]
	Ge	(010)	▲	[13]
	Sn	(010)	▼	[13]
	Sn	(001)	◆	[14]
	Ge	(001)	◀	[14]
Mist CVD	Sn	(010)	■	[21]
MOCVD	UID	(010)	■	[19]
MOVPE	Si	(010)	■	[16]
	Sn	(010)	●	[16]
	Sn	(100)	▲	[15]
	Si	(100) -4° miscut	▼	[17]
	Si	(100) -6° miscut	◆	[17]
PLD	Si	(010)	■	[22]
	Si	(010)	●	[23]
	Sn	(010)	⊠	This Work
	Sn	(001)	⊡	This Work
	Si	(010)	⊙	This Work

2.2.2 Molecular Beam Epitaxy

Similarly to the growth of other semiconductor materials, MBE is capable of providing thin films with qualities that exceed those of the other techniques. MBE technology has demonstrated the ability to precisely control the carrier concentration of homoepitaxial Ga₂O₃

across four order of magnitude ($10^{16} - 10^{20} \text{ cm}^{-3}$) using various dopants while still maintaining high carrier mobility. In the first reports of homoepitaxial Ga_2O_3 thin films grown by MBE, Sasaki *et al.* used Sn dopants to achieve carrier concentration and mobility ranges of $2.6 \times 10^{16} - 1.3 \times 10^{19} \text{ cm}^{-3}$ and $101 - 32 \text{ cm}^2/\text{V-s}$, respectively [11].

Figure 2.4 shows a (a) schematic diagram of an MBE system used for growing Sn-doped Ga_2O_3 and (b) the MBE interior where the substrate heater and ozone nozzle are visible [26]. A liquid-cooled turbomolecular pump is commonly used for MBE growth to help minimize chamber pressure. The Ga_2O_3 thin films are grown using either ozone or an oxygen RF-plasma as the oxygen source. A Knudsen effusion cell is used for supplying the Ga flux by evaporating high-purity Ga onto the heated substrate. Additional effusion cells can be added for providing dopants such as Si, Sn, and Ge. Aside from fine-tune control over effusion cell evaporation and gas flow rates, MBE is beneficial because the system is equipped with a reflection high-energy electron diffraction (RHEED) gun that allows for *in-situ* monitoring of the substrate and thin film surfaces during growth. Ozone MBE is capable of growing Ga_2O_3 films at rates of up to $3 \text{ }\mu\text{m}/\text{hour}$, but suffers with thickness uniformity in comparison to RF-plasma MBE. On the contrary, RF-plasma

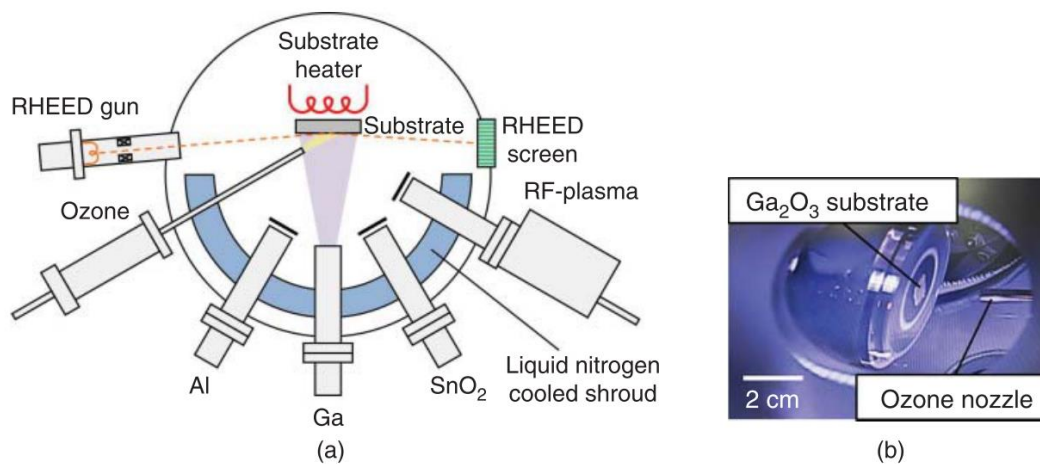


Figure 2.4 (a) Schematic drawing of an MBE system used for growing Sn-doped Ga_2O_3 and (b) an optical image from inside of an MBE growth chamber showing the substrate heater and ozone nozzle. Copyright (2019) John Wiley and Sons [26].

MBE is capable of growing films with a uniform thickness across an entire wafer, but the growth is reduced to about 1 $\mu\text{m}/\text{hour}$. Effusion cell temperatures and O_2 flow rates can be adjusted to manipulate Ga/Sn/O flux ratios using both methods.

Reports have shown that the MBE growth of Ga_2O_3 has three distinct growth regimes when using a constant oxygen flux [27]: (i) complete Ga incorporation in oxygen-rich conditions; (ii) growth rate saturation regardless of increased Ga flux; and (iii) growth rate decrease regardless of increased Ga flux. Vogt and Bierwagen speculated that the MBE growth kinetics of Ga_2O_3 involves the two chemical reactions shown below.



In reaction (1) we see the formation of a gaseous Ga_2O suboxide resulting from a Ga flux and constant oxygen flow. In reaction (2) the suboxide completes a desorption process from the growth front, reacts with two additional oxygen atoms, and then forms the solid phase Ga_2O_3 . This is interesting because normally the Ga_2O suboxide is volatile to growth, but here it plays a governing role in forming the Ga_2O_3 growth front.

To date, Sn and Si dopants have been studied more intensively than the Ge dopant. Using MBE for Si-doped Ga_2O_3 has proven to be an effective method when growing film with higher carrier densities (e.g. $n > 10^{18} \text{ cm}^{-3}$). One area of active research where this is beneficial is in the development of devices like MODFETs where modulation and delta doping are desired. Achieving lower carrier concentrations with Si is difficult because of O_2 reactions with the Si surface within the effusion cell [28]. For this reason Sn is often the dopant of choice for achieving lower carrier densities in Ga_2O_3 when using MBE. In 2014, Okumura *et al.* showed material with carrier concentrations as low as $1 \times 10^{17} \text{ cm}^{-3}$ and mobilities up to $80 \text{ cm}^2/\text{V-s}$ when using Sn

dopants [12]. However, Higashiwaki *et al.* later reported that Sn atoms tend to segregate from the Ga₂O₃ atoms and migrate to the surface of the film, causing doping non-uniformity issues [29].

2.2.3 Metal Organic Vapor Phase Epitaxy

Aside from material properties, one reason for choosing Ga₂O₃ over GaN or SiC in future high-power electronics is that it can be produced at a lower cost. From this standpoint, the optimization of high-throughput growth methods such as MOVPE is crucial. Ga₂O₃ thin films have been grown by MOVPE using either trimethylgallium (TMGa), triethylgallium (TEGa), or gallium dipivaloylmethanate (Ga(DPM)₃) as Ga precursors and either pure O₂ or H₂O as oxygen precursors [16], [30]. Sn dopants are incorporated using tetraethyltin (TESn, C₈H₂₀Sn) as the tin precursor [31]. Bubbler temperatures of 5 °C and -10 °C are typical for Ga and Sn precursors, respectively. An Ar carrier gas with a 300-1000 sccm flow rate is commonly employed as a carrier when H₂O is used for the oxygen precursor.

Contrary to the MBE (i.e. plasma-enhanced, ozone) Ga₂O₃ thin film growth rate typically limited to 3 μm/hour [32], [33], the CVD-based growth methods are capable of growth rates up to 10 μm/hour [30]. Shown in **Figure 2.5** is the (-201)-oriented Ga₂O₃ growth rate as a function of substrate temperature using TEGa and pure oxygen as Ga and O sources, respectively. It was found that the growth increased with TEGa flow rate and decreased with temperature, and a maximum growth rate of about 6.45 μm/hour was observed when using a substrate temperature of 850 °C, chamber pressure of 40 Torr, and 75 μmol/min TEGa flow rate.

(010)-oriented Si-doped Ga₂O₃ thin films grown on Fe-doped Ga₂O₃ substrates by MOVPE had reported carrier concentration and mobility values ranging from $1 \times 10^{17} - 1 \times 10^{20} \text{ cm}^{-3}$ and $130 - 50 \text{ cm}^2/\text{V-s}$ [17]. In the same work, films grown on (100)-oriented Ga₂O₃ had a maximum

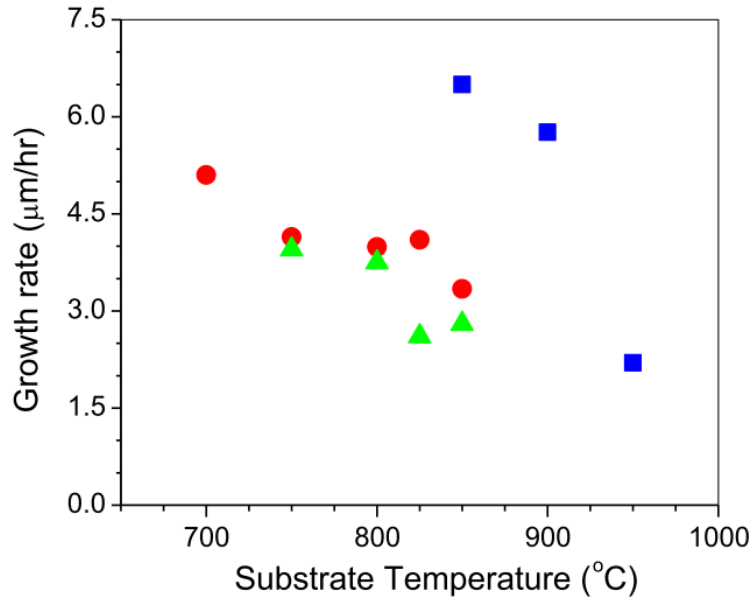


Figure 2.5 Growth rate dependence on substrate temperature for Ga_2O_3 films grown from TEGa precursor at the chamber pressure and TEGa molar flow rate of: 40 Torr and 50 $\mu\text{mol}/\text{min}$ (●), 60 Torr and 50 $\mu\text{mol}/\text{min}$ (▲), and 40 Torr and 75 $\mu\text{mol}/\text{min}$ (■). The oxygen flow rate was 300 sccm. Copyright (2017) Elsevier [30].

electron mobility of only 50 $\text{cm}^2/\text{V}\cdot\text{s}$. The decreased film quality was attributed to a high concentration of planar defects which were thought to be twin lamella stacking faults since they were parallel to the (100) plane and had a $c/2$ glide reflection. It was speculated that these crystal domains with different orientations along the c -plane resulted in the formation of incoherent twin boundaries with dangling bonds that lead to charge carrier compensation and reduced electron mobility. The film quality was increased substantially (mobility of 110 $\text{cm}^2/\text{V}\cdot\text{s}$ for $1 \times 10^{18} \text{ cm}^{-3}$ carrier density) when using (100)-oriented substrates with a miscut angle of -6° . Incorporating a (100)- 6° miscut decreased the width of terraces on the substrate surface, allowing for the adatom diffusion length to be long enough for the development of step-flow growth. The films resulting from the use of a substrate miscut had transport properties that were superior to those grown by MBE, as shown in **Figure 2.3**.

One known issue with MOVPE-grown Ga_2O_3 is the unintentional inclusion of carbon impurities that originate from the metalorganic precursors [34]. It has been reported that carbon impurities form shallow donors in $\beta\text{-Ga}_2\text{O}_3$ which can cause instability in doping control and result in elevated doping levels that are higher than intended [35]. This is an issue when growing drift layers for Schottky barrier diode applications where a low carrier concentration is desired. This could help explain the relatively-high minimal doping concentration of $1 \times 10^{17} \text{ cm}^{-3}$ observed in MOVPE-grown films as shown in **Figure 2.3**. On the contrary, a benefit of MOVPE growth is its capability to grow films at increased temperatures since the chamber pressure is significantly higher. Reports have shown that using growth temperatures greater than $800 \text{ }^\circ\text{C}$ benefits $\beta\text{-(Al}_x\text{Ga}_{1-x})_2\text{O}_3$ thin film growth by increasing its solubility limit and allowing for films where $x > 40\%$, enabling the growth of abrupt super lattice interfaces using $\beta\text{-(Al}_x\text{Ga}_{1-x})_2\text{O}_3/\beta\text{-Ga}_2\text{O}_3$ heterostructures [36].

2.2.4 Pulsed Laser Deposition

Pulsed laser deposition (PLD) is a physical vapor deposition method that was first demonstrated in 1965 by Smith and Turner where they used a ruby laser to ablate a wide variety of materials including Sb_2S_3 , ZnTe , MoO_3 , and Ge [37]. Laser technology advancement has resulted in the availability of lasers with higher energy densities, shorter wavelengths, faster repetition rates, and shorter pulse times, which increased the capability of PLD by expanding the materials that can be grown. During growth, a high-power laser is used to ablate the target material, creating a plasma which is propelled away from the target and onto the substrate surface as shown in **Figure 2.6** using an **(a)** optical image [38] and **(b)** schematic drawing. A large quantity of parameters can be altered to fine-tune the growth, including the laser (energy density, repetition

rate, number of pulses), chamber ambient (pressure, ambient gas flow rates), mechanical (target and substrate rotation velocities, target rastering velocity), thermal (substrate temperature), and the composition of the target species.

Targets are fabricated by mixing predefined molar concentrations of powders, pressing the powder into a cylinder, and sintering in a high-temperature furnace to increase density. In this work, 5N Ga₂O₃ powder was mixed with 3N SnO₂ or SiO₂ powders with molar concentrations of the dopant species ranging from 0.1 – 10 mol%. Targets were pressed into a 1” diameter cylinder at 5300 psi and sintered for 12 hours at 1600 °C. Targets fabricated in industry are commonly processed using a ‘hot press’ technique where the target is pressed and sintered simultaneously.

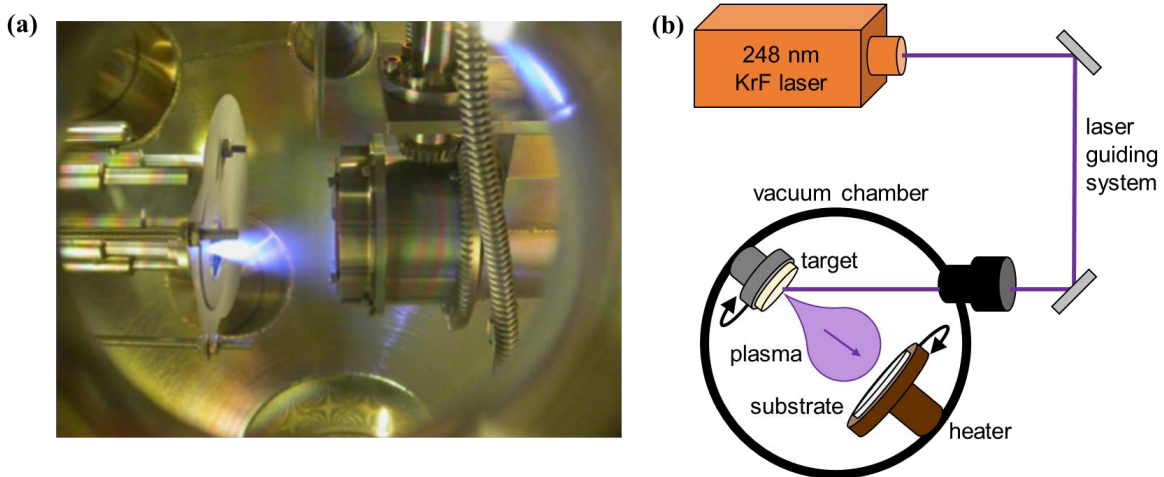


Figure 2.6 (a) Optical image showing the inside of the PLD chamber used in this work during growth [38] and (b) schematic drawing of the PLD growth technique.

One supposed benefit of PLD is that the target composition can be directly translated into the film composition, assuming equilibrium throughout the target. However, as depicted in **Figure 2.7**, reports on PLD-grown Si-doped Ga₂O₃ have shown that this is not always the case. The dashed line represents the theoretical concentration of Si atoms present in the film as calculated by **Equation 2.1**, where $\rho_{\text{Ga}_2\text{O}_3}$ is the density of Ga₂O₃ (6.44 g/cm³), M is molecular mass, x is the fractional mass of the target, and N_A is Avogadro’s number (6.022x10²³ atoms/mol) [39]. Zhang

et al. grew a multi-layer Si-doped Ga₂O₃ structure using different targets for each layer with increasing SiO₂ weight percentages [40]. The structure was evaluated using secondary ion mass spectroscopy (SIMS), and it was found that the Si concentration in the layers increased linearly from $7 \times 10^{18} - 4 \times 10^{20} \text{ cm}^{-3}$ when varying the target SiO₂ content from 0.01 – 0.7 wt.%, respectively. Leedy *et al.* published a similar report where a series of thin films were grown using commercial targets with SiO₂ content varying from 0.01 – 1 wt.% [23]. The Si profile of each film was measured by SIMS, and despite the target SiO₂ composition varying over three orders of magnitude, a small Si concentration variation in the range of $9.25 \times 10^{19} - 4.15 \times 10^{20} \text{ cm}^{-3}$ was observed. This discrepancy was attributed to the target composition containing more SiO₂ than advertised at lower concentrations [23].

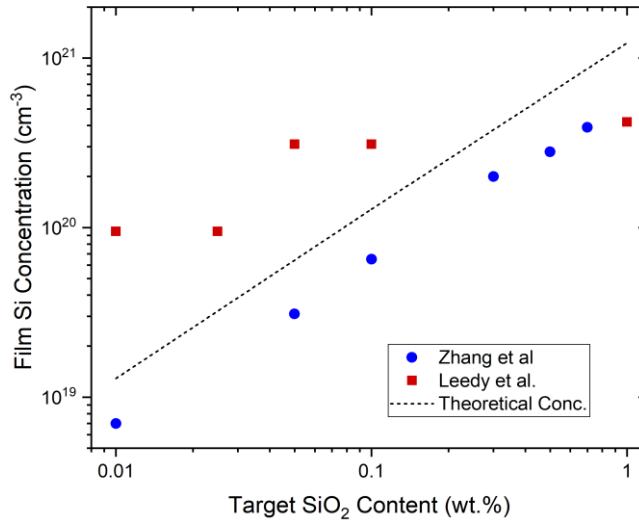


Figure 2.7 Si concentration of Si:Ga₂O₃ homoepitaxial thin films as a function of SiO₂ wt.% in PLD targets. Films were evaluated by SIMS [23], [40].

$$N_{Si} = \frac{\frac{\rho_{Ga_2O_3} N_A}{M_{Ga_2O_3}}}{1 + \left(\frac{1-x}{2x}\right) \left(\frac{M_{SiO_2}}{M_{Ga_2O_3}}\right)} \quad [cm^{-3}] \quad (2.1)$$

PLD has shown to be a great method for producing Ga₂O₃ thin films when a carrier concentration of more than $1 \times 10^{17} \text{ cm}^{-3}$ is desired as shown in **Figure 2.8**. Interestingly, among all of the analyzed growth methods, PLD has also shown capable of growing the most conductive

Ga₂O₃ films. In this work, a conductivity of 1591 Ω⁻¹cm⁻¹ was achieved using Si doping. Additional discussion on this achievement will be provided in the following chapters. One downside of PLD is the relatively low mobility of the films grown in comparison to other growths methods, most likely caused by an increased defect density in the films. As mentioned, the source material used during growth is made of 5N Ga₂O₃ and SiO₂/SnO₂ powders, but it is possible that additional impurities are incorporated into the targets during fabrication. Whereas in other growth methods the source material remains in the original packaging and is not susceptible to the incorporation of unwanted impurities.

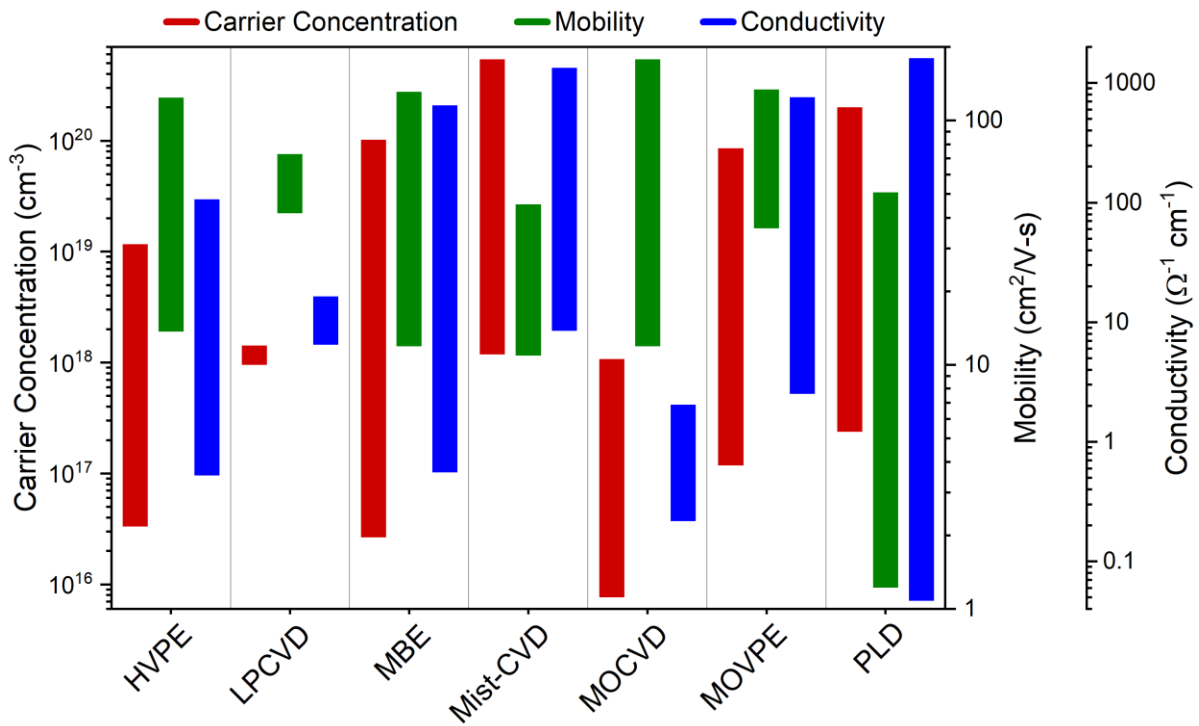


Figure 2.8 Carrier concentration, mobility, and conductivity values of homoepitaxial Ga₂O₃ thin films grown by different growth methods.

2.3 Ga₂O₃ Device Types

2.3.1 Overview

Ga₂O₃ has a wide variety of attributes that making it useful in many possible applications. Its optical transparency and wide bandgap alignment give rise to devices like deep-UV photodetectors, while its critical electric field strength gives promise for high-power devices such as Schottky barrier diodes and a variety of field-effect transistors.

2.3.2 Ultraviolet Photodetectors

Solar-blind deep-ultraviolet photodetectors (PDs) are useful for applications including ozone monitoring, missile tracking, combustion process monitoring, flame detection, and chemical/biological analysis [41]. The UV spectrum (10 – 400 nm) can be broken into subdivisions of UV-A (315 – 400 nm), UV-B (280 – 315 nm), UV-C (100 – 280 nm), and V-UV (10 – 200 nm). Solar radiation occupies the UV-C spectrum, but is absorbed by diatomic oxygen (100 – 200 nm) or triatomic oxygen (200 – 280 nm) in the Earth’s atmosphere [42]. This spectral range of 200 – 280 nm is referred to as being ‘solar-blind’ because of this phenomenon, and it is important because signal within this wavelength range can be efficiently detected without noise from solar-generated UV light. The Ga₂O₃ direct bandgap of 4.9 eV corresponds to a wavelength of 250 nm, making it a promising material for deep-UV detection. Ga₂O₃-based UV PDs have been demonstrated using a wide variety of structures including Ga₂O₃ thin films [41], [43], nanostructures [44], [45], and heterojunctions [46], [47]. One of the most common device structures used for fabricating UV-PDs is the metal-semiconductor-metal (MSM) type. As shown in **Figure 2.9**, the MSM PD has a series of interdigitated fingers extending from two Schottky contacts on the face of the semiconductor into the center of the device where UV radiation is

absorbed and creates electron-hole pairs [41]. The carriers are swept to the electrodes by applying a constant DC bias across the two contacts.

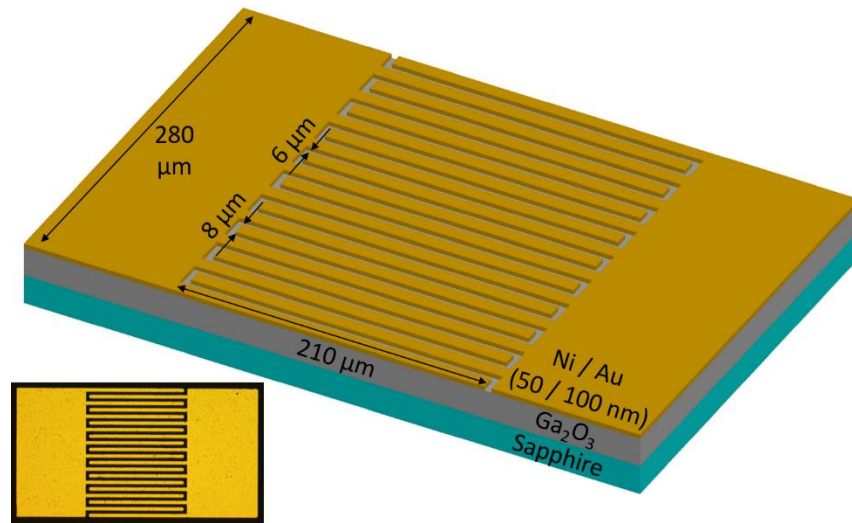


Figure 2.9 Schematic diagram of a MSM UV Photodetector fabricated using Au/Ni/Ga₂O₃/Ni/Au on a sapphire substrate. Inset shows an optical image of the device surface. Copyright (2019) John Wiley and Sons [41].

While the MSM PD structure is relatively simple from a fabrication standpoint, there are instances of Ga₂O₃ PDs that involved additional attributes to enhance their performance. **Figure 2.10(a)** shows responsivity and response time data for UV PDs fabricated using bulk or thin film Ga₂O₃ [41], [48]–[62]. Qin *et al.* was able to obtain a record-high Ga₂O₃ PD responsivity of 3000 A/W using the enhancement-mode metal-oxide-semiconductor field-effect phototransistor shown in **Figure 2.10(b)** [51]. The phototransistor had an incredibly low dark current of 0.7 pA when using a fixed V_{DS} of 20 V. When under 254 nm illumination the drain-source current (I_{DS}) increased by over six orders of magnitude to 1 μA. Chen *et al.* achieved a 1 μs response time using the Au/β-Ga₂O₃ nanowire array shown in **Figure 2.10(c)**, which is the highest reported response time for Ga₂O₃ PDs [57]. Given the nature of the utilized Schottky junction, the device was operable without an externally applied bias at the cost of two decades of responsivity. The device

already had a low responsivity of just 2.9 mA/W, so the self-powered option is not ideal. Under a 30 V reverse bias, the photocurrent had a linear relationship with incident light intensity from 0.1 – 2.0 mW/cm², suggesting that the device could function as a solar-blind UV light amplitude photodetector. Lee *et al.* fabricated a flexible Ga₂O₃ PD using a polyimide substrate, as shown in **Figure 2.10(d)** [60]. The added functionality of a flexible PD could prove to be useful for a variety of sensing applications. It is more likely that the merit of this work is in the high UV detection performance obtained from a PD with an amorphous Ga₂O₃ film. The PD had a fast 2.97 μs response time and high responsivity of 45 A/W. This indicates that Ga₂O₃ PDs could likely be fabricated on any surface and still have more than capable detection performance.

The Ga₂O₃ PDs discussed here have better performance than what is currently available on the market. **Figure 2.10(a)** also shows the performance of three non-Ga₂O₃-based PDs available from Thor Labs. These detectors were made using GaP (model# FGAP71), Si (model# FDS101), and UV-enhanced Si (model# SM1PD2A). These detectors were chosen because they are advertised as being capable of detection in the UV region. The GaP- and Si-based PDs are capable of faster response times, but lack severely in responsivity. Only a single response time was reported for each detector and it is unlikely that it was measured under UV incidence, which could increase the response time. Responsivity values shown here are for wavelengths of 250 nm. None of the shown PDs are solar-blind, which limits their potential even further when compared to Ga₂O₃ PDs.

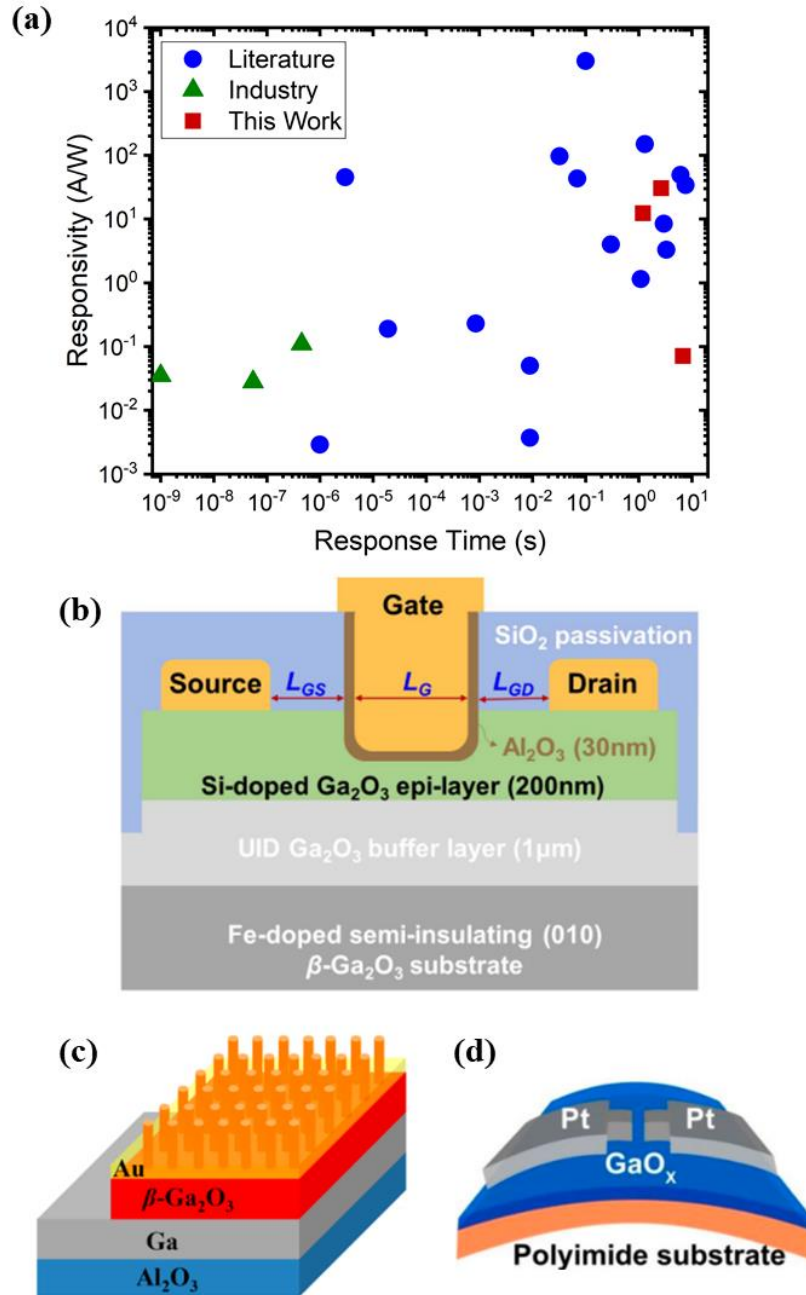


Figure 2.10 (a) Responsivity and response time of UV PDs fabricated using bulk and thin film Ga_2O_3 [41], [48]–[62]. Three non- Ga_2O_3 -based PDs from industry are also shown. (b) Schematic diagram of enhancement-mode MOSFEPT. Copyright (2019) IEEE [51]. (c) Schematic diagram of Au/ β - Ga_2O_3 nanowire array. Copyright (2016) American Chemical Society [57]. (d) Ga_2O_3 PD fabricated on flexible polyimide substrate. Copyright (2017) American Chemical Society [60].

2.3.3 Schottky Barrier Diodes

Gallium oxide is expected to control a significant portion of the high-power Schottky barrier diode (SBD) application space because of its R_{ON} - V_{BR} metric as determined by **Equation 1.1**. These two parameters are key for determining the device performance. Avalanche breakdown voltage for SBDs determined from the critical electric field strength of the material. Given that the E_C of Ga_2O_3 is 8 MV/cm, the only semiconductors that could challenge this application space are AlN (15.4 MV/cm) and diamond (10.0 MV/cm). There are challenges associated with each material. Ga_2O_3 and AlN cannot be doped p-type, while the potential of diamond material suffers from availability of substrates with sufficient size and quality. AlN substrates are currently being manufactured by multiple commercial suppliers (HexaTech and Crystal IS), but are very expensive and somewhat limited in availability when compared to what is commercially available for Ga_2O_3 [63]. This is partially due to the difficulty in producing AlN from a melt, which as previously discussed is a major upside for Ga_2O_3 . High-quality single crystals are the basis of producing device-ready epitaxial layers, and hence, it is currently more favorable to study Ga_2O_3 in the area of SBDs because of the device structure requiring a quality drift layer.

Sasaki *et al.* reported the first SBD fabricated using Ga_2O_3 in 2013 [64]. The device structure was fabricated from an undoped (010) Ga_2O_3 substrate with a top-side Pt/Ti/Au Schottky metal layer and backside Ti/Au ohmic metal layer. As shown in **Figure 2.11(a)**, the device exhibited an impressive 150 V reverse breakdown voltage, regardless of no drift layer, passivation layer, or edge termination being used.

Yang *et al.* showed that SBD performance could be enhanced by incorporating a low-doped Ga_2O_3 drift layer [65]. The vertical device was fabricated onto an (001)-oriented Sn-doped Ga_2O_3 substrate with a carrier concentration of $3.6 \times 10^{18} \text{ cm}^{-3}$. A 20- μm -thick lightly Si-doped (2×10^{16}

cm⁻³) Ga₂O₃ drift layer was grown using HVPE. Chemical mechanical polishing (CMP) was performed to remove any top-side pits, resulting in a final epilayer thickness of 10 μm. Topside Schottky and bottom side ohmic metal layers of Ni/Au (20 nm/80 nm) and Ti/Au (20 nm/80 nm) were used, respectively. The analyzed SBDs exhibited a reverse breakdown voltage of over 1 KV and R_{ON} of 6.7 mΩ-cm², resulting in a V_{BR}²/R_{ON} figure-of-merit of 154 MW/cm². The device schematic and resulting reverse I-V characteristic can be seen in **Figure 2.11(b)**.

Konishi *et al.* was able to obtain similar SBD performance when field-plating the device [66]. A 10-μm-thick Si-doped (2x10¹⁶ cm⁻³) Ga₂O₃ drift layer was grown on a (001) Sn-doped Ga₂O₃ substrate using HVPE. CMP was used to remove pits that can result from HVPE growth, giving a final epilayer thickness of 7 μm. A 300-nm-thick SiO₂ layer was deposited onto the top patterned surface to form a field-plated Schottky contact with Pt/Ti/Au (15 nm/5 nm/500 nm). Ti/Au (20 nm/230 nm) was used for the backside ohmic contact. The SBD had an R_{ON} of 5.1 mΩ-cm² and reverse breakdown voltage of 1076 V. The device schematic and resulting reverse I-V characteristic can be seen in **Figure 2.11(c)**. The two-dimensional electric field distribution was simulated for the measured -1076 V breakdown condition. These simulations indicated that the maximum electric field reached 5.1 MV/cm in the Ga₂O₃ drift layer underneath the anode foot edge, which is much larger than what is capable in GaN and SiC SBDs.

The Ga₂O₃ SBD performance was further improved with the realization of drift layers with even lower carrier densities. Yang *et al.* were able to grow a 20-μm-thick Si-doped Ga₂O₃ drift layer with low carrier concentration of 2x10¹⁵ cm⁻³ by HVPE to achieve excellent device characteristics [67]. Edge termination and metal layer details can be seen in the schematic diagram of **Figure 2.11(d)**. A reverse breakdown voltage of 2300 V was observed, with forward current densities of more than 1 A/cm² at a 3 V bias.

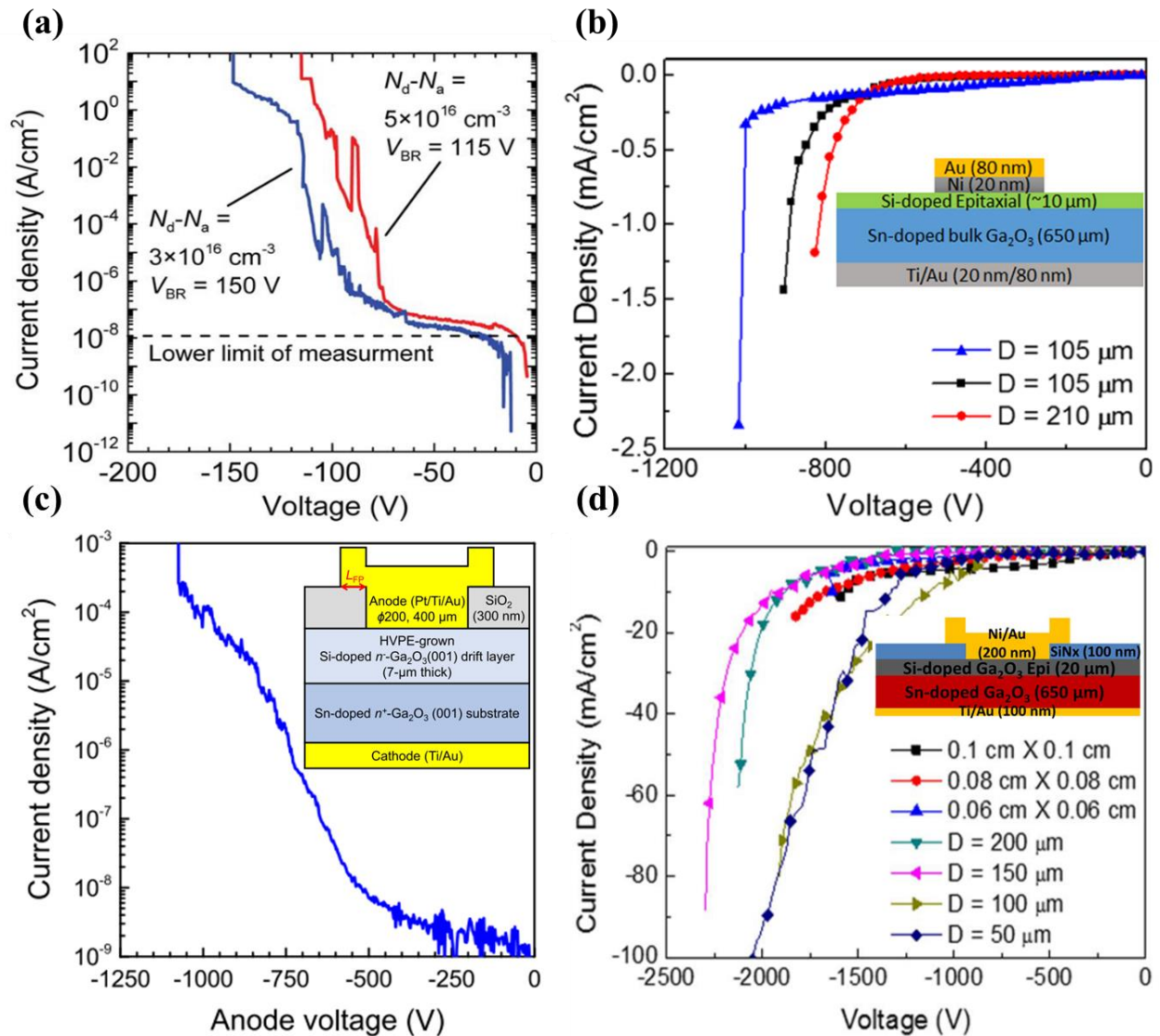


Figure 2.11 State-of-the-art Schottky barrier diodes. (a) Copyright (2013) IEEE [64]. (b) Copyright (2017) AIP Publishing [65]. (c) Copyright (2017) AIP Publishing [66]. (d) Copyright (2018) Electrochemical Society [67].

2.3.4 Field-Effect Transistors

In 2012, Higashiwaki *et al.* reported on the first fully-functional single-crystal MESFET using Sn-doped Ga_2O_3 grown on a (010) semi-insulating Mg-doped Ga_2O_3 using MBE [68]. The device could be pinched off using a gate-source voltage (V_{GS}) of $< -20 V$ and had an off-state VBR of over 250 V. The device had a relatively low leakage current of just 3 μA , resulting in an

ON/OFF drain current ratio of over 10^4 . While this performance was not impressive by today's standards, the work represented a breakthrough in Ga_2O_3 device development. It showed that a pathway for functional Ga_2O_3 devices was available, and presented a baseline for comparison in future Ga_2O_3 transistor advancements. Since this time, the Ga_2O_3 FET research area has been mostly dominated by the Air Force Research Laboratory – Sensors Directorate (AFRL, USA) and the National Institute of Information and Communications Technology (NICT, Japan). Over the last eight years, these two groups, along with a group from Ohio State University (OSU, USA), have led the Ga_2O_3 FET research endeavor. NICT has focused on the development of depletion-mode FETs, AFRL has published on a wide variety of high-performance transistors with different applications and operating modes, and OSU has reported on delta-doped and modulation-doped FETs with high current amplitudes. Their results will be discussed in the remainder of this section.

In 2013, Higashiwaki *et al.* reported on the first depletion-mode Ga_2O_3 MOSFET [69]. He then expanded on that work using a Si ion-implantation process to greatly reduce the source/drain ohmic metal contact resistance to just $8 \times 10^{-6} \Omega\text{-cm}^2$ [70]. This allowed for an I_{DS} of 65 mA/mm while applying V_{DS} and V_{G} biases of 30 V and 6 V, respectively, resulting in an ON/OFF current ratio that was greater than ten orders of magnitude. The device had an OFF-state V_{BR} of 415 V while applying a V_{GS} of -30 V. As shown in **Figure 2.12**, Wong *et al.* was able to increase the V_{BR} to 755 V by field-plating the MOSFET, which remains to be the highest reported breakdown voltage to date for depletion-mode operating lateral FETs that were measured in ambient (i.e. no fluorinert or vacuum) [71]. The MOSFET transfer curve showed a max transconductance (g_{m}) of about 3.4 mS/mm, and the I-V characteristic remained as expected while operating the device up to 300 °C. The increasing temperature did result in a lower I_{DS} ON/OFF ratio, which dropped from 10^9 to 10^3 for temperatures of 25 °C to 300 °C, respectively.

Until 2016, reports on Ga₂O₃ transistors were mostly limited to depletion-mode devices for high-power applications. Chabak *et al.* then reported on an enhancement-mode Ga₂O₃ wrap-gate FinFET [72]. A device schematic is shown in **Figure 2.13(a)**. The device was fabricated by first growing a 300 nm Sn-doped Ga₂O₃ channel ($N_D = 2.3 \times 10^{17} \text{ cm}^{-3}$) on an Mg-doped (100) Ga₂O₃ substrate using MOVPE. Electron beam lithography was used for forming the fin channels of 300 nm widths and 900 nm pitch. Two Cr masks were evaporated over top of the device to create bulk mesa contacts for source and drain electrodes. The Cr layers were then etched using a BCl₃ inductively coupled plasma process, resulting in triangle-shaped fins. Ti/Al/Ni/Au (20/100/50/50 nm) ohmic metal was deposited, followed by a 20 nm Al₂O₃ gate dielectric and Ni/Au (20/480 nm) gate metal layers. A false-colored SEM image of the device is shown in **Figure 2.13(b)**. The device showed excellent performance, with an I_{DS} ON/OFF ratio of over 10^5 . A V_{BR} of 612 V was achieved, which is still the highest reported value for Ga₂O₃ enhancement-mode transistors and could likely be improved with the addition of field-plating.

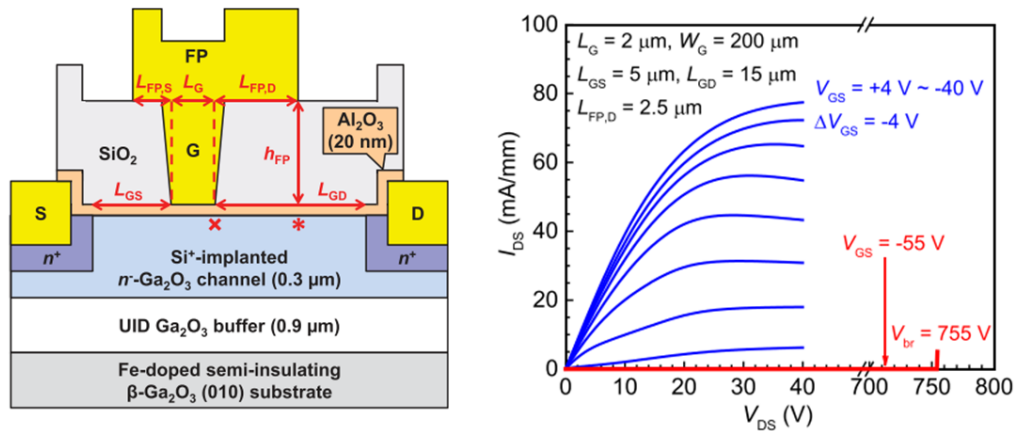


Figure 2.12 Device schematics and I - V characteristics for field-plated depletion-mode Ga₂O₃ MOSFETs with a 750 V breakdown voltage. Copyright (2016) IEEE [71].

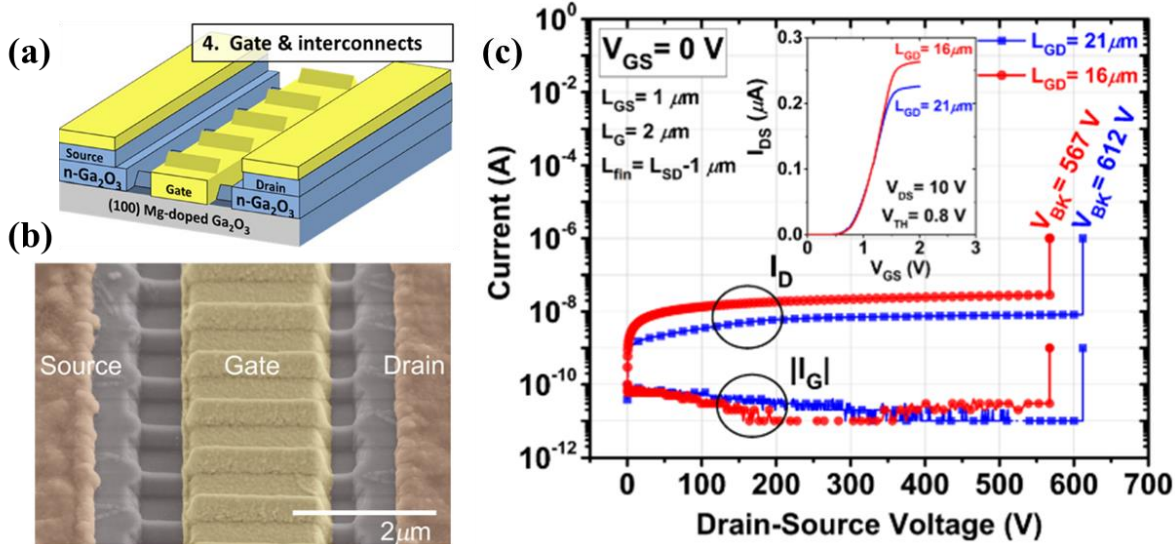


Figure 2.13 (a) Device schematic and (b) false-colored SEM image of enhancement-mode FinFET device. (c) I_{DS} - V_{DS} characteristic showing V_{BR} of 612 V. Copyright (2016) AIP Publishing [72].

Around the same time, Green *et al.* reported on depletion-mode MOSFETs with record-breaking electric field strength of more than 3.8 MV/cm [73]. At the time of publication, this was the highest reported E_C for Ga_2O_3 , experimentally surpassing GaN and SiC for the first time. In 2017, Green *et al.* also reported findings on Ga_2O_3 MOSFETs for RF applications with a record-high g_m of 21 mS/mm and current density of 150 mA/mm [74]. A sub-micron gate recess process was used to implement a highly-doped ohmic cap layer during fabrication that enabled the device to reach extrinsic cutoff (f_T) and maximum operating (f_{max}) frequencies of 3.3 and 12.9 GHz, respectively.

Xia *et al.* demonstrated a two-dimensional electron gas (2DEG) in Ga_2O_3 by Si delta-doping with MBE [75]. The thin film was grown on a (010) Fe-doped Ga_2O_3 substrate using Ga and Si effusion cells and an oxygen plasma source. The epitaxial structure shown in **Figure 2.14(a)** contained a 100 nm undoped Ga_2O_3 buffer layer, a Si delta-doped layer, and a 20 nm undoped Ga_2O_3 barrier layer. The Si delta-doped layer was obtained by opening the Si effusion cell shutter for 4 seconds, which corresponds to a 0.2 nm thickness. The energy band diagram and

corresponding charge profile shown in **Figure 2.14(b)** were calculated through Schrodinger-Poisson simulations, and resulted in a sheet concentration of $1.2 \times 10^{13} \text{ cm}^{-2}$ in the delta-doped layer. MESFET fabrication began by first patterning the surface and using a CF_4 ICP-RIE process to etch trenches into the Ga_2O_3 epilayer. Heavily Si-doped Ga_2O_3 was re-grown over the trenches to create source/drain regions with doping concentrations of $2 \times 10^{20} \text{ cm}^{-3}$. A Ti/Au/Ni (30/100/30 nm) ohmic metal stack was deposited for source/drain contacts, and resulted in a low contact resistance of $1.5 \ \Omega\text{-mm}$. A Ni/Au/Ni (30/100/30 nm) metal stack was used to form a Schottky gate barrier. The fabricated device has excellent I-V characteristics, with a peak I_{DS} of 140 mA/mm and g_{m} of 34 mS/mm, as shown in **Figure 2.14(c)**. The device was fully pinched-off at $V_{\text{GS}} = -5 \text{ V}$. A density-dependent field electric mobility that varied from $55 - 95 \text{ cm}^2/\text{V-s}$ was obtained from the transfer characteristic. The breakdown voltage of the device was estimated to be 170 V, but was not determined experimentally.

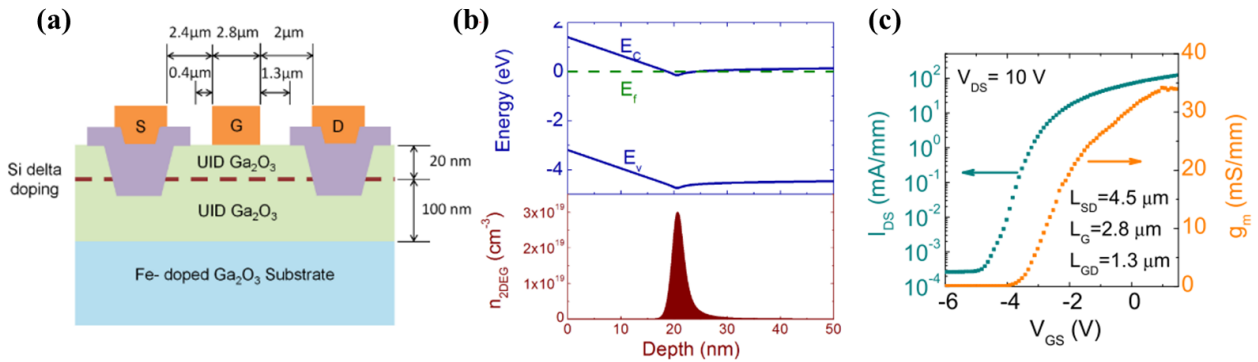


Figure 2.14 (a) Schematic drawing of delta-doped Ga_2O_3 MOSFET with corresponding (b) energy band diagram and 2DEG charge profile. (c) Transfer characteristic showing high peak I_{DS} and g_{m} values with pinch-off at $V_{\text{GS}} = -5 \text{ V}$. Copyright (2018) IEEE [75].

2.3.5 Challenges to Explore

Many promising results have been published on $\beta\text{-Ga}_2\text{O}_3$ that appear promising for the future device applications, but the material is still maturing and much work is required. Developing $\beta\text{-Ga}_2\text{O}_3$ for its intended role in high-power electronics requires better growth optimization and

understanding of fundamental material properties. In particular, thermal properties need to be further explored and heat dissipation solutions should be optimized in order to fully realize the theoretical capability of β -Ga₂O₃. The research of this work is focused on four topics with particular objectives listed for each:

- (i) Growth optimization of high-quality single-crystalline Ga₂O₃ layers using PLD.
 - Optimize heteroepitaxial growth conditions on sapphire substrates.
 - Develop an epitaxial growth recipe using native Ga₂O₃ substrates.
 - Evaluate structural properties by XRD, AFM, and TEM.
- (ii) Development of doping mechanisms to achieve controllable n-type conductivity.
 - Investigate Si- and Sn-doping to achieve a wide range of conductivity and carrier concentration control.
 - Evaluate electrical properties by Hall, SIMS, and time-domain terahertz spectroscopy characterization methods.
- (iii) Investigation of anisotropic thermal properties and scattering mechanisms in Ga₂O₃.
 - Investigate bulk Ga₂O₃ anisotropy to evaluate thermal properties in unexplored crystallographic directions.
 - Explore the effects of doping on thermal properties and identify the associated scattering mechanisms.
 - Develop methodology for analyzing fundamental thermal properties of epitaxial material.
- (iv) Device optimization of different Schottky diode structures.
 - Develop Schottky barrier diode structures for enhanced heat dissipation purposes.
 - Evaluate the effects of substrate orientation and thickness using chemical-mechanical-polishing wafer thinning methods.
 - Optimize drift layer thickness and doping for high performance.
 - Characterize electrical performance using I-V, C-V, EBIC, and breakdown voltage measurement techniques.
 - Analyze thermal dissipation effects of wafer thinning by optical thermography.

2.4 References

- [1] N. Suzuki, S. Ohira, M. Tanaka, T. Sugawara, K. Nakajima, and T. Shishido, “Fabrication and characterization of transparent conductive Sn-doped β -Ga₂O₃ single crystal,” *Phys. status solidi*, vol. 4, no. 7, pp. 2310–2313, 2007.
- [2] J. Zhang et al., “Growth and spectral characterization of β -Ga₂O₃ single crystals,” *J. Phys. Chem. Solids*, vol. 67, no. 12, pp. 2448–2451, 2006.
- [3] Z. Galazka et al., “Czochralski growth and characterization of Ga₂O₃ single crystals,” 2010, 12th ed., vol. 45, pp. 1229–1236.
- [4] Z. Galazka et al., “Scaling-up of bulk β -Ga₂O₃ single crystals by the Czochralski method,” *ECS J. Solid State Sci. Technol.*, vol. 6, no. 2, pp. Q3007–Q3011, 2017.
- [5] O. Ueda et al., “High-quality β -Ga₂O₃ single crystals grown by edge-defined film-fed growth,” *Jpn. J. Appl. Phys.*, vol. 55, no. 12, pp. 0–6, 2016.
- [6] S. J. Pearton et al., “A review of Ga₂O₃ materials, processing, and devices,” *Appl. Phys. Rev.*, vol. 5, no. 1, p. 011301, Mar. 2018.
- [7] Tamura Corporation and Novel Crystal Technology, “Available Ga₂O₃ Substrates,” 2019. [Online]. Available: <https://www.tamuracorp.com/file.jsp?id=13281>.
- [8] S. B. Reese, T. Remo, J. Green, and A. Zakutayev, “How Much Will Gallium Oxide Power Electronics Cost?,” *Joule*, vol. 3, no. 4, pp. 903–907, 2019.
- [9] M. Higashiwaki and G. H. Jessen, “Guest Editorial: The dawn of gallium oxide microelectronics,” *Appl. Phys. Lett.*, vol. 112, no. 6, p. 060401, 2018.
- [10] M. Orita, H. Ohta, M. Hirano, and H. Hosono, “Deep-ultraviolet transparent conductive β -Ga₂O₃ thin films,” *Appl. Phys. Lett.*, vol. 77, no. 25, pp. 4166–4168, 2000.
- [11] K. Sasaki, A. Kuramata, T. Masui, E. G. Villora, K. Shimamura, and S. Yamakoshi, “Device-quality β -Ga₂O₃ epitaxial films fabricated by ozone molecular beam epitaxy,” *Appl. Phys. Express*, vol. 5, no. 3, pp. 17–20, 2012.
- [12] H. Okumura, M. Kita, K. Sasaki, A. Kuramata, M. Higashiwaki, and J. S. Speck, “Systematic investigation of the growth rate of β -Ga₂O₃(010) by plasma-assisted molecular beam epitaxy,” *Appl. Phys. Express*, vol. 7, no. 9, pp. 3–7, 2014.
- [13] E. Ahmadi et al., “Ge doping of β -Ga₂O₃ films grown by plasma-assisted molecular beam epitaxy,” *Appl. Phys. Express*, vol. 10, no. 4, pp. 1–5, 2017.
- [14] S.-H. Han, A. Mauze, E. Ahmadi, T. Mates, Y. Oshima, and J. S. Speck, “n-type dopants in (001) β -Ga₂O₃ grown on (001) β -Ga₂O₃ substrates by plasma-assisted molecular beam epitaxy,” *Semicond. Sci. Technol.*, vol. 33, no. 045001, p. 6, 2018.

- [15] M. Baldini et al., “Semiconducting Sn-doped β -Ga₂O₃ homoepitaxial layers grown by metal organic vapour-phase epitaxy,” *J. Mater. Sci.*, vol. 51, no. 7, pp. 3650–3656, 2016.
- [16] M. Baldini, M. Albrecht, A. Fiedler, K. Irmscher, R. Schewski, and G. Wagner, “Si- and Sn-doped homoepitaxial β -Ga₂O₃ layers grown by MOVPE on (010)-oriented substrates,” *ECS J. Solid State Sci. Technol.*, vol. 6, no. 2, pp. Q3040–Q3044, 2017.
- [17] M. Baldini, Z. Galazka, and G. Wagner, “Recent progress in the growth of β -Ga₂O₃ for power electronics applications,” *Mater. Sci. Semicond. Process.*, vol. 78, no. July 2017, pp. 132–146, 2018.
- [18] J. H. Leach, K. Udworthy, J. Rumsey, G. Dodson, H. Splawn, and K. R. Evans, “Halide vapor phase epitaxial growth of β -Ga₂O₃ and α -Ga₂O₃ films,” *APL Mater.*, vol. 7, no. 2, pp. 1–8, 2019.
- [19] Y. Zhang et al., “MOCVD grown epitaxial β -Ga₂O₃ thin film with an electron mobility of 176 cm²/V s at room temperature,” *APL Mater.*, vol. 7, no. 2, 2019.
- [20] X. Du et al., “Preparation and characterization of Sn-doped β -Ga₂O₃ homoepitaxial films by MOCVD,” *J. Mater. Sci.*, vol. 50, no. 8, pp. 3252–3257, 2015.
- [21] S. D. Lee, K. Kaneko, and S. Fujita, “Homoepitaxial growth of beta gallium oxide films by mist chemical vapor deposition,” *Jpn. J. Appl. Phys.*, vol. 55, no. 12, 2016.
- [22] K. D. Leedy et al., “Highly conductive homoepitaxial Si-doped Ga₂O₃ films on (010) β -Ga₂O₃ by pulsed laser deposition,” *Appl. Phys. Lett.*, vol. 111, no. 1, pp. 2–6, 2017.
- [23] K. D. Leedy et al., “Si content variation and influence of deposition atmosphere in homoepitaxial Si-doped β -Ga₂O₃ films by pulsed laser deposition,” *APL Mater.*, vol. 6, no. 10, 2018.
- [24] N. Ma et al., “Intrinsic electron mobility limits in β -Ga₂O₃,” *Appl. Phys. Lett.*, vol. 109, no. 21, pp. 1–6, 2016.
- [25] K. D. Chabak et al., “Lateral β -Ga₂O₃ field effect transistors,” *Semicond. Sci. Technol.*, vol. 35, no. 013002, p. 22, 2020.
- [26] M. Higashiwaki, “MBE Growth and Device Applications of Ga₂O₃,” in *MBE Growth and Device Applications of Ga₂O₃*, John Wiley and Sons Inc., 2019, pp. 411–422.
- [27] P. Vogt and O. Bierwagen, “Reaction kinetics and growth window for plasma-assisted molecular beam epitaxy of Ga₂O₃: Incorporation of Ga vs. Ga₂O desorption,” *Appl. Phys. Lett.*, vol. 108, no. 7, pp. 1–5, 2016.
- [28] S. Krishnamoorthy et al., “Modulation-doped β -(Al_{0.2}Ga_{0.8})₂O₃/Ga₂O₃ field-effect transistor,” *Appl. Phys. Lett.*, vol. 111, no. 2, pp. 3–7, 2017.
- [29] M. Higashiwaki, A. Kuramata, H. Murakami, and Y. Kumagai, “State-of-the-art technologies of gallium oxide power devices,” *J. Phys. D. Appl. Phys.*, vol. 50, no. 33, 2017.

- [30] F. Alema, B. Hertog, A. Osinsky, P. Mukhopadhyay, M. Toporkov, and W. V. Schoenfeld, "Fast growth rate of epitaxial β -Ga₂O₃ by close coupled showerhead MOCVD," *J. Cryst. Growth*, vol. 475, pp. 77–82, 2017.
- [31] D. Gogova, M. Schmidbauer, and A. Kwasniewski, "Homo- and heteroepitaxial growth of Sn-doped β -Ga₂O₃ layers by MOVPE," *CrystEngComm*, vol. 17, no. 35, pp. 6744–6752, 2015.
- [32] H. Masataka et al., "Recent progress in Ga₂O₃ power devices," *Semicond. Sci. Technol.*, vol. 31, no. 3, p. 34001, 2016.
- [33] K. Sasaki, M. Higashiwaki, A. Kuramata, T. Masui, and S. Yamakoshi, "MBE grown Ga₂O₃ and its power device applications," *J. Cryst. Growth*, vol. 378, pp. 591–595, 2013.
- [34] E. Ahmadi and Y. Oshima, "Materials issues and devices of α - and β -Ga₂O₃," *J. Appl. Phys.*, vol. 126, no. 16, 2019.
- [35] J. L. Lyons, D. Steiauf, A. Janotti, and C. G. Van De Walle, "Carbon as a shallow donor in transparent conducting oxides," *Phys. Rev. Appl.*, vol. 2, no. 6, pp. 1–8, 2014.
- [36] R. Miller, F. Alema, and A. Osinsky, "Epitaxial β -Ga₂O₃ and β -(Al_xGa_{1-x})₂O₃/ β -Ga₂O₃ Heterostructures Growth for Power Electronics," *IEEE Trans. Semicond. Manuf.*, vol. 31, no. 4, pp. 467–474, 2018.
- [37] H. M. Smith and A. F. Turner, "Vacuum Deposited Thin Films Using a Ruby Laser," *Appl. Opt.*, vol. 4, no. 1, p. 147, 1965.
- [38] I. P. Wellenius, "Rare-Earth Doped Wide Bandgap Oxide Semiconductor Materials and Devices," North Carolina State University, 2009.
- [39] D. C. Look, K. D. Leedy, D. H. Tomich, and B. Bayraktaroglu, "Mobility analysis of highly conducting thin films: Application to ZnO," *Appl. Phys. Lett.*, vol. 96, no. 6, pp. 18–21, 2010.
- [40] F. Zhang et al., "Toward controlling the carrier density of Si doped Ga₂O₃ films by pulsed laser deposition," *Appl. Phys. Lett.*, vol. 109, no. 10, 2016.
- [41] N. Blumenschein, T. Paskova, and J. F. Muth, "Effect of Growth Pressure on PLD-Deposited Gallium Oxide Thin Films for Deep-UV Photodetectors," *Phys. Status Solidi Appl. Mater. Sci.*, vol. 216, no. 20, pp. 1–8, 2019.
- [42] X. Chen, F.-F. Ren, J. Ye, and S. Gu, "Gallium Oxide-based solar-blind ultraviolet photodetectors," *Semicond. Sci. Technol.*, 2019.
- [43] T. Oshima, T. Okuno, and S. Fujita, "Ga₂O₃ thin film growth on c-plane sapphire substrates by molecular beam epitaxy for deep-ultraviolet photodetectors," *Jpn. J. Appl. Phys.*, vol. 46, no. 11R, p. 7217, 2007.
- [44] P. Feng, J. Y. Zhang, Q. H. Li, and T. H. Wang, "Individual β -Ga₂O₃ nanowires as solar-blind photodetectors," *Appl. Phys. Lett.*, vol. 88, no. 15, pp. 2–5, 2006.

- [45] C. Zhengwei, W. Xianghu, S. Katsuhiko, T. Tooru, N. Mitsuhiro, and G. Qixin, “The impact of growth temperature on the structural and optical properties of catalyst-free β -Ga₂O₃ nanostructures,” *Mater. Res. Express*, vol. 3, no. 2, p. 25003, 2016.
- [46] R. Lin et al., “High-Performance Graphene/ β -Ga₂O₃ Heterojunction Deep-Ultraviolet Photodetector with Hot-Electron Excited Carrier Multiplication,” *ACS Appl. Mater. Interfaces*, vol. 10, no. 26, pp. 22419–22426, 2018.
- [47] D. Guo et al., “Self-Powered Ultraviolet Photodetector with Superhigh Photoresponsivity (3.05 A/W) Based on the GaN/Sn:Ga₂O₃ pn Junction,” *ACS Nano*, vol. 12, no. 12, pp. 12827–12835, 2018.
- [48] D. Guo et al., “Zero-power-consumption solar-blind photodetector based on β -Ga₂O₃/NSTO heterojunction,” *ACS Appl. Mater. Interfaces*, vol. 9, no. 2, pp. 1619–1628, 2017.
- [49] N. Kumar, K. Arora, and M. Kumar, “High performance, flexible and room temperature grown amorphous Ga₂O₃ solar-blind photodetector with amorphous indium-zinc-oxide transparent conducting electrodes,” *J. Phys. D. Appl. Phys.*, vol. 52, no. 33, 2019.
- [50] T. Oshima, T. Okuno, N. Arai, N. Suzuki, H. Hino, and S. Fujita, “Flame detection by a β -Ga₂O₃-based sensor,” *Jpn. J. Appl. Phys.*, vol. 48, no. 1, pp. 0–7, 2009.
- [51] Y. Qin et al., “Enhancement-Mode β -Ga₂O₃ Metal-Oxide-Semiconductor Field-Effect Solar-Blind Phototransistor With Ultrahigh Detectivity and Photo-to-Dark Current Ratio,” *IEEE Electron Device Lett.*, vol. 40, no. 5, pp. 742–745, 2019.
- [52] A. S. Pratiyush et al., “Demonstration of zero bias responsivity in MBE grown β -Ga₂O₃ lateral deep-UV photodetector,” *Jpn. J. Appl. Phys.*, vol. 57, no. 6, 2018.
- [53] Q. Feng et al., “Comparison Study of β -Ga₂O₃ Photodetectors on Bulk Substrate and Sapphire,” *IEEE Trans. Electron Devices*, vol. 63, no. 9, pp. 3578–3583, 2016.
- [54] Y. Xu et al., “Solar blind deep ultraviolet β -Ga₂O₃ photodetectors grown on sapphire by the Mist-CVD method,” *Opt. Mater. Express*, vol. 8, no. 9, p. 2941, 2018.
- [55] K. Arora, N. Goel, M. Kumar, and M. Kumar, “Ultrahigh Performance of Self-Powered β -Ga₂O₃ Thin Film Solar-Blind Photodetector Grown on Cost-Effective Si Substrate Using High-Temperature Seed Layer,” *ACS Photonics*, vol. 5, no. 6, pp. 2391–2401, 2018.
- [56] L. X. Qian, H. Y. Liu, H. F. Zhang, Z. H. Wu, and W. L. Zhang, “Simultaneously improved sensitivity and response speed of β -Ga₂O₃ solar-blind photodetector via localized tuning of oxygen deficiency,” *Appl. Phys. Lett.*, vol. 114, no. 11, 2019.
- [57] X. Chen et al., “Self-Powered Solar-Blind Photodetector with Fast Response Based on Au/ β -Ga₂O₃ Nanowires Array Film Schottky Junction,” *ACS Appl. Mater. Interfaces*, vol. 8, no. 6, pp. 4185–4191, 2016.

- [58] S. Cui, Z. Mei, Y. Zhang, H. Liang, and X. Du, "Room-Temperature Fabricated Amorphous Ga₂O₃ High-Response-Speed Solar-Blind Photodetector on Rigid and Flexible Substrates," *Adv. Opt. Mater.*, vol. 5, no. 19, pp. 1–9, 2017.
- [59] A. S. Pratiyush et al., "Optical float-zone grown bulk β -Ga₂O₃-Based Linear MSM Array of UV-C Photodetectors," *IEEE Photonics Technol. Lett.*, vol. 31, no. 12, pp. 923–926, 2019.
- [60] S. H. Lee et al., "High-Responsivity Deep-Ultraviolet-Selective Photodetectors Using Ultrathin Gallium Oxide Films," *ACS Photonics*, vol. 4, no. 11, pp. 2937–2943, 2017.
- [61] X. Chen et al., "Highly Narrow-Band Polarization-Sensitive Solar-Blind Photodetectors Based on β -Ga₂O₃ Single Crystals," *ACS Appl. Mater. Interfaces*, vol. 11, no. 7, pp. 7131–7137, 2019.
- [62] A. Singh Pratiyush et al., "High responsivity in molecular beam epitaxy grown β -Ga₂O₃ metal semiconductor metal solar blind deep-UV photodetector," *Appl. Phys. Lett.*, vol. 110, no. 22, pp. 1–6, 2017.
- [63] J. Y. Tsao et al., "Ultrawide-Bandgap Semiconductors: Research Opportunities and Challenges," *Adv. Electron. Mater.*, vol. 4, no. 16, p. 1600501, 2018.
- [64] K. Sasaki, M. Higashiwaki, A. Kuramata, T. Masui, and S. Yamakoshi, "Ga₂O₃ Schottky Barrier Diodes Fabricated by Using Single-Crystal β -Ga₂O₃ (010) Substrates," *IEEE Electron Device Lett.*, vol. 34, no. 4, pp. 493–495, 2013.
- [65] J. Yang et al., "High reverse breakdown voltage Schottky rectifiers without edge termination on Ga₂O₃," *Appl. Phys. Lett.*, vol. 110, no. 19, 2017.
- [66] K. Konishi, K. Goto, H. Murakami, A. Kuramata, S. Yamakoshi, and M. Higashiwaki, "1-kV vertical Ga₂O₃ field-plated Schottky barrier diodes," *Appl. Phys. Lett.*, vol. 111, no. 22, p. 222104, 2017.
- [67] J. Yang, F. Ren, M. Tadjer, S. J. Pearton, and A. Kuramata, "2300V Reverse Breakdown Voltage Ga₂O₃ Schottky Rectifiers," *ECS J. Solid State Sci. Technol.*, vol. 7, no. 5, pp. Q92–Q96, 2018.
- [68] M. Higashiwaki, K. Sasaki, A. Kuramata, T. Masui, and S. Yamakoshi, "Gallium oxide (Ga₂O₃) metal-semiconductor field-effect transistors on single-crystal β -Ga₂O₃ (010) substrates," *Appl. Phys. Lett.*, vol. 100, no. 1, p. 13504, 2012.
- [69] M. Higashiwaki et al., "Depletion-mode Ga₂O₃ metal-oxide-semiconductor field-effect transistors on β -Ga₂O₃ (010) substrates and temperature dependence of their device characteristics," *Appl. Phys. Lett.*, vol. 103, no. 12, p. 123511, 2013.
- [70] M. Higashiwaki et al., "Depletion-mode Ga₂O₃ MOSFETs on β -Ga₂O₃ (010) substrates with Si-ion-implanted channel and contacts," *Tech. Dig. - Int. Electron Devices Meet. IEDM*, vol. 3, no. 010, pp. 707–710, 2013.

- [71] M. H. Wong, K. Sasaki, A. Kuramata, S. Yamakoshi, and M. Higashiwaki, "Field-plated Ga₂O₃ MOSFETs with a breakdown voltage of over 750V," *IEEE Electron Device Lett.*, vol. 37, no. 2, pp. 212–215, 2016.
- [72] K. D. Chabak et al., "Enhancement-mode Ga₂O₃ wrap-gate fin field-effect transistors on native (100) β -Ga₂O₃ substrate with high breakdown voltage," *Appl. Phys. Lett.*, vol. 109, no. 21, 2016.
- [73] A. J. Green et al., "3.8-MV/cm Breakdown Strength of MOVPE-Grown Sn-Doped β -Ga₂O₃ MOSFETs," *IEEE Electron Device Lett.*, vol. 37, no. 7, pp. 902–905, 2016.
- [74] A. J. Green et al., " β -Ga₂O₃ MOSFETs for Radio Frequency Operation," *IEEE Electron Device Lett.*, vol. 38, no. 6, pp. 790–793, 2017.
- [75] Z. Xia, C. Joishi, S. Krishnamoorthy, S. Bajaj, Y. Zhang, and M. Brenner, "Delta Doped β -Ga₂O₃ Field Effect Transistors With Regrown Ohmic Contacts," *IEEE Electron Device Lett.*, vol. 39, no. 4, pp. 568–571, 2018.

CHAPTER 3 – GROWTH

3.1 Gallium Oxide Crystal Structure

The gallium oxide beta polymorph has a monoclinic crystal structure with lattice parameters a , b , c , α , β , and γ equal to 12.214 Å, 3.037 Å, 5.798 Å, 90.00°, 103.83°, and 90.00°, respectively [1]. β -Ga₂O₃ belongs to the $C2/m$ space group and has eight unique symmetry operators. The unit cell has a cell volume of 208.85 Å³ and contains 12 gallium atoms, located on two crystallographically different gallium atom arrangements (Ga_(I) and Ga_(II)), and 18 oxygen atoms, located on three different oxygen atom arrangements (O_(I), O_(II), and O_(III)). As shown in **Figure 3.1**, the O_(I) and O_(III) atoms are located on the {010} planes while the O_(II) atoms are aligned along the b-axis [2]. Each unit cell of β -Ga₂O₃ contains six Ga_(I) atoms, six Ga_(II) atoms, six O_(I) atoms, six O_(II) atoms, and six O_(III) atoms. The Ga_(I), Ga_(II), and O atoms are located in tetrahedral, octahedral, and distorted octahedral arranged sites, respectively.

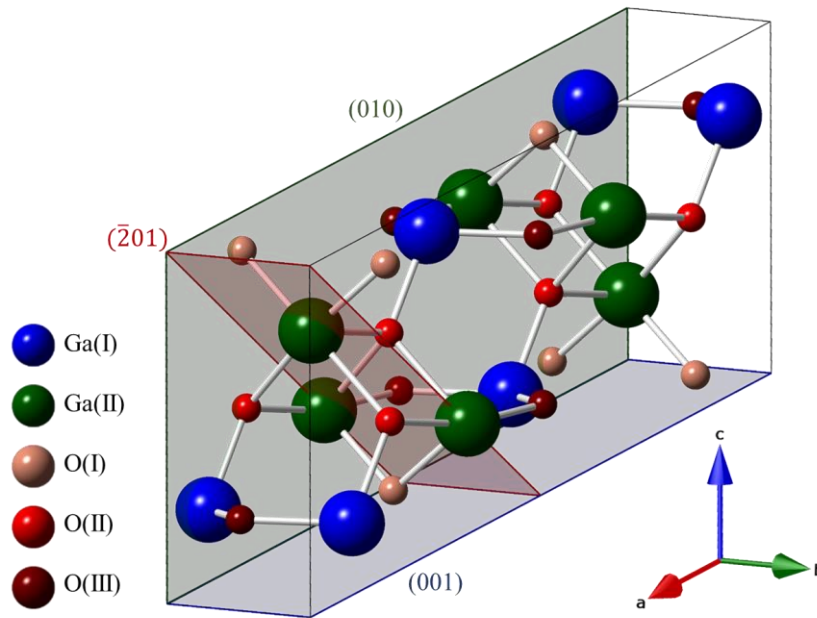


Figure 3.1 β -Ga₂O₃ unit cell with (010), (001), and $(\bar{2}01)$ crystallographic planes shown with green, blue, and red planes, respectively.

3.2 Gallium Oxide Thin Film Growth

3.2.1 Target Fabrication and Substrate Preparation

Ablation targets were formed using Ga₂O₃ powder (Alfa Aesar – 99.999% purity) and either SiO₂ (Sigma Aldrich – 99.5% purity) or SnO₂ (Cerac – 99.9% purity) powders for intentional doping with Si or Sn. The fabricated cylindrical targets had a diameter and thickness of 2.5 cm and 5 mm, respectively, and were comprised of 4.5 grams of the powder mixture.

When preparing the ablation target mixture, the amount of dopant powder needed was calculated by satisfying **Equations 3.1** and **3.2**, where m_T is the total mass (grams) of the mixture, M_x is the molar mass of element x (grams/mol), n_x is the number of moles in element x , and C_{dopant} is the molar concentration (%) of the dopant in the mixture. Additionally, one can solve for the impurity concentration (N) in the target using **Equation 3.3**, where ρ_{dopant} is the density of the dopant powder (g/cm³) and N_A is Avogadro's number (6.02×10²³ atoms/cm³). The molar mass and density of Ga₂O₃, SnO₂, and SiO₂ are shown in Table 1.

$$m_T = M_{Ga_2O_3}n_{Ga_2O_3} + M_{dopant}n_{dopant} \quad (3.1)$$

$$C_{dopant} = \frac{n_{dopant}}{100 \times (n_{dopant} + n_{Ga_2O_3})} \quad (3.2)$$

$$N = \left(\frac{m_{dopant}}{m_T}\right) \left(\frac{\rho_{dopant}}{M_{dopant}}\right) N_A \quad (3.3)$$

After preparing the powder, it is inserted into a beaker with 10 mL of ethanol per gram of powder and placed onto an orbital shaker until dry. After grinding the dried powder with a mortar and pestle, the target was baked at 500°C for 3 hours to ensure solvents were evaporated. Next the material was formed into a cylinder using a hydraulic press at 5500 psi and sintered at 1600°C

for 12 hours. A commercially available undoped Ga₂O₃ target was purchased (Plasmaterials) to compare the quality with what was fabricated in this work. X-ray diffraction measurements were performed to evaluate the crystalline quality of the thin films grown by the different targets. Films grown by using homemade targets showed no noticeable differences to those grown using the commercial target.

Table 3.1 Molar mass and density of powders used for fabricating PLD targets.

Compound	Ga ₂ O ₃	SnO ₂	SiO ₂
Molar Mass, M _x (g/mol)	187.44	150.71	60.08
Density, ρ _x (g/cm ³)	6.44	6.95	2.60

An ultrasonic bath was used to clean substrates prior to thin film deposition. Substrates were placed in acetone and methanol for 5 minutes each then dried using nitrogen. An RF plasma batch asher was used to further clean the substrate surface. The substrates were placed in the plasma chamber for 2 minutes using an O₂ descum process which used a 600 mT chamber pressure, 80 sccm O₂ gas flow, and RF forward power of 250 W.

3.2.2 Heteroepitaxial Growth

The most commonly used substrate for heteroepitaxial growth of gallium oxide thin films is c-plane sapphire, or (0001)-oriented α-Al₂O₃. The oxygen atoms located in the Ga₂O₃ {201} family of planes have a similar arrangement to the oxygen atoms in the Al₂O₃ (0001) plane [3]. The lattice mismatch between Ga₂O₃ (010) planes and Al₂O₃ (01 $\bar{1}$ 0) planes is only 1.6% [4]. While the lattice mismatch between Ga₂O₃ ($\bar{2}$ 01) planes and Al₂O₃ (2 $\bar{1}$ $\bar{1}$ 0) planes is 3.13% [4].

Figure 3.2 shows a schematic drawing of the two possible in-plane epitaxial arrangements between $(\bar{2}01)$ -oriented Ga_2O_3 and c-plane sapphire [5]. In this image, a top slice of the sapphire crystal is shown with oxygen atom locations denoted using red circles. Likewise, a slice of the $(\bar{2}01)$ plane through the Ga_2O_3 unit cell is shown using black lines. The unit cell of $(\bar{2}01)$ -oriented Ga_2O_3 contains lateral in-plane order along the $[102]$ and $[010]$ directions, which are separated by a 90° rotation. The first possible arrangement shown in **Figure 3.2 (a)** occurs when $[102]_{\text{Ga}_2\text{O}_3} \parallel [10\bar{1}0]_{\text{Al}_2\text{O}_3}$ and $[010]_{\text{Ga}_2\text{O}_3} \parallel [21\bar{3}0]_{\text{Al}_2\text{O}_3}$. This arrangement leads to an offset of 1.8° between $[132]_{\text{Ga}_2\text{O}_3}$ and $[1\bar{1}00]_{\text{Al}_2\text{O}_3}$. The second possible arrangement shown in **Figure 3.2 (b)** occurs when $[132]_{\text{Ga}_2\text{O}_3} \parallel [1\bar{1}00]_{\text{Al}_2\text{O}_3}$, which results in a 1.8° offset between $[102]_{\text{Ga}_2\text{O}_3}$ and $[10\bar{1}0]_{\text{Al}_2\text{O}_3}$ and also between $[010]_{\text{Ga}_2\text{O}_3}$ and $[21\bar{3}0]_{\text{Al}_2\text{O}_3}$. The lattice mismatch (δ) between these three β - Ga_2O_3 and α - Al_2O_3 crystallographic directions can be calculated once the interplanar spacing (d_{hkl}) of each direction is known. The d_{hkl} is calculated for hexagonal and monoclinic crystal systems using **Equations 3.4** and **3.5**, respectively, where h , k , and l are the Miller indices [6]. The lattice mismatch can be calculated using **Equation 3.6**, where m and p are integers representing the number of lattice units occurring to satisfy $m \cdot d_f \approx p \cdot d_s$ [7]. The lattice mismatch calculated for each epitaxial relation of **Figure 3.2** is shown in **Table 3.2**.

In this work, the c-plane sapphire was used as a template for heteroepitaxial growth of β - Ga_2O_3 thin films. Heteroepitaxial growth experiments were beneficial because they provided a way to analyze Ga_2O_3 thin film growth kinetics while using substrates which were relatively inexpensive in comparison to the currently available the Ga_2O_3 single crystals. Fortunately, previous reports on Ga_2O_3 thin film growth provided a rough estimate of initial growth parameters that could be used to grow films with fair quality by pulsed laser deposition [8]–[10]. Substrate temperature was the first growth parameter optimized for our specific growth system. Growths

were performed while varying the substrate temperature from 500 – 900 °C, and the resulting θ - 2θ X-ray diffraction data can be seen in **Figures 3.3(a)**. The films shown here were grown using the growth conditions listed in **Table 3.3** and all had a thickness of about 200 nm. It was found that the crystalline quality of the β -Ga₂O₃ grown at 500 °C was of very poor quality, but the film quality became significantly improved when a higher growth temperature was used. Similar findings were reported previously, where substrate temperature was evaluated during Ga₂O₃ thin film growth on c-plane sapphire using pulsed laser deposition [11], molecular beam epitaxy [12], and metal-organic chemical vapor deposition [13]. It is possible that when growing at lower temperatures the material does not have enough energy to relax into the desired ($\bar{2}01$) orientation, but instead the ions remain in a more randomly oriented distribution. **Figure 3.3(b)** shows θ - 2θ XRD data for a series of β -Ga₂O₃ films which were grown at temperatures ranging from 800 – 900 °C. The θ - 2θ scan for each of the films shown contained both ($\bar{2}01$) and ($\bar{4}02$) diffraction peaks, but the undesired (110) peak was present for each temperature.

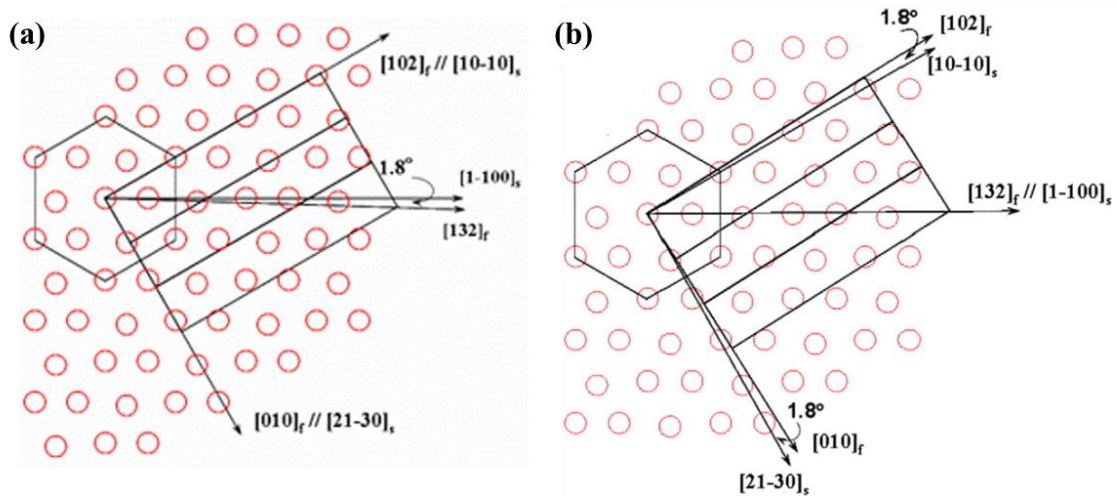


Figure 3.2 Schematic diagram showing the two possible in-plane epitaxial relationships which can occur for ($\bar{2}01$)-oriented β -Ga₂O₃ on c-plane Al₂O₃. Sapphire oxygen atom locations are shown using red circles. ($\bar{2}01$) plane of the Ga₂O₃ lattice is shown using black lines. Copyright (2015) Elsevier [5].

$$d_{hkl}(\text{Hexagonal}) = \frac{1}{\sqrt{\frac{4}{3a^2}(h^2 + hk + k^2) + \frac{l^2}{c^2}}} \quad (3.4)$$

$$d_{hkl}(\text{Monoclinic}) = \frac{1}{\sqrt{\left[\frac{h^2}{a^2} + \frac{l^2}{c^2} - \frac{2hl \cos(\beta)}{ac}\right] \frac{1}{\sin^2(\beta)} + \frac{k^2}{b^2}}} \quad (3.5)$$

$$\delta = 2 \left(\frac{m \cdot d_f - p \cdot d_s}{m \cdot d_f + p \cdot d_s} \right) \quad (3.6)$$

Table 3.2 Interplanar spacing and lattice mismatch between the epitaxial crystallographic directions of (201)-oriented Ga₂O₃ grown on c-plane sapphire.

Crystallographic Direction		d_{hkl} (Å)		$m \cdot d_f \approx p \cdot d_s$	Lattice Mismatch
Ga ₂ O ₃	Al ₂ O ₃	Ga ₂ O ₃	Al ₂ O ₃		
[102]	[10 $\bar{1}$ 0]	2.603	4.124	$3d_f \approx 2d_s$	5.482%
[010]	[21 $\bar{3}$ 0]	3.037	1.559	$1d_f \approx 2d_s$	2.615%
[132]	[1 $\bar{1}$ 00]	0.943	4.124	$9d_f \approx 2d_s$	2.906%

Table 3.3 Growth conditions for films of **Figure 3.3**.

Growth Parameter	Value
Substrate Temperature	500 – 900 °C
Base Chamber Pressure	1 – 5x10 ⁻⁷ Torr
Oxygen Pressure, P _{O2}	5x10 ⁻³ Torr
Oxygen Flow Rate	5 sccm
Laser Energy	248 mJ/pulse
Laser Repetition Rate	10 Hz
Laser Pulses	25k – 45k

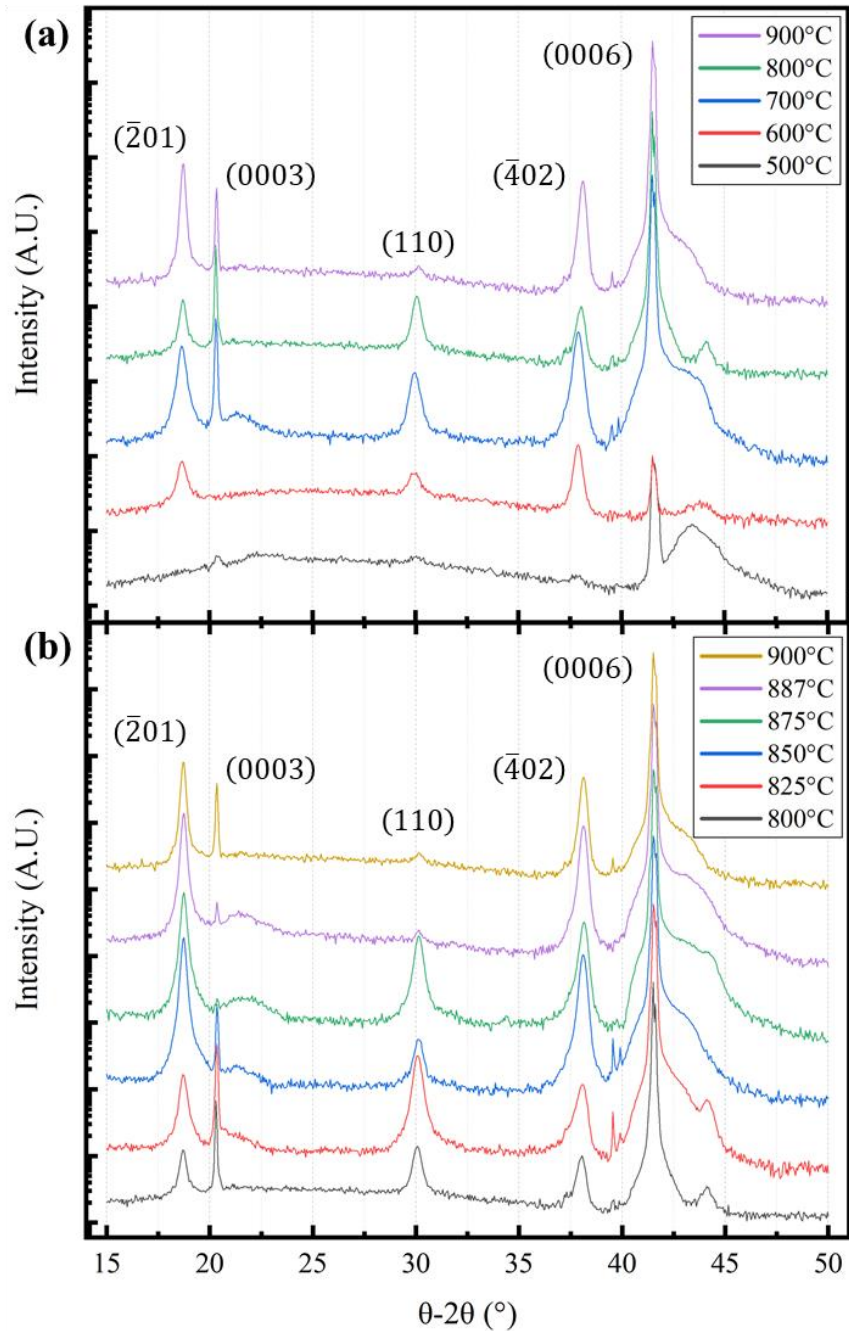


Figure 3.3 θ - 2θ XRD data gathered for β - Ga_2O_3 thin films while varying growth temperature from (a) 500 – 900 $^\circ\text{C}$ and (b) 800 – 900 $^\circ\text{C}$.

The crystalline plane associated with each Ga_2O_3 and Al_2O_3 reflection was determined by first calculating d_{hkl} for all θ - 2θ peaks. Once d_{hkl} is known, the 2θ angle can be calculated using Bragg's Law as shown in **Equation 3.7**, where m is a positive non-zero integer representing the

order of diffraction and λ is the wavelength of incident radiation. The XRD measurements in this work were performed by a Rigaku SmartLab X-ray diffractometer using copper K-alpha (Cu K α) radiation with a wavelength of 1.5406 Å. The observed β -Ga $_2$ O $_3$ and α -Al $_2$ O $_3$ reflections were attributed to the $\{\bar{2}01\}$ and $\{0003\}$ family of planes, respectively. Additionally, for β -Ga $_2$ O $_3$, the reflections occurring at 30 degrees were attributed to the (110) plane, as summarized in **Table 3.4**.

$$m\lambda = 2d_{hkl} \sin(\theta) \quad (3.7)$$

Table 3.4 XRD reflection planes calculated for α -Al $_2$ O $_3$ and β -Ga $_2$ O $_3$. Calculated and measured values of reflection angles are shown for comparison.

	a, b, c (Å)	α, β, γ (°)	hkl	d_{hkl} (Å)	Calc. 2θ (°)	Meas. 2θ (°)
α -Al $_2$ O $_3$	4.762,	90,	003	4.332	20.487	20.350
	4.762,	90,	006	2.166	41.669	41.500
	12.995	120	009	1.444	64.484	64.350
β -Ga $_2$ O $_3$	12.214,	90,	-201	4.680	18.949	18.750
	3.037,	103.83,	110	2.942	30.355	30.150
	5.798	90	-402	2.340	38.443	38.200
			-603	1.560	59.185	58.950

The undesired (110) Ga $_2$ O $_3$ reflection was further evaluated by analyzing its intensity as a function of substrate temperature. **Figure 3.4 (a)** and **(b)** show the intensity of the measured $(\bar{2}01)$ and (110) reflections, respectively, for a series of growths which varied in substrate temperature from 700 to 900 °C. The intensity of each $(\bar{2}01)$ and (110) reflection was normalized to its respective (0006) sapphire peak intensity. While the intensity of the $(\bar{2}01)$ increases with temperature, so does the (110) reflection intensity. As shown in **Figure 3.4(c)**, the $(\bar{2}01)_{Ga_2O_3}/(110)_{Ga_2O_3}$ ratio can be used to determine the temperature at which the thin film

exhibits its most oriented composition with the sapphire substrate. The XRD analysis shows that the optimal growth temperature for growing $(\bar{2}01)$ -oriented β -Ga₂O₃ on c-plane sapphire is 887 °C, which is significantly higher than what has been reported previously. The optimized growth temperature typically reported is in the range of 650 – 850 °C [11]–[13]. One negative effect of the higher growth temperature is a reduced growth rate [10]. One possible explanation is that the reduced growth rate was not compensated for by increasing the number of laser pulses in the previous reports. If the films grown using a higher growth temperature were not as thick as those grown at the reported optimal temperatures, the resulting film could be more strained and its crystalline quality would likely be degraded. There have been other reports where a series of β -Ga₂O₃ films were annealed under various temperatures and ambients after growth. Changes to the annealing ambient (O₂, N₂, and vacuum) had no effect, but it was shown that the film quality could be enhanced by fine-tuning the annealing temperature [14]. This could explain the benefit of growing the films at a higher temperature, since the reported annealing temperatures are similar to the growth temperature used in this work.

Achieving the optimal chamber ambient is one of the most important details when growing high quality Ga₂O₃. Similarly to other oxygen-based semiconductor materials such as ZnO, the stoichiometry of the Ga₂O₃ crystal will be incorrect if grown in an improper ambient [15]. There are three subclasses of Ga₂O₃ that can be produced depending on chamber ambient – oxygen-rich, stoichiometric, and gallium-rich [16]. Deviance from the stoichiometric Ga:O ratio of 2:3 will cause intrinsic defects such as oxygen and gallium vacancies and hydrogen interstitials which deteriorate the film quality. As shown in **Figure 3.5**, Varley *et al.* reported on the formation of these defects using density function theory [17]. It was shown that the defects present in the film were strongly influenced by whether the Ga₂O₃ was grown under O-rich or Ga-rich conditions.

Defects in Ga₂O₃ thin films can be mitigated by maintaining stoichiometric chamber conditions during growth. One way of achieving this is by controlling the oxygen partial pressure (P_{O2}) [12].

The optimized P_{O2} findings from previous reports using pulsed laser deposition have shown

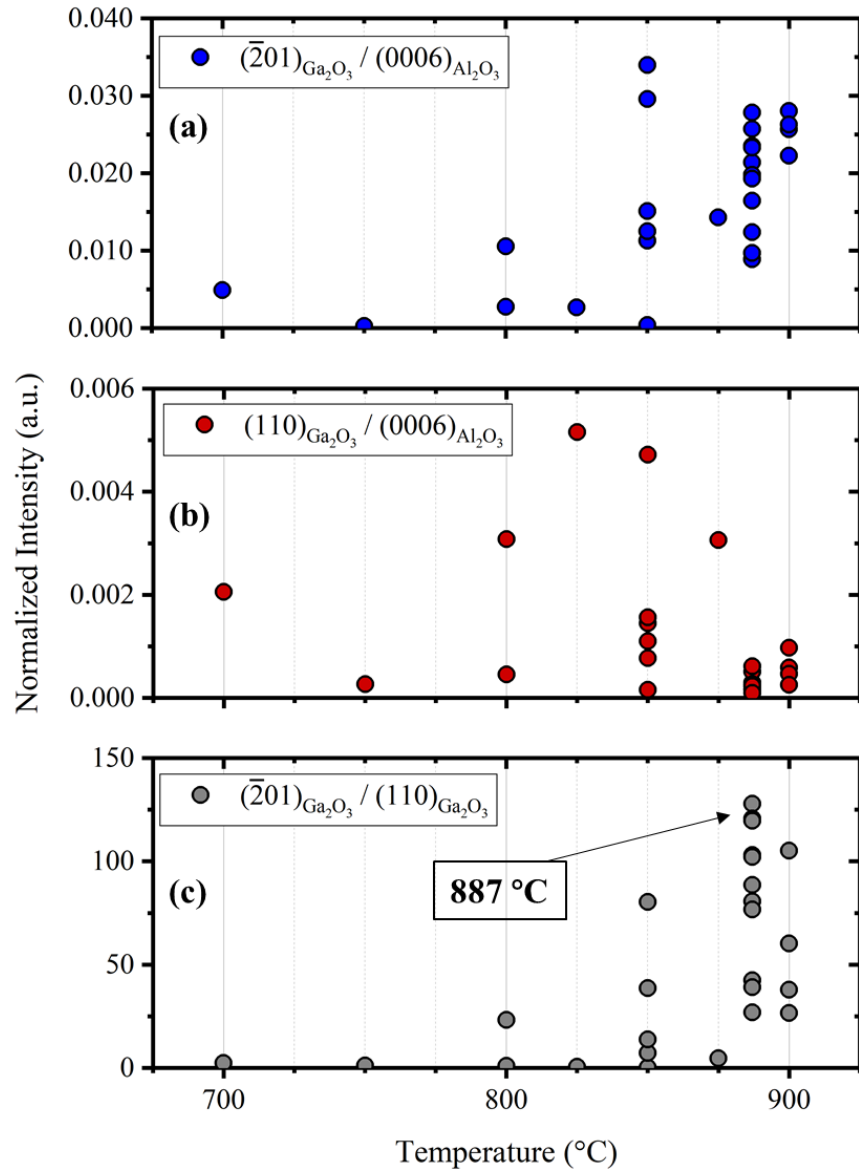


Figure 3.4 Normalized θ - 2θ intensity of (a) $(\bar{2}01)$ and (b) (110) reflections measured by XRD. Data was normalized to (0006) sapphire reflection. (c) Ratio of $(\bar{2}01)/(110)$ reflections as a function of substrate temperature.

significant variance, where P_{O2} values ranged from 1x10⁻⁴ to 2x10⁻¹ Torr [10], [11], [18]–[20]. In this work the P_{O2} was varied over three orders of magnitude from 1x10⁻⁴ to 1x10⁻² Torr, which was

controlled by the oxygen gas flow ranging from 1 to 8 sccm. The Ga_2O_3 thin films were grown using a substrate temperature of 887 °C, base chamber pressure of 1×10^{-7} Torr, laser repetition rate of 10 Hz, and laser energy density of 3 J/cm^2 .

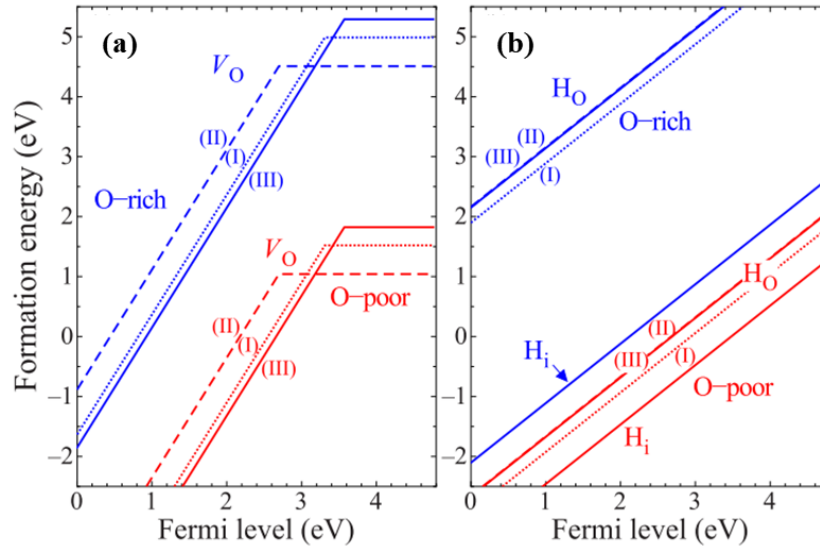


Figure 3.5 Formation energy – fermi level relationship of (a) oxygen vacancies and (b) hydrogen impurities in $\beta\text{-Ga}_2\text{O}_3$. Copyright (2010) AIP Publishing [17].

Figure 3.6 shows the resulting XRD (a) θ - 2θ , (b) ω , and (c) ϕ spectra. During the measurement each sample was aligned using the (0006) sapphire reflection prior to performing the full-ranged θ - 2θ scan. The $(\bar{2}01)$, $(\bar{4}02)$, and $(\bar{6}03)$ Ga_2O_3 diffractions were observed in each θ - 2θ scan. The (110) reflection was also present ($2\theta = 30.2^\circ$) for P_{O_2} ranging from 1×10^{-3} to 1×10^{-2} , indicating the presence of a domain with (110) surface orientation. The (110) reflection intensity was reduced by lowering P_{O_2} , indicating that lower oxygen pressures can be used to mitigate the formation of unwanted domains. It should be noted that the broad feature occurring from 21 to 23° was due to a reflection off of the (0006) Al_2O_3 diffraction which is why it was located at half of the (0006) peak position. The rocking curve measurements shown in **Figure 3.6(b)** were performed by scanning across $(\bar{2}01)$ for the samples grown using a P_{O_2} of 1×10^{-4} , 1×10^{-3} , and

1×10^{-2} Torr, and the resulting FWHM values were found to be 1.84° , 1.86° , and 2.49° , respectively. The broadening of $\{\bar{2}01\}$ was reduced with a lower P_{O_2} , indicating a greater crystalline quality. These results are consistent with previously reported FWHM values of heteroepitaxial $(\bar{2}01)$ -oriented Ga_2O_3 grown on $\alpha-Al_2O_3$ [21], [22]. **Figure 3.6(c)** shows ϕ scans of the Al_2O_3 $(01\bar{1}2)$ and Ga_2O_3 (002) . The Al_2O_3 $(01\bar{1}2)$ scan was measured by aligning to $2\theta = 25.560^\circ$ and $\psi = 57.597^\circ$, while the Ga_2O_3 (002) scan was measured by aligning to $2\theta = 31.692^\circ$ and $\psi = 50.152^\circ$. Three-fold symmetry was observed for the Al_2O_3 $(01\bar{1}2)$ reflection. The Ga_2O_3 (002) scan resulted in six sharp peaks separated by 60° for the samples grown using a P_{O_2} of 1×10^{-4} and 1×10^{-3} , indicating an epitaxial relationship with twofold symmetry. These Al_2O_3 $(01\bar{1}2)$ and Ga_2O_3 (002) ϕ scan results are consistent with previous reports [23]. The ϕ scan for the film grown using $P_{O_2} = 1 \times 10^{-2}$ also contained the six (002) reflections at 60° intervals, but their intensity was significantly less. Additionally present was a series of reflections with a 60° interval, which were attributed to the (110) domain observed in the θ - 2θ scan.

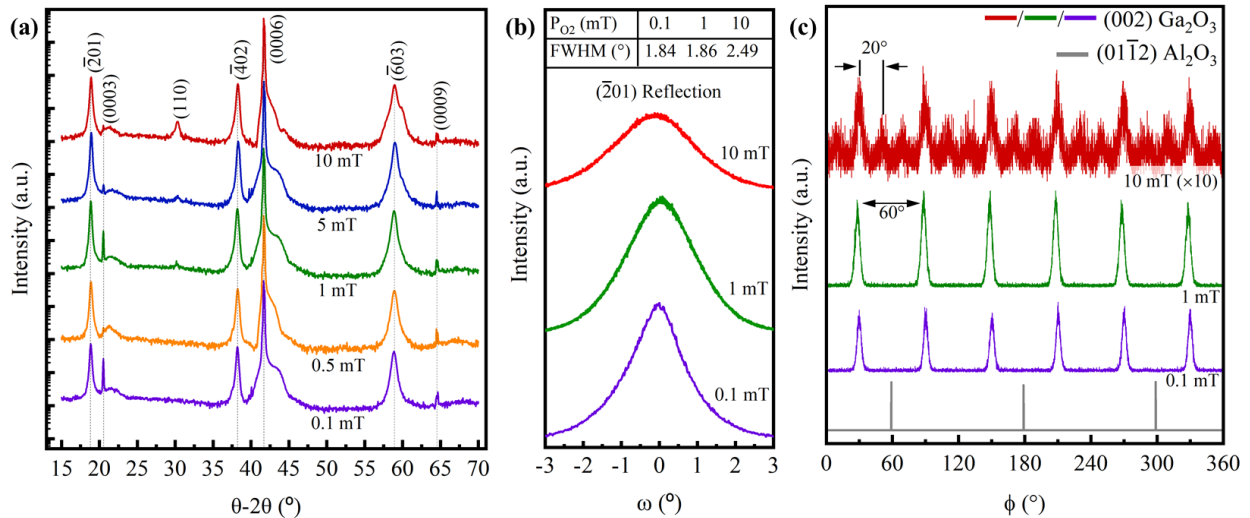


Figure 3.6 (a) θ - 2θ , (b) ω , and (c) ϕ XRD data gathered for $\beta-Ga_2O_3$ thin films with varying P_{O_2} . Copyright (2019) John Wiley and Sons [24].

Surface morphology was also investigated in order to better understand the effects of oxygen pressure on the thin film composition and growth kinetics. **Figure 3.7** shows SEM images of the samples grown at five representative oxygen pressures. The images were taken at 100kX magnification. It can be seen that the surface becomes more granular with increasing the pressure, and appears to be more uniform as P_{O_2} is decreased. Atomic force microscopy was used to quantitatively analyze the evolution of grains. **Figure 3.8 (a-e)** shows AFM images of five samples, and the surface morphology statistics are shown in **Figure 3.8 (f)**. The RMS roughness, peak-to-valley distance (PVD), and average grain size (AGS) were estimated for each sample. Interestingly, all three parameters were highest for the sample grown using a 5 mT oxygen pressure. The maximum RMS roughness, PVD, and AGS were found to be 5.1 nm, 35.7 nm, and 66.5 nm, respectively. The most uniform morphology was observed for the 0.1 mT pressure, resulting in an RMS roughness, PVD, and AGS of 1.9 nm, 11.8 nm, and 33.9 nm, respectively. These results are consistent with previous findings on PLD-grown Ga_2O_3 thin films [20].

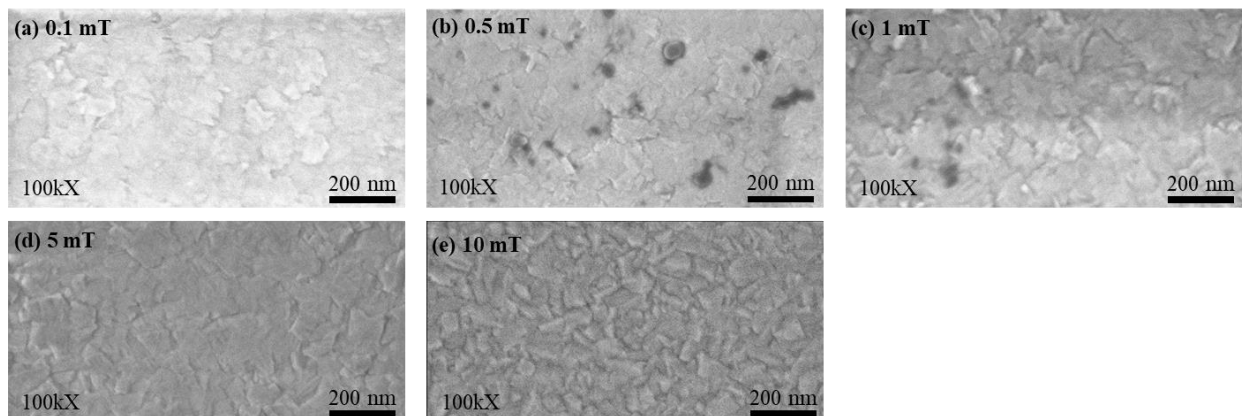


Figure 3.7 SEM images taken at 100 kX for samples with P_{O_2} of (a) 0.1 mT, (b) 0.5 mT, (c) 1 mT, (d) 5 mT, and (e) 10 mT.

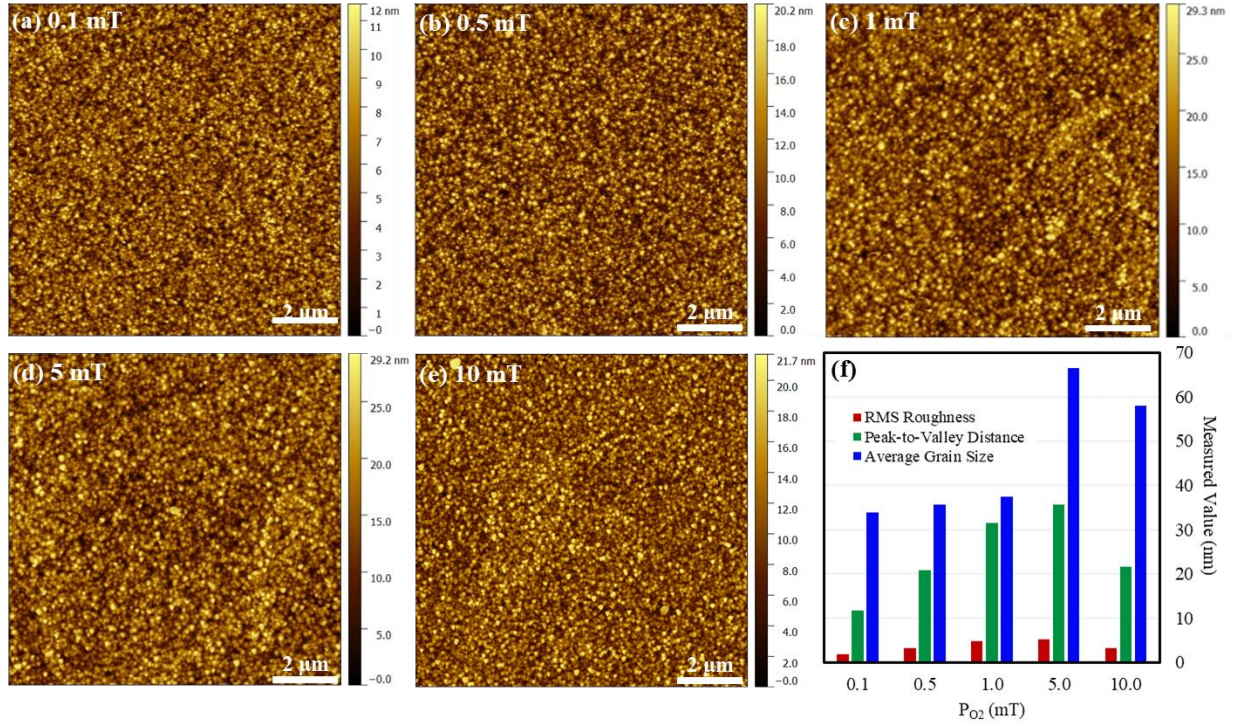


Figure 3.8 AFM images samples with P_{O_2} of (a) 0.1 mT, (b) 0.5 mT, (c) 1 mT, (d) 5 mT, and (e) 10 mT. Copyright (2019) John Wiley and Sons [24].

The five thin film samples analyzed here were grown on double-side polished $\alpha\text{-Al}_2\text{O}_3$ substrates, allowing for the optical transmission spectra to be recorded. **Figure 3.9** shows the transmission spectra for samples grown with P_{O_2} of 0.1 mT, 1 mT, and 10 mT. The incident radiation was varied from 200 to 800 nm. The transmittance was higher than 90% for all samples when the incident radiation was greater than 300 nm. A cutoff wavelength of 255 nm was observed for all samples. **Equations 3.8** and **3.9** were used to calculate the optical bandgap of the samples. Here, α is the absorption coefficient, h is Plank's constant (4.136×10^{-15} eV-s), ν is the photon frequency, E_g is the bandgap energy, d is film thickness, A is absorbance, and B is a proportionality constant [25]. The value of r is determined based on the electronic transition. For direct allowed transitions, direct forbidden transitions, indirect allowed transitions, and indirect forbidden transitions, r is equal to 1/2, 3/2, 2, and 3, respectively. Considering $\beta\text{-Ga}_2\text{O}_3$ as a direct bandgap semiconductor with allowed transitions, r is set equal to 1/2, resulting in a linear region of the

$(\alpha h\nu)^2 - h\nu$ curve just above the optical absorption edge. Extrapolating this linear curve to the photon energy axis provides the optical bandgap of the semiconductor, which is shown in the inset of **Figure 3.9**. The optical bandgap of each sample was found to be 5 eV, which is consistent with previous reports [12], [20]. The trends identified in crystalline structure, surface morphology, and optical transmission properties show that the films have the highest quality grown using an oxygen partial pressure between 0.1 and 1 mT. The optimized growth recipe shown in **Table 3.5** was used for the remaining growth-related analysis.

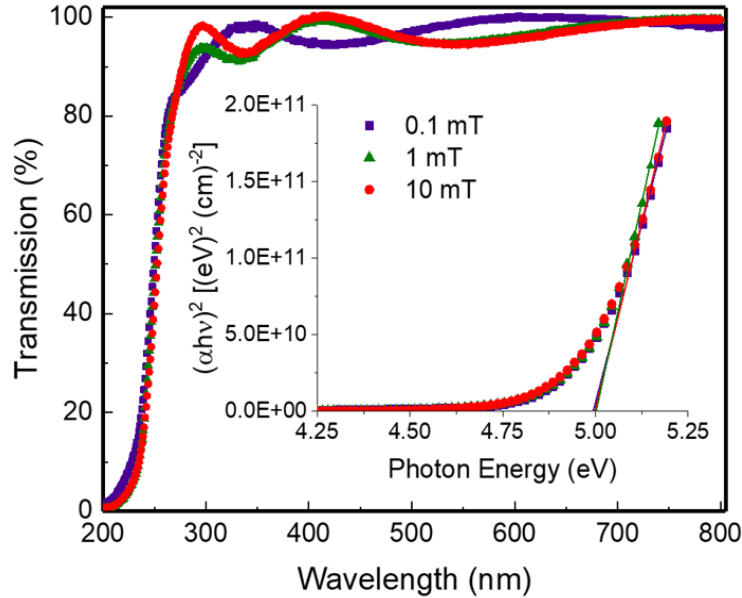


Figure 3.9 Transmission spectra of Ga_2O_3 thin films. Inset shows an estimation of bandgap energy for the three samples. Copyright (2019) John Wiley and Sons [24].

$$(\alpha h\nu)^{1/r} = B(h\nu - E_g) \quad (3.8)$$

$$\alpha = \frac{1}{d} \ln(10^A) \quad (3.9)$$

Sn dopants were used to increase the film conductivity. The doping was varied by changing the Sn content in the ablation targets from 1 to 10 mol%. A series of thin films was grown by using the optimized recipe summarized in **Table 3.5**, aside from of an increasing number of laser

pulses to vary the film thickness from 100 nm to 1200 nm. Hall measurements were performed on the resulting samples by depositing Ni/Au (50 nm/100 nm) contacts using electron beam deposition. The conductivity of the samples can be seen in **Figure 3.10(a)**. A thickness dependence was observed for the samples grown using an undoped, 1 mol% Sn-doped, and 10 mol% Sn-doped ablation target. It is likely that this dependence was affected by the films becoming less strained with increased thickness. As expected, the 10 mol% Sn-doped target produced the most conductive films, with the film of 1200 nm thickness having a conductivity of $0.029 (\Omega\text{-cm})^{-1}$. **Figure 3.10(b)** shows the Hall concentration plotted as a function of ablation target Sn content, where a content of zero is just referring to an unintentionally doped Ga_2O_3 target. One disadvantage of PLD when growing doped films is that the amount of dopant in the source material needs to be physically verified. This can lead to a substantial amount of error in the resulting thin film carrier concentration, as evident by the ΔN_D shown at each target Sn content amount. The highest carrier concentration achieved here ($2 \times 10^{17} \text{ cm}^{-3}$) is three orders of magnitude lower than in homoepitaxial thin films, where the maximum achievable carrier concentration is on the order of $2 \times 10^{20} \text{ cm}^{-3}$ [26].

Table 3.5 *Optimized PLD growth recipe for $\beta\text{-Ga}_2\text{O}_3$.*

Growth Parameter	Value
Substrate Temperature	887 °C
Base Chamber Pressure	1×10^{-7} Torr
Oxygen Pressure, P_{O_2}	1×10^{-3} Torr
Oxygen Flow Rate	16 sccm
Laser Energy	248 mJ/pulse
Laser Repetition Rate	10 Hz
Laser Pulses	45k

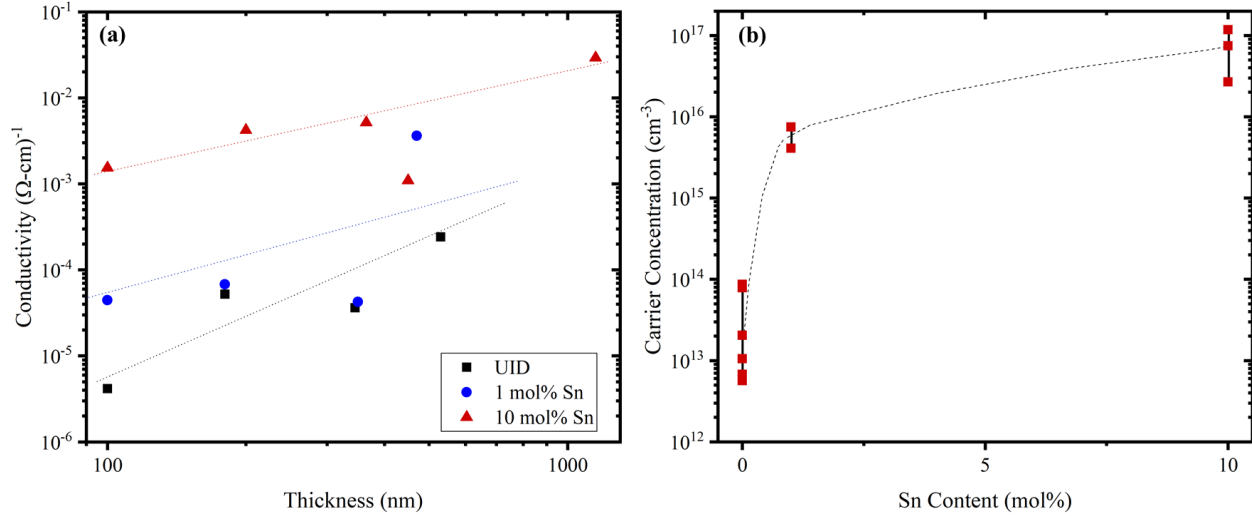


Figure 3.10 (a) Conductivity of Sn-doped $\beta\text{-Ga}_2\text{O}_3$ thin films with varying thicknesses grown on *c*-plane Al_2O_3 . (b) Carrier concentration of Sn-doped thin films as a function of ablation target Sn content.

To further investigate this, two Sn-doped Ga_2O_3 thin films were sent to EAG Laboratories for secondary ion mass spectroscopy (SIMS) analysis. **Figure 3.11** (a) and (b) shows the resulting SIMS data for a 1 mol% Sn-doped Ga_2O_3 thin film and 10 mol% Sn-doped Ga_2O_3 thin film, respectively. The compositional data showed that both samples contained 40% Ga atoms and 60% O atoms, as is expected for stoichiometric Ga_2O_3 . The 1 mol% Sn and 10 mol% Sn films contained $\sim 0.001\%$ Sn and 0.1% Sn, respectively. The estimated number of atoms per unit volume was calculated by multiplying the compositions by Avogadro's Number. For both samples, the number of Ga atoms (N_{GA}) and number of O atoms (N_{O}) were found to be $5 \times 10^{22} \text{ cm}^{-3}$ and $8 \times 10^{22} \text{ cm}^{-3}$, respectively. The number of Sn atoms (N_{Sn}) was found to be $1 \times 10^{18} \text{ cm}^{-3}$ and $1 \times 10^{20} \text{ cm}^{-3}$ for the 1 mol% Sn and 10 mol% Sn films, respectively. Interestingly, these concentrations are more closely aligned to the values expected. The carrier density observed from the Hall measurements is approximately three orders of magnitude lower than the Sn concentration estimated from SIMS. The difference observed here is likely due to carrier trapping, which can be expected in heteroepitaxial Ga_2O_3 .

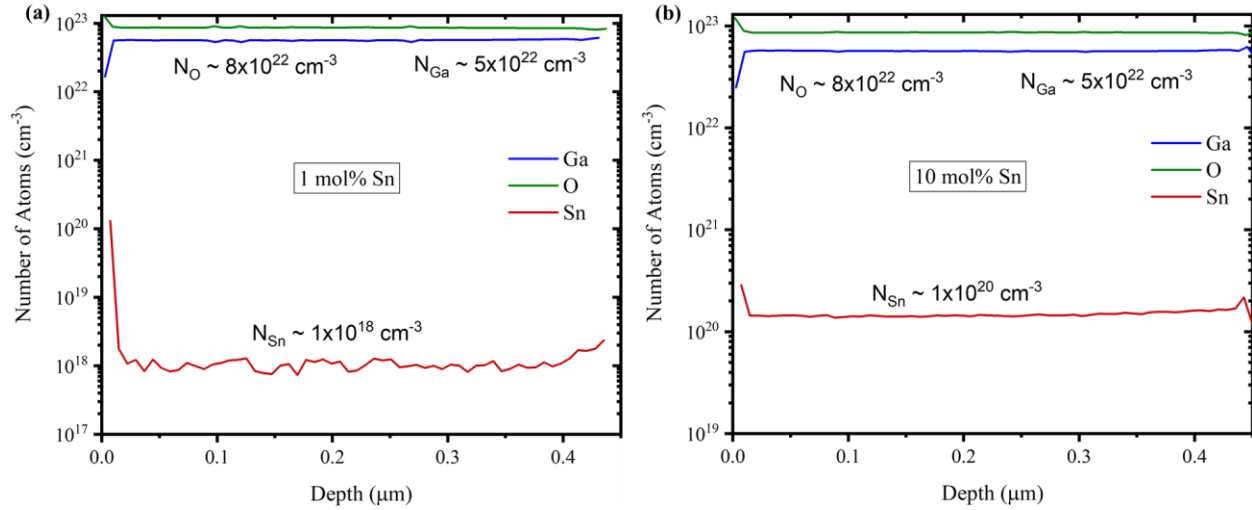


Figure 3.11 SIMS profiles of Sn-doped Ga_2O_3 thin films grown using ablation targets containing (a) 1 mol% Sn and (b) 10 mol% Sn.

3.2.3 Homoepitaxial Growth

Homoepitaxial $\beta\text{-Ga}_2\text{O}_3$ growth was carried out using Fe-doped Ga_2O_3 substrates with (001) and (010) orientations. **Figure 3.12** shows XRD θ - 2θ profiles for $(\bar{2}01)$ -, (010)-, and (001)-oriented $\beta\text{-Ga}_2\text{O}_3$, which are also shown schematically in the unit cell of **Figure 3.1**. The Fe-doped Ga_2O_3 substrates are an insulating material, making them useful for gathering mobility and carrier concentration data through Hall measurements. Tin and silicon dopants were investigated. The material properties were analyzed using a combination of XRD and Hall measurements. Unless otherwise stated, the films were grown using the recipe depicted in **Table 3.5**.

A series of Sn-doped $\beta\text{-Ga}_2\text{O}_3$ thin films were grown on (010)- and (001)-oriented Fe-doped Ga_2O_3 substrates using 0.1 mol% Sn and 1 mol% Sn ablation targets. Two ablation targets were used for each amount of target Sn content, one of which was fabricated in-house using the procedure described in *Section 3.2.1* and one was purchased from Kurt J. Lesker. The crystalline quality of the resulting thin films was analyzed by recording θ - 2θ and ω XRD spectra. **Figure**

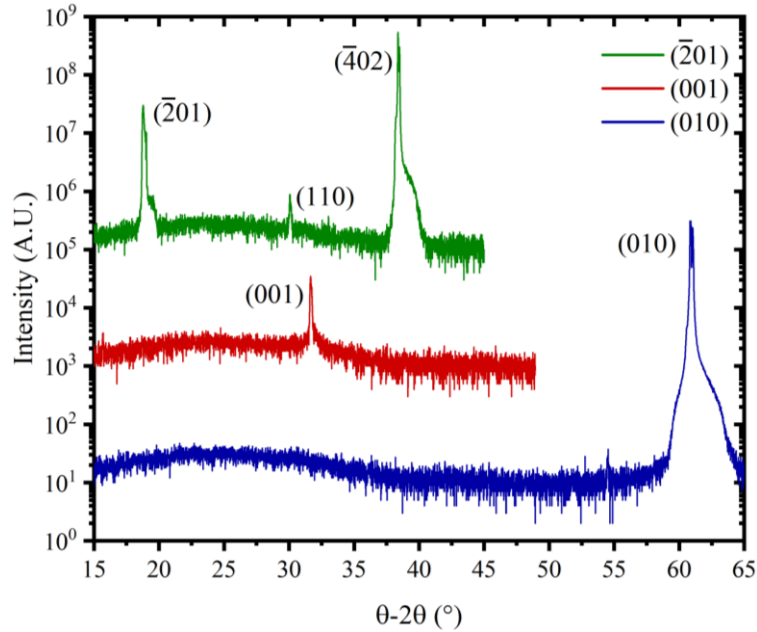


Figure 3.12 θ - 2θ XRD profiles for single-crystalline β - Ga_2O_3 substrates with different orientations.

3.13 shows the θ - 2θ and ω XRD scans for **(a, b)** (001)-oriented Sn-doped Ga_2O_3 and **(c, d)** (010)-oriented Sn-doped Ga_2O_3 homoepitaxial thin films. Additionally, four Si-doped β - Ga_2O_3 thin films were grown on (010)-oriented Fe-doped Ga_2O_3 substrates. The Si-doped films were grown using three ablation targets fabricated here with 0.001 mol% Si, 0.01 mol% Si, and 1 mol% Si, as well as one 1 mol% Si target purchased from Kurt J. Lesker. The resulting θ - 2θ and ω XRD scans are shown in **Figure 3.13 (e)** and **(f)**, respectively. Films grown using targets fabricated in this work are labeled ‘NCSU’, while the films grown using targets purchased from Kurt J. Lesker are labeled ‘KJL’.

The θ - 2θ XRD profile of the (001)-oriented thin films contains three reflections: (110), (002) from the thin film, and (002) from the substrate, as labeled in the figure. The θ - 2θ scan of the (010)-oriented samples contain two reflections: (002) from the film and (002) from the substrate. A PANalytical Empyrean Alpha-1 high-resolution X-ray diffractometer (HRXRD) equipped with a PIXcel3D detector was used to differentiate between the two (002) reflections.

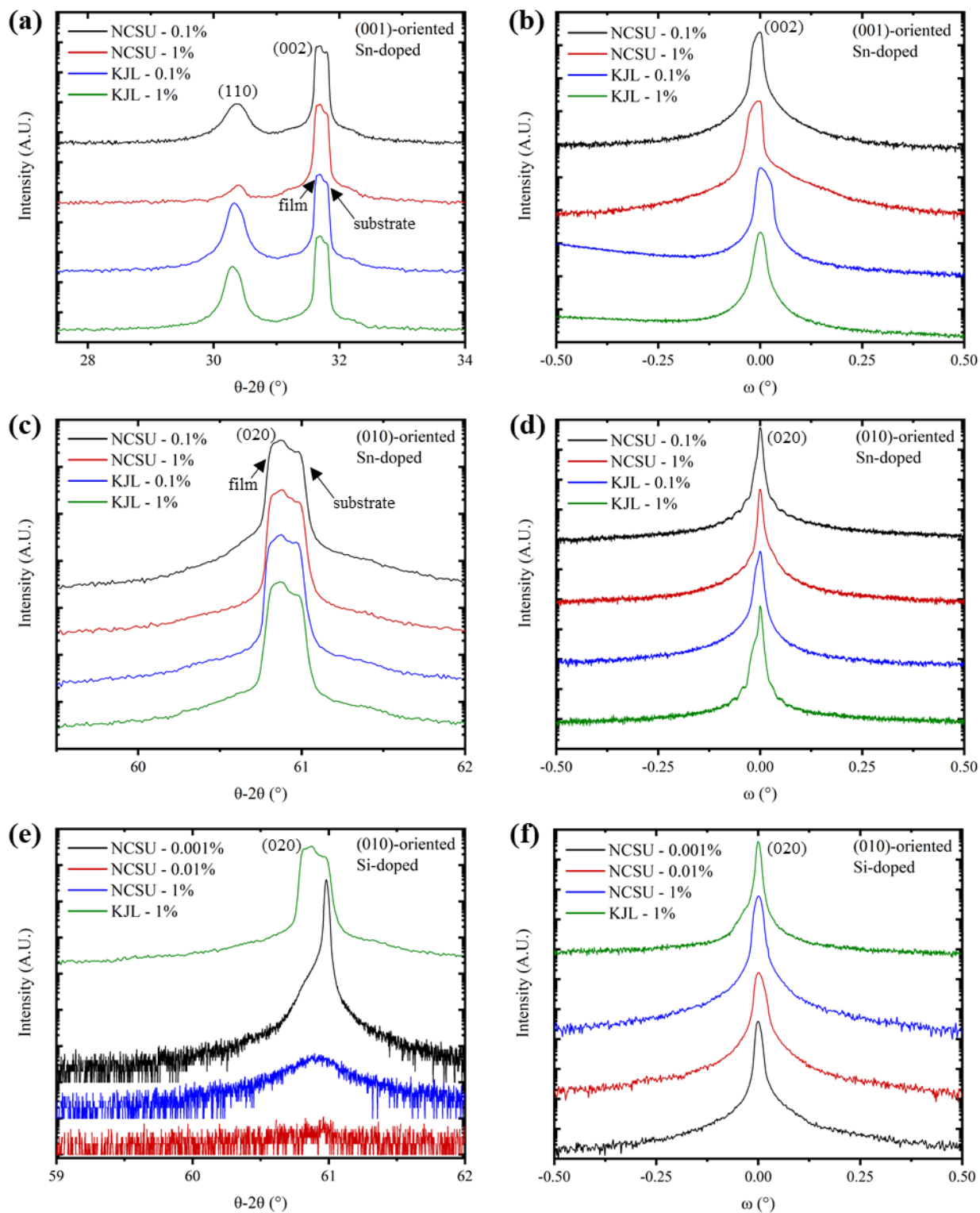


Figure 3.13 θ - 2θ and ω XRD profiles for (a, b) (001)-oriented Sn-doped, (c, d) (010)-oriented Sn-doped, and (e, f) (010)-oriented Si-doped homoepitaxial β -Ga₂O₃ thin films. Films of each orientation and dopant were grown using varying ablation target impurity content.

After completing the θ - 2θ scan, the 2θ axis was aligned to the film (002) peak and the omega spectra was recorded for each sample. A similar procedure was used for gathering the omega scan of (010)-oriented Sn-doped Ga₂O₃ and (010)-oriented Si-doped Ga₂O₃ thin films. The resulting FWHM data for each series of thin films can be seen in **Figure 3.14**. The ablation target impurity content (mol%) is shown above each data point in the figure. The FWHM of the (001)-oriented films were the highest measured. This is likely due to the (001) substrates being of lesser crystalline quality than that of the (010) substrates. No significant differences were observed in the crystalline quality for the films grown using NCSU- and KJL-fabricated ablation targets. The (010)-oriented Sn-doped Ga₂O₃ films had the best crystalline quality, where the FWHM ranged from 21.6 to 30.2 arcseconds. These FWHM values prove that the crystalline quality of PLD-grown Ga₂O₃ is excellent in comparison to other semiconductor materials that are more matured. For instance, Irwinska *et al.* reported XRD ω scans on Si-doped GaN thin films and a GaN seed crystal used for bulk crystal growth [27]. The resulting FWHM of the seed crystal and thin film were 28 and 32 arcseconds, respectively. The (001) Sn-doped Ga₂O₃ films and (010) Si-doped Ga₂O₃ films had FWHM values that ranged from 70.9 to 103.0 arcseconds and 35.3 to 67.8 arcseconds, respectively.

Transport properties of the Sn-doped and Si-doped Ga₂O₃ thin films were evaluated by Hall measurements. Ohmic contacts were formed on the film surface by first depositing a Ti/Al/Ni/Au (20/100/50/50 nm) metal stack using E-beam deposition and then rapid thermal annealing the metals for 60 seconds at 470 °C in an N₂ ambient. The mobility and carrier concentration data gathered for each sample is shown in **Figure 3.15**. The mobility approximation is shown using a dashed line, and the governing equation is shown inset on the plot [28]. The carrier concentration of the Sn-doped Ga₂O₃ films was varied over two orders of magnitude

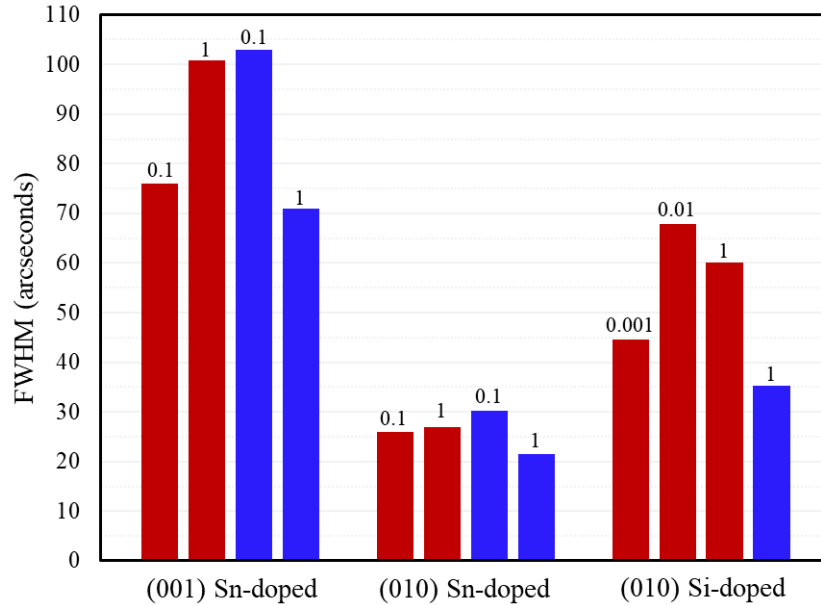


Figure 3.14 FWHM values obtained by XRD rocking curve measurement. Films grown using NCSU- and KJL-fabricated ablation targets are shown using red and blue bars, respectively. The molar percentage of the impurity contained in the target is shown above each bar.

($2.4 \times 10^{17} - 4.1 \times 10^{19} \text{ cm}^{-3}$) while maintaining mobility values in the range of $14.1 - 28.5 \text{ cm}^2/\text{V}\cdot\text{s}$. The carrier concentration of the Si-doped Ga_2O_3 films was varied slightly more in the range of $8.9 \times 10^{18} - 2.0 \times 10^{20} \text{ cm}^{-3}$, but the mobility was exceedingly higher, reaching a maximum value of $56.7 \text{ cm}^2/\text{V}\cdot\text{s}$ at a carrier concentration of $1.1 \times 10^{20} \text{ cm}^{-3}$.

Interestingly, the mobility of the films shown here did not trend with carrier concentration as described by the Ga_2O_3 mobility approximation. Half of the Si-doped films exceeded the theoretical mobility for their given carrier concentration. Furthermore, to the best of my knowledge, the data point for the Si-doped film appears to be the most conductive Ga_2O_3 thin film reported to-date, with a conductivity value of $1592 \text{ } (\Omega\cdot\text{cm})^{-1}$. This conductivity is similar to that of indium tin oxide, which is a commonly used material for transparent conductor applications, and has a conductivity that varies from 1×10^3 to $1 \times 10^4 \text{ } \Omega^{-1}\cdot\text{cm}^{-1}$ depending on the SnO_2 content [29]–[31]. Temperature-dependent Hall data was gathered for the highly conductive Si-doped Ga_2O_3 film while varying the temperature from 14 to 320 K. The resulting $\mu(T)$, $N_D(T)$, and $\sigma(T)$

profiles are shown in **Figure 3.16**. The carrier concentration varied slightly from 1.93×10^{20} – $1.96 \times 10^{20} \text{ cm}^{-3}$ over the studied temperature range. At 14 K, the mobility and conductivity reached maximum values of $68.59 \text{ cm}^2/\text{V-s}$ and $2159.90 \text{ } \Omega^{-1}\text{cm}^{-1}$, respectively. The temperature-dependent trends observed here are similar to those reported previously for Si- and Sn-doped Ga_2O_3 [28].

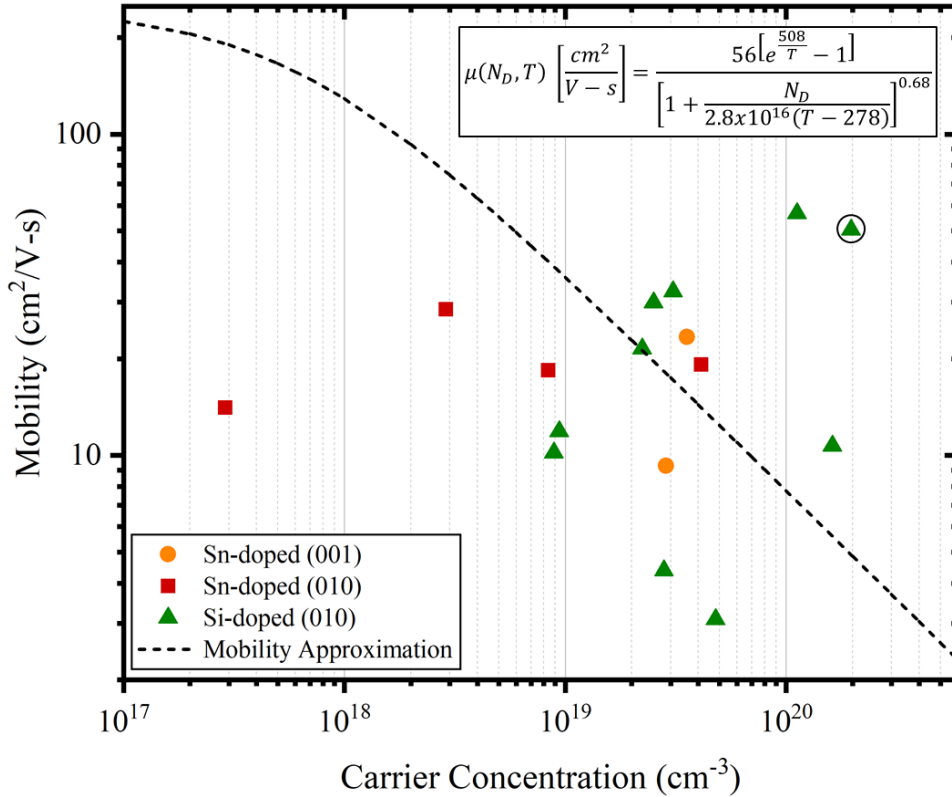


Figure 3.15 Mobility and carrier concentration data of homoepitaxial Sn-doped and Si-doped Ga_2O_3 thin films gathered by Hall measurements. The Ga_2O_3 mobility approximation is shown using a dashed line and the representative equation is inset [28].

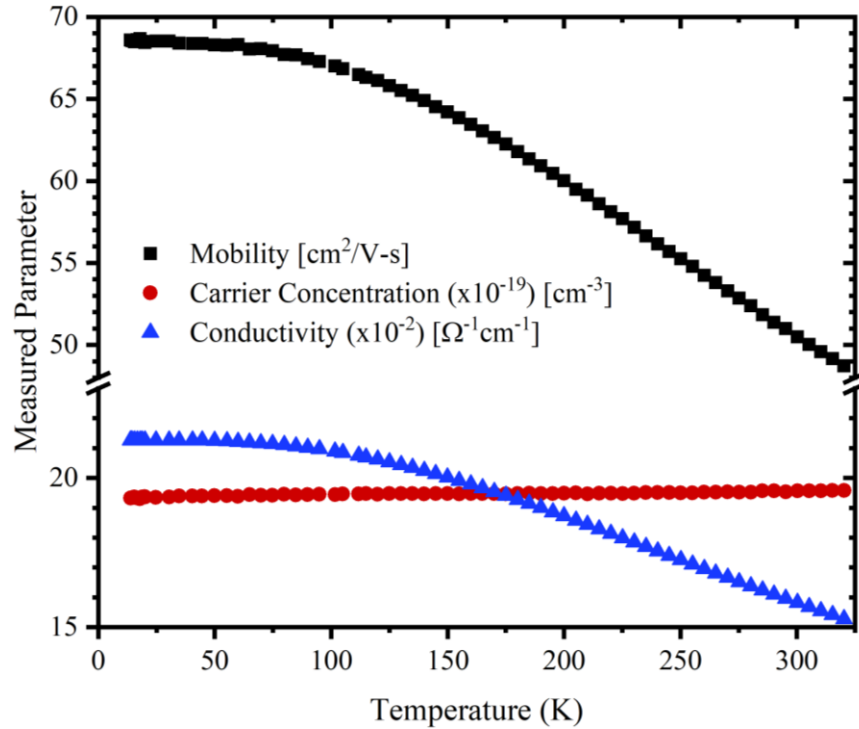


Figure 3.16 Mobility, carrier concentration, and conductivity of Si-doped Ga_2O_3 thin film as a function of temperature.

3.3 Conclusions

Undoped, Sn-doped, and Si-doped Ga_2O_3 ablation targets were fabricated for Ga_2O_3 thin film growth on c-plane sapphire and native bulk substrates. The crystalline quality of the resulting thin films was characterized by XRD. Ga_2O_3 - Al_2O_3 lattice matching analysis was performed to develop a better understanding about the evolution of undesired XRD reflections present in the heteroepitaxial thin films. Temperature and PO_2 growth conditions were optimized to enhance crystalline, morphological, and optical properties of the undoped thin films and found to be 887°C and 1×10^{-3} Torr, respectively. Sn- and Si-doped Ga_2O_3 homoepitaxial thin films were grown on (001)-, (010)-, and $(\bar{2}01)$ -oriented native Ga_2O_3 substrates. The homoepitaxial films were evaluated using XRD and Hall measurements. A wide conductivity range of 1.4×10^{-2} to 1.6×10^3

$\Omega^{-1}\text{cm}^{-1}$ was accomplished by varying the doping content in the films from $2 \times 10^{17} \text{ cm}^{-3}$ to $2 \times 10^{20} \text{ cm}^{-3}$ using Sn and Si dopants. The thin films possessed mobilities of up to $56.7 \text{ cm}^2/\text{V}\cdot\text{s}$.

Low doping levels are desired for applications such as Schottky barrier diode drift layers since the depletion region width (W_D) scales by $1/\sqrt{N_D}$, and increasing the W_D will reduce reverse leakage current that results from Schottky barrier tunneling. Highly-doped Ga_2O_3 films could be used for transparent conducting oxide (TCO) applications such as liquid crystal displays and solar cells. The current market for these applications is dominated primarily by indium tin oxide, which can be relatively expensive in comparison to other TCOs.

3.4 References

- [1] J. Åhman, G. Svensson, and J. Albertsson, "A reinvestigation of β -gallium oxide," *Acta Crystallogr. Sect. C Cryst. Struct. Commun.*, vol. 52, no. 6, pp. 1336–1338, 1996.
- [2] S. J. Pearton et al., "A review of Ga₂O₃ materials, processing, and devices," *Appl. Phys. Rev.*, vol. 5, no. 1, p. 011301, 2018.
- [3] S. Nakagomi and Y. Kokubun, "Crystal orientation of β -Ga₂O₃ thin films formed on c-plane and a-plane sapphire substrate," *J. Cryst. Growth*, vol. 349, no. 1, pp. 12–18, 2012.
- [4] H. Ohta, M. Orita, M. Hirano, K. Ueda, and H. Hosono, "Epitaxial growth of transparent conductive oxides," *Int. J. Mod. Phys. B*, vol. 16, no. 1–2, pp. 173–180, 2002.
- [5] W. Seiler, M. Selmane, K. Abdelouhadi, and J. Perrière, "Epitaxial growth of gallium oxide films on c-cut sapphire substrate," *Thin Solid Films*, vol. 589, pp. 556–562, 2015.
- [6] M. De Graef and M. E. McHenry, *Structure of Materials - An Introduction to Crystallography, Diffraction, and Symmetry*, 2nd ed. Cambridge University Press, 2012.
- [7] P. R. Willmott, R. Timm, and J. R. Huber, "RHEED analysis of interface growth modes of TiN films on Si (001) produced by crossed beam laser ablation," *Appl. Surf. Sci.*, vol. 127–129, pp. 105–110, 1998.
- [8] I. P. Wellenius, "Rare-Earth Doped Wide Bandgap Oxide Semiconductor Materials and Devices," North Carolina State University, 2009.
- [9] H. L. Porter, "Thin Film Growth and Doping Characteristics of ZnO AND β -Ga₂O₃," North Carolina State University.
- [10] F. B. Zhang, K. Saito, T. Tanaka, M. Nishio, and Q. X. Guo, "Structural and optical properties of Ga₂O₃ films on sapphire substrates by pulsed laser deposition," *J. Cryst. Growth*, vol. 387, pp. 96–100, 2014.
- [11] F.-P. Yu, S.-L. Ou, and D.-S. Wu, "Pulsed laser deposition of gallium oxide films for high performance solar-blind photodetectors," *Opt. Mater. Express*, vol. 5, no. 5, pp. 1240–1249, 2015.
- [12] T. Oshima, T. Okuno, and S. Fujita, "Ga₂O₃ thin film growth on c-plane sapphire substrates by molecular beam epitaxy for deep-ultraviolet photodetectors," *Jpn. J. Appl. Phys.*, vol. 46, no. 11R, p. 7217, 2007.
- [13] Y. Lv, J. Ma, W. Mi, C. Luan, Z. Zhu, and H. Xiao, "Characterization of β -Ga₂O₃ thin films on sapphire (0001) using metal-organic chemical vapor deposition technique," *Vacuum*, vol. 86, no. 12, pp. 1850–1854, 2012.

- [14] T. Sheng, X.-Z. Liu, L.-X. Qian, B. Xu, and Y.-Y. Zhang, "Photoelectric properties of β -Ga₂O₃ thin films annealed at different conditions," *Rare Met.*, pp. 1–5, 2015.
- [15] H. J. Ko, T. Yao, Y. Chen, and S. K. Hong, "Investigation of ZnO epilayers grown under various Zn/O ratios by plasma-assisted molecular-beam epitaxy," *J. Appl. Phys.*, vol. 92, no. 8, pp. 4354–4360, 2002.
- [16] H. Okumura, M. Kita, K. Sasaki, A. Kuramata, M. Higashiwaki, and J. S. Speck, "Systematic investigation of the growth rate of β -Ga₂O₃(010) by plasma-assisted molecular beam epitaxy," *Appl. Phys. Express*, vol. 7, no. 9, pp. 3–7, 2014.
- [17] J. B. Varley, J. R. Weber, A. Janotti, and C. G. Van De Walle, "Oxygen vacancies and donor impurities in β -Ga₂O₃," *Appl. Phys. Lett.*, vol. 97, no. 14, pp. 10–13, 2010.
- [18] S. C. Siah et al., "Dopant activation in Sn-doped Ga₂O₃ investigated by X-ray absorption spectroscopy," *Appl. Phys. Lett.*, vol. 107, no. 25, p. 252103, 2015.
- [19] S.-L. Ou et al., "Growth and etching characteristics of gallium oxide thin films by pulsed laser deposition," *Mater. Chem. Phys.*, vol. 133, no. 2–3, pp. 700–705, 2012.
- [20] Z. Chen et al., "Effects of dopant contents on structural, morphological and optical properties of Er doped Ga₂O₃ films," *Superlattices Microstruct.*, vol. 90, pp. 207–214, 2016.
- [21] Y. Chen et al., "The lattice distortion of β -Ga₂O₃ film grown on c-plane sapphire," *J. Mater. Sci. Mater. Electron.*, vol. 26, no. 5, pp. 3231–3235, 2015.
- [22] M. Orita, H. Hiramatsu, H. Ohta, M. Hirano, and H. Hosono, "Preparation of highly conductive, deep ultraviolet transparent β -Ga₂O₃ thin film at low deposition temperatures," *Thin Solid Films*, vol. 411, no. 1, pp. 134–139, 2002.
- [23] T. S. Ngo, D. D. Le, D. K. Tran, J. H. Song, and S. K. Hong, "In Situ Oxidation of GaN Layer and Its Effect on Structural Properties of Ga₂O₃Films Grown by Plasma-Assisted Molecular Beam Epitaxy," *J. Electron. Mater.*, vol. 46, no. 6, pp. 3499–3506, 2017.
- [24] N. Blumenschein, T. Paskova, and J. F. Muth, "Effect of Growth Pressure on PLD-Deposited Gallium Oxide Thin Films for Deep-UV Photodetectors," *Phys. status solidi*, vol. 216, no. 20, p. 1900098, Oct. 2019.
- [25] B. D. Vriezicke, S. Patel, B. E. Davis, and D. P. Birnie III, "Evaluation of the Tauc Method for Optical Absorption Edge Determination: ZnO Thin Films as a Model System," *Phys. Status Solidi Basic Res.*, vol. 252, no. 17, pp. 1700–1710, 2015.
- [26] K. D. Chabak et al., "Lateral β -Ga₂O₃ field effect transistors," *Semicond. Sci. Technol.*, vol. 35, no. 013002, p. 22, 2020.

- [27] M. Iwinska et al., “Homoepitaxial growth of HVPE-GaN doped with Si,” *J. Cryst. Growth*, vol. 456, pp. 91–96, Dec. 2016.
- [28] N. Ma et al., “Intrinsic electron mobility limits in β -Ga₂O₃,” *Appl. Phys. Lett.*, vol. 109, no. 21, pp. 1–6, 2016.
- [29] Z. Chen, W. Li, R. Li, Y. Zhang, G. Xu, and H. Cheng, “Fabrication of Highly Transparent and Conductive Indium–Tin Oxide Thin Films with a High Figure of Merit via Solution Processing,” *Langmuir*, vol. 29, no. 45, pp. 13836–13842, Nov. 2013.
- [30] H. Hosono, H. Ohta, M. Orita, K. Ueda, and M. Hirano, “Frontier of transparent conductive oxide thin films,” *Vacuum*, vol. 66, no. 3–4, pp. 419–425, Aug. 2002.
- [31] C. G. Granqvist and A. Hultåker, “Transparent and conducting ITO films: new developments and applications,” *Thin Solid Films*, vol. 411, no. 1, pp. 1–5, May 2002.

CHAPTER 4 – THERMAL CONDUCTIVITY

4.1 3ω Technique

One fundamental limitation of β -Ga₂O₃ is its poor thermal conductivity (10 – 30 W/m-K), which can lead to many issues considering its intended role in high-power electronics. A better understanding of the β -Ga₂O₃ anisotropic thermal conductivity could be potentially helpful in developing high-power device along a preferred crystallographic direction that may mitigate a poor thermal dissipation. It has already been shown that the β -Ga₂O₃ thermal conductivity varies with crystal direction, but the number of analyzed directions have been limited and requires further attention. Additionally, effects from doping and crystal quality have been relatively unexplored.

The room temperature thermal conductivity of β -Ga₂O₃ was predicted from first principle calculations and estimated to be 11 W/m-K, 21.5 W/m-K, and 21 W/m-K along the [100], [010], and [001] crystal directions, respectively [1]. There have also been experimental reports of β -Ga₂O₃ thermal conductivity using several different experimental techniques. The laser flash method was used to measure a thermal conductivity of 21 W/m-K along the [010] direction in Czochralski grown β -Ga₂O₃ [2]. Time-domain thermoreflectance (TDTR) was used to study the thermal conductivity in different crystal directions of Sn-doped β -Ga₂O₃ [3]. It was found that the thermal conductivity varied from 10.9 W/m-K in the [100] direction to 27 W/m-K in the [010] direction. The 3ω technique was used to measure the thermal conductivity of undoped and Mg-doped β -Ga₂O₃ along the [100] direction with a room temperature value of 13 W/m-K found for both samples [4]. Furthermore, the temperature dependent measurements down to 25 K revealed a maximum thermal conductivity of 530 W/m-K. The 2ω technique has been used to measure the thermal conductivity in Mg-doped β -Ga₂O₃ at room temperature [5]. The thermal conductivity

measured in the [100], [010], and [001] directions was found to be 11 W/m-K, 29 W/m-K, and 21 W/m-K, respectively.

The method used to measure the thermal conductivity in this work is the 3ω technique which was first introduced by Cahill and Pohl in 1987 [6]. One benefit of the 3ω technique over some other commonly used thermal conductivity characterization methods is that it results in a direct measurement of the material thermal conductivity rather than its diffusivity. Like all other thermal conductivity characterization methods, the 3ω technique requires a heat source and thermometer, which is implemented by depositing a thin metal strip on the sample surface as shown in **Figure 4.1**.

To understand how the 3ω technique works, it is important to first discuss three aspects of the measurement from a physics standpoint: the introduction of thermal waves into the medium, detection of temperature change, and thermal conductivity extraction.

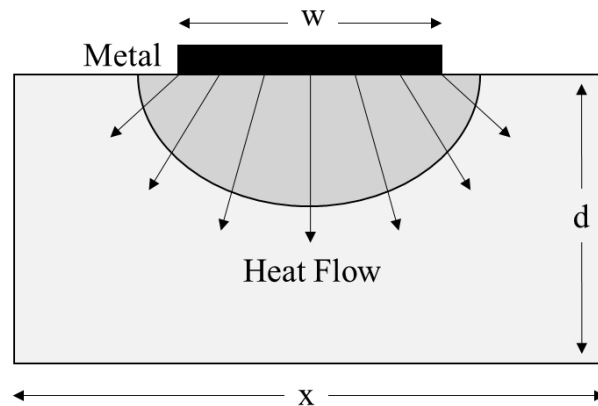


Figure 4.1 Side-view representation on the basis of the 3ω technique depicting radial diffusion of thermal waves through the material from the metal heat source.

4.1.1 Heat Source

The thermal diffusion in the 3ω technique can be described as a radial flow of thermal waves from a 1-dimensional source as shown in **Figure 4.1**. It was shown by Carslaw and Jaeger that the temperature oscillations resulting from this thermal diffusion process are a function of distance (r) from the heater center as shown in **Equation 4.1** [7]. Here, P is the generated power in the line source, l is the length of the line, κ is the thermal conductivity of the material, K_0 is the Bessel function of the zeroth order, and λ is the thermal penetration depth. The thermal penetration depth can be described by **Equation 4.2**, where ρ is density and C_p is the specific heat.

$$\Delta T(r) = \frac{P}{\pi l \kappa} K_0\left(\frac{r}{\lambda}\right) \quad (4.1)$$

$$\lambda = \sqrt{\frac{\kappa}{2\omega\rho C_p}} \quad (4.2)$$

A thin metal strip with a resistance of R_0 is deposited onto the sample surface to serve as a heat source as shown in **Figure 4.2**. A time-dependent AC current is driven through the outer electrodes at an angular frequency of ω as depicted in **Equation 4.3**. If the heat source metal has a resistance of R_0 , we can consider the time-dependent power component of **Equation 4.4** as the energy source that is dissipating into the material.

$$I(t) = I_0 \cos(\omega t) \quad (4.3)$$

$$P(t) = I^2(t)R_0 = I_0^2 \cos^2(\omega t) R_0 = \frac{I_0^2 R_0}{2} [1 + \cos(2\omega t)] \quad (4.4)$$

If we consider only the first power component, $P(t) = P_0 \cdot e^{2i\omega t}$, then the heat flux per unit area is just $Q_A \cdot e^{2i\omega t} = (P_1 / 2b) \cdot e^{2i\omega t}$, where P_1 is the power per unit length and b is the metal line

half-width. Using this simplified analysis, thermal and electrical effects due to the heater can be disregarded and the heater only serves as a heat carrier [8], [9]. Thus, the sinusoidal heat flux

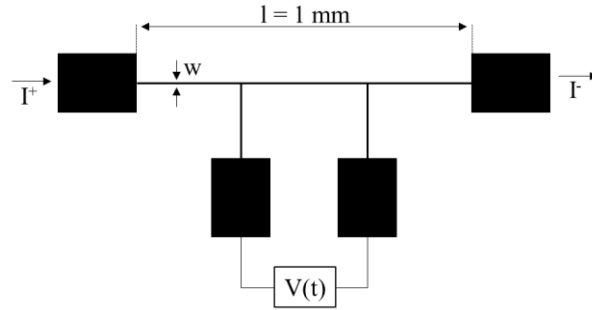


Figure 4.2 Schematic of metal heat source/thermometer layout on sample surface.

would result in complex temperature oscillations in the material beneath the heat source that take the form of $T(x,y,z) \cdot e^{2i\omega t}$ which was proven to be a solution to **Equation 4.5** [10], [11].

$$\Delta T - i \frac{2\omega}{\alpha} T = 0 \quad (4.5)$$

There are other possible solutions to **Equation 4.5** that vary depending on spatial considerations, thermal conductivity of the material, penetration depth, and any applied boundary conditions. We know that the heat flux amplitude will be zero on the surface everywhere except for the heat source. Because of **Equations 4.1** and **4.2**, we also know that the amplitude of these temperature oscillations will decrease with distance from the source. For the case of a heat source with a half-width b , Cahill showed that the complex temperature oscillations can be described by **Equation 4.6** [9].

$$\Delta T = \frac{1}{2b} \int_{-b}^{+b} T(x, y = 0) dx = \frac{P}{\pi l \kappa_{th}} \int_0^{\infty} \frac{\sin^2(u)}{u^2} \frac{du}{\sqrt{u^2 + i \frac{b^2}{\lambda^2}}} \quad (4.6)$$

For the case where $b/\lambda \ll 1$, **Equation 4.6** becomes:

$$\Delta T = \Delta T_{in} + i \Delta T_{out} = \frac{P_l}{\pi \kappa_{th}} \left[\frac{1}{2} \ln \left(\frac{\alpha}{b^2} \right) + 0.923 \ln(2\omega) - \frac{i\pi}{4} \right] \quad (4.7)$$

This solution allows us to separate out the real in-phase temperature oscillations ΔT_{in} from the imaginary out-of-phase oscillations $i\Delta T_{out}$. Examining **Equation 4.7**, we can see that ΔT_{in} is proportional to the angular frequency, inversely proportional to the thermal conductivity, and approximately equal to the solution shown in **Equation 4.8**.

$$\frac{\Delta T_{in}}{P} = -\frac{\ln(\omega)}{\pi\kappa_{th}} + C \quad (4.8)$$

4.1.2 Heat Sensor

Joule heating causes a finite heat flux within the metal strip that then dissipates into the material. Let us assume that the material is a semi-infinite dielectric medium in vacuum. As previously shown by Cahill, we can then assume that any radiation losses will be negligible over a large temperature range when using the 3ω technique [6], [8]. The temperature fluctuations that arise from Joule heating result in thermal waves that propagate through the material at a frequency and phase shift of 2ω and θ as shown in **Equation 4.9**.

$$\Delta T = \Delta T_0 \cos(2\omega t + \theta) \quad (4.9)$$

Since we are introducing temperature fluctuations we must also account for any change in the resistance of the metal. All metals have a finite temperature coefficient of resistance (α_{TCR}) causing its resistance to change according to **Equation 4.10**. For example, gold is a commonly used metal for making such measurements and has a α_{TCR} of 0.0031 K^{-1} .

$$R = R_0(1 + \alpha_{TCR}\Delta T) \quad (4.10)$$

Let us consider the voltage across the metal wire by starting with Ohm's Law and using **Equations 4.3** and **4.10**.

$$\begin{aligned} V(t) &= I(t)R = I_0 \cos(\omega t) R_0[1 + \alpha_{TCR}\Delta T_0 \cos(2\omega t + \theta)] \\ &\approx V_0 \cos(\omega t) + V_0 \left(\frac{\alpha_{TCR}\Delta T_0}{2} \right) \cos(3\omega t + \theta) \end{aligned} \quad (4.11)$$

Equation 4.11 proves the existence of a third harmonic voltage for $3\omega t + \theta \neq n\pi/2$. It can be seen that the third harmonic voltage scales with the induced temperature oscillations. Thus, at a frequency which is three times larger than that of the AC current oscillation frequency, we can measure the third harmonic voltage and extract thermal conductivity information from the material as shown in **Equation 4.12**.

$$V_{3\omega} = \frac{1}{2} V_{1\omega} \alpha_{TCR} \Delta T_0 \cos(3\omega t + \theta) \quad (4.12)$$

By combining **Equations 4.8** and **4.12**, we can see that the in-phase temperature oscillations are directly related to the thermal conductivity as shown in **Equation 4.13**.

$$\Delta T_{in} = P \frac{\ln(\omega)}{\pi \kappa_{th}} + C = \frac{V_{3\omega}}{V_{1\omega}} \frac{2}{\alpha_{TCR}} \quad (4.13)$$

Mathematically, the thermal conductivity can be extracted by taking the derivate of ΔT_{in} with respect to $\ln(\omega)$, as shown in **Equation 4.14**. However, in experimental practice, this is accomplished by simply taking the slope of a $\Delta T_{in} - \ln(\omega)$ dataset.

$$\kappa = -\frac{P}{2\pi l} \left[\frac{d \Delta T_{in}}{d \ln(\omega)} \right]^{-1} \quad (4.14)$$

A few assumptions were made during the derivation of **Equation 4.13** which cannot be forgotten during experimentation and data interpretation. The following assumptions must be considered in order for the slope method to be valid:

a) Infinite Sample Thickness

A finite sample thickness imposes a boundary onto the thermal waves such that $d > \lambda$. It is known that the penetration depth must be five times smaller than the sample thickness to obtain a measurement error of less than 1% [12]. For example, we consider a Ga_2O_3 sample with thermal conductivity of ~ 23 W/m-K, density of 5950 kg/m³, specific heat capacity of 490 J/kg-K, and thickness of 650 μm . The penetration depth is plotted as a

function of frequency in **Figure 4.3**. The penetration depth must be less than 130 μm , limiting the minimum frequency to 233 Hz.

b) *Line Source Heater*

The slope method derivation assumes a penetration depth which is much greater than the heater width ($\lambda \gg w$), allowing for the heater to be treated as a line source. If λ approaches $w/2$, then the slope method is invalidated. **Equation 4.15** provides a parameter (z) which considers the relationship between w , λ , and sample thermal conductivity anisotropy (κ_{xy}) [12]. This equation can be simplified to $w/2\lambda$ for an isotropic sample. In the derivation provided by Borca-Tasciuc, it was reported that an error of less than 1% can be achieved when $z < 0.2$, or when the penetration depth is five times larger than the heater half-width. A typical heater width is 10 μm , corresponding to a penetration depth of 25 μm and upper frequency limit of 6.3 kHz.

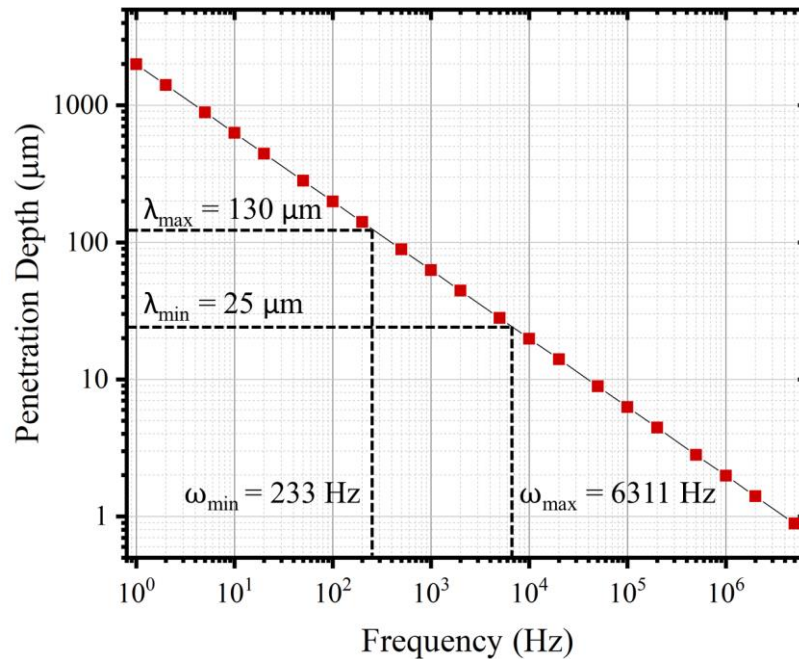


Figure 4.3 Penetration depth as a function of frequency. The dotted lines show frequency limitations for commercially available Ga_2O_3 with thickness of 650 μm to achieve measurement errors of less than 1%.

$$z = \frac{w}{2\lambda\sqrt{\kappa_{xy}}} \quad (4.15)$$

c) *Heater is Infinitely Thin and Has Zero Heat Capacity*

The final assumption is that the heater is infinitely thin and has a specific heat capacity of zero. However, this is not physically possible. Typical heater width and thickness values are 10 μm and 275 nm, respectively. Heater source with such dimensions will have a non-zero heat capacity, which can introduce error at higher frequencies. These errors have been previously discussed elsewhere [12].

4.1.3 *Device Fabrication*

Considering the discussed boundary conditions and derivation assumptions, the device fabrication steps details used in this work are shown below.

1. *Sample Cleaning:* Cleanliness of the sample surface is extremely important, especially prior to 3ω device fabrication. Any particles on the surface can lead to poor adhesion between the sample and the metal contacts. Furthermore, since the dimensions of the 3ω device are on the order of microns, any surface particulates can affect the thermal diffusion processes that are being measured. For these reasons, the samples were cleaned by a solvent (acetone/methanol) ultra-sonication process followed by an O_2 plasma cleaning process.
2. *SiO₂ Deposition:* A thin 100 nm SiO_2 isolation layer was deposited onto the sample surface using plasma-enhanced chemical vapor deposition (PECVD). The SiO_2 layer is particularly beneficial when measuring samples that are highly conductive to eliminate any

added errors resulting from noise. It has been experimentally shown that the incorporation of this SiO₂ film has no impact on the experimental results when using the 3 ω thermal conductivity measurement technique [9].

3. Sample Cleaning: The previously described cleaning procedure was repeated.
4. Photolithography/Patterning: For the next step, the samples were placed onto a 115°C hotplate for 5 minutes. Negative photoresist (AZ-5214E) was coated onto surface at 3000 RPM for 20 seconds. The samples were then heated on a 90°C hotplate for 2 minutes and exposed to 20 mW UV radiation for 3 seconds while under 3 ω device photomask. An additional bake on a 115°C hotplate was performed for 90 seconds, followed by a flood exposure for 90 seconds under 20 mW UV radiation without photomask. The sample was then placed into developer solution (MF-319) for 40 seconds, rinsed in DI H₂O for 1 minute, and dried using N₂ gas.
5. Sample Cleaning: An O₂ plasma cleaning process was used. No solvents were involved.
6. Metal Deposition: Metal contacts were then deposited using E-beam deposition. In this work we have chosen to use a Nickel (5 nm) / Gold (270 nm) stack. The nickel was used to help promote adhesion between gold and SiO₂. The chamber was typically pumped down to $\sim 5 \times 10^{-5}$ Torr prior to deposition.

7. Lift-Off: The samples were dipped into acetone directly following the metal deposition and left to soak in the acetone for a couple hours before any agitation was applied to assist with metal lift-off.
8. Sample Cleaning: The previously described cleaning procedure was repeated.
9. Analysis: Visual inspections were performed to ensure that the device were ready for testing. Any lithography/lift-off errors could result in electrical discontinuities since the metal heater/sensor line was very thin. For this reason, the devices always underwent a visual inspection after the lift-off and final cleaning process. If the devices passed the visual check, the exact metal line dimensions were then measured using a Dektak profilometer.

4.2 Single-Crystal Ga₂O₃

Measurements were performed by first driving an AC current with frequency (ω) through the device and then measuring the third harmonic voltage ($V_{3\omega}$) at the deposited voltage taps. Temperature dependent measurements were also performed while heating the samples from 295 to 400 K. The $\ln(\omega/2\pi)-V_{3\omega}$ linear dependence can be used to validate the 3ω slope method measurement integrity. **Figure 4.4** shows example $V_{3\omega}$ measurements at four temperatures on a representative undoped (010)-oriented Ga₂O₃ sample while driving the AC current with input frequencies that ranged from 30 – 1100 Hz. The observed linear relationship confirms thermal wave containment such that the previously defined boundary conditions are satisfied and minimal measurement error of less than 1% is achieved at each temperature.

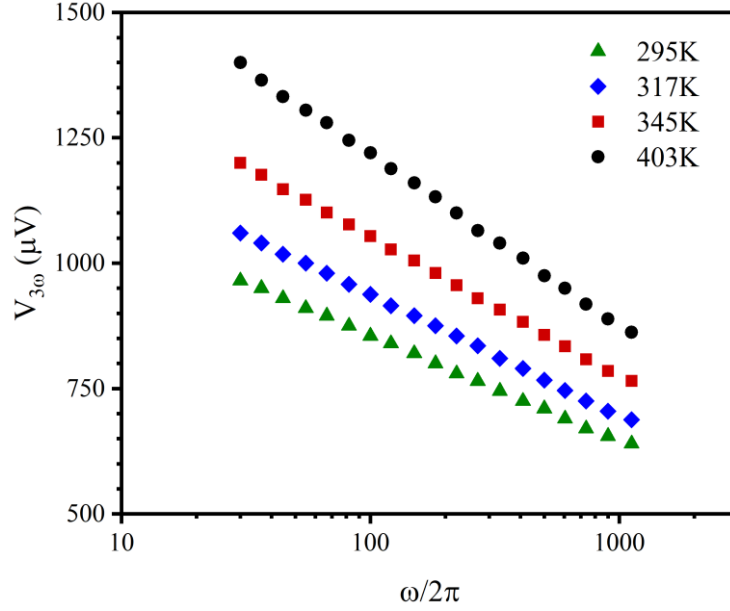


Figure 4.4 Example $V_{3\omega}$ measurements as a function of input frequency (30 – 1100 Hz) for validation of the 3ω slope method. Data shown was gathered for a representative undoped (010)-oriented Ga_2O_3 sample.

In non-anisotropic materials, the 3ω technique results in a thermal conductivity value which is of the same amplitude regardless of crystallographic direction. This thermal conductivity extraction relies on a two-dimensional cylindrical heat flow which radiates from the heater/sensor device according to **Equation 4.16** where κ' is the measured thermal conductivity, κ_x is the lateral component, and κ_y is the transverse component. This equation was presented in 2012 by Ramu and Bowers, where they demonstrated that the measured average of in-plane and cross-plane thermal conductivity can be separated into lateral and transverse components [13]. By carefully choosing Ga_2O_3 samples with unique crystallographic orientations and knowing the crystallographic directions perpendicular to those planes we can use the 3ω technique to evaluate anisotropic thermal conductivity.

$$\kappa' = \kappa_x \left[\frac{\eta+1}{2} \right] \left[1 - \frac{(\eta-1)^2}{4\eta(\eta+1)} \right] \quad (4.16)$$

$$\eta = \frac{\kappa_y}{\kappa_x} \quad (4.17)$$

For example, shown in **Figure 4.5** is a (010)-oriented Ga₂O₃ sample with the heater/sensor device aligned along either the **(a)** $\perp[102]$ or along the **(b)** $[102]$ directions. When aligned along the $\perp[102]$ direction, lateral and transverse heat flow will then be in the $[102]$ ($\kappa_x = \kappa_{[102]}$) and $[010]$ ($\kappa_y = \kappa_{[010]}$) directions, respectively. By rotating the heater/sensor metals by 90 degrees such that they are aligned along the $[102]$ direction, we can measure heat flow in an additional crystal direction ($\kappa_x = \kappa_{\perp[102]}$) while maintaining the same direction of transverse heat flow ($\kappa_y = \kappa_{[010]}$). Using this methodology, undoped, Sn-doped, and Fe-doped single-crystal Ga₂O₃ samples with (010) and $(\bar{2}01)$ orientations grown by EFG were evaluated. The samples were carefully chosen such that the carrier concentration of each dopant type was nearly identical regardless of growth orientation. **Table 4.1** shows the samples measured in this work and the particular crystallographic directions in which transverse and lateral heat flow was extracted from each.

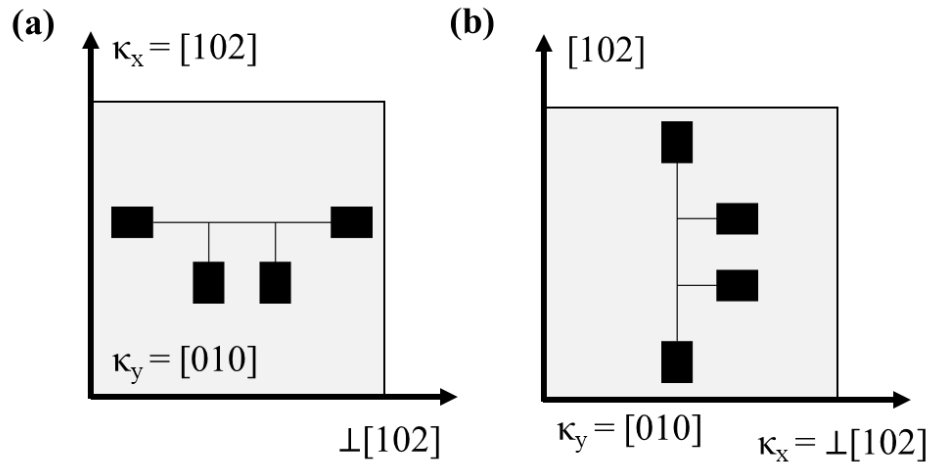


Figure 4.5 Example of 3ω heat source and sensor configuration.

Table 4.1 Sample set used for analyzing anisotropic thermal conductivity as a function of Ga_2O_3 orientation and doping.

Dopant (N_D-N_A [cm^{-3}])	Growth Orientation	Transverse Heat Flow Direction	Device Orientation	Lateral Heat Flow Direction	κ' Equation
Undoped (3.0×10^{17})	$(\bar{2}01)$	$\perp (\bar{2}01)$	[010]	[102]	κ'_1
			[102]	[010]	κ'_2
Undoped (2.7×10^{17})	(010)	[010]	\perp [102]	[102]	κ'_3
			[102]	\perp [102]	κ'_4
Sn (3.5×10^{18})	$(\bar{2}01)$	$\perp (\bar{2}01)$	[010]	[102]	κ'_1
			[102]	[010]	κ'_2
Sn (3.2×10^{18})	(010)	[010]	\perp [102]	[102]	κ'_3
			[102]	\perp [102]	κ'_4
Fe (Insulating)	(010)	[010]	\perp [102]	[102]	κ'_3
			[102]	\perp [102]	κ'_4

It can be seen that there exists four unique heat flow directions for the undoped and Sn-doped samples: [010], [102], \perp [102], and $\perp(\bar{2}01)$. The system of equations used to solve for the four unknown directional heat flow values within the undoped and Sn-doped samples are shown below in **Equations 4.18 – 4.25**. Commercially available Fe-doped Ga_2O_3 is only grown in the (010) orientation, resulting in three unknown heat flow values: [010], [102], and \perp [102]. This requires an alternative approach to solve for the three unknowns using just two equations. Solving for the Fe-doped sample thermal anisotropy required substitution of the values obtained from the undoped samples to be used. This substitution was justified given that the effect of doping was negligible on the Ga_2O_3 thermal conductivity. For example, it was found that $\eta_3 = \kappa_{[010]}/\kappa_{[102]}$ for the undoped and Sn-doped samples was 1.59 and 1.60, respectively. This small variation gave confidence in the approach and allowed for reduction of the Fe-doped sample system of equations to only two equations and two unknown variables.

$$\kappa'_1 = \kappa_{[102]} \left[\frac{\eta_1+1}{2} \right] \left[1 - \frac{(\eta_1-1)^2}{4\eta_1(\eta_1+1)} \right] \quad (4.18)$$

$$\eta_1 = \frac{\kappa_{\perp(\bar{2}01)}}{\kappa_{[102]}} \quad (4.19)$$

$$\kappa'_2 = \kappa_{[010]} \left[\frac{\eta_2+1}{2} \right] \left[1 - \frac{(\eta_2-1)^2}{4\eta_2(\eta_2+1)} \right] \quad (4.20)$$

$$\eta_2 = \frac{\kappa_{\perp(\bar{2}01)}}{\kappa_{[010]}} \quad (4.21)$$

$$\kappa'_3 = \kappa_{[102]} \left[\frac{\eta_3+1}{2} \right] \left[1 - \frac{(\eta_3-1)^2}{4\eta_3(\eta_3+1)} \right] \quad (4.22)$$

$$\eta_3 = \frac{\kappa_{[010]}}{\kappa_{[102]}} \quad (4.23)$$

$$\kappa'_4 = \kappa_{\perp[102]} \left[\frac{\eta_4+1}{2} \right] \left[1 - \frac{(\eta_4-1)^2}{4\eta_4(\eta_4+1)} \right] \quad (4.24)$$

$$\eta_4 = \frac{\kappa_{[010]}}{\kappa_{\perp[102]}} \quad (4.25)$$

Table 4.2 shows the extracted room temperature thermal conductivity values for undoped, Sn-doped, and Fe-doped samples. It can be seen that the samples were highly anisotropic, where the highest thermal conductivity values measured for each dopant type were in the [010] crystallographic direction. The highest thermal conductivity measured here was found to be 29.21 W/m-K in the undoped sample, which is consistent with TDTR measurements performed elsewhere on undoped Ga₂O₃ samples grown by Tamura Corporation [14]. The room temperature thermal conductivity findings shown here clearly demonstrate the anisotropic nature of Ga₂O₃, where κ varied by ~ 50% from the [010] direction to the minimum of ~ 15 W/m-K in the \perp [102] direction. It is commonly assumed that acoustic phonons will dominate thermal transport and the variation of thermal conductivity implies a difference in acoustic phonon velocity in different

crystallographic directions. However, in Ga_2O_3 , it has been reported that the relatively high thermal conductivity in the [010] direction is a result of both optical and acoustic phonon contributions [2]. Santia *et al.* showed that because of a lack in optical phonon gap in the dispersion for modes propagating along [010], the optical phonons only contribute to $\sim 44\%$ of the room temperature thermal conductivity in the [010] direction.

Table 4.2 Room temperature anisotropic thermal conductivity of undoped, Sn-doped, and Fe-doped Ga_2O_3 samples.

Dopant	$\kappa_{[010]}$	$\kappa_{[102]}$	$\kappa_{\perp[102]}$	$\kappa_{\perp(\bar{2}01)}$
Undoped	29.21	18.39	16.12	17.02
Sn	29.13	18.21	15.67	16.32
Fe	29.06	18.30	15.30	---

The thermal conductivity of each sample was also analyzed as a function of temperature using a heated baseplate while carefully monitoring the temperature conditions within the enclosure during the measurement. The thermal conductivity measurements took place while varying the temperature from 295 – 405 K. The experimental procedure used for gathering temperature dependence was the same as when room temperature data was gathered – the 3ω technique was used for data acquisition and then the lateral and transverse solutions were solved. **Figure 4.6** shows the resulting temperature-dependent thermal conductivity data for (a) undoped, (b) Sn-doped, and (c) Fe-doped Ga_2O_3 samples. The anisotropy was evident in all Ga_2O_3 samples measured for all orientations and dopants. A reduced thermal conductivity was also observed with increasing temperature for all dopants and crystallographic directions. This behavior is common in semiconductor materials, and is attributed to the Umklapp phonon-phonon scattering mechanism dominating at elevated temperatures.

The temperature dependence of thermal conductivity is often described for semiconductor materials using the power law of **Equation 4.26**, where α is the slope of the power law. α can be used to compare thermal conductivity temperature dependence as well as evaluating crystal purity. The thermal conductivity data of **Figure 4.6** was fit using the power law. The values of α were extracted and are shown in **Table 4.3**. It was found that α was dependent upon crystal direction and doping.

$$\kappa(T) = \kappa_{295} \left(\frac{295}{T} \right)^\alpha \quad (4.26)$$

On average, α was highest in the undoped samples for all crystallographic directions besides [010]. In semiconductor materials, Umklapp phonon-phonon scattering is the dominant scattering mechanism at temperatures near the Debye temperature, where the value of α is expected to be near unity. The Debye temperature of Ga₂O₃ is still largely unknown, but it has been speculated to be somewhere from 700 – 900 K. Values of 738 K and 872 K have been estimated from heat capacity measurements [14] and density functional theory calculations [15], respectively. As expected, the α values obtained in this work are all significantly lower than that extracted near the Debye temperature. This finding can be attributed to a large contribution of both point-defect-phonon scattering and free-carrier-phonon scattering mechanisms. Similar behavior has been reported in Si-doped GaN, where α decreased with an increased doping concentration [16].

Figure 4.7 shows the effect of doping on the Ga₂O₃ thermal conductivity for (a) [010], (b) [102], (c) \perp [102], and (d) \perp (-201) crystallographic directions. It can be seen that the effect of doping was minimal in comparison to the effect of crystal direction. The maximum amplitude deviation was less than 5% in any direction when considering different dopants. Aside from the

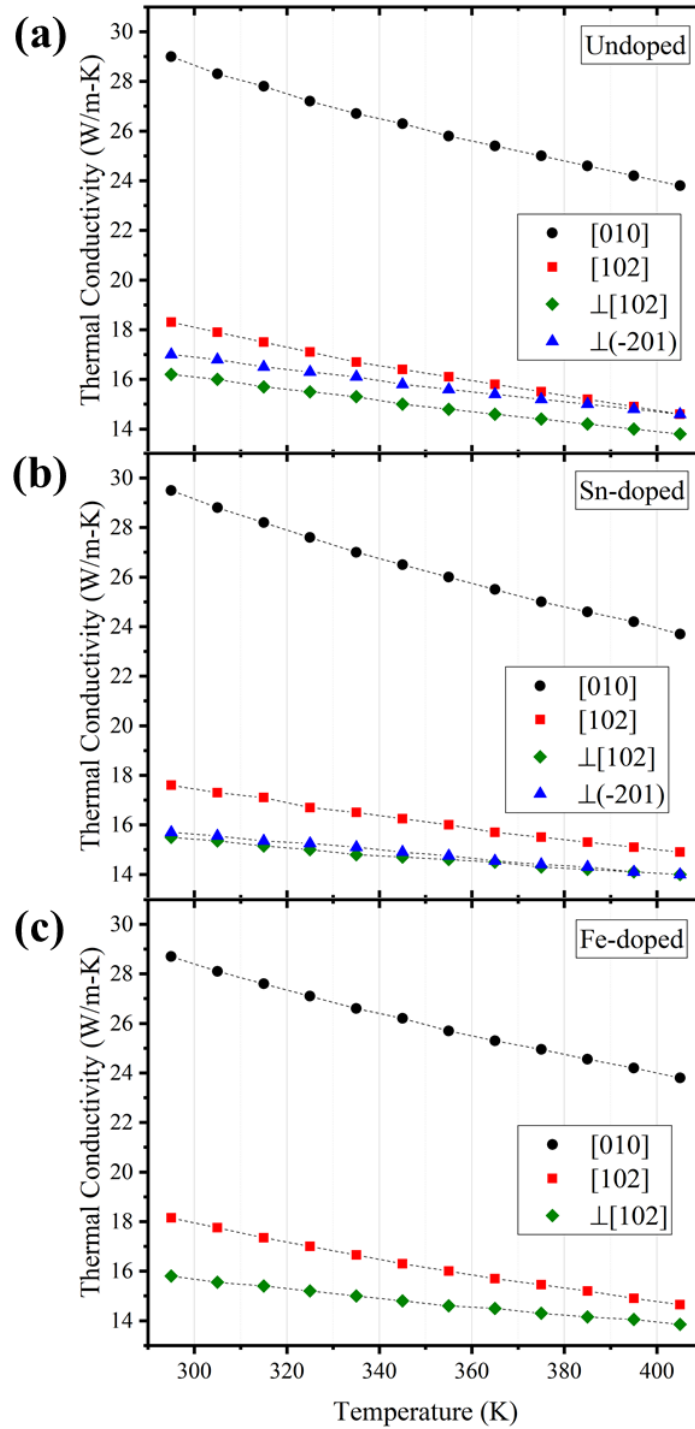


Figure 4.6 Temperature-dependent thermal conductivity along various crystallographic directions in (a) undoped, (b) Sn-doped, and (c) Fe-doped Ga₂O₃.

Table 4.3 Values of the power slope (α) found by fitting the temperature-dependent thermal conductivity in Ga_2O_3 samples with different dopants and crystal orientations.

Dopant	$\alpha_{[010]}$	$\alpha_{[102]}$	$\alpha_{\perp[102]}$	$\alpha_{\perp(\bar{2}01)}$
Undoped	0.611	0.697	0.506	0.471
Sn	0.679	0.523	0.316	0.366
Fe	0.579	0.665	0.408	---

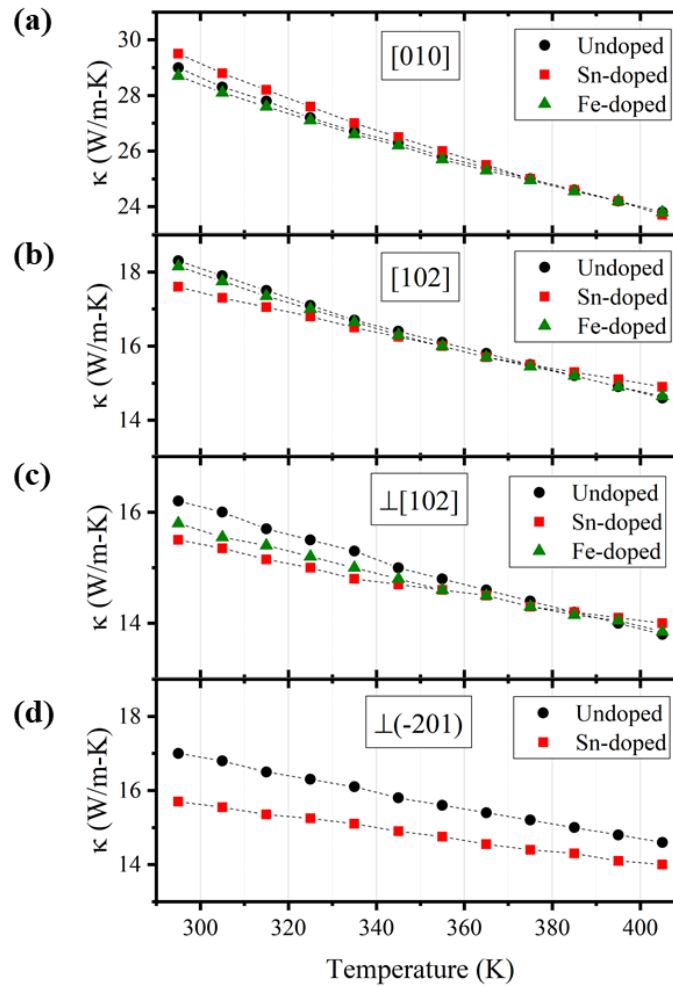


Figure 4.7 Effect of Sn and Fe doping on the temperature-dependent thermal conductivity of Ga_2O_3 along the (a) $[010]$, (b) $[201]$, (c) $\perp[201]$, and (d) $\perp(-201)$ crystallographic directions.

thermal conductivity measured along [010] in the lower temperature regime, the thermal conductivity decreased with the addition of intentional impurities which was attributed to increased phonon-point-defect scattering. Overall, the samples with Fe-doping had thermal conductivities which were lower than that of the undoped and Sn-doped samples. The higher thermal conductivity observed in Sn-doped samples with respect to Fe-doped samples is likely due to a couple of contributing scattering mechanisms. Sn doping increases the contribution of both phonon-point-defect scattering and phonon-free-carrier scattering mechanisms, decreasing the thermal conductivity, while Fe doping will only see a contribution from phonon-point-defect scattering. This is evident in **Table 4.3**, where α is generally lower for Sn- and Fe-doped samples in comparison to undoped samples, and where a lower α is observed for Sn-doped samples than for Fe-doped Ga₂O₃ samples.

4.3 Thin Film Ga₂O₃

The 3ω technique is primarily used for evaluating thermal effects in bulk material, but it can also be used to extract similar properties in multilayered structures. Boundary condition preservation allows for the 3ω technique differential method to be applied for film/substrate structures. The differential method was first reported in 1994 by Cahill *et al.* where α -Si:H thin films on MgO and Si substrates were evaluated [17]. It was shown that the temperature oscillations at the film/substrate interface were identical to that of bulk material, and could be evaluated by **Equation 4.27**, where ΔT_S is amplitude of the temperature oscillation at the substrate, P is the generated power in the line source, l is the length of the line, K_S is the thermal conductivity of the substrate, k is the wave vector of the mode, b is the heater line half-width, and D is thermal

diffusivity, and ω is frequency. Cahill reported an experimental agreement over a wide temperature range when measuring the α -Si:H/MgO structures. The differential method requires that the thin film thermal conductivity is smaller compared to the substrate ($K_F < K_S$) and the film thickness is much less than the heater line half-width ($d_F < 2b$). If true, the thermal conductivity of the film can be determined by using **Equations 4.28**, where ΔT_F , ΔT_S , and ΔT_{F+S} are the temperature oscillations in the film, substrate, and measured value of combined film and substrate, K_F is the thermal conductivity of the film, and d_F is film thickness.

$$\Delta T_S = \frac{P}{\pi K_S} \int_0^\infty \frac{\sin^2(kb)}{(kb)^3 \sqrt{k^2 + \left(\frac{2i\omega}{D}\right)^2}} dk \quad (4.28)$$

$$\Delta T_{F+S} - \Delta T_S = \Delta T_F = \frac{P d_F}{2lb K_F} \quad (4.28)$$

In this work, gallium oxide thin films were grown on c-plane sapphire for determining the thermal conductivity of the films as a function of thickness and Sn doping. The Ga₂O₃ layers were grown on only half of the sapphire surface using a glass slide as a shadow mask during the growth. The films were grown using ablation targets containing Ga₂O₃ and Sn:Ga₂O₃ (10 mol% Sn concentration) using the optimized growth conditions outlined in Chapter 3, but with a varying number of laser pulses for obtaining films with different thicknesses. The remaining fabrication details used here are the same as those outlined in *Section 4.1.3*, and resulted in the structure shown in **Figure 4.8**. The undoped and Sn-doped Ga₂O₃ thin films used in this study are shown in **Table 4.4**. Undoped and Sn-doped ($\bar{2}01$)-oriented bulk Ga₂O₃ are also included in order to provide a baseline for the thermal conductivity data that is measured. The thickness of the films ranged from 100 to 1150 nm, so a 5 μ m heater line half-width was used to satisfy the $d_F < 2b$ boundary condition. The second boundary condition requires that the thermal conductivity of the Ga₂O₃ films are less than that of sapphire substrates. The thermal conductivity of sapphire is 23 W/m-K.

The thermal conductivity of bulk Ga_2O_3 measured here was higher than this along the [010] direction, which would go against the boundary condition. However, prior to experimentation it was assumed that the thermal conductivity of the thin film samples would be much less for a couple of reasons. First, the films are $(\bar{2}01)$ -oriented, and the thermal conductivity of similarly oriented bulk Ga_2O_3 was below 20 W/m-K. Secondly, since the films were grown on sapphire rather than native Ga_2O_3 , they were expected to have poorer quality and contain a higher quantity of defects that could increase phonon-point-defect scattering and further lower the thermal conductivity from the bulk value.

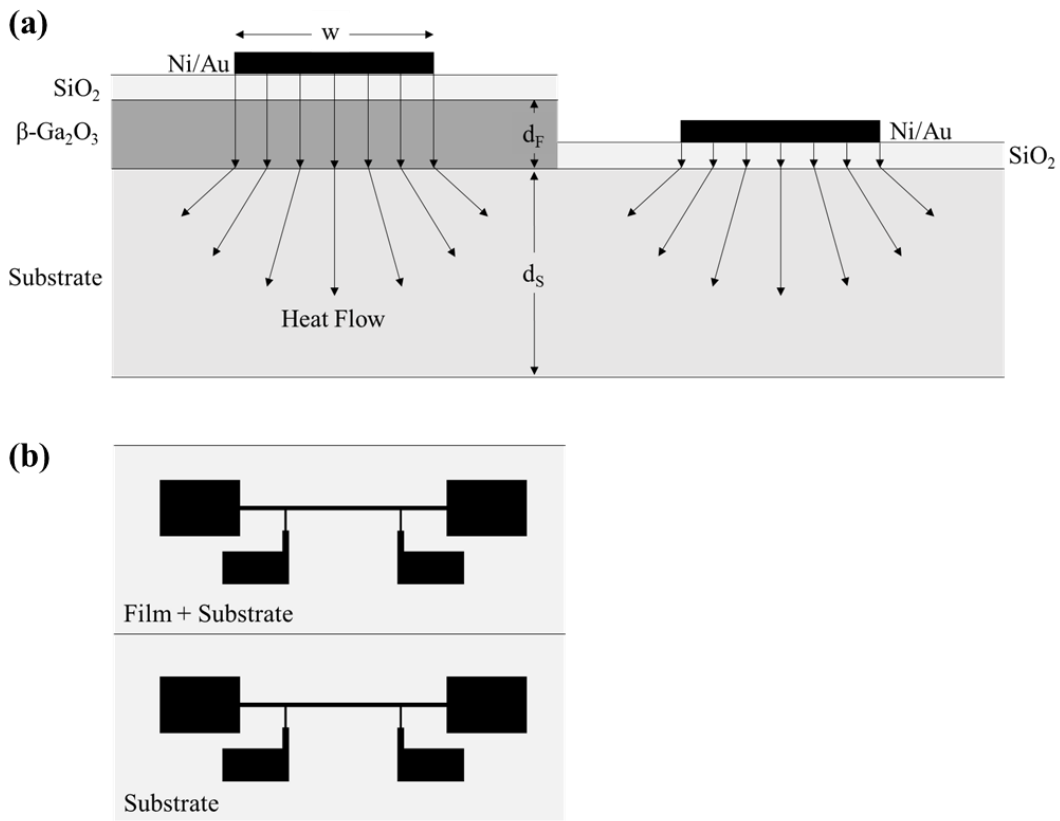


Figure 4.8 (a) Side-view and (b) top-side-view schematic drawings of $\text{Ga}_2\text{O}_3/\text{Al}_2\text{O}_3$ structures.

Table 4.4 Undoped and Sn-doped Ga₂O₃ thin films grown on c-plane sapphire with varying film thicknesses used for thermal conductivity experiments. (201)-oriented bulk samples grown by Tamura Corporation using EFG.

	Doping (target composition)	Thickness (nm)
Thin Films	undoped	100, 200, 350, 500
	10 mol% Sn	100, 200, 350, 500, 1150
	N _D – N _A (cm ⁻³)	Thickness (μm)
Bulk	undoped: 3.0x10 ¹⁷	650
	Sn-doped: 3.5x10 ¹⁸	650

The 3 ω technique – differential method proceeded by first driving an AC current $I(\omega)$ through the device and measuring $V_{3\omega}$ at the deposited voltage taps located on both regions of the sample (film+substrate ($F+S$) and substrate only (S) regions). Similarly to with the bulk samples, the $V_{3\omega}$ data can be validated when a linear $\ln(\omega/2\pi)$ – $V_{3\omega}$ dependence is observed. **Figure 4.9(a)** shows example $V_{3\omega}$ measurements for the 500 nm undoped Ga₂O₃ thin film sample when varying the AC current frequency from 30 – 950 Hz. Shown here is the $V_{3\omega}$ data acquired for $F+S$ and S regions of the sample. The desired linear relationship is observed for both regions of the sample. **Figure 4.9(b)** shows the extracted temperature oscillation amplitudes $\Delta T_{F+S}(\omega)$ and $\Delta T_S(\omega)$ which were calculated using **Equation 4.13**. **Figure 4.9(c)** shows the amplitude of temperature oscillations in the thin film, $\Delta T_F(\omega)$, which was calculated by $\Delta T_{F+S} - \Delta T_S$. Once $\Delta T_F(\omega)$ is obtained, it is averaged across all frequencies and used with **Equation 4.28** to calculate the thermal conductivity of the film. For this particular example, the thermal conductivity was found to be 6.32 W/m-K.

This experimental procedure was repeated for all samples listed in **Table 4.4**, and the resulting thermal conductivity data is shown in **Figure 4.10** as a function of film thickness for undoped and Sn-doped Ga₂O₃ samples. The thermal conductivity of (201)-oriented undoped and

Sn-doped Ga_2O_3 bulk samples, which ranged from 16.32 – 18.39 W/m-K, are also included for comparison purposes. In 2015, Szwejkowski *et al.* published the first experimental report on Ga_2O_3 thin film thermal conductivity using time-domain thermoreflectance [18], which is also shown in **Figure 4.10** and denoted as ‘Literature Values’. An interesting κ - d_F dependence was observed here for the undoped and Sn-doped samples. The thermal conductivity of undoped, Sn-doped, and undoped literature data was fit using the power law of **Equation 4.29**, where a and b are fitting constants tabulated in **Table 4.5**. Interestingly, the thermal conductivity data reported

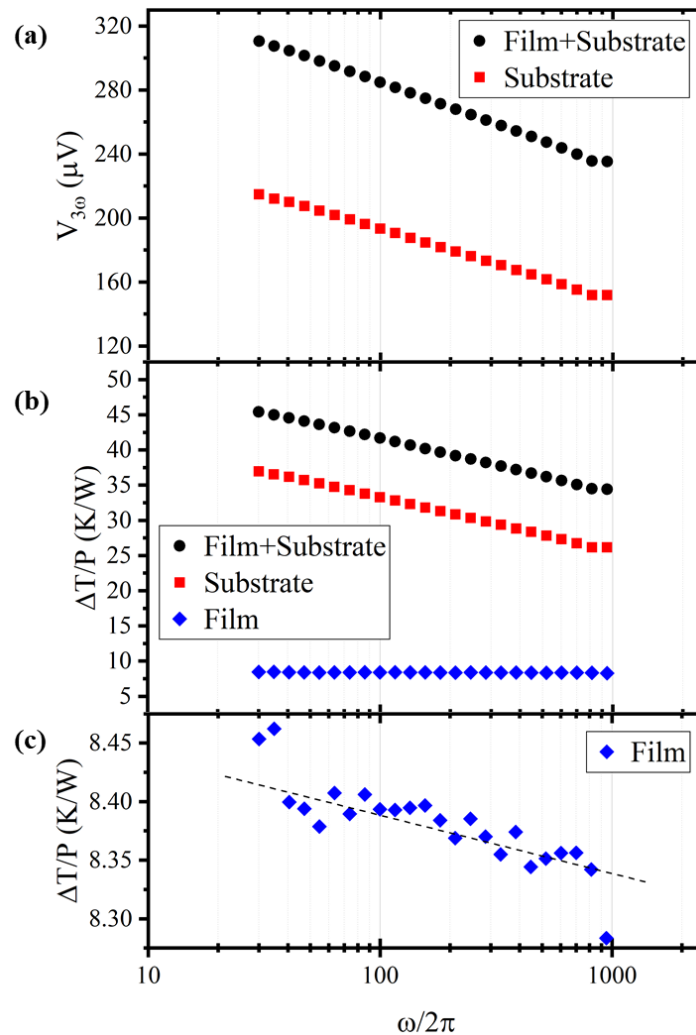


Figure 4.9 Example differential method measurement using the 500 nm undoped Ga_2O_3 thin film sample showing the linear dependencies of (a) $\ln(\omega/2\pi) - V_{3\omega}$ and (b) $\Delta T/P$ for Film+Substrate and Substrate regions of the sample. (c) Extracted temperature oscillation amplitude in the thin film, $\Delta T_F/P$, and linear fit denoted with dashed line.

by Szwejkowski *et al.* was gathered by measuring undoped Ga₂O₃, and it has a near-identical κ - d_F slope as found in this work regardless of major differences in the sample structures. The thermal conductivity decreases with the addition of Sn doping, as has been observed previously [19]. The thickest Sn-doped film of 1150 nm had a thermal conductivity of only 3.12 W/m-K, which was only 6.8% higher than that of the 100 nm thick undoped film. When studying the thermal conductivity of Ga₂O₃, it was found that the thermal conductivity ratio between Sn-doped and undoped ($\bar{2}01$)-oriented samples ($K_{Sn}/K_{undoped}$) varied from 0.959 – 0.990. For the thin film samples $K_{Sn}/K_{undoped}$ was found to be 0.233 and 0.603 for 500 nm and 100 nm thick films, respectively. The highest thermal conductivity measured in the thin film samples was 12.34 W/m-K, which was found for the 1150 nm thick Sn-doped film.

Figure 4.11 shows the electrical conductivity of the undoped and Sn-doped films plotted as a function of thickness. Conductivity data was gathered by performing Hall measurements using Van Der Pauw contacts of nickel/gold (50nm/50nm). The dotted lines represent fits that were acquired using **Equation 4.30**, where a_σ and b_σ are just fitting constants which are shown in **Table 4.6**. The largest variation in conductivity was found in the 100 nm films, where undoped and Sn-doped films had conductivity values of $4.15 \times 10^{-6} \Omega^{-1} \text{cm}^{-1}$ and $1.54 \times 10^{-3} \Omega^{-1} \text{cm}^{-1}$, respectively. The 1150 nm thick Sn-doped film had the highest conductivity of $2.93 \times 10^{-2} \Omega^{-1} \text{cm}^{-1}$. Interestingly, the thickness dependence was greater for the electrical conductivity than in thermal conductivity. The conductivity ratio of the 500 nm thick undoped film to the 100 nm thick undoped film was 58.07, while for the Sn-doped samples of equal thicknesses the ratio was 19.03.

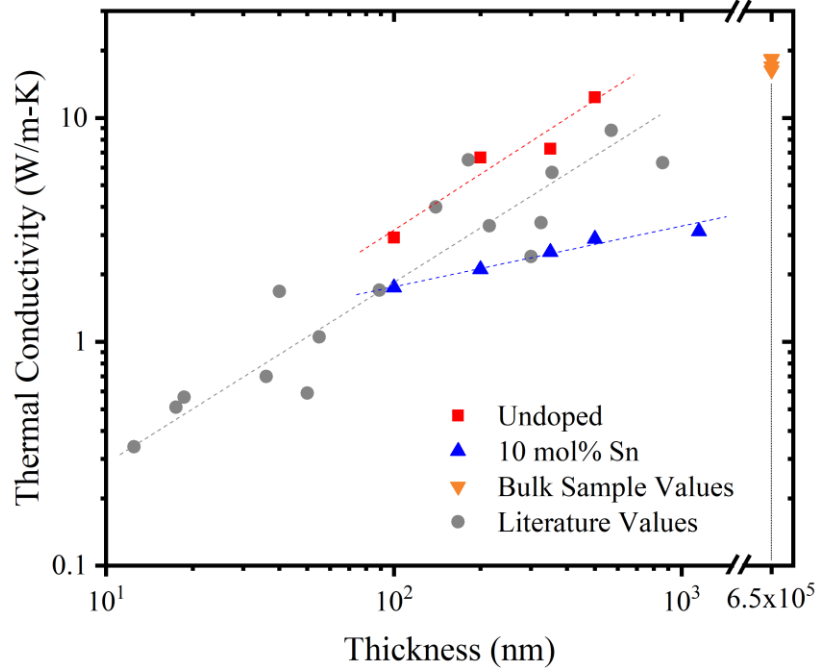


Figure 4.10 Thermal conductivity of undoped and Sn-doped heteroepitaxial Ga_2O_3 thin films grown on c -plane sapphire. Bulk sample thermal conductivity values are shown for comparison purposes. Additional Ga_2O_3 thin film thermal conductivity data acquired using TDTR is shown here and denoted as ‘Literature Values’ [18]. Each data set was fit using Equation 4.29 and shown with a dashed line.

$$\kappa = a \cdot d_F^b \quad (4.29)$$

Table 4.5 Fitting constants for κ - d_F data of **Figure 4.10**. Literature values from Ref. [18].

Doping	Undoped	10 mol% Sn	Undoped (Ref. [18])
a	0.072 ± 0.09	0.576 ± 0.13	0.061 ± 0.06
b	0.817 ± 0.22	0.247 ± 0.04	0.744 ± 0.15
R^2	0.914	0.934	0.668

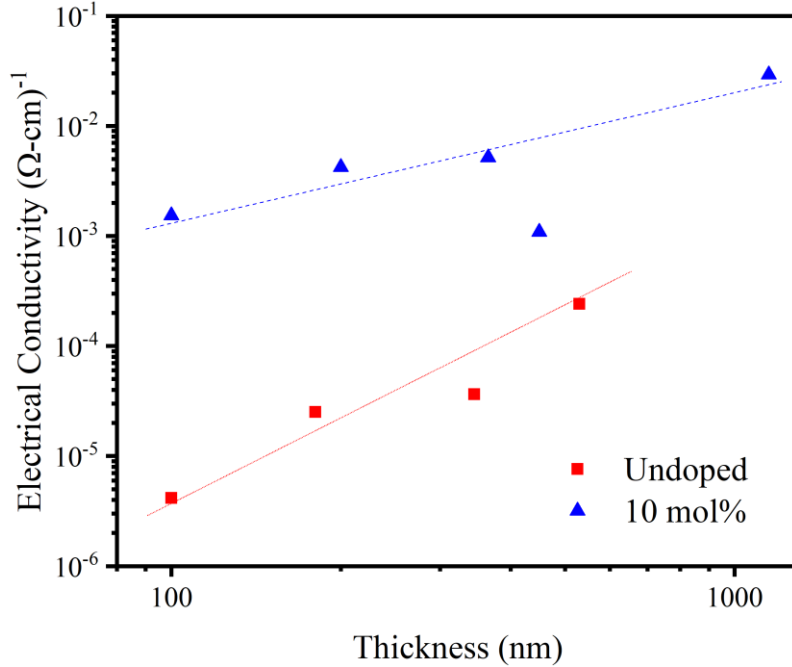


Figure 4.11 Electrical conductivity of undoped and Sn-doped heteroepitaxial Ga_2O_3 thin films grown on c -plane sapphire. Each data set was fit using Equation 4.30 and shown with a dotted line.

$$\sigma = a_\sigma + b_\sigma d_F \quad (4.30)$$

Table 4.6 Fitting constants for σ - d_F data of **Figure 4.11**.

Doping	Undoped	10 mol% Sn
a_σ	-9.69 ± 1.12	-4.82 ± 1.51
b_σ	2.18 ± 0.46	0.96 ± 0.59
R^2	0.917	0.469

High-resolution transmission electron microscopy (TEM) measurements were made to gather more insight into the observed electrical and thermal conductivity thickness dependence. As shown in **Figure 4.12**(a, b), cross-sectional TEM measurements were made on the 500 nm undoped Ga_2O_3 sample. **Figure 4.12**(c) shows an overlaid model of the $(\bar{2}01)$ -orientated Ga_2O_3 unit cell, which confirms the formation of a structured gallium oxide layer on the c -plane sapphire

substrate. The bright dots in the image correspond to Ga sites while the O sites are not visible. This is in agreement with previous reports and has been attributed to oxygen having a lower Z in comparison to gallium [20]. The image indicates a highly-ordered atomic arrangement of the crystalline thin film, despite the presence of structural defects. The thickness dependence on electrical and conductivity was attributed to a reduced defect/dislocation density in the films as the thickness increased. Similar thickness-dependence findings have been previously reported in GaN thin films, where dislocation defects were found to decrease as the films grew thicker away from the substrate [21].

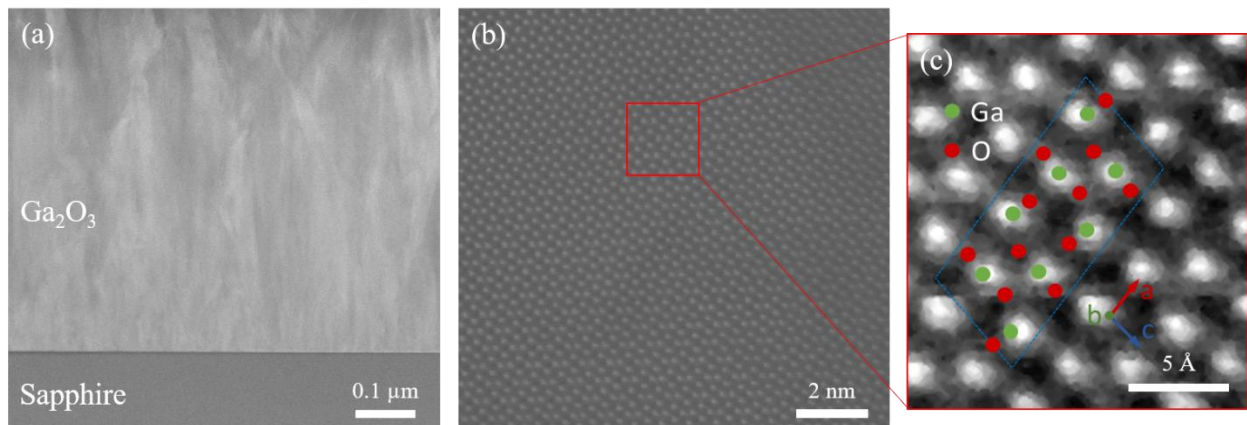


Figure 4.12 (a) Cross-sectional TEM image of the 500 nm thick undoped Ga_2O_3 thin film showing the film/substrate interface. (b) High-resolution image shows an ordered atomic arrangement. (c) Overlaid model of the Ga_2O_3 unit cell with $(\bar{2}01)$ orientation.

4.4 Conclusions

The thermal conductivity bulk and thin film Ga_2O_3 samples with various dopants and surface orientations was evaluated using the 3ω measurement technique. The 3ω methodology and fabrication details were discussed for both single-layer and multi-layer measurements.

An anisotropic thermal conductivity was observed in the undoped, Sn-doped, and Fe-doped Ga_2O_3 bulk samples. It was found that the room temperature thermal conductivity reached a peak value of 29.21 W/m-K along the [010] crystallographic direction in the undoped sample. The

room temperature thermal conductivity decreased along all other directions observed here, ranging from 16.12 – 18.39 W/m-K. The effect of doping on thermal conductivity was much less than that of crystal direction. The samples were evaluated within a temperature range of 295 – 405 K. The power slope coefficient, α , was extracted using the temperature-dependent thermal conductivity power law for all samples, which varied from 0.316 – 0.697. The scattering mechanisms responsible for the observed variation in thermal conductivity were discussed.

The thermal conductivity of undoped and Sn-doped Ga₂O₃ thin films with varying thicknesses were grown on α -Al₂O₃ substrates and evaluated using the 3ω differential method. The thermal conductivity of both sample types were found to have a κ - d_F power law dependence. The electrical conductivity of the films also varied with film thickness. The thickness dependency was further analyzed by TEM, and it was found that a decreased quantity of structural defects were present in the Ga₂O₃ as the film thickness increased.

4.5 References

- [1] M. D. Santia, N. Tandon, and J. D. Albrecht, “Lattice thermal conductivity in β - Ga₂O₃ from first principles,” *Appl. Phys. Lett.*, vol. 107, no. 4, 2015.
- [2] Z. Galazka et al., “On the bulk β -Ga₂O₃ single crystals grown by the Czochralski method,” *J. Cryst. Growth*, vol. 404, pp. 184–191, 2014.
- [3] A. Kuramata, M. Higashiwaki, D. Jena, and T. Luo, “Anisotropic thermal conductivity in single crystal b-gallium oxide,” vol. 111909, pp. 1–5, 2015.
- [4] M. Handweg, R. Mitdank, Z. Galazka, and S. F. Fischer, “Temperature-dependent thermal conductivity in Mg-doped and undoped β -Ga₂O₃ bulk-crystals,” *Semicond. Sci. Technol.*, vol. 30, no. 2, 2015.
- [5] M. Handweg, R. Mitdank, Z. Galazka, and S. F. Fischer, “Temperature-dependent thermal conductivity and diffusivity of a Mg-doped insulating β -Ga₂O₃ single crystal along [100], [010] and [001],” *Semicond. Sci. Technol.*, vol. 31, no. 12, pp. 1–6, 2016.
- [6] D. G. Cahill and R. O. Pohl, “Thermal conductivity of amorphous solids above the plateau,” *Phys. Rev. B*, vol. 35, no. 8, pp. 4067–4073, Mar. 1987.
- [7] H. S. Carslaw and J. C. Jaeger, *Conduction of Heat in Solids*, 2nd ed. Oxford, 1986.
- [8] C. Mion, “Investigation of the Thermal Properties of Gallium Nitride Using the Three Omega Technique,” North Carolina State University, 2005.
- [9] D. G. Cahill, “Thermal conductivity measurement from 30 to 750 K: the 3 ω method,” *Rev. Sci. Instrum.*, vol. 61, no. 802, 1990.
- [10] A. Feldman, “Algorithm for Solutions of the Thermal Diffusion Equation in a Stratified Medium with a Molulated Heating Source,” *High Temp. High Press.*, vol. 31, no. 3, pp. 293–298, 1999.
- [11] J. H. Kim, A. Feldman, and D. Novotny, “Application of the three omega thermal conductivity measurement method to a film on a substrate of finite thickness,” *J. Appl. Phys.*, vol. 86, no. 3959, 1999.
- [12] T. Borca-Tasciuc, A. R. Kumar, and G. Chen, “Data reduction in 3 ω method for thin-film thermal conductivity determination,” *Rev. Sci. Instrum.*, vol. 72, no. 4, pp. 2139–2147, 2001.
- [13] A. T. Ramu and J. E. Bowers, “Analysis of the ‘3-Omega’ method for substrates and thick films of anisotropic thermal conductivity,” *J. Appl. Phys.*, vol. 112, no. 4, 2012.
- [14] Z. Guo et al., “Anisotropic thermal conductivity in single crystal β -gallium oxide,” *Appl. Phys. Lett.*, vol. 106, no. 11, pp. 1–6, 2015.

- [15] H. He, M. A. Blanco, and R. Pandey, “Electronic and thermodynamic properties β -Ga₂O₃,” *Appl. Phys. Lett.*, vol. 88, no. 26, pp. 2–5, 2006.
- [16] M. Slomski, P. P. Paskov, J. H. Leach, J. F. Muth, and T. Paskova, “Thermal conductivity of bulk GaN grown by HVPE: Effect of Si doping,” *Phys. Status Solidi Basic Res.*, vol. 254, no. 8, pp. 1–5, 2017.
- [17] D. G. Cahill, M. Katiyar, and J. R. Abelson, “Thermal conductivity of alpha-Si:H thin films,” *Phys. Rev. B*, vol. 50, no. 9, pp. 6077–6081, 1994.
- [18] C. J. Szejowski et al., “Size effects in the thermal conductivity of gallium oxide (β -Ga₂O₃) films grown via open-atmosphere annealing of gallium nitride,” *J. Appl. Phys.*, vol. 117, no. 8, 2015.
- [19] M. Slomski, N. Blumenschein, P. P. Paskov, J. F. Muth, and T. Paskova, “Anisotropic thermal conductivity of β -Ga₂O₃ at elevated temperatures: Effect of Sn and Fe dopants,” *J. Appl. Phys.*, vol. 121, no. 23, p. 235104, Jun. 2017.
- [20] G. Wagner et al., “Homoepitaxial growth of β -Ga₂O₃ layers by metal-organic vapor phase epitaxy,” *Phys. status solidi*, vol. 211, no. 1, pp. 27–33, 2014.
- [21] T. Paskova et al., “Defect and emission distributions in bulk GaN grown in polar and nonpolar directions: a comparative analysis,” *Proc. SPIE*, vol. 6894, no. 919, p. 68940D, 2008.

CHAPTER 5 – TIME-DOMAIN TERAHERTZ SPECTROSCOPY

5.1 TDTS Fundamental Description

The rapid development of β -Ga₂O₃ has shown promise in the high-power and high-frequency application space. Optimization of such devices requires a deeper understanding of the β -Ga₂O₃ electronic properties at elevated temperatures and in the high-frequency regime. One technique that can be used for studying dynamic conductivity mechanisms is time-domain terahertz spectroscopy (TDTS). TDTS is capable of providing the dielectric properties (i.e. conductivity, permittivity, refractive index) of a material in the terahertz frequency range as well as electron transport information for short length scales. This technique has been used to study a wide variety of semiconductor and conducting oxide materials such as GaN [1]–[3], graphene [4]–[6], ZnO [7], [8], Na_xCoO₂ [9], and BaSnO₃ [10].

Important charge carrier information can be gathered within the 0.1 – 0.3 THz frequency range. The charge carrier diffusion length during the period of a THz electromagnetic wave is on the order of several to tens of nanometers in semiconductor materials, allowing for the determination of conductivity within extremely small areas [11]–[13]. Time-domain terahertz spectroscopy is often referred to as a probing technique and has many benefits over more traditional charge transport characterization methods [13]. TDTS is a phase sensitive measurement, meaning that real and imaginary parts of all dielectric properties can be obtained simultaneously. Furthermore, TDTS is a non-contact measurement technique, offering more flexibility than other methods (e.g. Hall measurements) since the deposition of metal contacts is not required. TDTS uses pulsed radiation which can easily result in time-resolved data by probing the THz conductivity of an optically excited material. The number of photogenerated carriers can

be easily controlled by changing the excitation power. Additionally, the conductivity decay can be analyzed with sub-picosecond resolution by varying the time delay between optical excitation and THz probe pulses. **Figure 5.1** shows a schematic diagram of the TDS experimental setup used in this work, which is located in the Institute of Physics at the Czech Academy of Sciences.

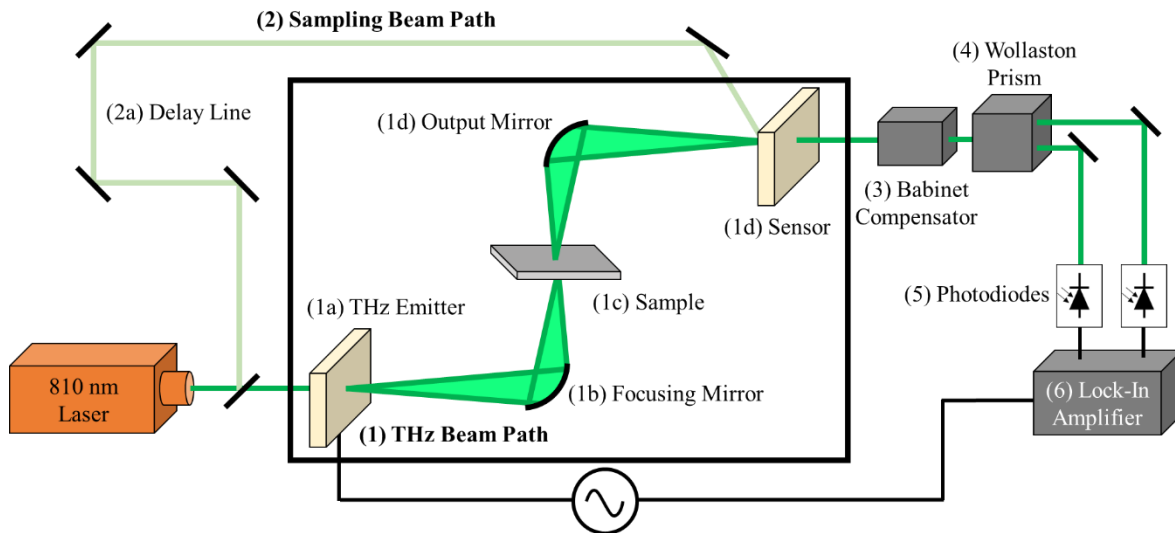


Figure 5.1 Schematic diagram of the TDS experimental setup.

The pulsed laser beam is split into two separate beam paths – the (1) THz beam path and (2) sampling beam path – and recombined at the Babinet compensator.

(1) THz Beam Path includes:

- a. *THz Emitter – Beam is used for excitation of a biased large-area interdigitated photoconductive THz emitter which produces linearly polarized THz pulses for probing the sample.*
- b. *Focusing Mirror – Focuses the THz emitter signal onto the sample.*
- c. *Sample*
- d. *Output Mirror – Directs the signal emitted through the sample onto the sensor.*

(2) Sampling Beam Path includes:

a. *Delay Line – Allows for fine-tuning the sampling delay time. The delay time between THz emitter and sampling pulses allows for the THz electric field time profile to be measured.*

(3) *Babinet Compensator – Transforms the linearly polarized signal into a signal with elliptical polarization.*

(4) *Wollaston Prism – Separates the beam into two linearly-polarized parts while also filtering out any signal which is not vertically- or horizontally-polarized.*

(5) *Photodiodes – Two coupled photodiodes are used to measure the intensity of each beam. Photodiodes are used prior to experimentation to calibrate the intensity of each beam such that the vertical and horizontally-polarized parts are equal.*

(6) *Lock-In Amplifier – The current generated from the photodiodes is driven into the LIA. LIA is used to maximize the signal-to-noise ratio by modulation of the THz emitter bias. During measurement, the LIA performs a Fourier transform on the signal such that only data at the modulation frequency is obtained.*

Once reaching the sensor, the THz signal generated by the emitter (E_0) can be described by **Equation 5.1**, where E_{meas} is the measured THz signal, P_{before} and P_{after} consider the propagation that occurs before and after the sample, t_{sample} is the complex transmittance of the sample, and R_{sensor} is the response function of the sensor [13]. The generated THz waveform, propagation functions, and sensor response function must be measured prior to measuring the sample. This can be accomplished by a reference measurement, where the waveform is transmitted through free space. The reference THz signal that is measured can be described by **Equation 5.2**, where t_{vacuum}

represents the complex transmittance of vacuum [13]. An example of these two waveforms are shown in **Figure 5.2(a)**, where black and red curves represent the measured THz waveforms measured in free space and when a $(\bar{2}01)$ -oriented Ga_2O_3 sample was in place. The inset shows the amplitude of the two waveforms after taking their Fourier transform. Once the Fourier transform of the two signals is known, the complex transmission function (T) can be obtained by taking their ratio as shown in **Equation 5.3** [13].

$$E_{meas}(t) = E_0 \times P_{before} \times t_{sample} \times P_{after} \times R_{sensor} \quad (5.1)$$

$$E_{ref}(t) = E_0 \times P_{before} \times t_{vacuum} \times P_{after} \times R_{sensor} \quad (5.2)$$

$$T(f) = \frac{t_{sample}(f)}{t_{vacuum}(f)} = \frac{E_{meas}(f)}{E_{ref}(f)} \quad (5.3)$$

After obtaining the complex transmission function of the bulk sample (single layer), the complex refractive index is extracted from the signal using **Equation 5.4**, where N is the complex refractive index ($n + ik$), c is the speed of light, d is sample thickness, and j represents each echo occurrence as shown in **Figure 5.2(b)** [13]. The echo is a result of the signal being partially reflected off of the sample surface and can be observed at time delays equal to multiples of the sample optical thickness. Portions of the measured waveform containing the reflected signal are truncated prior to calculating the Fourier transform.

A similar procedure can be performed to gather the complex refractive index from samples containing a thin film on bulk substrate, as shown in **Equation 5.5**, where T_{film} is the complex transmission function of the thin film, N_f is the complex refractive index of the film, N_s is the complex refractive index of the substrate, and d_f is the film thickness [13].

$$T_{bulk}(f) = \sum_{j=0}^{\infty} T_j(f) = \frac{4N}{(N+1)^2} \frac{e^{\frac{2\pi i f d(N-1)}{c}}}{1 - \left(\frac{1-N}{1+N} e^{\frac{2\pi i f d N}{c}} \right)^2} \quad (5.4)$$

$$T_{film}(f) = \frac{4N_f e^{\frac{2\pi i f N_f d_f}{c}}}{(N_f+1)(N_f+N_s) - (N_f-1)(N_f-N_s) e^{\frac{4\pi i f N_f d_f}{c}}} \quad (5.5)$$

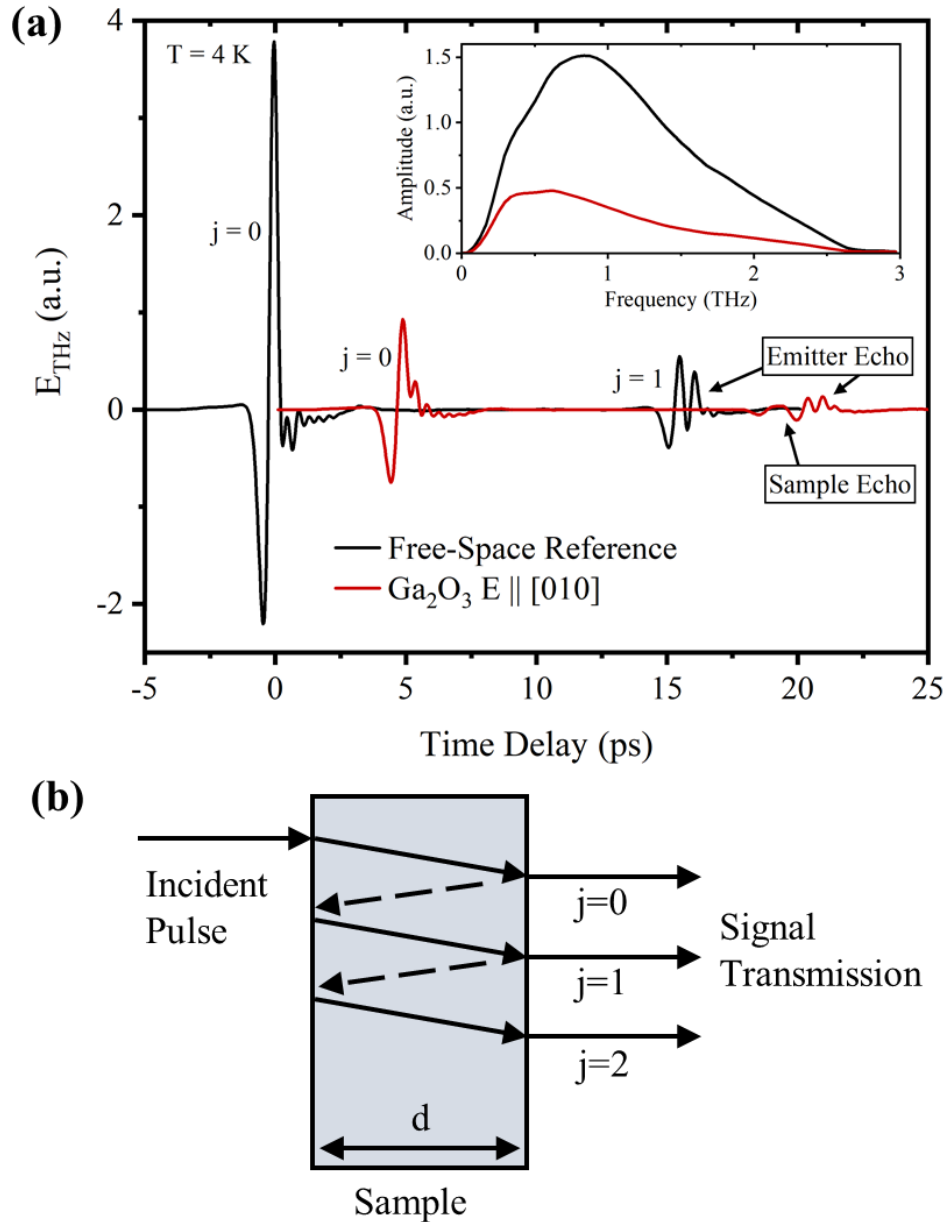


Figure 5.2 (a) Example THz waveforms measured at 4 K. The black curve shows the reference waveform measured in free space. The red curve shows a representative waveform measured when a $(\bar{2}01)$ -oriented Ga_2O_3 sample was in place with the THz electric field oriented parallel to the [010] Ga_2O_3 axis. The inset shows the amplitude of the corresponding THz waveforms after truncating the echo signals and performing a Fourier transform.

Once the complex refractive index of the material is obtained, the complex permittivity ($\varepsilon = \varepsilon' - i\varepsilon''$) and complex conductivity ($\sigma = \sigma' - i\sigma''$) can be calculated. **Equation 5.6** shows the relation between complex refractive index and complex permittivity, which can be rearranged into **Equations 5.7** and **5.8** by solving for n and k .

$$N^2 = \varepsilon \rightarrow (n + ik)^2 = \varepsilon' + i\varepsilon'' \quad (5.6)$$

$$n^2 = \frac{1}{2}[\sqrt{\varepsilon'^2 + \varepsilon''^2} + \varepsilon'] \quad (5.7)$$

$$k^2 = \frac{1}{2}[\sqrt{\varepsilon'^2 + \varepsilon''^2} - \varepsilon'] \quad (5.8)$$

During TDTS measurements, the applied THz electric field ($E_{THz} = E_0 \cdot e^{i\omega t}$) will generate charge carrier displacement (j) within the semiconductor that will obey **Equation 5.9**. After substitution of the complex permittivity components it can be seen that the imaginary permittivity is in phase while the real component is out of phase by 90° .

$$j(\omega) = \varepsilon(\omega) \frac{dE_{THz}}{dt} = i\omega\varepsilon(\omega)E_{THz}(\omega) \quad (5.9)$$

$$\rightarrow j = i\omega\varepsilon' E_{THz} [out\ of\ phase] + \omega\varepsilon'' E_{THz} [in\ phase]$$

By Ohm's law, the in-phase component of charge displacement is shown in **Equation 5.10** which contains a frequency-dependent conductivity ($\sigma = \omega\varepsilon''$). Substitution of this relation into **Equation 5.6** yields **Equation 5.11**. Since $n^2 - k^2 = \varepsilon'$, then $2nk$ must be equal to σ/ω . Substitution of these relations into **Equations 5.7** and **5.8** yields the real and imaginary permittivity as a function of complex conductivity as shown in **Equations 5.12** and **5.13**. Additional detail on the derivation of the dielectric functions used for TDTS data evaluation have been reported elsewhere [14].

$$j(\omega) = \omega\varepsilon''(\omega)E_{THz}(\omega) = \sigma(\omega)E_{THz}(\omega) \quad (5.10)$$

$$n^2 - k^2 + 2ink = \varepsilon' + i\left(\frac{\sigma}{\omega}\right) \quad (5.11)$$

$$n^2 = \frac{1}{2}\left[\sqrt{\varepsilon'^2 + \frac{\sigma^2}{4\omega^2}} + \varepsilon'\right] \quad (5.12)$$

$$k^2 = \frac{1}{2} \left[\sqrt{\varepsilon'^2 + \frac{\sigma^2}{4\omega^2}} - \varepsilon' \right] \quad (5.13)$$

5.2 Characterization

In this work, a custom-made TDTS setup was used. The laser source had a central wavelength, pulse width, and repetition rate of 810 nm, 80 fs, and 76 MHz, respectively. A (110)-oriented ZnTe THz emitter of 1 mm thickness was used. The emitter had a frequency range and peak electric field strength of 0.2 – 2.5 THz and 4 kV/cm, respectively. A 1 mm thick electro-optic ZnTe crystal was used for sensing the output signal. The THz signal was generated and measured in an enclosed vacuum chamber (held at ~ 2 Torr) to avoid water vapor absorption. The sample temperature was controlled over a wide range using two separate attachments. A liquid helium cryostat with Mylar windows was used for temperatures of 4 – 300 K. A furnace attachment was equipped for measurements at temperatures greater than 300 K.

Table 5.1 shows the bulk and thin film Ga₂O₃ samples that were analyzed by TDTS. Undoped and Sn-doped Ga₂O₃ was analyzed in both cases of both bulk and thin film samples. The bulk samples were ($\bar{2}01$)-oriented, 650- μm -thick, and grown by Tamura Corporation using edge-defined film-fed growth [15]. The undoped and Sn-doped bulk samples had free carrier concentrations of $2.2 \times 10^{17} \text{ cm}^{-3}$ and $4.6 \times 10^{18} \text{ cm}^{-3}$, respectively. The thin film samples with varied thickness and Sn-doping concentration were grown on 430 μm thick c-plane sapphire, which provided the same ($\bar{2}01$) orientation as the bulk Ga₂O₃ samples. **Figure 5.3** shows the unit cell of ($\bar{2}01$)-oriented Ga₂O₃ with the inset image showing a top-view of the crystal.

Each sample was first measured at a starting temperature of 4 K. However, as shown in **Table 5.1**, some of the samples were opaque and unable to be measured, meaning that the

absorption of THz waves passing through the sample was too high. Reflection losses on the sample surface also effect the signal amplitude, but the main factor is the absorption within the volume since the field amplitude decreases with sample thickness as shown in **Equation 5.14**, where E_0 is the incident electric field amplitude, z is distance into the material, and α is the absorption coefficient which is equal to the inverse of penetration depth and proportional to the imaginary refractive index ($\alpha = 4\pi k / \lambda$).

$$E = E_0 e^{-\alpha z} \quad (5.14)$$

If the transmitted power is weaker than the detection limit or experimental noise (1 μ W), then the spectra cannot be accurately obtained at the specific frequency interval. One possible solution is to thin the sample, decreasing z . Fortunately, two of the samples (undoped bulk and 1150 nm thick Sn-doped film) were able to be measured over a relatively wide temperature range. The remaining chapter will cover the findings associated with these two Ga_2O_3 samples.

Table 5.1 Bulk and thin film Ga_2O_3 samples analyzed by TDTS. Thin film samples were grown on 430 μm thick c-plane sapphire substrates.

	Dopant	$N_D - N_A$ (cm^{-3})	Thickness (μm)	Measurement Capability
Bulk	Undoped	2.2×10^{17}	650	≤ 80 K
	Sn	4.6×10^{18}	650	4 K

	Dopant	PLD Target Sn Composition	Film Thickness (nm)	Measurement Capability
Thin Films	Undoped	---	530	---
	Sn	1 mol%	200	---
	Sn	10 mol%	200	---
	Sn	10 mol%	1150	4 – 750 K

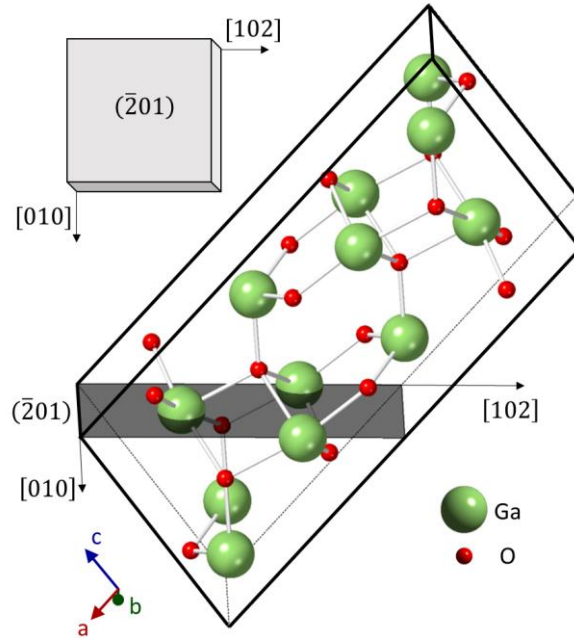


Figure 5.3 Unit cell of β - Ga_2O_3 and orientation of the bulk samples cut along the $(\bar{2}01)$ plane. The inset shows a top-side schematic view of the sample where the edges were along the $[010]$ and $[102]$ crystallographic directions. Copyright (2020) AIP Publishing [16].

5.2.1 Bulk Ga_2O_3

TDTS measurements of the undoped Ga_2O_3 bulk sample were performed by applying the THz electric field such that it was parallel to the $[102]$ crystallographic direction of the material. **Figure 5.4** shows the (a) real refractive index, (b) imaginary refractive index, (c) real permittivity, (d) imaginary permittivity, (e) real conductivity, and (f) imaginary conductivity of the undoped Ga_2O_3 sample. The ambient chamber temperature was varied from 4 – 80 K, above which the sample became opaque. The measurements were recorded at each temperature while applying a THz electric field with frequency ranging from 0.25 – 2.5 THz. The solid lines in (c) and (e) shows the fits obtained using the dual harmonic oscillator model which will be described later.

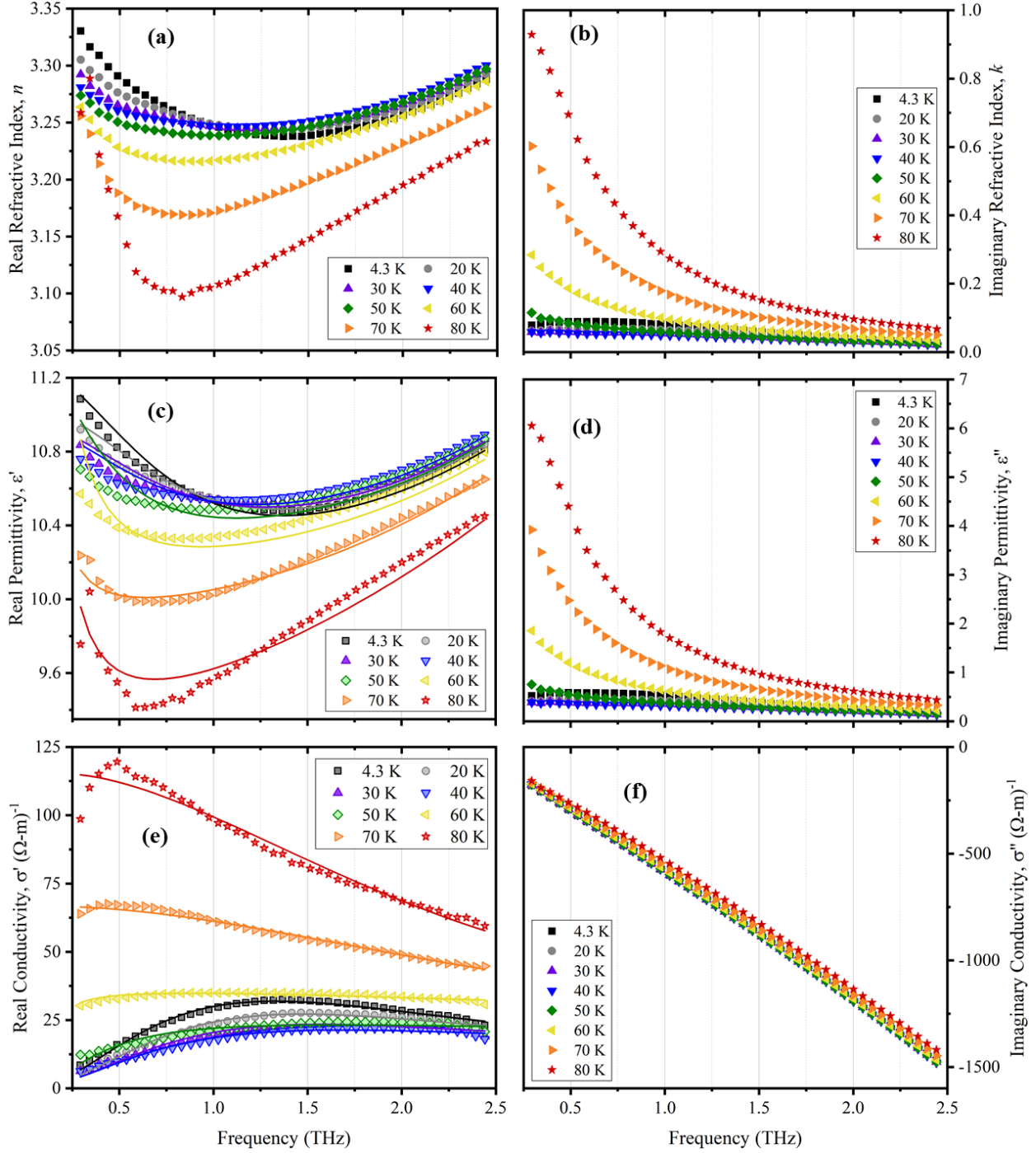


Figure 5.4 Resulting dielectric properties of the bulk Ga_2O_3 sample showing the (a) real refractive index, (b) imaginary refractive index, (c) real permittivity, (d) imaginary permittivity, (e) real conductivity, and (f) imaginary conductivity data measured using TDTS. Fits obtained using the double harmonic oscillator model are shown in (c) and (e) using dotted lines. Copyright (2020) AIP Publishing [16].

Within the 4 – 80 K temperature range, ϵ' varied only from 9.5 – 11.1, whereas σ' varied from around 6 – 125 $\Omega^{-1}\text{m}^{-1}$. An interesting trend was observed in all of the measured dielectric spectra. The amplitude of the imaginary conductivity increased linearly with the THz frequency. An interesting non-monotonic temperature dependence was observed in the ϵ' , ϵ'' , and σ' spectra. It can be seen that the spectra is comprised of two intervals where a transition occurs at ~ 45 K. At temperatures below 45 K, ϵ' decreased until reaching a frequency of 1 THz, then began increasing. The ϵ' amplitude began to decrease rapidly when increasing the temperature to greater than 45 K. Similarly for the σ' spectra, at temperatures below 45 K there existed a different frequency-dependence than for the data obtained at temperature greater than 45 K. The overall amplitude of σ' decreased with increasing temperature until 50 K, where it began to increase in amplitude and become almost linear aside from the pronounced peak at ~ 0.5 THz. The ϵ' and σ' spectra were evaluated further to better understand the high-frequency transport mechanisms that were taking place. Modelling of the ϵ' and σ' spectra were chosen over n , k , ϵ'' , and σ'' for a couple of reasons. First, the σ' spectra was beneficial because it contained peaks which occurred at the oscillation frequency, whereas the peaks observed in the ϵ'' spectra were influenced by damping. The σ'' was disregarded because it lacked in information that could be used for determining the cause of the temperature-dependent mechanism that was observed.

The Drude, Drude-Smith, and dual harmonic oscillator models were used in an attempt to fit the ϵ' and σ' spectra. **Equation 15** shows the Drude model formula, where N is carrier density, q is electron charge, τ is the Drude momentum scattering time, and m^* is the effective mass. **Equation 5.16** shows the formula describing the Drude-Smith model, which is similar to the Drude model aside from the addition of the second term containing the “persistence of velocity” parameter, c [17]. **Equation 5.17** shows the formula representing the dual harmonic oscillator

model, where ε_∞ is the sum of high-frequency phonons dielectric strengths, $\Delta\varepsilon_i$ is the dielectric strength, f_i is the oscillation frequency, and γ_i is the damping constant of the oscillators.

$$\sigma(\omega) = \frac{Nq^2\tau}{m^*} \frac{1}{1-i\omega\tau} \quad (5.15)$$

$$\sigma(\omega) = \frac{Nq^2\tau}{m^*(1-i\omega\tau)} \left[1 + \frac{c}{1-i\omega\tau} \right] \quad (5.16)$$

$$\varepsilon(f) = \varepsilon_\infty + \sum_{i=1,2} \frac{\Delta\varepsilon_i f_i^2}{f_i^2 - f^2 - i\gamma_i f} \quad (5.17)$$

Figure 5.5 shows a comparison between the fits obtained when using the Drude model and dual harmonic oscillator model for both ε' and σ' spectra. The measured data used in these fits were taken at 70 K. The Drude model was unable to predict the same $\varepsilon'(f)$ and $\sigma'(f)$ trends that were measured, producing a spectral shape that varied drastically at lower frequencies from the experimental data. The measured $\varepsilon'(f)$ spectra contained in sharp increase in amplitude as the frequency was reduced at all temperatures, whereas the Drude model predicts an opposite trend. The Drude model did produce a $\sigma'(f)$ spectra which was similar to that of the dual harmonic oscillator model. The Drude-Smith model is capable of providing a more realistic fit to the measured data, but the inclusion of the persistence of velocity parameter, which has no true interpretation and can vary anywhere between 0 and -1, leads to doubt in the model [18]. Cases where $c = -1$ is meant to represent the suppression of DC conductivity. However, while fitting the measured data with the Drude-Smith model the persistence of velocity continued to converge to a value of 0, resulting in a fit similar to that of the Drude model. It was found that the dual harmonic oscillator model was able to predict nearly all instances of both spectra without any issue.

The dual harmonic oscillator model contains a summation with indices of 1 and 2. The first contains an oscillator which originates at the measured permittivity and increases towards

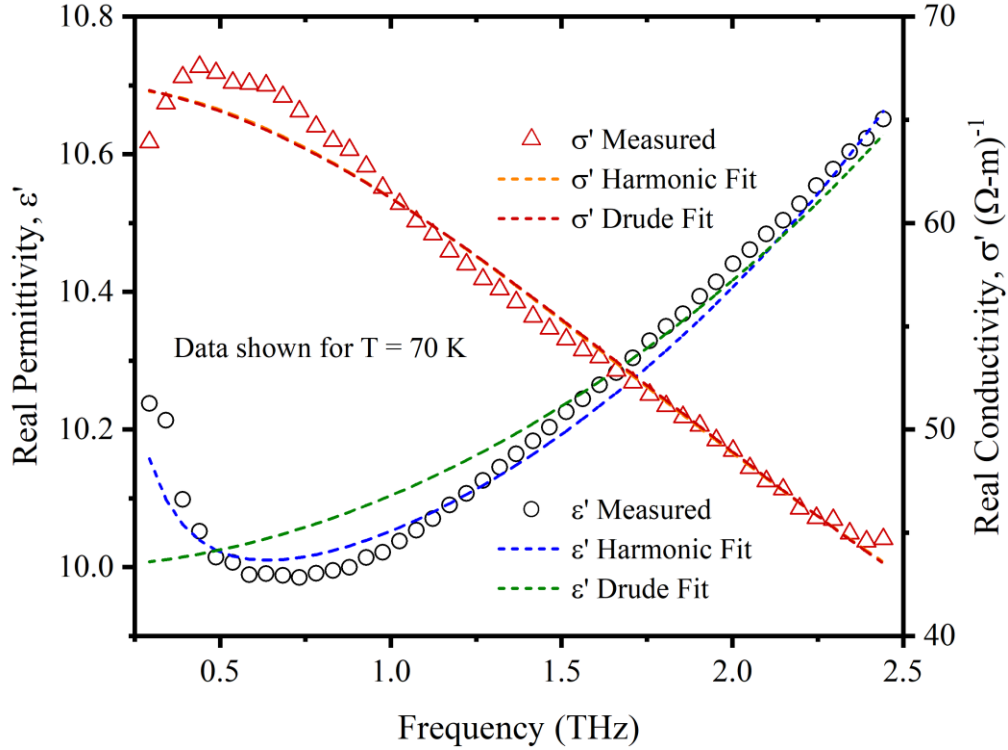


Figure 5.5 Real permittivity and real conductivity fitting results when using the double harmonic oscillator model and Drude model. The measured permittivity and conductivity data shown here is for $T = 70$ K. Measured data is shown using symbols and fitting results are shown with dashed lines. Copyright (2020) AIP Publishing [16].

lower frequencies, while the second contains an oscillator which resembles a phonon originating beyond the obtainable spectral range. In the measured data it can be seen that only the low-frequency phonons effect the spectra. For this reason, the second oscillator was given set parameters (Table 2 in Reference for the B_u -symmetry mode with $k = 8$: $\Delta\epsilon_2 = 3$, $f_2 = 6.5$ THz, and $\gamma_2(T) = \frac{0.03+(T \times 10^{-4})}{k}$ THz) that were reported previously from Schubert *et al.* where a combination of modelling and density functional theory calculations were used [19]. The temperature-dependence used for γ_2 was found by interpolation of the value estimated for 0 K [$\gamma_2(T = 0 \text{ K}) = 0.03$ THz] and the room-temperature value reported in the literature [19].

The dual harmonic oscillator model produced values of ϵ_∞ which were nearly independent of temperature and remained at a constant 7.3 ± 0.1 . This value includes the sum of dielectric

strengths for all high-frequency phonons aside from the phonon described by the second oscillator. **Figure 5.6** shows the temperature dependence of the three optimized parameters contained in the first oscillator (f_1 , γ_1 , and $\Delta\varepsilon_1$), which makes the previously discussed unusual temperature dependence even more pronounced. The oscillation frequency was 1.3 THz at 4 K, which then increased to a maximum of 1.6 THz at 40 K. When the temperature was increased further, f_1 rapidly decreased to a minimum value of 0.2 THz. An opposite trend was observed for the dielectric strength, which decreased from 4 – 40 K, then rapidly increased until reaching 1.6 THz. The damping constant showed a similar behavior to that of f_1 , but differed slightly since it increased until reaching a temperature of 60 K. This temperature-dependent transition occurred for each fitting parameter. The damping constant is larger than the oscillation frequency for the entire temperature range, meaning that the oscillator is overdamped. The parameters observed here show significantly different behavior than what is normally seen for phonons. The results obtained using the double oscillator model suggest charge carrier localization that is likely due to the presence of unintentional dopants. One explanation could be that the unintentional dopants are bound to the Ga₂O₃ lattice and supplying additional charge carriers which are localized. Kuramata *et al.* previously reported on the unintentional dopants found in undoped Ga₂O₃ crystals grown by Tamura using EFG [15]. 18 different impurities were identified in the bulk of the crystal using glow-discharge mass spectroscopy, with the most prevalent being silicon (1.8 wt. ppm), chlorine (1.5 wt. ppm), and aluminum (0.89 wt. ppm). The abundance of these unintentional dopants, each with varying energy barriers, could cause the observed complex potential for the uncompensated charges. The observed transition temperature of ~ 50 K could then be explained using two separate oscillation regimes; where one is dominant for $4 < T < 50$ K and the other for $T > 60$ K. The activation energy corresponding to 55 K is ~ 5 meV, and this energy is likely activating some of

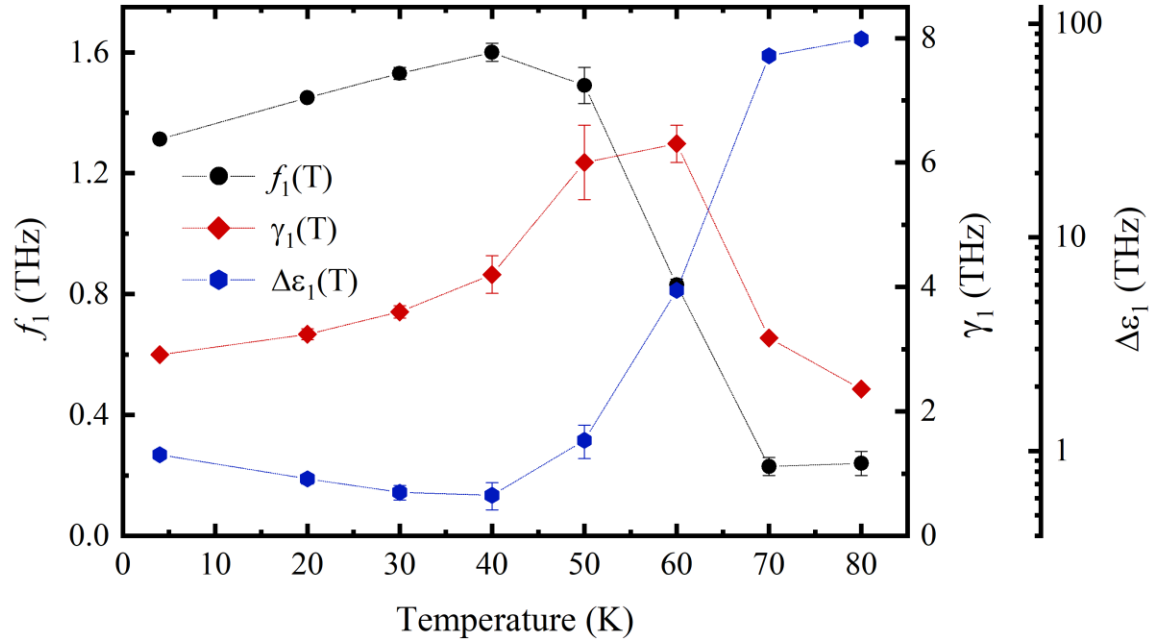


Figure 5.6 Temperature dependence of f_1 , γ_1 , and $\Delta\epsilon_1$ fitting parameters obtained when applying the double harmonic oscillator model to $\epsilon'(T)$ and $\sigma'(T)$ data. Copyright (2020) AIP Publishing [16].

the impurities within the crystal that were observed by Kuramata [15]. Above 50 K the oscillation frequency drops significantly, and its contribution to the relative permittivity is ~ 80 . This could be a result of charge carriers becoming thermally activated at the transition temperature of 55 K. Similar behavior in Ga_2O_3 single crystals has been previously reported by Villora *et al.*, where electrical conductivity and lattice expansion of the crystals were analyzed at temperatures below 100 K [20]. It was found that the electrical conductivity spectra contained two separate regimes with differing behavior, and the transition temperature between them was 50 K.

The THz spectroscopy results shown here indicate that localized charge carriers will need to be further studied in gallium oxide, as they will likely cause effects in high-frequency devices which were unaccounted for. When extrapolating the fit of the real conductivity to higher temperatures, it can be seen that the optical conductivity of the undoped Ga_2O_3 sample would likely reach a few hundred $(\Omega\text{-m})^{-1}$ at room temperature for the GHz frequency range. It is possible

that, similarly to GaN, lightly doping the Ga₂O₃ with other impurities might lead to controlled charge carrier compensation and help with the observed localized conductivity issues at GHz and THz frequencies [1].

5.2.2 Thin Film Ga₂O₃

As shown in **Table 5.1**, the Sn-doped bulk sample had a high optical density and became opaque at temperatures greater than 4 K. For this reason, an Sn-doped Ga₂O₃ thin film sample with similar properties was analyzed. Since the thickness of the material (1150 nm) was much less than that of the bulk Sn-doped sample, the optical density was able to be overcome. The THz spectroscopy measurements were made in two separate temperature regions. The low-temperature ($T < 300$ K) measurements were made first. The chamber temperature was then increased and the high-temperature ($T > 300$ K) measurements were made for temperatures up to 750 K. Following high-temperature measurements, the film was once again brought to 4 K and the measurements were repeated to ensure no sample degradation occurred at high temperatures. **Figure 5.7** shows the (a) real refractive index, (b) imaginary refractive index, (c) real permittivity, (d) imaginary permittivity, (e) real conductivity, and (f) imaginary conductivity of the Sn-doped Ga₂O₃ thin film sample. With respect to the dielectric properties of the undoped bulk sample, the amplitude of $n(f)$, $k(f)$, $\epsilon'(f)$, $\epsilon''(f)$, $\sigma'(f)$, and $\sigma''(f)$ spectra were all found to be much higher for the Sn-doped thin film. Nonetheless, a similar trend was observed for the real permittivity where the amplitude decreased when increasing the temperature from 4 K to 50 K, and then decreased in amplitude

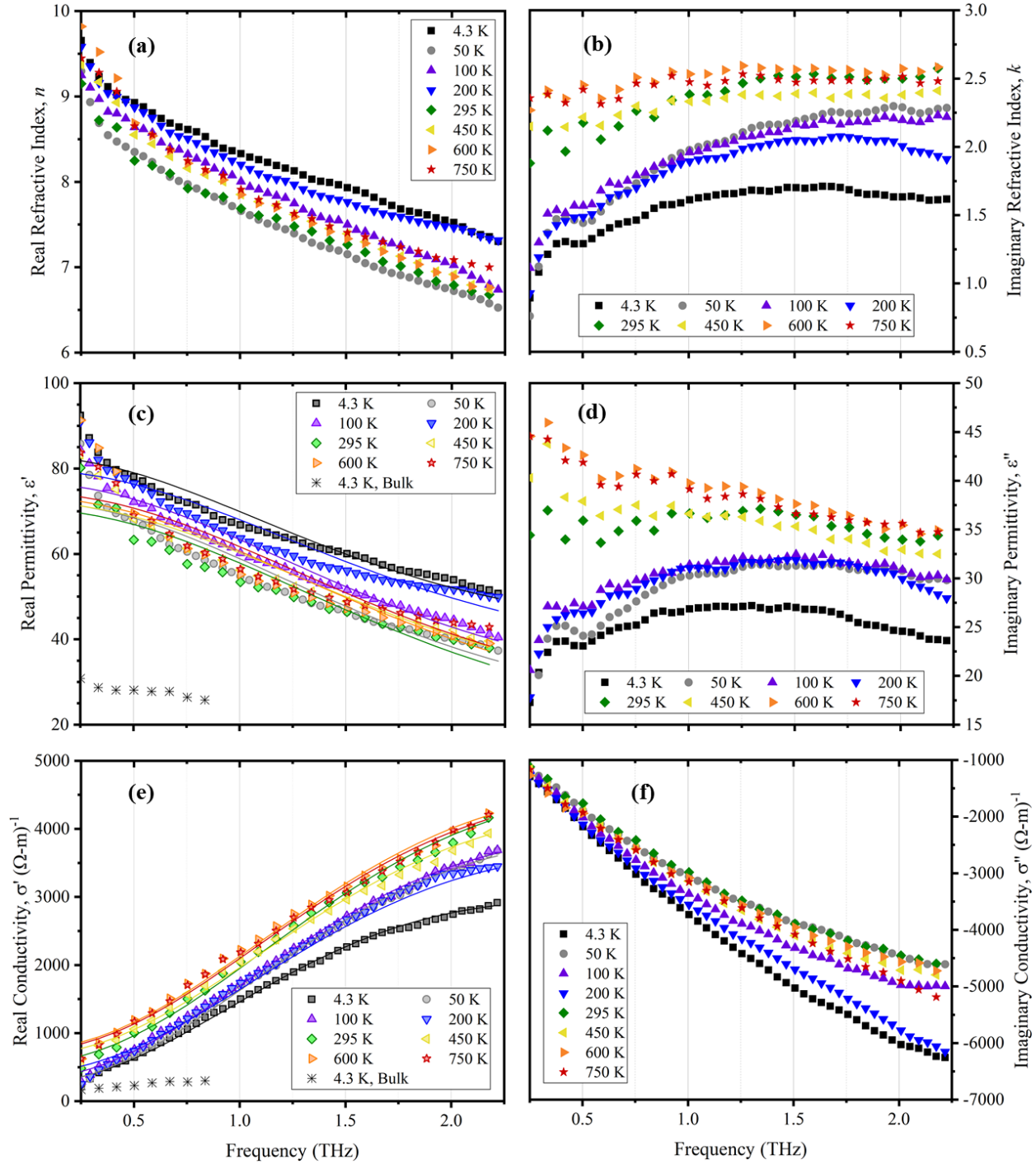


Figure 5.7 Resulting dielectric properties of the thin film Ga_2O_3 sample showing the (a) real refractive index, (b) imaginary refractive index, (c) real permittivity, (d) imaginary permittivity, (e) real conductivity, and (f) imaginary conductivity data measured using TDS. The Drude-Smith model was used to model the $\epsilon'(f)$ and $\sigma'(f)$ spectra, and the corresponding fits are shown in (c) and (e) with lines. Copyright (2020) AIP Publishing [16].

when further raising the temperature. Overall, the dielectric spectra obtained for the Sn-doped thin film are significantly different than what was observed in the undoped bulk sample. Regardless of temperature, the curves were much more linear and had a relatively smaller temperature dependency than the bulk crystal. While the undoped bulk crystal had dielectric spectra which varied by orders of magnitude at low temperatures, the thin film $\varepsilon'(f)$ and $\sigma'(f)$ amplitude varied by less than 10% and 20%, respectively. For comparison purposes, the obtainable data ($T = 4$ K) for the Sn-doped bulk sample is also shown in **Figure 5.7** (c) and (e).

Fits were obtained for the $\varepsilon'(f)$ and $\sigma'(f)$ thin film spectra and are shown using lines in **Figure 5.7** (c) and (e). **Equation 5.18** shows the model used to predict the spectra, where ε_∞ is the sum of high-frequency phonons dielectric strengths, N_c is the carrier concentration, q is electron charge, τ is the scattering time, m_e^* is effective mass, c is the Smith backscattering coefficient, ε_0 is vacuum permittivity, $\Delta\varepsilon_2$ is the dielectric strength of the oscillator, f_2 is the oscillation frequency, and γ_2 is the damping constant of the oscillator [17]. The equation shown here is the Drude-Smith model with an added harmonic oscillator to consider the lowest-lying phonon. The

$$\varepsilon(f) = \varepsilon_\infty - \frac{N_c q^2 \tau}{m_e^* (1 - 2\pi i f \tau)} \left[1 + \frac{c}{1 - 2\pi i f \tau} \right] \frac{1}{2\pi i f \varepsilon_0} + \frac{\Delta\varepsilon_2 f_2^2}{f_2^2 - f^2 - i\gamma_2 f} \quad (5.18)$$

model was able to describe the data with minimal error. **Figure 5.8** shows the (a) localization parameter, (b) carrier concentration, and (c) scattering time values as a function of temperature which were obtained using the model. The localization parameter amplitude decreased slightly with increased temperature, meaning that the charge carriers has a lessened probability of being reflected on the Ga_2O_3 grains. The temperature dependence of both N_c and τ were very weak. The two parameters are clearly coupled, meaning that an unknown amount of error exists in their

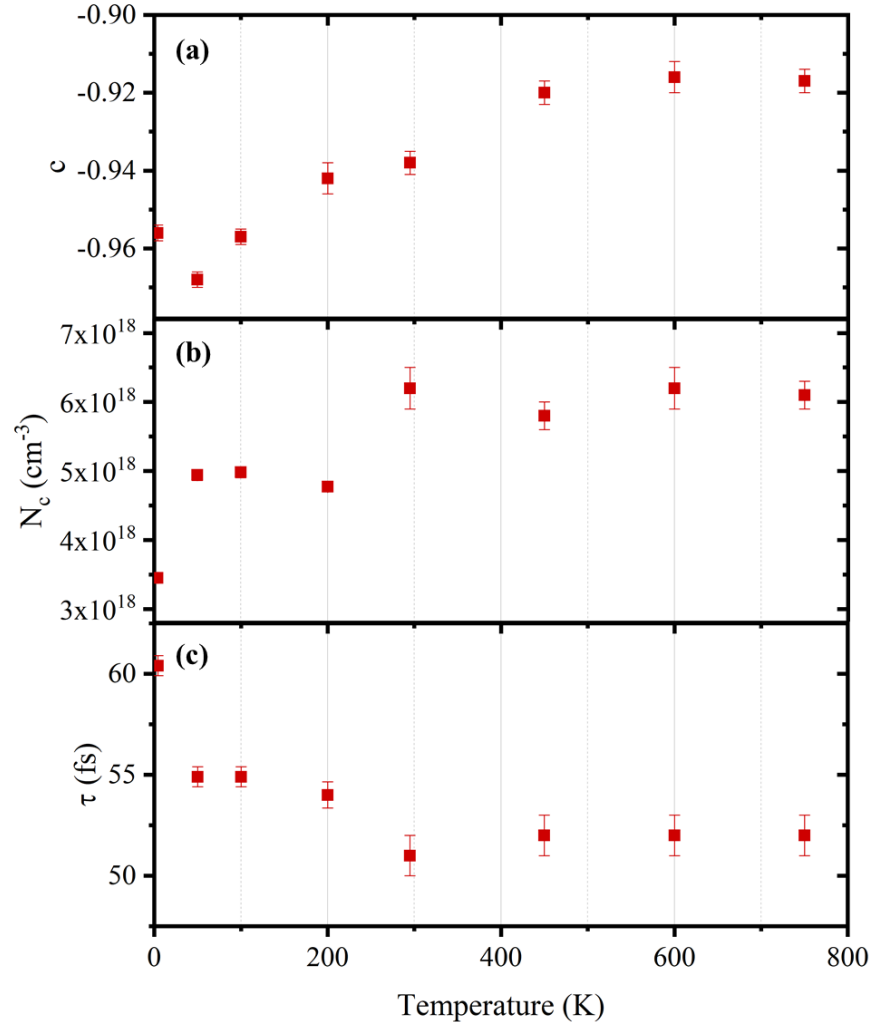


Figure 5.8 (a) ϵ , (b) N_c , and (c) τ fitting parameters obtained when using the Drude-Smith model to fit the real parts of permittivity and conductivity measured for the Sn-doped thin film sample. Copyright (2020) AIP Publishing [16].

overall amplitude, making them somewhat unusable for drawing any real conclusions. The carrier concentration of the film ranged from $4.9 - 6.1 \times 10^{18} \text{ cm}^{-3}$, while Hall measurements resulted in a density of only $7.3 \times 10^{16} \text{ cm}^{-3}$. Interestingly, the N_c extracted from the Drude-Smith model is almost identical to that of the Sn-doped bulk crystal at room temperature ($4.6 \times 10^{18} \text{ cm}^{-3}$). It is likely that the optical transparency of the two samples differed because of structural and morphological properties. **Figure 5.9** shows (a, b) topographical and (c, d) three-dimensional AFM images of the Sn-doped thin film and bulk crystal samples. The AFM measurements showed

that the thin film had an RMS roughness and average grain size of 2.179 nm and 9.953 nm, respectively. These properties of the thin film surface are consistent with previous reports on Ga_2O_3 films grown on c-plane sapphire using pulsed laser deposition [21]. The AFM data proves that the films are very smooth, yet the bulk crystals are superior in surface morphology quality. The Sn-doped bulk had an RMS roughness of 0.611 nm and did not contain any detectable grains. These results are in agreement with the hypothesis that the grain structure of the Sn-doped Ga_2O_3 thin film is likely the limited factor for its DC conductivity variability in comparison to the bulk sample.

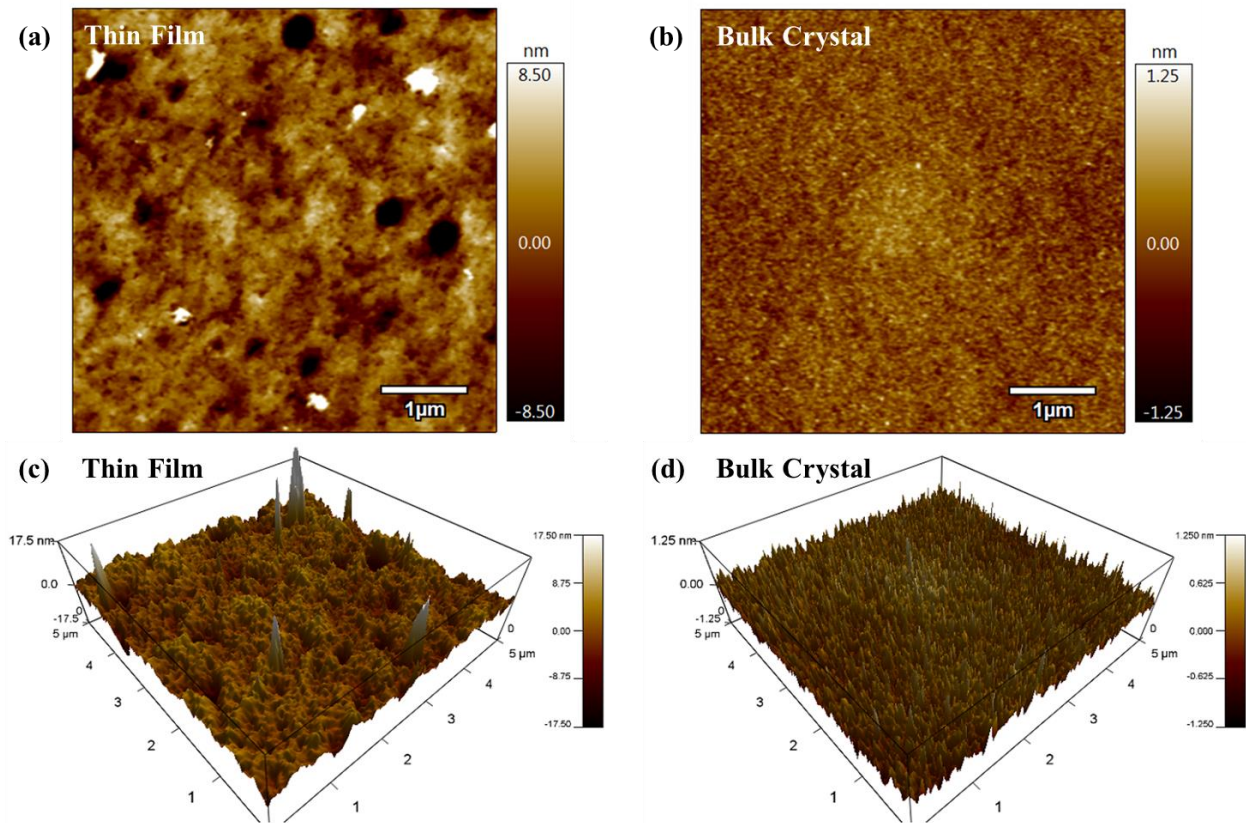


Figure 5.9 Top-view AFM images of the Sn-doped Ga_2O_3 (a) thin film and (b) bulk crystal. Three-dimensional images of the (c) thin film and (d) bulk crystal. Copyright (2020) AIP Publishing [16].

5.3 Conclusions

Time-domain terahertz spectroscopy was used to evaluate the complex dielectric properties of undoped and Sn-doped Ga_2O_3 samples within the 0.2 – 2.5 THz frequency range. TDTS characterization methodology and sample preparation was discussed in detail. The bulk and thin film Ga_2O_3 samples were measured at a starting temperature of 4 K, then continued until the samples became optically opaque at elevated temperatures due to reflection losses.

A dual harmonic oscillator model was proposed for fitting the dielectric spectra. The model was capable of predicting the conductivity and permittivity data with significantly less error than that of the Drude and Drude-Smith models. A non-monotonic temperature dependence observed in the spectra was accurately predicted using the dual harmonic oscillator model, and it is thought that the dependence is a result of charge carrier localization. Unintentional dopants present in the Ga_2O_3 lattice are supplying additional charge carriers which become thermally activated at 55 K.

A Sn: $\text{Ga}_2\text{O}_3/\alpha\text{-Al}_2\text{O}_3$ thin film sample with thickness of 1150 nm was measured from 4 – 750 K. The dielectric spectra of the thin film was vastly different than the bulk samples. The curves had a more-linear frequency dependence and were much less dependent on temperature. The spectra was fit using a version of the Drude-Smith model which contained an added harmonic oscillator term to describe the lowest-lying phonon. Temperature-dependent variables such as the localization parameter, charge carrier density, and carrier scattering time were extracted from the model. The localization parameter was inversely proportional to temperature, meaning that charge carriers were less likely to reflect from Ga_2O_3 grain boundaries. AFM measurements were used to inspect the film morphology, and it is thought that the grain structure of the film is limiting the DC conductivity when compared to the bulk samples.

5.4 References

- [1] F. Kadlec, C. Kadlec, T. Paskova, and K. Evans, “Effect of Fe doping on the terahertz conductivity of GaN single crystals,” *J. Phys. D. Appl. Phys.*, vol. 43, no. 14, p. 145401, 2010.
- [2] T.-R. Tsai, S.-J. Chen, C.-F. Chang, S.-H. Hsu, T.-Y. Lin, and C.-C. Chi, “Terahertz response of GaN thin films,” *Opt. Express*, vol. 14, no. 11, p. 4898, 2006.
- [3] W. Zhang, A. K. Azad, and D. Grischkowsky, “Terahertz studies of carrier dynamics and dielectric response of n-type, freestanding epitaxial GaN,” *Appl. Phys. Lett.*, vol. 82, no. 17, pp. 2841–2843, 2003.
- [4] I. Ivanov, M. Bonn, Z. Mics, and D. Turchinovich, “Perspective on terahertz spectroscopy of graphene,” *Epl*, vol. 111, no. 6, 2015.
- [5] P. R. Whelan, K. Iwaszczuk, R. Wang, S. Hofmann, P. Bøggild, and P. U. Jepsen, “Robust mapping of electrical properties of graphene from terahertz time-domain spectroscopy with timing jitter correction,” *Opt. Express*, vol. 25, no. 3, p. 2725, 2017.
- [6] X. Feng, M. Hu, J. Zhou, and S. Liu, “Calculation and Study of Graphene Conductivity Based on Terahertz Spectroscopy,” *J. Infrared, Millimeter, Terahertz Waves*, vol. 38, no. 7, pp. 874–884, 2017.
- [7] H. Němec et al., “Influence of the electron-cation interaction on electron mobility in dye-sensitized ZnO and TiO₂ nanocrystals: A study using ultrafast terahertz spectroscopy,” *Phys. Rev. Lett.*, vol. 104, no. 19, pp. 1–4, 2010.
- [8] S. B. N. et al., “Time-resolved terahertz spectroscopy reveals the influence of charged sensitizing quantum dots on the electron dynamics in ZnO,” *Phys. Chem. Chem. Phys.*, vol. 19, no. 8, pp. 6006–6012, 2017.
- [9] H. Němec, K. Knížek, Z. Jiráček, J. Hejtmánek, M. Soroka, and J. Buršík, “Charge transport in thin layer Na_xCoO₂ ($x \sim 0.63$) studied by terahertz spectroscopy,” *J. Phys. Condens. Matter*, vol. 28, no. 35, 2016.
- [10] S. Arezoomandan et al., “THz characterization and demonstration of visible-transparent/terahertz-functional electromagnetic structures in ultra-conductive La-doped BaSnO₃ Films,” *Sci. Rep.*, vol. 8, no. 1, pp. 2–10, 2018.
- [11] P. U. Jepsen, D. G. Cooke, and M. Koch, “Terahertz spectroscopy and imaging - Modern techniques and applications,” *Laser Photonics Rev.*, vol. 5, no. 1, pp. 124–166, 2011.
- [12] H. Němec, P. Kužel, and V. Sundström, “Far-infrared response of free charge carriers localized in semiconductor nanoparticles,” *Phys. Rev. B - Condens. Matter Mater. Phys.*, vol. 79, no. 11, pp. 1–7, 2009.

- [13] Z. Mics and P. Kuzel, “Dynamics of delocalized states in molecular systems studied by time-resolved THz spectroscopy,” Charles University, 2012.
- [14] F. Kadlec, C. Kadlec, P. Kužel, and J. Petzelt, “Study of the ferroelectric phase transition in germanium telluride using time-domain terahertz spectroscopy,” *Phys. Rev. B*, vol. 84, no. 20, p. 205209, Nov. 2011.
- [15] A. Kuramata, K. Koshi, S. Watanabe, Y. Yamaoka, T. Masui, and S. Yamakoshi, “High-quality β -Ga₂O₃ single crystals grown by edge-defined film-fed growth,” *Japan Soc. Appl. Phys.*, vol. 55, no. 1202A2, 2016.
- [16] N. Blumenschein, C. Kadlec, O. Romanyuk, T. Paskova, and J. F. Muth, “Dielectric and conducting properties of unintentionally and Sn-doped β -Ga₂O₃ studied by terahertz spectroscopy,” *J. Appl. Phys.*, vol. 127, no. 165702, 2020.
- [17] N. V. Smith, “Classical generalization of the Drude formula for the optical conductivity,” *Phys. Rev. B - Condens. Matter Mater. Phys.*, vol. 64, no. 15, 2001.
- [18] T. L. Cocker et al., “Microscopic origin of the Drude-Smith model,” *Phys. Rev. B*, vol. 96, no. 20, 2017.
- [19] M. Schubert et al., “Anisotropy, phonon modes, and free charge carrier parameters in monoclinic β -gallium oxide single crystals,” *Phys. Rev. B - Condens. Matter Mater. Phys.*, vol. 93, no. 12, pp. 1–18, 2016.
- [20] E. G. Víllora, K. Shimamura, T. Ujiie, and K. Aoki, “Electrical conductivity and lattice expansion of β -Ga₂O₃ below room temperature,” *Appl. Phys. Lett.*, vol. 92, no. 20, 2008.
- [21] Y. An et al., “Epitaxial growth of β -Ga₂O₃ thin films on Ga₂O₃ and Al₂O₃ substrates by using pulsed laser deposition,” *J. Adv. Dielectr.*, vol. 9, no. 4, pp. 3–9, 2019.

CHAPTER 6 – DEEP-ULTRAVIOLET PHOTODETECTORS

6.1 Photodetector Device Physics

In this work, metal-semiconductor-metal (MSM) photodetectors (PDs) were fabricated using undoped Ga₂O₃ thin films on c-plane sapphire substrates. The MSM PD is a lateral device which consists of a semiconductor layer with two Schottky contacts. Typically, each of the Schottky contacts consists of a pad used for applying a bias and a series of interdigitated electrodes, or ‘fingers’, that extend from the pads across the semiconductor layer. The MSM PD is a planar device with simplistic fabrication requirements, has a low dark current because of the two back-to-back Schottky metals, its planar device geometry results in a low capacitance and fast RC time constant, and it operates solely on drift current which is easily controlled by varying the electric field in the active area [1]. **Figure 6.1** shows the MSM PD structure band diagram when applying a **(a)** zero bias and **(b)** forward bias. The band structure of the detector is symmetrical when under zero bias conditions, causing the electrons to be trapped in the conduction band between the two potential barriers. Applying a forward bias causes potential barrier lowering and allows for four possible carrier transport mechanisms [2].

- (1) Photogenerated electrons are swept from the active layer into the anode metal*
- (2) Electron tunneling through the potential barrier on the negatively biased electrode*
- (3) Electron-hole pair recombination in the active layer space-charge region*
- (4) Hole injection from positively biased electrode to active layer*

The photocurrent will increase linearly until the applied voltage (V_A) is high enough to achieve punch-through conditions. At this point a flat-band voltage (V_{FB}) is achieved, and the

active layer depletion region width (W) will be equal to the electrode spacing (L). The V_{FB} can be estimated by **Equation 6.1**, where q is electron charge, N_D is doping concentration in the active layer, and ϵ is the permittivity of Ga_2O_3 . Because of the device symmetrical, the application of a forward and reverse bias will have the same effect on the device, with the only difference being current polarity.

$$V_{FB} = \frac{qN_D L^2}{2\epsilon} \quad (6.1)$$

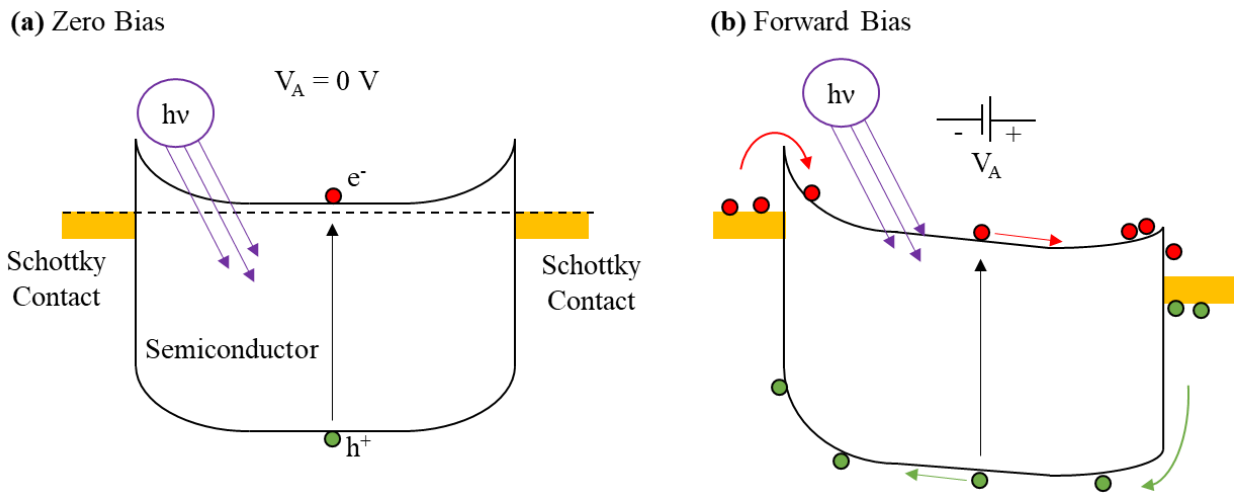


Figure 6.1 Band diagram of MSM photodetector under (a) zero bias and (b) forward bias.

6.2 Device Fabrication

Dimensional properties of the fabricated MSM PDs are listed in **Table 6.1**. A CAD drawing and optical image (inset) of sample A are shown in **Figure 6.2**. The fabrication details used in this work are described below.

1. **Substrate Cleaning:** The sapphire substrates were cleaned by ultra-sonication for 5 minutes in acetone and 5 minutes in methanol, and then dried using N_2 .

2. Thin Film Growth: Undoped Ga₂O₃ thin films were grown using the PLD recipe described in **Table 3.5**, with the exception of a varying oxygen pressure (P_{O2}). In this work, P_{O2} was varied from 1x10⁻⁴ to 1x10⁻² Torr.
3. Sample Cleaning: The Ga₂O₃/sapphire samples were cleaned using the previously described cleaning procedure.
4. Photolithography/Patterning: The samples were placed onto a 115°C hotplate for 5 minutes. Negative photoresist (AZ-5214E) was spincoated onto surface at 3000 RPM for 20 seconds. The samples were then placed on 90°C hotplate for 2 minutes and exposed to 20 mW UV radiation for 3 seconds while under the photomask, followed by an additional bake at 115°C hotplate for 90 seconds. The next step includes a flood exposure for 90 seconds under 20 mW UV radiation without the photomask. The sample were then placed into a developer solution (MF-319) for 40 seconds, rinsed in DI H₂O for 1 minute, and dried using N₂ gas.
5. Metallization: Nickel/gold (50/100 nm) contacts were deposited using E-beam deposition. The chamber was pumped down to less than 5x10⁻⁵ Torr prior to deposition.
6. Lift-Off: The samples were placed into an air-tight beaker with 100 mL acetone directly following the metal deposition. Samples were left to soak in the acetone for a couple of hours before any agitation was applied to assist with metal lift-off.
7. Sample Cleaning: Samples were cleaned using the previously described cleaning procedure.
8. Analysis: The samples were visually inspected using an optical microscope to ensure that the devices were functional. The microscope was used to measure the interdigitated electrode dimensions to use for later analysis of electrical characterization.

Table 6.1 Dimensional properties of fabricated devices.

Sample	A1	A2	A3	B	C
P _{O2} (mT)	0.1	1	10	1	1
Finger Count	20	20	20	11	11
Finger Width (μm)	8	8	8	12	12
Pad Width (μm)	280	280	280	200	400
Ga ₂ O ₃ :Metal Ratio	0.75	0.75	0.75	0.52	0.52

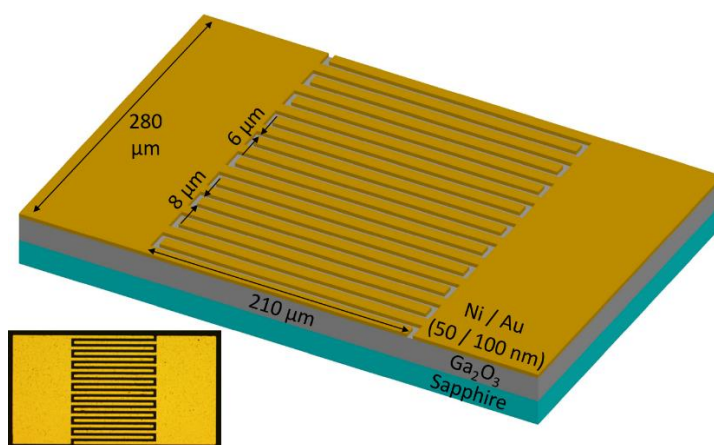


Figure 6.2 Schematic drawing and optical image of MSM PD structure. Physical dimensions shown here are for sample A. Copyright (2019) John Wiley and Sons [3].

6.3 Photodetector Performance

The MSM photodetectors I-V characteristic and transient response was analyzed using a Keithley characterization system. The PDs were tested under dark and 250 nm illumination conditions. A UV LED was used for illumination and was placed 5 cm above the detector surface during measurement. **Figure 6.3(a)** shows the I-V characteristic of the Ga₂O₃ MSM photodetectors containing active layers grown with varying P_{O2}, where devices A1, A2, and A3 correspond to a P_{O2} of 1x10⁻⁴, 1x10⁻³, 1x10⁻² Torr, respectively. The obtained I-V characteristics for dark and UV illumination conditions are shown using open and filled circles, respectively. For

$V_A = 10$ V, device A3 had the lowest dark current and photocurrent amplitudes of 4.2 nA and 26.1 nA, respectively. The electrical performance was significantly better for device A1, where a photocurrent of 4.39 μ A was observed at $V_A = 10$ V. Interestingly, the dark current was 307.7 nA, resulting in an $I_{\text{photo}}/I_{\text{dark}}$ ratio of only 14X. Device A2 showed superior performance, where the respective dark current and photocurrent were found to be 83.4 nA and 7.52 μ A for $V_A = 10$ V, resulting in an $I_{\text{photo}}/I_{\text{dark}}$ ratio of 90X. However, a maximum $I_{\text{photo}}/I_{\text{dark}}$ ratio of more than 700X was observed at a lower 6 V bias. A similar effect was observed for Device A1, where the peak $I_{\text{photo}}/I_{\text{dark}}$ ratio occurred at $V_A = 3$ V.

The P_{O_2} greatly effects the PDs electrical performance, a finding consistent with previous reports on heteroepitaxial Ga_2O_3 thin films grown on c-plane sapphire [4]. Muller *et al.* speculated that since oxygen atoms are much lighter than gallium, they are more prone to scattering when subject to increased pressure conditions. If the chamber pressure is too high, the increased scattering can result in oxygen deficient Ga_2O_3 thin films. Leedy *et al.* reported a maximum conductivity for PLD-grown homoepitaxial Si-doped Ga_2O_3 thin films for a P_{O_2} of 0.975 mT, which is nearly identical to the optimized P_{O_2} of 1 mT found in this work, despite the large differences in other growth parameters such as temperature [5]. Hall measurements were performed on the three Ga_2O_3 thin films. The film of device A3 was too insulating to obtain accurate data, but the films of devices A1 and A2 has conductivity values of $4.15 \times 10^{-6} \Omega^{-1} \text{cm}^{-1}$ and $5.22 \times 10^{-5} \Omega^{-1} \text{cm}^{-1}$, respectively. The film conductivity difference observed here is expected given the deviation in electrical performance between the PDs as shown in their I-V characteristic.

Figure 6.3(b) shows the I-V characteristic for devices A(2), B, and C, which were all grown using a P_{O_2} of 1 mT, but contained variation in the PD electrode geometry. Device B had the lowest photocurrent. The device consisted of 11 metal fingers each with a 12 μ m width. It is

likely that the relatively large spacing between fingers caused carrier recombination in the active layer before the electrons were able to be swept into the metal region. The photocurrent of device C was improved even though it contained a similar electrode layout to that of device B. Device C had 22 fingers with a 12 μm width, so the area was twice as large. The increased photocurrent was attributed to an increase in photon absorption within the active layer. Device A, consisting of 20 fingers with 8 μm spacing, had the best performance. The short distance between fingers likely increased the electron sweeping efficiency. Device A had a low dark current of 84.3 nA at a 10 V bias. When subject to 250 nm illumination and a 10 V bias the photocurrent increased by almost two orders of magnitude to 7.52 μA .

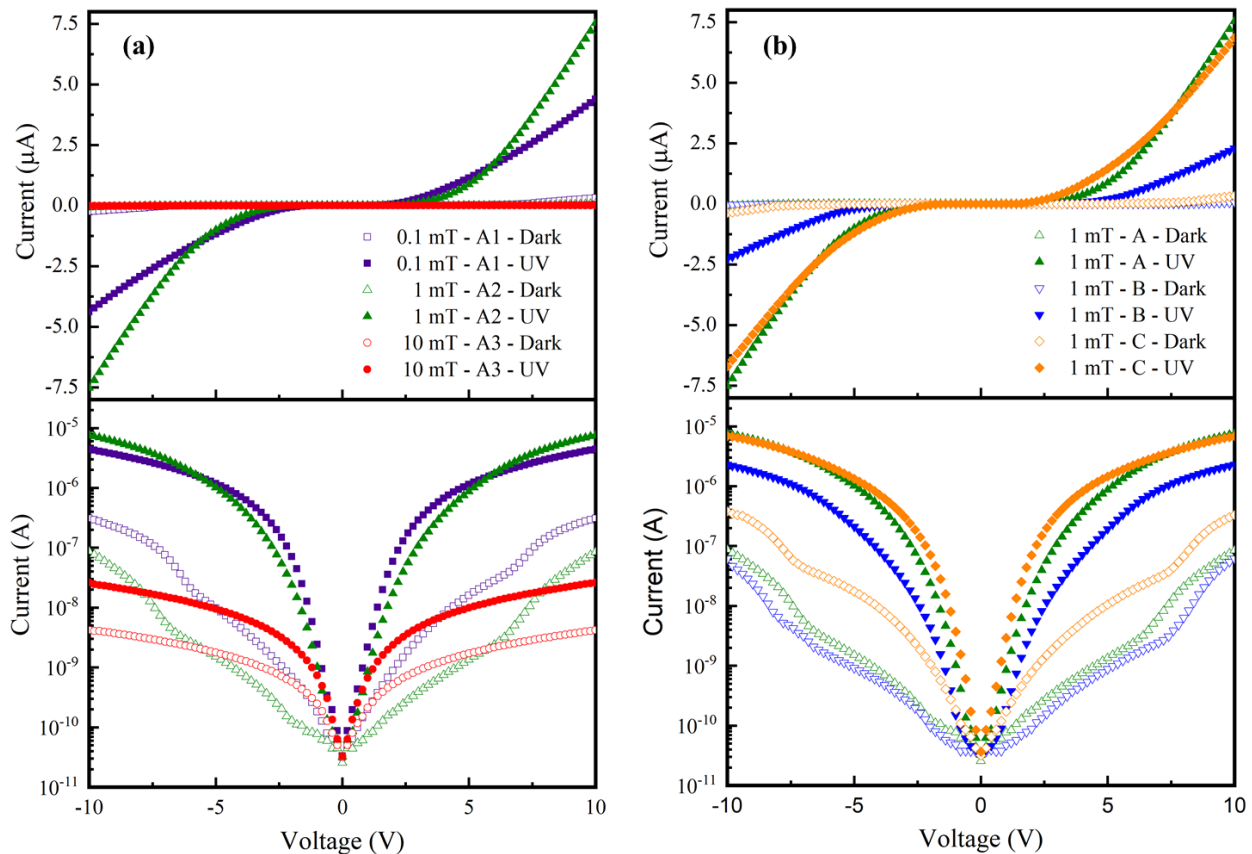


Figure 6.3 I-V characteristic of deep-UV MSM PDs for devices containing (a) films grown with varying P_{O_2} and (b) devices grown at the optimized P_{O_2} conditions of 1 mT with varying device geometrical properties. Copyright (2019) John Wiley and Sons [3].

The transient response of devices A1-A3 and A-C are shown in **Figure 6.4 (a) and (b)**, respectively. The transient response was gathered by alternating the 250 nm illumination while applying a constant 10 V bias. The transient response curves were fit using biexponential relaxation of **Equation 6.2**, where, I_0 is steady-state photocurrent, t is time, τ_1 and τ_2 are relaxation time constants for rise and decay photocurrent, and A and B are scaling constants. The relaxation time constant values are shown in **Table 6.2**. The transient response contains two separate relaxation processes – fast (τ_{r1} and τ_{d1}) and slow (τ_{r2} and τ_{d2}) – for both rise and decay. The fast response is caused by direct band-to-band transitions, whereas the slow rise time is likely due to a transition between defects and conduction band and the slow decay time is due to a transition from the conduction band to recombination centers in the Ga₂O₃ active layer [6], [7]. Relaxation time constants that are nearly identical were observed when comparing the results of devices A-C, meaning that the response time is a function of film quality rather than electrode spacing. The relaxation times observed for devices A1-A3 were quite different. Device A1 has the lowest response times, which could point towards a relatively lower number of oxygen-related defects. It can be seen that $\tau_{r1} < \tau_{d1}$ for device A1, $\tau_{r1} \sim \tau_{d1}$ for device A2, and $\tau_{r1} > \tau_{d1}$ for device A3, which is a direct result of the increased P_{O2}.

Figure 6.5 shows the spectral responsivity of devices A1-A3. The inset image shows the same data using a log scale to emphasize the lower responsivity of device A3. During measurement, the PDs were subject to incident radiation ranging from 200 – 300 nm while a constant 10 V bias was applied. For devices A2 and A3, the peak spectral responsivity occurred for 250 nm incident radiation, whereas device A1 had a peak spectral responsivity at 237.5 nm. These results are consistent with previous reports where the spectral responsivity of Ga₂O₃ photodetectors was measured for Ga₂O₃ thin films with varying P_{O2} [8]. The results reported by

Huang *et al.* were for films grown using a minimum P_{O_2} of 7.5 mT, but there are a large number of other growth-related discrepancies when comparing to this work such as growth temperature, laser energy density, and laser repetition rate, making it difficult to draw any conclusions between the two sets of data. Device A2 had the highest spectral responsivity of 30.45 A/W at 250 nm, which is comparable to previous findings on Ga_2O_3 MSM PDs where peak spectral responsivities of 45 – 70 A/W were

$$I(t) = I_0 + Ae^{-\frac{t}{\tau_1}} + Be^{-\frac{t}{\tau_2}} \quad (6.2)$$

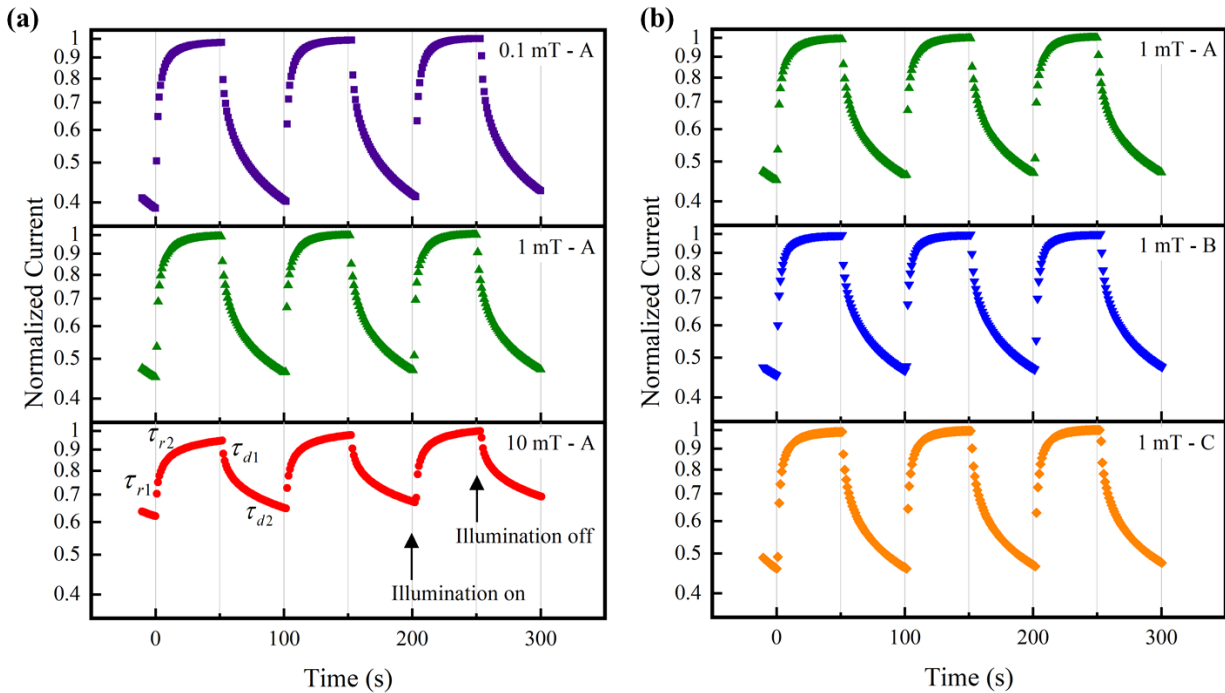


Figure 6.4 Transient response of MSM PDs for devices containing (a) films grown with varying P_{O_2} and (b) devices grown at the optimized P_{O_2} conditions of 1 mT with varying device geometrical properties. Copyright (2019) John Wiley and Sons [3].

Table 6.2 Rise and decay time constants gathered by fitting the transient response curves of Figure 6.4 using Equation 6.2. Copyright (2019) John Wiley and Sons [3].

P_{O_2} (mT)	PD Layout	Time Constants (s)				P_{O_2} (mT)	PD Layout	Time Constants (s)			
		τ_{r1}	τ_{r2}	τ_{d1}	τ_{d2}			τ_{r1}	τ_{r2}	τ_{d1}	τ_{d2}
0.1	A	1.20	7.79	2.46	11.16	1	A	2.66	8.70	2.61	12.91
1	A	2.66	8.70	2.61	12.91	1	B	2.69	9.57	2.52	12.19
10	A	6.81	10.76	3.70	13.97	1	C	2.46	9.97	2.75	12.89

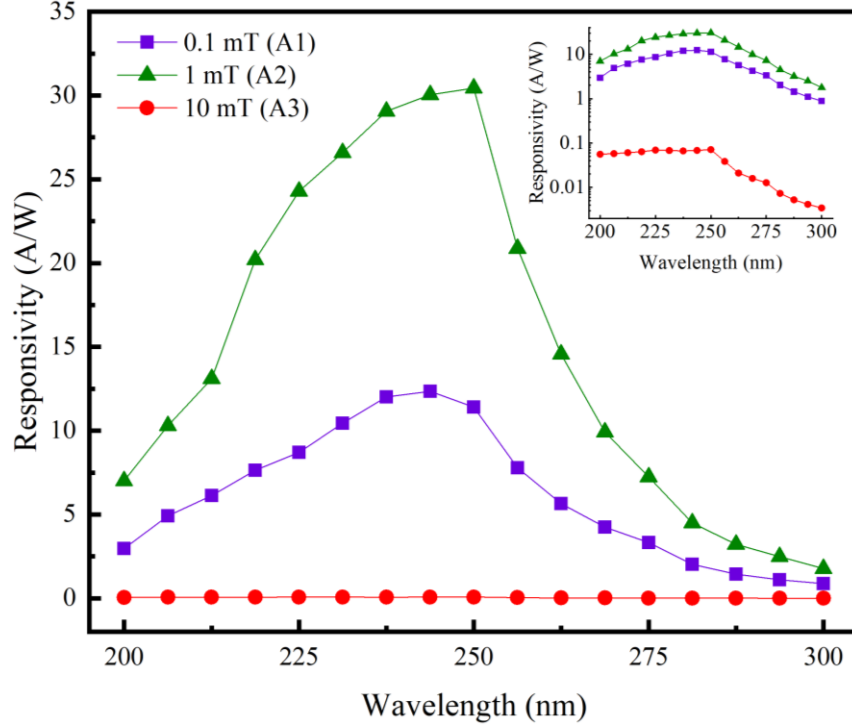


Figure 6.5 Spectral responsivity of MSM PDs containing Ga_2O_3 thin films grown with varying P_{O_2} . The inset plot contains the spectral responsivity on a log scale. Copyright (2019) John Wiley and Sons [3].

observed [9], [10]. The high spectral responsivities observed here are attributed to internal gain in the active layer and minority carrier trapping at the metal/ Ga_2O_3 interface. The internal gain (G) was calculated using **Equation 6.3**, where R is spectral responsivity, h is Planck's constant, c is the speed of light, η is quantum efficiency, q is electron charge, and λ is incident radiation wavelength. It was assumed that the incident photons were completely absorbed, allowing for the quantum efficiency to be set at unity when calculating gain. When using 250 nm incidence, the internal gain of devices A1 – A3 was found to be 56.7, 151.3, and 0.4, respectively.

$$G = \frac{Rhc}{\eta q \lambda} \quad (6.3)$$

6.4 Conclusions

Ga₂O₃-based MSM solar-blind UV photodetectors were fabricated on c-plane sapphire substrates. The four possible carrier transport mechanisms that occur in MSM PDs are described. Device performance was investigated while varying electrode geometry to maximize the $I_{\text{photo}}/I_{\text{dark}}$. An optimal Ga₂O₃:metal ratio of 0.75 was realized due to a combination of UV radiation and carrier sweeping capability in the device active region. The oxygen partial pressure used during thin film growth was also analyzed by varying P_{O₂} over three decades within the range of 0.1 – 10 mT. It was found that the devices containing a film grown using a P_{O₂} of 1 mT offered the highest $I_{\text{photo}}/I_{\text{dark}}$ and spectral responsivity values of 90X and 30.45 A/W, respectively. The transient response of the devices was measured and it was found that two separate relaxation processes were present during rise and decay. It was speculated that the fast response was caused by direct band-to-band transitions, the slow rise response was due to a transition between defects and the conduction bands, and the slow decay response was due to a transition between the conduction band and recombination centers. The increased response times observed in films grown at a higher P_{O₂} were attributed to an increased number of oxygen-related defects.

6.5 References

- [1] P. R. Berger, “MSM photodiodes,” *IEEE Potentials*, vol. 15, no. 2. pp. 25–29, 1996.
- [2] F. Haas, “Metal-Semiconductor-Metal Photodetectors for Optical Interconnect Applications,” 1997.
- [3] N. Blumenschein, T. Paskova, and J. F. Muth, “Effect of Growth Pressure on PLD-Deposited Gallium Oxide Thin Films for Deep-UV Photodetectors,” *Phys. status solidi*, vol. 216, no. 20, p. 1900098, Oct. 2019.
- [4] S. Muller, H. Von Wenckstern, D. Splith, F. Schmidt, and M. Grundmann, “Control of the conductivity of Si-doped β -Ga₂O₃ thin films via growth temperature and pressure,” *Phys. Status Solidi Appl. Mater. Sci.*, vol. 211, no. 1, pp. 34–39, 2014.
- [5] K. D. Leedy *et al.*, “Si content variation and influence of deposition atmosphere in homoepitaxial Si-doped β -Ga₂O₃ films by pulsed laser deposition,” *APL Mater.*, vol. 6, no. 10, p. 101102, 2018.
- [6] D. Y. Guo *et al.*, “Oxygen vacancy tuned Ohmic-Schottky conversion for enhanced performance in β -Ga₂O₃ solar-blind ultraviolet photodetectors,” *Appl. Phys. Lett.*, vol. 105, no. 2, 2014.
- [7] D. Guo *et al.*, “Fabrication of β -Ga₂O₃ thin films and solar-blind photodetectors by laser MBE technology,” *Opt. Mater. Express*, vol. 4, no. 5, pp. 1067–1076, 2014.
- [8] L. Huang *et al.*, “Comparison Study of β -Ga₂O₃ Photodetectors Grown on Sapphire at Different Oxygen Pressures,” *IEEE Photonics J.*, vol. 9, no. 4, 2017.
- [9] L. X. Qian, Z. H. Wu, Y. Y. Zhang, P. T. Lai, X. Z. Liu, and Y. R. Li, “Ultrahigh-responsivity, rapid-Recovery, solar-Blind photodetector based on highly nonstoichiometric amorphous gallium oxide,” *ACS Photonics*, vol. 4, no. 9, pp. 2203–2211, 2017.
- [10] S. H. Lee *et al.*, “High-Responsivity Deep-Ultraviolet-Selective Photodetectors Using Ultrathin Gallium Oxide Films,” *ACS Photonics*, vol. 4, no. 11, pp. 2937–2943, 2017.

CHAPTER 7 – METAL-OXIDE-SEMICONDUCTOR FIELD-EFFECT TRANSISTORS

7.1 Device Fabrication

The β -Ga₂O₃ metal-oxide field-effect transistors (MOSFETs) studied in this work were fabricated by the Air Force Research Laboratory – Sensors Directorate at the Wright-Patterson Air Force Base. The devices were fabricated using a (010)-oriented Fe-doped Ga₂O₃ semi-insulating substrate with a thickness of 650 μm . Metal-organic vapor phase epitaxy (MOVPE) was used for growing the homoepitaxial Si-doped Ga₂O₃ thin film channel with thickness of 65 nm. Hall measurements were used to gather the donor concentration, sheet concentration, and mobility of the film, and found to be $2.0 \times 10^{18} \text{ cm}^{-3}$, $1.3 \times 10^{13} \text{ cm}^{-2}$, and $90 \text{ cm}^2/\text{V-s}$, respectively. Source and drain ohmic contacts were formed by depositing a Ti/Al/Ni/Au (20/100/50/50 nm) stack using electron beam deposition. The contacts were annealed for one minute at 470 °C in an N₂ ambient using rapid thermal annealing (RTA). Transmission line measurements later revealed that the ohmic contacts had a low contact resistance of only 11 Ω -mm. Atomic layer deposition (ALD) was used to deposit a 20 nm Al₂O₃ gate dielectric layer. A 90 nm SiO₂ layer was then deposited using plasma-enhanced chemical vapor deposition (PECVD). The SiO₂ would serve as a field-oxide layer for the ungated access regions. A trench with a length of 0.14 μm was etched into the SiO₂ layer by reactive ion etching (RIE) using a CF₄-based recipe. The Al₂O₃ layer served as an etch-stop for the gate-trench process. A Ni/Au layer was deposited onto the 0.7- μm -wide trench region using electron-beam deposition to form a T-gate. The Au gate pad was electroplated to a thickness of 5 μm for heat dissipation purposes. **Figure 7.1** shows a schematic drawing of the fabricated β -Ga₂O₃ MOSFET. The depletion-mode MOSFET had source-to-drain (L_{SD}) and gate-to-source (L_{GS}) lengths of 8 and 0.5 μm , respectively.

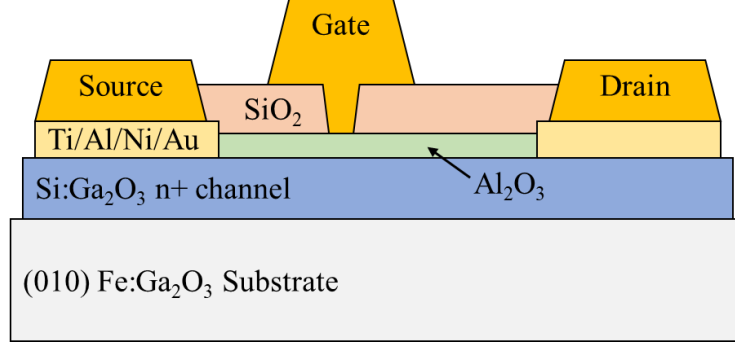


Figure 7.1 Schematic drawing of the β -Ga₂O₃ thin-channel MOSFET used in this work. Copyright (2020) IEEE [1].

7.2 MOSFET Device Physics

The β -Ga₂O₃ metal-oxide field-effect transistors (MOSFETs) studied in this work were depletion-mode devices which operated in a normally-on state with a gate voltage of zero volts. With a constant drain-to-source voltage (V_{DS}) applied, the devices are turned off by negatively increasing the gate voltage (V_G) until pinch-off occurs at full depletion of the active layer. The pinch-off voltage (V_{off}) can be determined using **Equation 7.1**, where V_{FB} is the flat-band voltage, d is active layer thickness, q is electron charge, N_d is the average active ionized dopant concentration in the active layer, $\epsilon_s \epsilon_0$ is the dielectric constant of Ga₂O₃, and C_{ox} is the oxide capacitance per unit area (equal to $\epsilon_{ox} \epsilon_0 / t_{ox}$) [2].

$$V_{off} = V_{FB} - dqN_d \left(\frac{d}{2\epsilon_s \epsilon_0} + \frac{1}{C_{ox}} \right) \quad (7.1)$$

The flat-band voltage can be determined using **Equation 7.2**, where where Φ_M and Φ_S are work functions of metal and semiconductor, χ_S is the electron affinity of Ga₂O₃, ϕ_t is the thermal voltage, and N_C is the effective density of states in the conduction band [2].

$$V_{FB} = \Phi_M - \Phi_S = \Phi_M - \left(\chi_S + \phi_t \ln \left(\frac{N_C}{N_d} \right) \right) \quad (7.2)$$

The V_{off} and V_{FB} determine when the device will operate within the linear and saturation regions of the I-V curve, as shown in **Figure 7.2**. The drain current (I_D) for the linear and saturation regions can be estimated using **Equations 7.3** and **7.4**, respectively, where W_g is the gate width, L_g is the gate length, C_{ox} is the gate oxide capacitance, μ is the active layer mobility, V_{GS} is the gate-to-source voltage, and V_T is the threshold voltage.

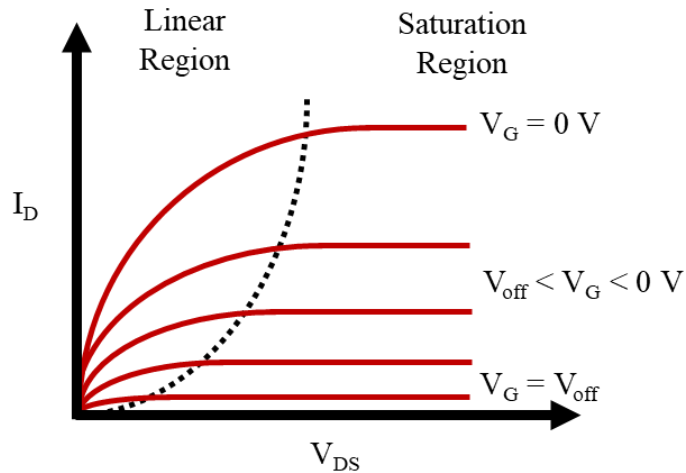


Figure 7.2 I-V characteristic of depletion-mode MOSFET.

$$I_D(\text{linear}) = \frac{W_g}{2L_g} C_{ox} \mu (V_{GS} - V_T) V_{DS} \quad (7.3)$$

$$I_D(\text{saturation}) = \frac{W_g}{2L_g} C_{ox} \mu (V_{GS} - V_T)^2 \quad (7.4)$$

An important property of thin-channel MOSFETs is the on-resistance (R_{ON}) because it directly controls the current density amplitude. As shown in **Equation 7.5**, R_{ON} is the sum of channel resistance (R_{CH}), source access resistance (R_S), and drain access resistance (R_D) [3]. R_S and R_D scale with sheet resistance (R_{SH}) and contact resistance (R_C). The contact resistance can be controlled by implementing self-aligned gate implant technology or using epitaxial regrowth over the source and drain access regions [3]. Gate scaling can be used to reduce the channel resistance, but this can lead to negative effects such as punch-through. R_{ON} is also important because it results

in switching power losses (P_{loss}) as shown in **Equation 7.6**, where $I_{OUT}^2 R_{ON}$ and $C_{IN} V_G^2 f$ are responsible for conduction losses and dynamic losses, respectively.

$$R_{ON} = R_{CH} + R_S + R_D \quad (7.5)$$

$$P_{loss} = I_{OUT}^2 R_{ON} + C_{IN} V_G^2 f \quad (7.6)$$

7.3 DC Performance

Figure 7.3(a) shows the DC I-V characteristic of the Ga₂O₃ MOSFET analyzed in this work while varying V_{DS} from 0 to 10 V and V_G from -16 to 0 V in 2 V increments. **Figure 7.3(b)** shows the transfer characteristic obtained while biasing the MOSFET at a constant V_{DS} of 10 V. The inset shows the I_D transfer curve plotted on a log scale. The device has a peak g_m of 12.8 mS/mm at $V_{GS} = -13.2$ V. The threshold voltage of -15.1 V was found through extrapolation of the I_D - V_G curve linear region.

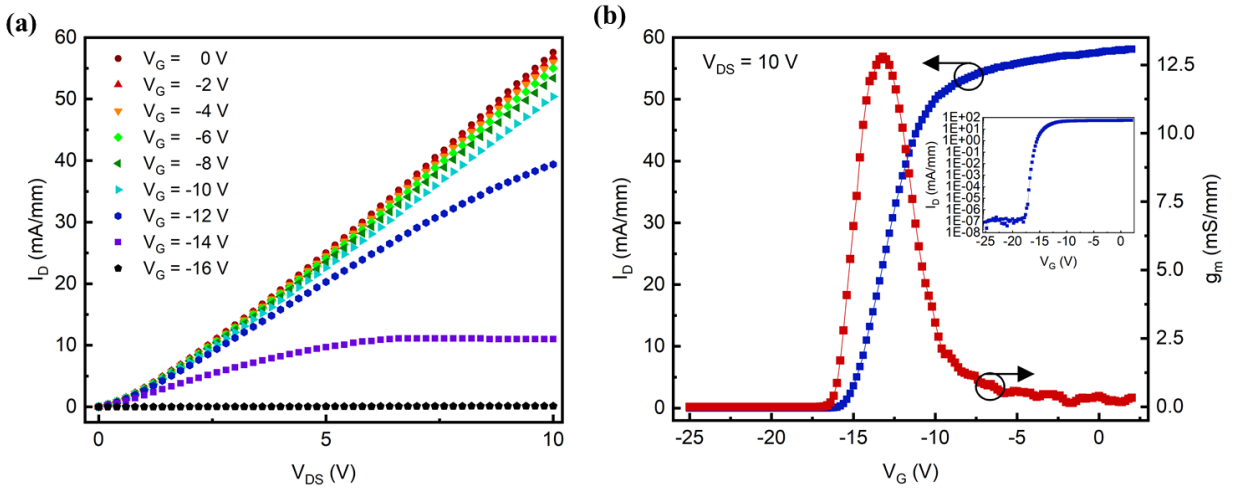


Figure 7.3 (a) DC I_D - V_{DS} characteristic while varying the gate voltage from -16 to 0 V. (b) Transfer characteristic using a drain voltage of 10 V. The inset shows I_D plotted on a log scale to show the turn-off gate voltage of -17.5 V. Copyright (2020) IEEE [1].

7.4 Pulsed I-V Measurement Technique

Pulsed I-V measurements were performed within the 23 – 200 °C temperature range using a DiVA D265 dynamic I-V analyzer equipped with an Au-plated thermal baseplate. The I-V analyzer allowed for simultaneous control of V_{DS} and V_G switching times with sub- μ s precision. This switching capability allowed for channel temperature acquisition using a pulsed I-V method previously demonstrated by Joh *et al.* on GaN HEMTs [4]. The technique involves a calibration step and measurement step. During the calibration step, temperature-dependent I-V data is acquired while varying the baseplate temperature ($T_{baseplate}$). The I-V data is captured while pulse biasing the MOSFET using zero quiescent gate and drain voltage conditions ($V_{GSQ} = 0$ V, $V_{DSQ} = 0$ V) and minimizing the time in which the device can self-heat. This is accomplished by minimizing the quiescent biasing (V_{GS} , V_{DS}) time using a short 200 ns pulsewidths and low 0.02% duty cycle as shown in **Figure 7.4**. The previous report by Joh *et al.* showed that using a 200 ns pulsewidth and 0.02% duty cycle resulted in a small channel temperature error of only 6 °C [4]. It was shown that the error could be further reduced using a shorter 100 ns pulsewidth. Unfortunately, this capability was not available with the equipment used in this work. When using the 200 ns pulsewidth and 0.02% duty cycle, it was assumed that device temperature was unaffected by power dissipation, and thus, the MOSFET channel temperature was the same as the baseplate temperature ($T_{CH} = T_{baseplate}$). The I-V characteristic was measured by applying $V_{GS} = 0$ V and sweeping V_{DS} from 0 to 15 V. The on resistance (R_{ON}) and maximum drain current ($I_{D,max}$) were extracted from each I-V curve. R_{ON} was determined from the slope of the I_D - V_{DS} curve and $I_{D,max}$ was defined as $I_{D,max}(V_{DS} = 15$ V). Acquisition of these parameters and plotting them versus T_{CH} for each temperature condition concludes the calibration step. During the measurement step self-heating is induced within the MOSFET channel by applying non-zero quiescent bias

conditions while maintaining a constant 23 °C baseplate temperature. V_{DSQ} and V_{DS} were varied from 0 to 15 V during these measurements. Once again R_{ON} and $I_{D,max}$ were extracted from each I-V curve. Since T_{CH} was unknown, R_{ON} and $I_{D,max}$ were plotted as a function of dissipated power ($P_D = V_{DSQ} \times I_{DQ}$) which was calculated for each V_{DSQ} condition.

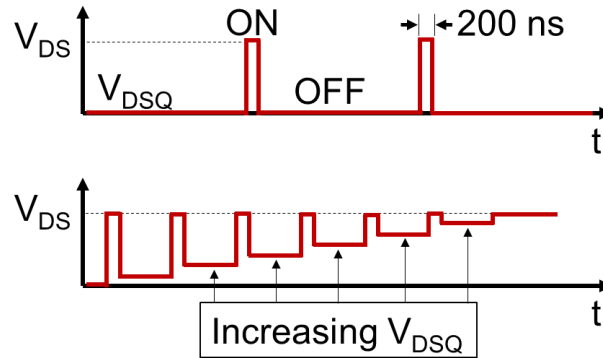


Figure 7.4 Depiction of $V_{DS}(t)$ waveforms used during the pulsed I-V characterization.

7.5 Self-Heating Characterization

Figure 7.5(a) shows the effect of pulsewidth on the I_D - V_{DS} characteristic. Here the I-V characteristic was acquired using a $T_{baseplate} = 23$ °C, $V_G = 5$ V, $V_{DS} = 0 - 15$ V, and varying the pulsewidth from 200 ns to 1 ms. Each I-V curve was fit for linearity, and the resulting R^2 values are plotted as a function of pulsewidth in the inset. Higher pulsewidth resulted in a drain current which saturated at lower values of V_{DS} , indicating higher amounts of self-heating were present. For the 200 ns pulsewidth, the I_D - V_{DS} curve remained linear through the entire $V_{DS} = 0 - 15$ V range. **Figure 7.5(b)** shows the I_D - V_{DS} characteristic when using a 200 μ s pulsewidth and varying $T_{baseplate}$ from 23 to 100 °C. As $T_{baseplate}$ is increased, R_{ON} increased and $I_{D,max}$ decreased almost linearly. The I-V curve begins to saturate at a 5 V bias as if a DC bias were being applied. The current collapse is a result of the 200 μ s pulsewidth and 20% duty cycle being used, which is

causing heat to build up in the MOSFET channel. It was previously shown in AlGaN/GaN devices that lowering the pulsewidth into the sub-microsecond range has the benefit of reduced self-heating effects [5]. A 200 ns pulsewidth and 0.02% duty cycle were used during the calibration step to mitigate self-heating. The resulting I_D - V_{DS} characteristic is shown in **Figure 7.5(c)**, where $T_{baseplate}$ was varied from 23 to 200 °C. Using these pulsed I-V conditions, the desired I_D - V_{DS} linearity was observed, indicating the absence of any self-heating in the channel. At room temperature R_{ON} was 67.9 Ω -mm, then increased by 24% to 84.0 Ω -mm at 200 °C. At room temperature $I_{D,max}$ had a value of 215.2 mA/mm, then decreased by 22% to 176.4 mA/mm at 200 °C. **Figure 7.5(d)** shows R_{ON} and $I_{D,max}$ plotted as a function of T_{CH} .

The same 200 ns pulsewidth and 0.02% duty cycle conditions were used in the measurement step. The $T_{baseplate}$ was set to a constant 23 °C for all remaining measurements. During the measurement step the device was subject to increasing amounts of self-heating, caused by using a non-zero V_{DSQ} which ranged from 2 to 15 V. The resulting I_D - V_{DS} characteristic is shown in **Figure 7.6(a)**. The parameters R_{ON} and $I_{D,max}$ were extracted from the I-V characteristic and plotted as a function of P_D as shown in **Figure 7.6(b)**. **Equations 7.7 – 7.10** were constructed from the R_{ON} - T_{CH} and $I_{D,max}$ - T_{CH} of **Figure 7.5(d)** and R_{ON} - P_D and $I_{D,max}$ - P_D of **Figure 7.6(b)**. From these four equations, **Equations 7.11** and **7.12** were obtained, providing a relationship between channel temperature and dissipated power. The two equations are nearly identical despite being obtained from different I-V parameters. **Figure 7.7** shows the estimated T_{CH} versus P_D as obtained from **Equations 7.11** and **7.12**. The thermal resistance (R_{TH}) was extracted from the slope of the two T_{CH} - P_D curves using a least squares fit approximation and estimated to be 73 °C-mm/W.

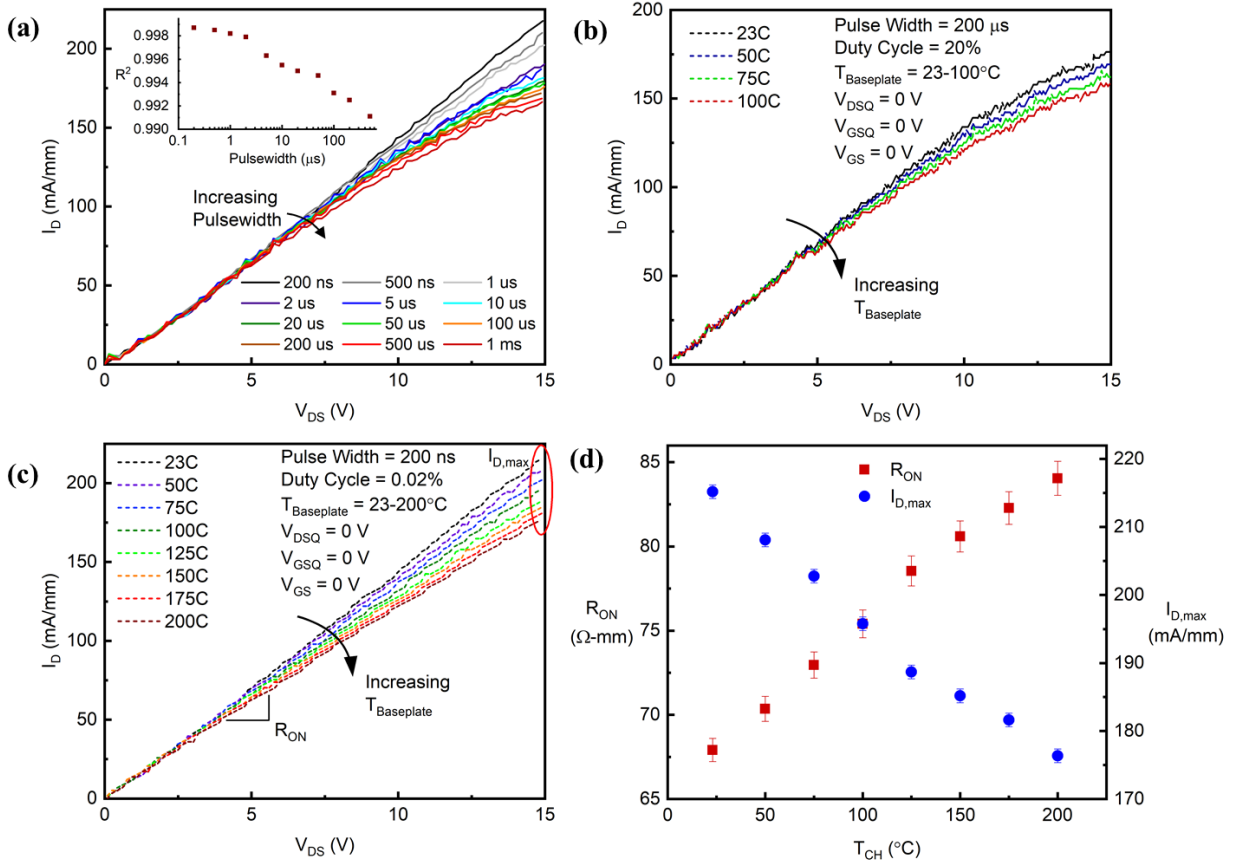


Figure 7.5 (a) Pulsed I_D - V_{DS} characteristic obtained for increasing pulsewidths while holding the baseplate temperature at 23°C and using $V_G = 0\text{ V}$. The inset shows R^2 values of the I_D - V_{DS} curves to demonstrate a decreased linearity with increasing pulsewidth. Pulsed I_D - V_{DS} characteristic obtained while varying the baseplate temperature and using pulsewidths of (b) 200 μs and (c) 200 ns. (d) R_{ON} and $I_{D,\text{max}}$ values extracted from the I_D - V_{DS} characteristic and plotted as a function of channel temperature. Copyright (2020) IEEE [1].

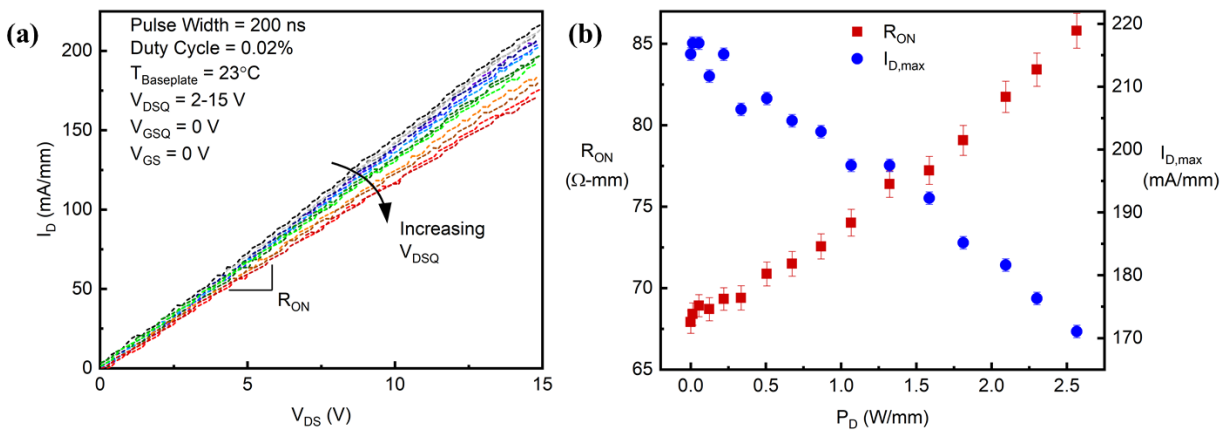


Figure 7.6 (a) Pulsed I_D - V_{DS} characteristic obtained when varying V_{DSQ} from 2 to 15 V. (b) R_{ON} and $I_{D,\text{max}}$ plotted as a function of dissipated power. Copyright (2020) IEEE [1].

$$R_{ON} = (0.094 \pm 0.003)T_{CH} + 65.962 \pm 0.407 \quad (7.7)$$

$$I_{D,max} = (-0.220 \pm 0.010)T_{CH} + 218.865 \pm 1.217 \quad (7.8)$$

$$R_{ON} = (6.476 \pm 0.203)P_D + 67.763 \pm 0.218 \quad (7.9)$$

$$I_{D,max} = (-16.868 \pm 0.627)P_D + 216.329 \pm 0.809 \quad (7.10)$$

$$T_{CH} = \frac{(6.476 \pm 0.203)P_D + 1.801 \pm 0.625}{0.094 \pm 0.003} \quad (7.11)$$

$$T_{CH} = \frac{(16.868 \pm 0.627)P_D + 2.536 \pm 0.408}{0.220 \pm 0.010} \quad (7.12)$$

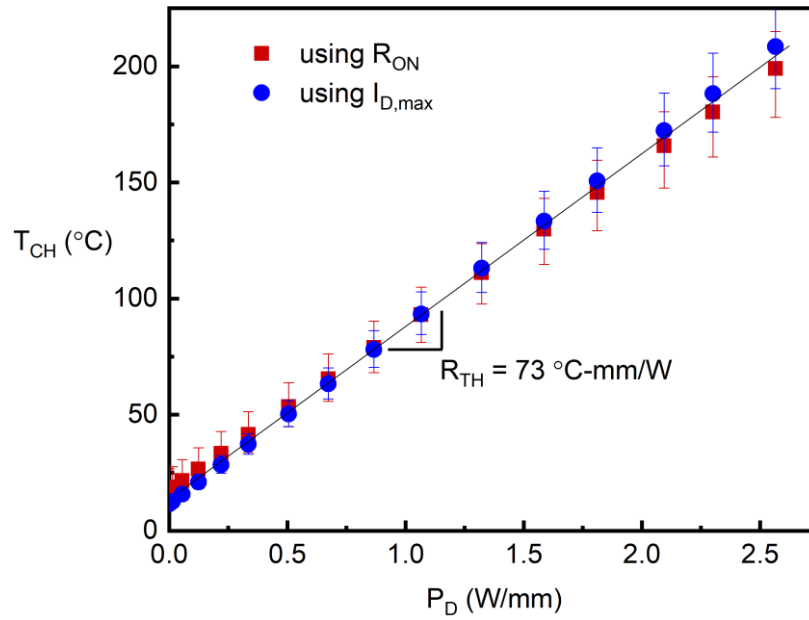


Figure 7.7 Two approximations of T_{CH} - P_D data that were separately obtained using R_{ON} and $I_{D,max}$. The estimated thermal resistance was obtained using the slope of T_{CH} - P_D and found to be $73 \text{ }^\circ\text{C-mm/W}$. Copyright (2020) IEEE [1].

7.6 Raman Nanothermography and Thermal Simulations

Raman nanothermography was used for verification of the pulsed I-V findings. Titanium dioxide (TiO_2) nanoparticles with 30 nm diameter were used to measure the temperature at four locations on the device surface. The TiO_2 particles were dispersed onto the device surface using a suspension of TiO_2 particles in ethanol. The suspension was made uniform by sonication prior

to dispersion onto the device. Once the particles were dispensed, the device was operated using DC bias conditions ($V_G = 0$ V, $V_{DS} = 2 - 8$ V in 2 V increments). Self-heating effects were evaluated during device operation by measuring the Raman peak shift of the particles, which was then used to extract channel temperature. During the measurements, the wafer was mounted to an electrically grounded baseplate and held at a constant temperature of 25 °C. The Raman signature of the TiO₂ particles was acquired using a 532 nm Ar⁺ laser with 0.5 NA objective lens with a 0.543 μm beam radius on the sample. Additional details on the Raman nanothermography technique used here have been previously described elsewhere [6]–[9].

Figure 7.8(a) shows the four TiO₂ particle locations on the MOSFET surface. The Raman spectra of each TiO₂ particle was measured during device operation for four varying amounts of power dissipation (0.228, 0.517, 0.698, and 0.904 W/mm) by increasing the DC V_{DS} (4, 6, 7, and 8 V). As shown in **Figure 7.3(a)**, the device is fully on when biasing from 4 to 8 V, which is important for the purpose of these experiments because the temperature profile is greatly impacted by the state of the depletion zone. If the device was only partially on there would be a localized heating in the depletion region at the drain edge of the gate and the temperature profile would be different than what is observed here [10]. **Figure 7.8(b)** shows the resulting temperature profile as a function of TiO₂ particle position along the channel. The maximum T_{CH} observed for each P_D was located on the drain edge of the gate (2.46 μm from the source contact edge). This finding is consistent with previous thermal characterization reports on Ga₂O₃ MOSFETs [11].

The pulsed I-V thermal characterization method provides a spatially averaged T_{CH} , whereas Raman nanothermography provides the temperature at discrete locations along the channel. To better compare the two techniques, the T_{CH} data of **Figure 7.8(b)** was plotted as a function of P_D for each TiO₂ particle location as shown in **Figure 7.8(c)**. The colored lines show the linear fits

for each TiO_2 particle. The slope of each fit was used to calculate the R_{TH} of each TiO_2 particle. The resulting R_{TH} values ranged from 50 to 69 $^\circ\text{C}\cdot\text{mm}/\text{W}$ and are shown in the legend.

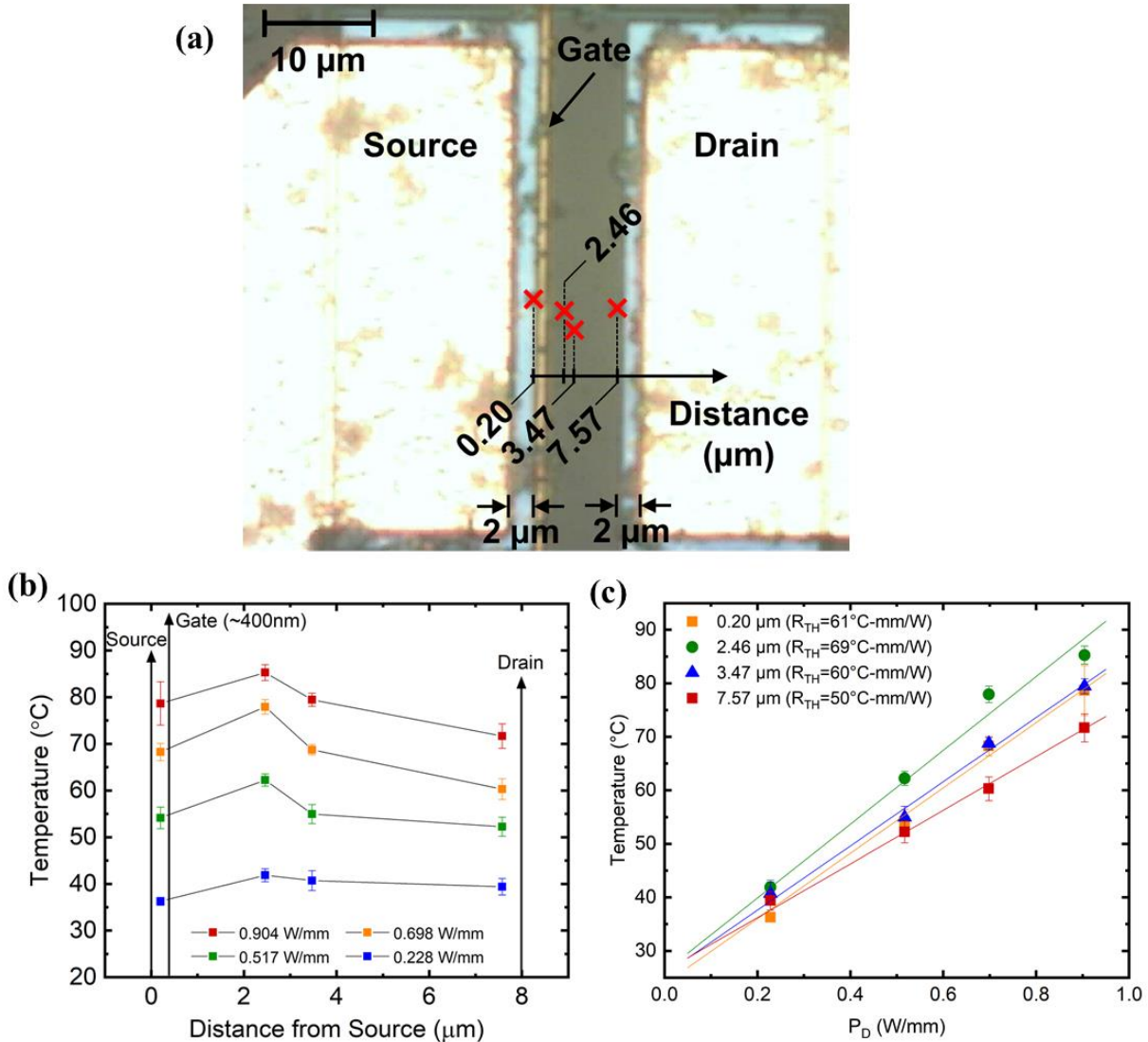


Figure 7.8 (a) Location of TiO_2 nanoparticles on the MOSFET surface (denoted with red X on the image). (b) T_{CH} data measured using Raman nanothermography for four increasing amounts of dissipated power. (c) T_{CH} - P_D data obtained for each nanoparticle location. The linear approximations used to extract R_{TH} for each TiO_2 particle location are shown with colored lines. Copyright (2020) IEEE [1].

Figure 7.9 (a)-(c) show ANSYS thermal simulations of the Ga_2O_3 MOSFET for $P_D = 0.9$ W/mm and $V_G = 0$ V at three resolutions. Device modelling proved that the device was operating

with an open channel under the chosen bias conditions. **Figure 7.9 (d)** and **(e)** show temperature profiles along the channel length and gate width, respectively. The channel length profile was taken at a position of 25 μm along the gate width (channel length center). The gate width profile was taken at the channel center where the maximum simulation temperature was observed. No sharp temperature gradients were observed for either profile. The gate width temperature profile remained nearly constant when considering the location of TiO_2 particles used during Raman nanothermography experiments. The maximum ΔT observed across all of the TiO_2 particle locations was only 3 $^\circ\text{C}$.

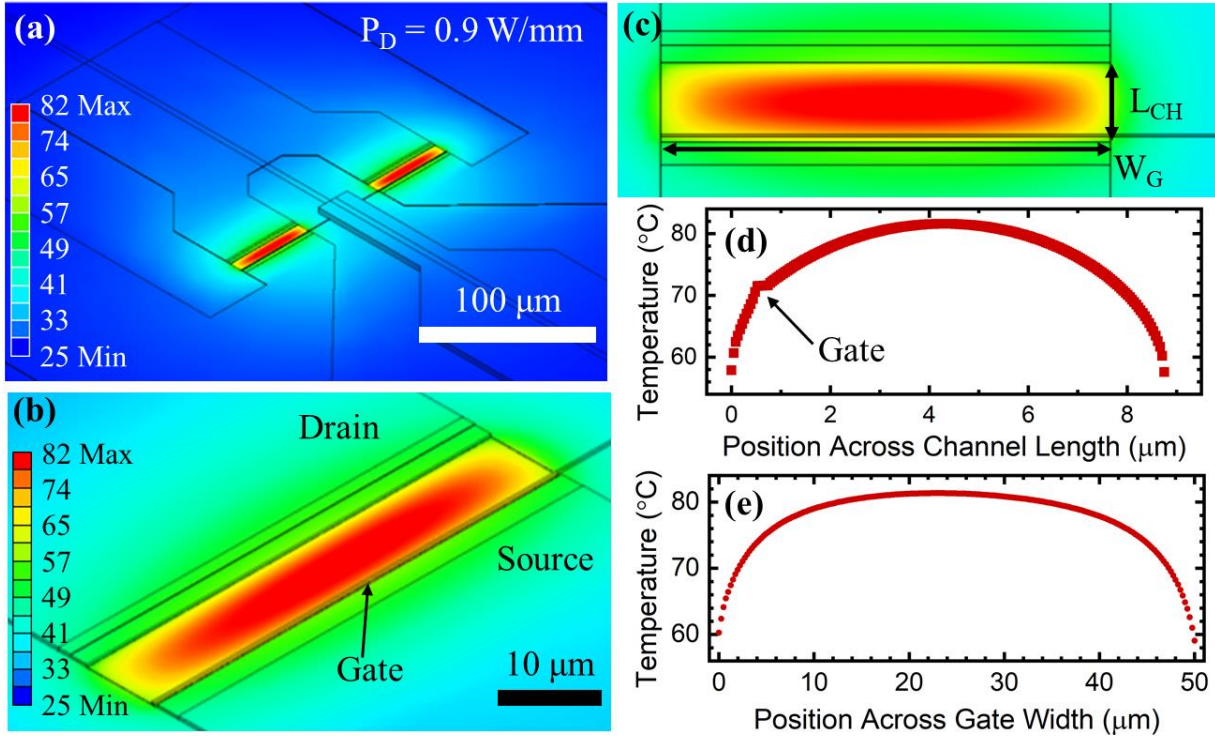


Figure 7.9 (a)-(c) Thermal simulation images of the MOSFET while applying 0.9 W/mm of dissipated power at three varying magnification levels. (d) Channel length and (e) gate width profiles are also shown. Copyright (2020) IEEE [1].

Figure 7.10 shows the $T_{CH}-P_D$ obtained from pulsed I-V, Raman nanothermography, and temperature averages of channel length and gate width profile simulations when using $P_D = 0.9$ W/mm. The pulsed I-V data shown here is an average of the two $T_{CH}-P_D$ relationships found using

R_{ON} and $I_{D,max}$. For comparison purposes between the three techniques, the Raman nanothermography data shown here was averaged for all TiO_2 particles. This average resulted in an R_{TH} of $60 \text{ }^\circ\text{C}\text{-mm/W}$, which is 17.8% lower than the R_{TH} obtained from pulsed I-V ($73 \text{ }^\circ\text{C}\text{-mm/W}$). It is possible that the R_{TH} values would converge if the number of TiO_2 particles used during Raman nanothermography measurements was increased, especially if the added TiO_2 particles were located in the channel center where the highest temperatures were observed. The variation in R_{TH} could also be partially due to individual error from each method. For example, it was assumed that no self-heating occurred during pulsed I-V calibration measurements because of the 200 ns pulsewidth. However, it is possible that a small amount of self-heating was present.

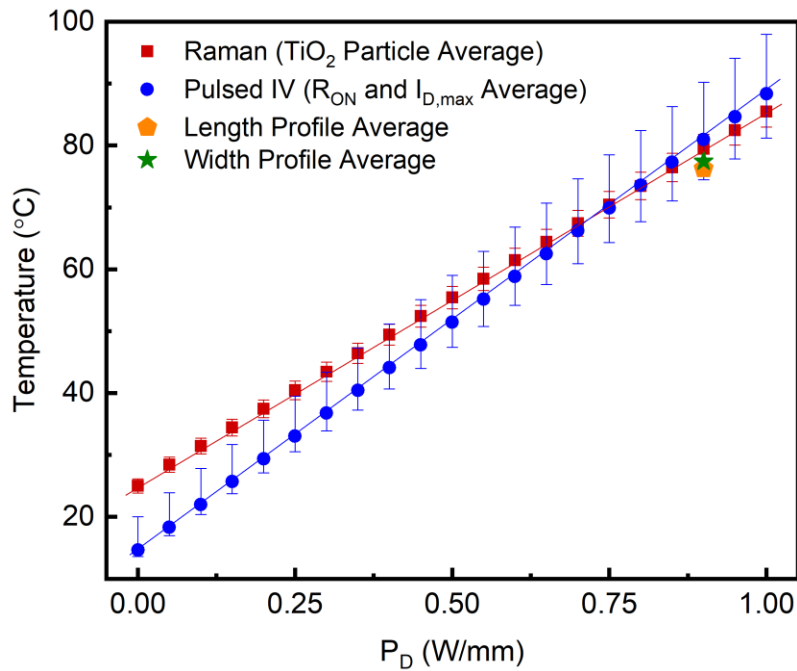


Figure 7.10 T_{CH} - P_D data obtained for pulsed I-V and Raman nanothermography characterization techniques. The gate width and channel length profiles obtained by simulation are also shown for 0.9 W/mm of dissipated power. Copyright (2020) IEEE [1].

Table 7.3 shows R_{TH} findings from this work along (Device A) with other thermal reports from the literature on Ga_2O_3 MOSFETs, including pulsed I-V data from Wong *et al.* (Device B) [12], simulation data from Singh *et al.* (Device C) [13], and Raman nanothermography data from

Pomeroy *et al.* (Device D) [11]. Additionally, some geometry-related device parameters are shown tabulated for comparison purposes. The data presented for Device C included a plot of $T_{CH}-P_D$ at an ambient temperature of 25 °C, but no R_{TH} value was reported. The R_{TH} value listed in the table was calculated here using the previously described method and found to be 116 °C-mm/W, which is significantly higher than the other tabulated values. Interestingly, Devices B and C had nearly identical layouts, were both fabricated on an (010)-oriented Fe-doped Ga₂O₃ substrate, and their results were gathered while under a temperature ambient difference of only 5 °C. Device B reported on a slightly altered version of the experimental technique used by Joh *et al.* where instead of identifying a $T_{CH}-P_D$ relationship using R_{ON} and $I_{D,max}$ they performed calibration using a V_{DS} -dependent $I_{DS}-T_{CH}$ result. After calibrating, they identified a relation between T_{CH} and DC power density which resulted in an R_{TH} of only 48 °C-mm/W at 20 °C. The data for Device C was obtained using single-pulse thermal simulations where T_{CH} transients were evaluated while varying P_D . Despite some relevant differences in device geometry, the R_{TH} of 88 °C-mm/W reported for Device D is similar to the findings of this work.

One major difference between the tabulated devices is that the MOSFET used in this work was much more tightly scaled than the others. The MOSFET had a smaller L_G and higher channel doping, which leads to a more tightly confined depletion region. It has been shown that a significant portion of heat is generated in the channel center during open channel operation. It is thought that the physically smaller region for this thermal load will result in a reduced R_{TH} in comparison to the other devices listed in **Table 7.3**. Concerning the TCH results obtained by Raman nanothermography and thermal simulations, a temperature variance of 1 to 6 °C was observed. This error could be due to the TiO₂ particle located at 3.47 μm being slightly off-center, though this error should be relatively small since the particles are within the 20 – 23 μm gate width

Table 7.3 Comparison of reports on β -Ga₂O₃ MOSFET thermal resistance and corresponding device fabrication properties. Device A represents the data obtained in this work. HFP represents field-plate height. Thermal resistances denoted with * were not reported in the literature, but have instead been calculated here by linear fitting of the reported $T_{CH} - P_D$ data. Copyright (2020) IEEE [1].

Parameter	A [this work]	B [12]	C [13]	D [11]
R_{TH} ($^{\circ}\text{C}\text{-mm/W}$)	73 / 60	48 / 56	116*	88
$T_{Ambient}$ ($^{\circ}\text{C}$)	23 / 25	20 / 125	25	25
Meas. Tech.	PIV / Raman	PIV	Sim.	Raman
Substrate	(010)-Oriented Fe-Doped Ga ₂ O ₃ with 650 μm Thickness			
d_{CH} (nm)	65	300	300	300
N_D (cm^{-3})	2E18	3E17	3E17	3E17
L_{SD} (μm)	8	22	22	44
L_G (μm)	0.14	2	2	4
L_{GD} (μm)	7.36	15	15	30
L_{GS} (μm)	0.5	5	5	10
W_G (μm)	50	200	500	200
# of Fingers	2	1	-	1
$d_{Al_2O_3}$ (nm)	20	20	20	20
H_{FP} (nm)	90	400	400	400

range, and the temperature variance within this region was only 0.1 $^{\circ}\text{C}$. It is possible that channel length differences caused the R_{TH} variation between tabulated devices. In particular, Device B had channel dimensions were are significantly larger than the other devices. Since the pulsed I-V method results in a spatially averaged R_{TH} , the heat generated in the channel center will have a greater impact on the overall R_{TH} when a small device is being analyzed.

7.7 Conclusions

Thin-channel MOSFETs were fabricated by the Air Force Research Laboratory – Sensors Directorate and characterized using pulsed I-V to evaluate the effects of self-heating. The DC I_D - V_{DS} and transfer characteristics of the MOSFETs were measured, showing V_{off} , V_{th} , and peak g_m values of -17.5 V, -15.1 V, and 12.8 mS/mm, respectively. The pulsed I-V method was successful in providing two independent T_{CH-PD} estimations which varied by less than 3 °C. The MOSFET had a R_{TH} of 73 °C-mm/W. Raman nanothermography and ANSYS simulations were used to validate the pulsed I-V method. A maximum temperature deviance of less than 10 °C was observed throughout the dissipated power limit of 1 W/mm. The self-heating results were compared to previously reported findings obtained elsewhere and the various techniques were discussed in detail.

7.8 References

- [1] N. A. Blumenschein *et al.*, “Self-Heating Characterization of β -Ga₂O₃ Thin-Channel MOSFETs by Pulsed I-V and Raman Nanothermography,” *IEEE Trans. Electron Devices*, vol. 67, no. 1, pp. 1–8, 2019.
- [2] N. A. Moser *et al.*, “High pulsed current density β -Ga₂O₃ MOSFETs verified by an analytical model corrected for interface charge,” *Appl. Phys. Lett.*, vol. 110, no. 14, pp. 0–5, 2017.
- [3] K. D. Chabak *et al.*, “Lateral β -Ga₂O₃ field effect transistors,” *Semicond. Sci. Technol.*, vol. 35, no. 013002, p. 22, 2020.
- [4] J. Joh, J. A. del Alamo, U. Chowdhury, T.-M. Chou, H.-Q. Tserng, and J. L. Jimenez, “Measurement of Channel Temperature in GaN High-Electron Mobility Transistors,” *IEEE Trans. Electron Devices*, vol. 56, no. 12, pp. 2895–2901, Dec. 2009.
- [5] G. J. Riedel *et al.*, “Nanosecond Timescale Thermal Dynamics of AlGa_N/Ga_N Electronic Devices,” *IEEE Electron Device Lett.*, vol. 29, no. 5, pp. 416–418, May 2008.
- [6] J. Anaya *et al.*, “Simultaneous determination of the lattice thermal conductivity and grain/grain thermal resistance in polycrystalline diamond,” *Acta Mater.*, vol. 139, pp. 215–225, Oct. 2017.
- [7] J. Dallas *et al.*, “Thermal characterization of gallium nitride p-i-n diodes,” *Appl. Phys. Lett.*, vol. 112, no. 7, p. 073503, Feb. 2018.
- [8] R. B. Simon, J. W. Pomeroy, and M. Kuball, “Diamond micro-Raman thermometers for accurate gate temperature measurements,” *Appl. Phys. Lett.*, vol. 104, no. 21, p. 213503, May 2014.
- [9] Z. W F, H. Y L, Z. M S, Y. Z, and C. Q, “Raman scattering study on anatase TiO₂ nanocrystals,” *J. Phys. D: Appl. Phys.*, vol. 33, pp. 912–916, 2000.
- [10] S. Choi, E. R. Heller, D. Dorsey, R. Vetry, and S. Graham, “The impact of bias conditions on self-heating in AlGa_N/Ga_N HEMTs,” *IEEE Trans. Electron Devices*, vol. 60, no. 1, pp. 159–162, 2013.
- [11] J. W. Pomeroy *et al.*, “Raman thermography of peak channel temperature in β -Ga₂O₃ MOSFETs,” *IEEE Electron Device Lett.*, vol. PP, no. c, pp. 1–1, 2018.
- [12] M. H. Wong, Y. Morikawa, K. Sasaki, A. Kuramata, S. Yamakoshi, and M. Higashiwaki, “Characterization of channel temperature in Ga₂O₃ metal-oxide-semiconductor field-effect transistors by electrical measurements and thermal modeling,” *Appl. Phys. Lett.*, vol. 109, no. 19, p. 193503, Nov. 2016.

- [13] M. Singh *et al.*, “Pulsed Large Signal RF Performance of Field-Plated Ga₂O₃ MOSFETs,” *IEEE Electron Device Lett.*, vol. 39, no. 10, pp. 1–1, 2018.

CHAPTER 8 – SCHOTTKY BARRIER DIODES

8.1 SBD Device Physics

The metal-semiconductor junction is an important aspect of Schottky barrier diode operation. **Figure 8.1(a)** the metal-Ga₂O₃ interface using energy band diagrams. The energy bands were aligned to the vacuum energy level (E_{vac}) using the metal work function (Φ_M), semiconductor work function (Φ_S), electron affinity (χ_S), conduction band energy level (E_C), valence band energy level (E_V), and fermi energy level of metal (E_{FM}) and semiconductor (E_{FS}). The Schottky barrier height (Φ_B) formed at the interface can be calculated by **Equation 8.1** [1].

$$\Phi_B = \Phi_M - \chi_S \quad (8.1)$$

Figure 8.1(b) shows the energy band diagram after the metal-semiconductor junction reaches thermal equilibrium, revealing the potential barrier and depletion region that are formed at the interface. The depletion region width (W_D) can be calculated using **Equation 8.2**, where ϵ is the permittivity, V_{bi} is the built-in potential, V_A is the applied voltage, and N_D is the doping concentration. The built-in potential is the energy required for a carrier to overcome the depletion region, and it can be calculated by **Equation 8.3**.

$$W_D = \sqrt{\frac{2\epsilon(V_{bi}-V_A)}{qN_D}} \quad (8.2)$$

$$V_{bi} = \Phi_M - \Phi_S \quad (8.3)$$

Figure 8.1(c)-(e) shows the energy band diagram when applying a forward bias, reverse bias, and large reverse bias, respectively. Forward biasing the diode reduces the depletion region width, raises E_{FS} , and lowers the potential barrier energy. This allows the electrons to easily overcome the Schottky barrier and reach the metal through a carrier transport mechanism process known as thermionic emission. The forward current (I_F) that is caused by thermionic emission can

be described by **Equation 8.4**, where A is active area of metal contact on the semiconductor, A^* is the Richardson's constant, T is temperature, q is electron charge, k is Boltzmann constant, R_s is the series resistance, n is the ideality factor, and I_0 is the reverse saturation current. If the applied voltage is greater than $3kT$, this equation can be simplified to **Equation 8.5** [2].

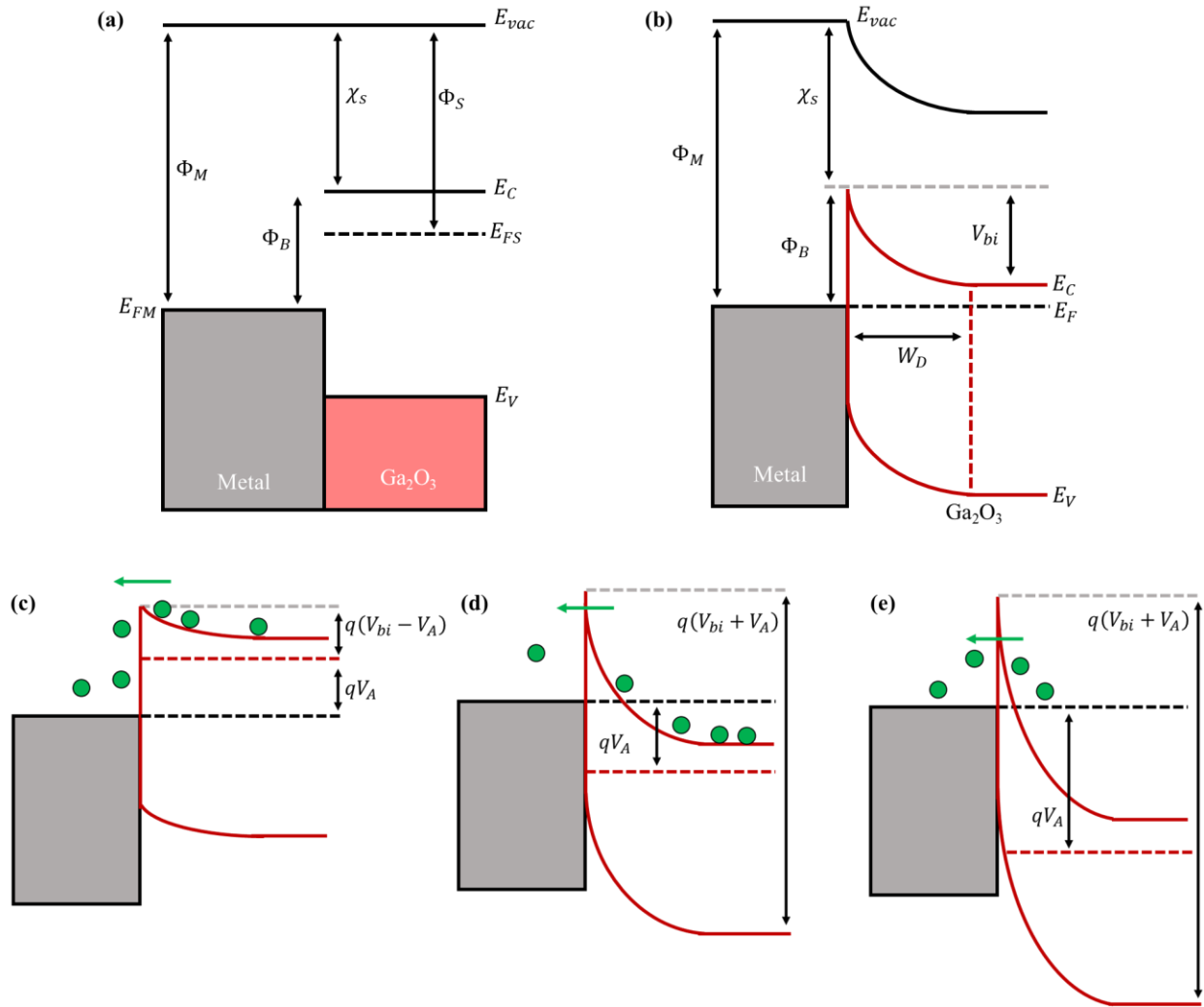


Figure 8.1 Energy band diagram of metal- Ga_2O_3 junction (a) before and (b) after equilibrium. Band bending caused when the junction subject to a (c) forward bias, (d) reverse bias, and (e) large reverse bias where breakdown can occur.

$$I_F = AA^*T^2 e^{-\frac{q\Phi_B}{kT}} \left[e^{\frac{q(V_A - IR_s)}{nkT}} \right] \left[1 - e^{-\frac{q(V_A - IR_s)}{kT}} \right] = I_0 \left[e^{\frac{qV_A}{nkT}} - 1 \right] \quad (8.4)$$

$$I_F = I_0 \left[e^{\frac{qV_A}{nkT}} \right] \quad (8.5)$$

Reverse biasing the diode increases the depletion region width, lowers the fermi energy level, and increases the potential energy barrier. These effects all reduce the probability that an electron will reach the metal layer. Further reverse biasing the diode causes the potential barrier to be extremely thin, allowing carriers to tunnel through the barrier into the metal region through a carrier transport process known as field emission, or quantum mechanical tunneling [2]. If the diode is reverse biased too heavily there are several different breakdown mechanisms that can occur, such as Zener or avalanche breakdown. The breakdown voltage (V_{Br}) can be estimated using **Equation 8.6**, where ϵ is the permittivity, E_C is the critical electric field of the material, and N_D is the doping concentration. Since the critical electric field of Ga_2O_3 is 8 MV/cm the breakdown voltage is exceptionally high, making it likely that oxide layers degrade before the semiconductor material.

$$V_{BR} = \frac{\epsilon E_C^2}{2qN_D} \quad (8.6)$$

8.2 Device Fabrication

The Schottky barrier diodes developed in this work were fabricated using the following processing procedure.

1. Substrate Thinning: 650- μm -thick 5x5 mm^2 Sn-doped Ga_2O_3 substrates were thinned down to 300 μm using a polishing tool. Substrates were first mounted to a puck using crystal bond wax then polished using a 1 μm grit diamond lapping film at 60 rpm for 3 hours (Note: not all substrates were thinned).

2. Substrate Cleaning: 5x5 mm² Sn-doped Ga₂O₃ substrates were cleaned by ultra-sonication for 5 minutes in acetone and 5 minutes in methanol. The substrates were dried using N₂. The substrates were then cleaned by O₂ plasma using a Nordson MARCH O₂ asher for 5 minutes at 250 W plasma power, 600 mT pressure, and 80 sccm of O₂ gas flow.
3. Substrate Mounting: Sn-doped Ga₂O₃ substrates were bonded to a 2” Si wafer using silver paste. Silver paste was cured for 15 minutes at 110 °C using a hot plate.
4. Thin Film Growth: Sn-doped Ga₂O₃ drift layers were grown using the PLD recipe described in **Table 3.5**. The source material used was a 0.1 mol% Sn:Ga₂O₃ ablation target purchased from Kurt J. Lesker.
5. Sample Cleaning: Ga₂O₃ samples were cleaned using the previously described cleaning procedure.
6. Backside Ohmic Metal Patterning: Samples were placed onto a 115 °C hotplate for 5 minutes. An HMDS layer was coated onto the substrate surface using an HMDS/IR oven. Spincoat SPR220 photoresist onto surface at 4000 RPM for 40 seconds, resulting in a thickness of 2.5 μm. Soft bake at 115 °C for 90 seconds using a hotplate. A Heidelberg μP-101 Direct Write lithography tool was used for patterning. Samples were exposed using 14 mW UV radiation followed by a post-exposure bake on 115°C hotplate for 90 seconds. Samples were then placed into CD-26 developer for 60 seconds with minor agitation, rinsed using DI H₂O for 60 seconds, then dried with N₂.
7. Ohmic Layer Metallization: Titanium/gold (50/150 nm) metal contacts were deposited using E-beam deposition. The chamber was pumped down to less than 5x10⁻⁵ Torr prior to deposition.

8. Lift-Off: The samples were placed into an air-tight beaker with 100 mL acetone directly following the metal deposition. Samples were left to soak in the acetone for a couple of hours before any agitation was applied to assist with metal lift-off.
9. Sample Cleaning: Samples were cleaned using the previously described cleaning procedure.
10. Annealing: Samples were annealed using a Heatpulse 610 rapid thermal annealing tool for 60 seconds at 470 °C in an N₂ ambient to enhance metal ohmic properties.
11. Sample Cleaning: Samples were cleaned using the previously described cleaning procedure.
12. Topside Schottky Metal Patterning: Sample top side was patterned using the previously described patterning procedure.
13. Schottky Layer Metallization: Nickel/gold (50/150 nm) metal contacts were deposited using E-beam deposition. The chamber was pumped down to less than 5×10^{-5} Torr prior to deposition.
14. Lift-Off: Previously described lift-off procedure was used.
15. Sample Cleaning: Samples were cleaned using the previously described cleaning procedure.

The ohmic metal layer included a 4x4 mm² blanket for biasing the Schottky barrier diodes. The outer 0.5 mm periphery included circle TLM test structures for characterizing the ohmic contact resistance using the test procedure demonstrated by Klootwijk *et al.* [3]. The TLM structures contained an inner radius of 30 μm and outer radii ranging from 34 to 78 μm. The

Schottky metal layer contained circular contacts with diameter ranging from 40 μm to 1 mm. A schematic drawing of the fabricated Schottky barrier diodes can be seen in **Figure 8.2**.

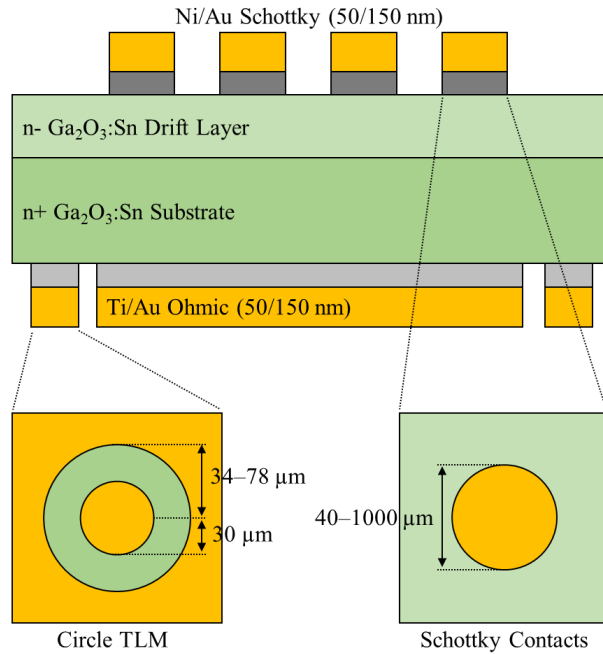


Figure 8.2 Schematic drawing of fabricated Ga₂O₃ Schottky barrier diodes.

8.3 Device Performance

8.3.1 Electrical Characterization

Figure 8.3(a) shows the I-V characteristic of a Schottky barrier diode with Schottky cap diameters ranging from 20 to 300 μm . The device contained a Sn-doped Ga₂O₃ drift layer with thickness and doping concentration of 1.25 μm and $1.8 \times 10^{18} \text{ cm}^{-3}$, respectively. The inset shows current density of the devices plotted on a log scale. It can be seen that the devices have excellent forward characteristic performance, where the current density begins saturation at 0.8 V and exceeds 100 A/cm². At a forward voltage of 1.5 V, the current density exceeds that of many Schottky barrier diodes from the literature that were fabricated using a Ga₂O₃ drift layer [4]–[7].

However, the devices suffered from high leakage current when subject to a reverse bias. This is likely due to the increased drift layer doping concentration used here, which is 2-3 orders of magnitude higher than the cited work. The specific on-resistance ($R_{ON,sp}$) was taken from the slope of the I-V characteristic linear region ($V_A = 0$ to 0.8 V) and varied from 0.17 to 5 $m\Omega\text{-cm}^2$ (increasing with Schottky cap diameter). The devices shown here had ideality factors of around 1.5 .

Figure 8.3(b) shows the C-V characteristic of the Schottky barrier diodes with Schottky cap diameters of 60 and 400 μm . The diode capacitance can be described using **Equation 8.7**, where ϵ is permittivity, A is the Schottky contact area, W is depletion region width, N_D is the drift layer doping density, V_{bi} is the built-in voltage, and V_A is the applied voltage. The inset shows the C-V profiles plotted within the linear regions that were used to extract the drift region carrier density using **Equation 8.8** [2]. Plotting $(A/C)^2$ versus V_A provides a linear curve whose slope is equal to $2/q\epsilon N_D$. The carrier density of the device shown here was found to be 1.8×10^{18} cm^{-3} . Furthermore, the C-V profile can provide the built-in voltage of the device by extrapolating the $(A/C)^2$ curve to the V_A axis for $(A/C)^2$ equal to zero as shown with **Equation 8.8** [2].

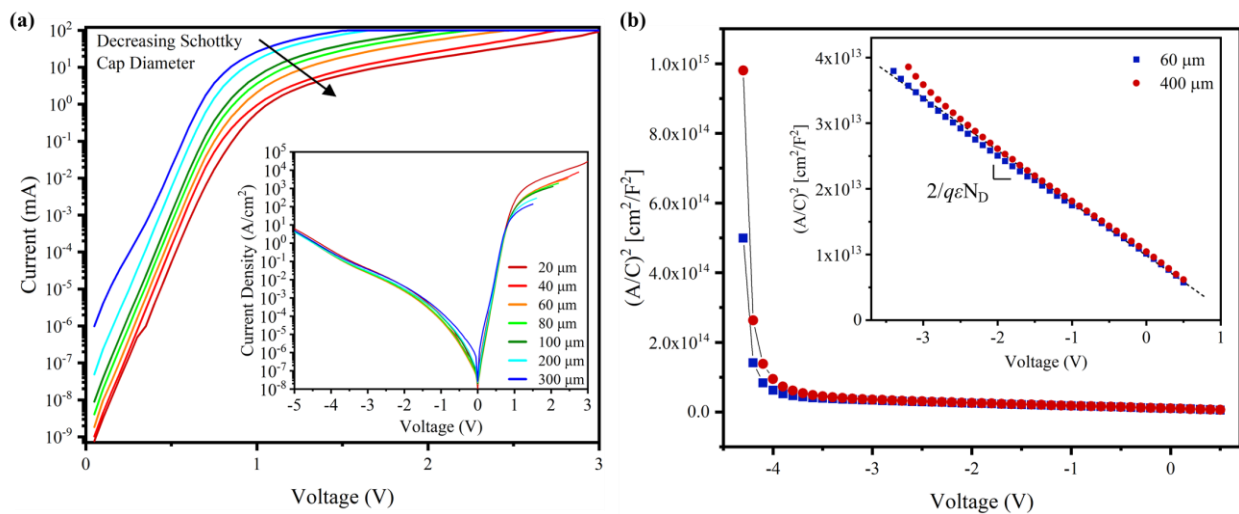


Figure 8.3 Effect of Schottky cap diameter on (a) I-V and (b) C-V characteristics

$$C = \frac{\epsilon A}{W} = A \sqrt{\frac{\epsilon N_D}{2(V_{bi} - V_A)}} \quad (8.7)$$

$$\left(\frac{A}{C}\right)^2 = \frac{2(V_{bi} - \frac{kT}{q})}{q\epsilon N_D} + \frac{2V}{q\epsilon N_D} \quad (8.8)$$

The leakage current present in the shown device is likely due to a combination of thermionic emission and Schottky barrier tunneling currents. Tunneling current can be reduced by lowering the drift layer doping concentration. Reducing N_D will increase the depletion region width according to **Equation 8.2**. The thermionic emission current amplitude can be reduced by incorporating a Schottky metal with a higher metal work function. Previous reports have shown that using a platinum/titanium/gold Schottky metal stack resulted in an increased SBH height of approximately 1.5 eV due to the larger work function of Pt (6.35 eV) when compared to Ni (5.01 eV), which significantly reduces reverse bias leakage and allows for a larger reverse breakdown voltage [4], [5]. **Figure 8.4 (a)** shows the estimated $E_C - E_F$ spacing and depletion region width for a Ga_2O_3 drift layer with varying carrier concentration when using Ni/Au and Pt/Ti/Au Schottky metal contacts. Considering the SBD discussed here containing a drift layer with doping concentration of $1.8 \times 10^{18} \text{ cm}^{-3}$, it is estimated that the depletion region width is only 24 nm. However, this depletion width can be increased to 38 nm when using a Pt/Ti/Au Schottky contact. Energy band diagrams for these two metal-semiconductor structures are shown in **Figure 8.4 (b)** and **(c)**.

Table 8.1 shows details for the additional SBDs that were fabricated to reduce leakage current. Pt/Ti/Au (35nm/15nm/150nm) Schottky contacts and Ga_2O_3 drift layers containing reduced carrier concentrations were implemented. Sample A is the previously discussed device and is shown here for reference. **Table 8.2** shows the device parameters that were extracted for each sample.

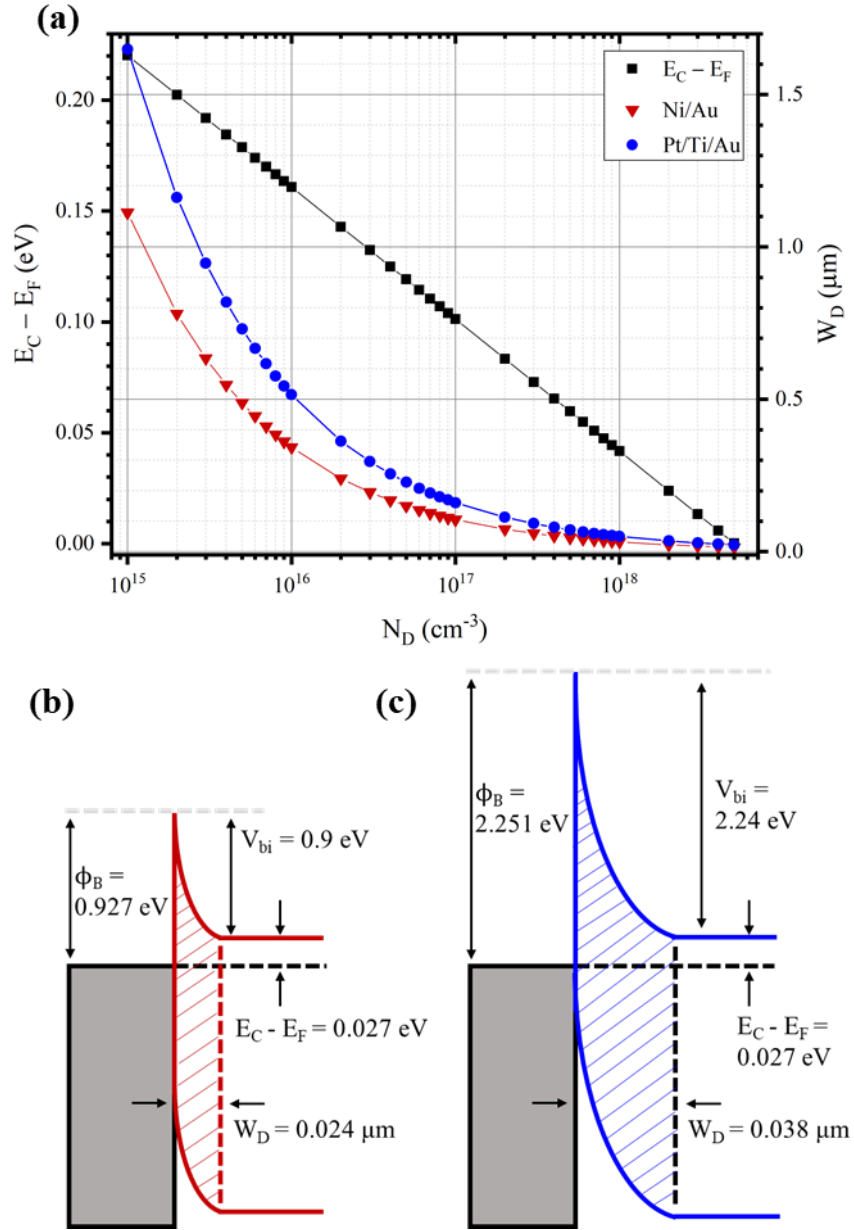


Figure 8.4 (a) $E_C - E_F$ and depletion region width as a function of drift layer doping concentration for Ga_2O_3 when using Ni/Au and Pt/Ti/Au Schottky contacts. Energy band diagrams for (b) Ni/ Ga_2O_3 and (c) Pt/ Ga_2O_3 metal-semiconductor junctions with drift layer doping concentration of 1×10^{18} cm^{-3} .

C-V profiles for the devices are shown in **Figure 8.5**. The drift layer doping concentration of samples A, B, and C were extracted by the $(A/C)^2$ -V profile and found to be 1.8×10^{18} cm^{-3} , 7.3×10^{16} cm^{-3} , and 1.2×10^{16} cm^{-3} respectively. The built-in voltage, $V_{bi,CV}$, of samples A and B were measured as 1.23 V and 2.38 V, respectively. The $V_{bi,CV}$ measured for sample B is only 0.14

V higher than the theoretical Pt/Ti/Au value, but the value for sample A differs from the theoretical Ni/Au value by over 0.3 V. The C-V profile obtained for sample C was unordinary for a couple of reasons. First, the capacitance was in saturation while under an applied bias ranging from -20 V to -2.5 V, and remained in saturation rather than increasing once the voltage exceeded V_{bi} . Additionally, the $(A/C)^2$ was exceptionally high in comparison to the other samples. Extrapolating the $(A/C)^2$ curve to the voltage axis yields a $V_{bi,CV}$ of 65 V, which is obviously an incorrect value. It is possible that some trapping effect is present at the Schottky interface which is causing the $V_{bi,CV}$ to greatly increase. This effect was be discussed further along in the chapter.

The J-V characteristic of the three samples are shown in **Figure 8.6 (a)**. Rectification was observed in each sample, and as expected, the overall current amplitude increased with drift layer doping concentration. **Figure 8.6 (b) – (d)** show the forward characteristic of each device plotted on a linear scale. From linear fitting the measured data within the current density linear region, the specific on-resistance ($R_{ON,sp}$) was extracted for each device and found to be 0.803 m Ω -cm², 0.105 Ω -cm², and 6.529 k Ω -cm² for devices A, B, and C, respectively. Additionally, the built-in voltage ($V_{bi,JV}$) was identified by extrapolating the linear curve to the V-axis and found to be 1.074 V, 2.368 V, and 0.924 V for devices A, B, and C, respectively.

Taking the natural log of **Equation 8.5** yields the I_F - V_A relation shown in **Equation 8.9**. Plotting $\ln(I_F)$ versus V_A results in a linear curve with intercept $\ln(I_s)$ and slope q/nkT . From this methodology, the $\ln(I_F)$ - V_A plot of **Figure 8.6 (e)** was used to extract the saturation current density and ideality factor of each device. The ideality factor and saturation current density of devices A, B, and C were found to be 1.54, 1.53, and 1.57, and 3.5×10^{-8} A/cm², 9.0×10^{-9} A/cm², and 7.0×10^{-10} A/cm², respectively. The barrier height at saturation (ϕ_{B,J_S}) was then calculated using **Equation 8.10**, where A^* is the effective Richardson constant [8]. A^* was calculated using **Equation 8.11**,

where m^* is the effective electron mass, k is Boltzmann's constant, and h is Plank's constant. Using the electron effective mass for β -Ga₂O₃ of $0.342m_0$ [9], A^* was calculated to be $41.1 \text{ A/cm}^2 \text{ K}^2$. The extracted J-V and C-V parameters were used to calculate the Schottky barrier heights $\phi_{B,JV}$ and $q\phi_{B,CV}$ using **Equations 8.12** and **8.13**. Here $E_C - E_F$ is the energy difference between conduction band minima and fermi energy at thermal equilibrium, and calculated using **Equation 8.14**, where N_C is the effective density of states calculated using **Equation 8.15** [5]. The values of $\phi_{B,JV}$ and $\phi_{B,CV}$ calculated here for the three devices are listed on **Table 8.2**.

Table 8.1 Schottky barrier diode sample details.

Sample	Film Species	Film Thickness (nm)	Ablation Target Sn Content	Substrate Doping (cm^{-3})	Schottky Contacts
A	Sn:Ga ₂ O ₃	1250	1 mol%	3.5×10^{18}	Ni/Au
B	Sn:Ga ₂ O ₃	1200	0.1 mol%	3.2×10^{18}	Pt/Ti/Au
C	Ga ₂ O ₃	1200	---	3.0×10^{18}	Pt/Ti/Au

Table 8.2 Device parameters extracted from J-V and C-V profiles.

Sample	$N_d - N_a$ (cm^{-3})	from J-V			from C-V		
		J_s (A/cm^2)	$q\phi_{B,J_s}$ (eV)	$qV_{bi,JV}$ (eV)	$q\phi_{B,JV}$ (eV)	$qV_{bi,CV}$ (eV)	$q\phi_{B,CV}$ (eV)
A	1.8×10^{18}	3.5×10^{-8}	0.832	1.074	1.098	1.229	1.256
B	7.3×10^{16}	9.0×10^{-9}	0.862	2.368	2.469	2.384	2.493
C	1.2×10^{16}	7.0×10^{-10}	0.936	0.924	*1.14-1.20	---	---

$$\ln(I_F) = \ln(I_s) + \frac{q}{nkT} V_A \quad (8.9)$$

$$\phi_{B,J_s} = kT \ln\left(\frac{A^* T^2}{J_s}\right) \quad (8.10)$$

$$A^* = \frac{4\pi q m^* k^2}{h^3} \quad (8.11)$$

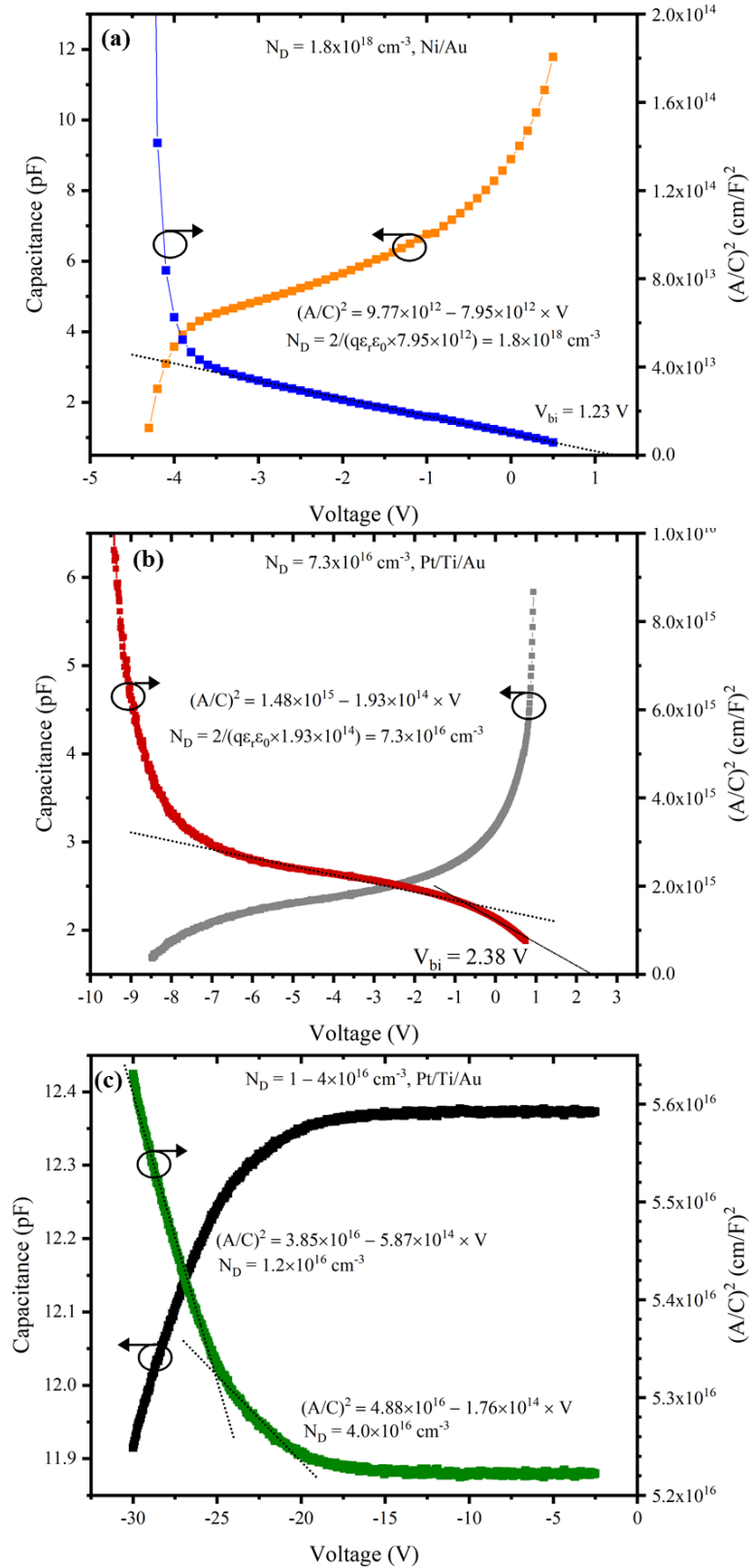


Figure 8.5 C-V and $(A/C)^2$ profiles for (a) sample A, (b) sample B, and (c) sample C.

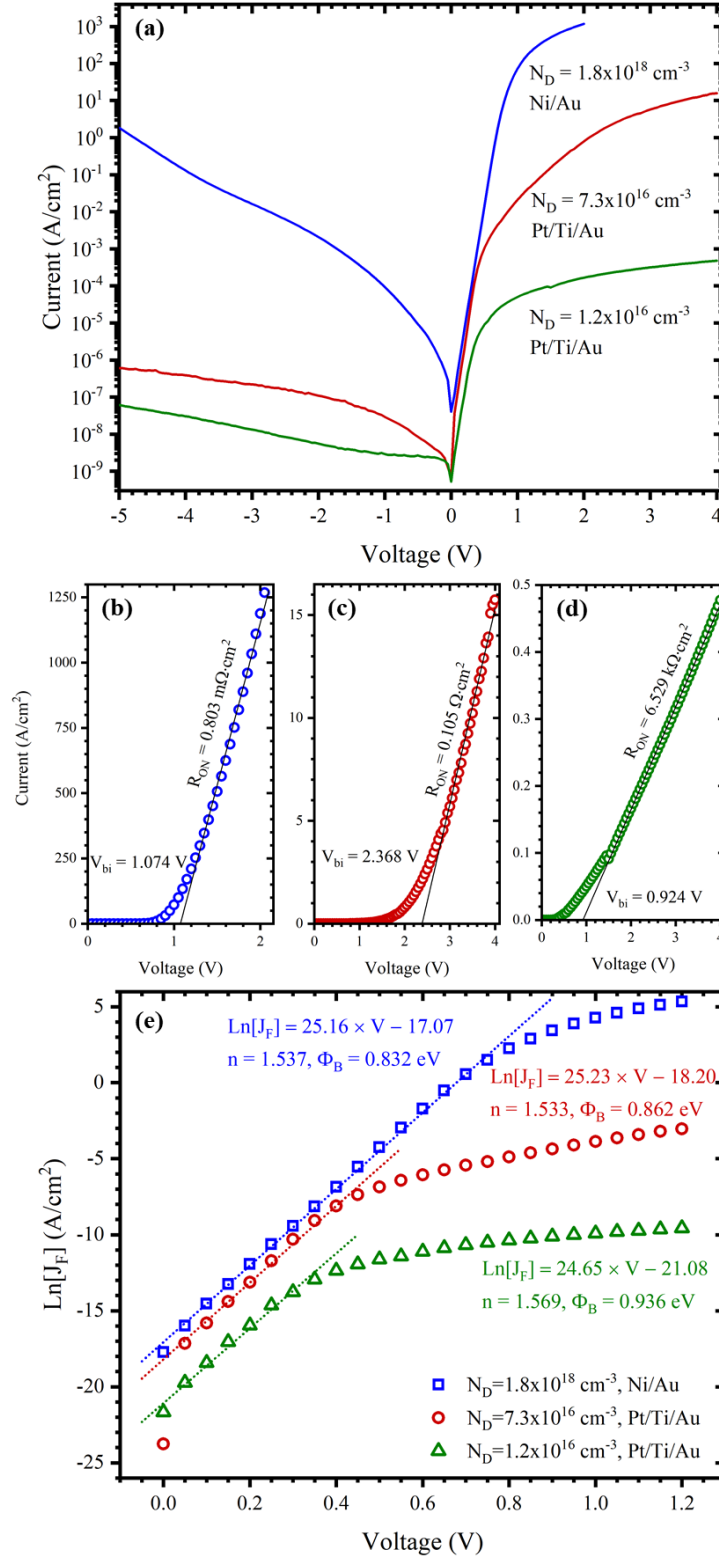


Figure 8.6 (a) J - V characteristic of samples A, B, and C. Linearly scaled J - V of (b) sample A, (c) sample B, and (d) sample C. The J - V curves were used to extract R_{ON} and $V_{bi,JV}$. (e) Natural log of forward current density is plotted as a function of voltage to extract the ideality factor and saturation current density using **Equation 8.9**.

$$q\phi_{B,JV} = qV_{bi,JV} + (E_C - E_F) \quad (8.12)$$

$$q\phi_{B,CV} = qV_{bi,CV} + (E_C - E_F) \quad (8.13)$$

$$E_C - E_F = kT \ln\left(\frac{N_C}{n}\right) \quad (8.14)$$

$$N_C = 2 \left(\frac{2\pi m^* kT}{h^2}\right)^{\frac{3}{2}} \quad (8.15)$$

Reverse breakdown voltage measurements for the three samples are shown in **Figure 8.7**. The -10 V breakdown voltage of sample A was incredibly low in comparison to the other two samples. This was in-part due to the sample containing a drift layer with doping concentration of $1.8 \times 10^{18} \text{ cm}^{-3}$ causing a significantly higher current density at lower voltages, which contributes to thermal deterioration of the Ni/Au Schottky metal by tunneling processes. The breakdown voltage of samples B and C was greatly increased by implementing the Pt/Ti/Au Schottky contact and reducing the drift layer doping concentration. Samples B and C has reverse breakdown voltages of -112 V and -186 V, respectively. It is interesting that the breakdown voltage of sample C is significantly higher than that of Sample B, given they had the sample Schottky metals and a minor difference in drift layer doping concentration. This could be due to the ϕ_B variation measured between the samples. It is possible that image charge is present in the Schottky metal, causing potential barrier lowering ($\Delta\phi_B$). It is known that as an electron approaches the Schottky metal, a mirrored charge of the same magnitude becomes present in the metal at an equal distance from the metal-semiconductor interface, producing an electrostatic force on the electron. The attractive force between electrons generates a negative potential energy in the semiconductor layer. This negative potential combines with the positive potential of the Schottky barrier, lowering the overall potential at the Schottky-semiconductor interface by $\Delta\phi_B$ [10]. $\Delta\phi_B$ can be expressed using **Equation 8.16**, where E_M is the maximum electric-field present at the Schottky metal

calculated with **Equation 8.17**. The leakage current density (J_L) of the Schottky barrier diode will increase as a function of $\Delta\phi_B$ according to **Equation 8.18** [11]. Shown in **Figure 8.8 (a)** is the theoretical amplitude of barrier lowering for devices A – C. It can be seen that the estimated $\Delta\phi_B$ is highest in sample A. This is due to its high N_D and resulting maximum electric field, which explains the reduced $\Delta\phi_B$ amplitude for samples B and C.

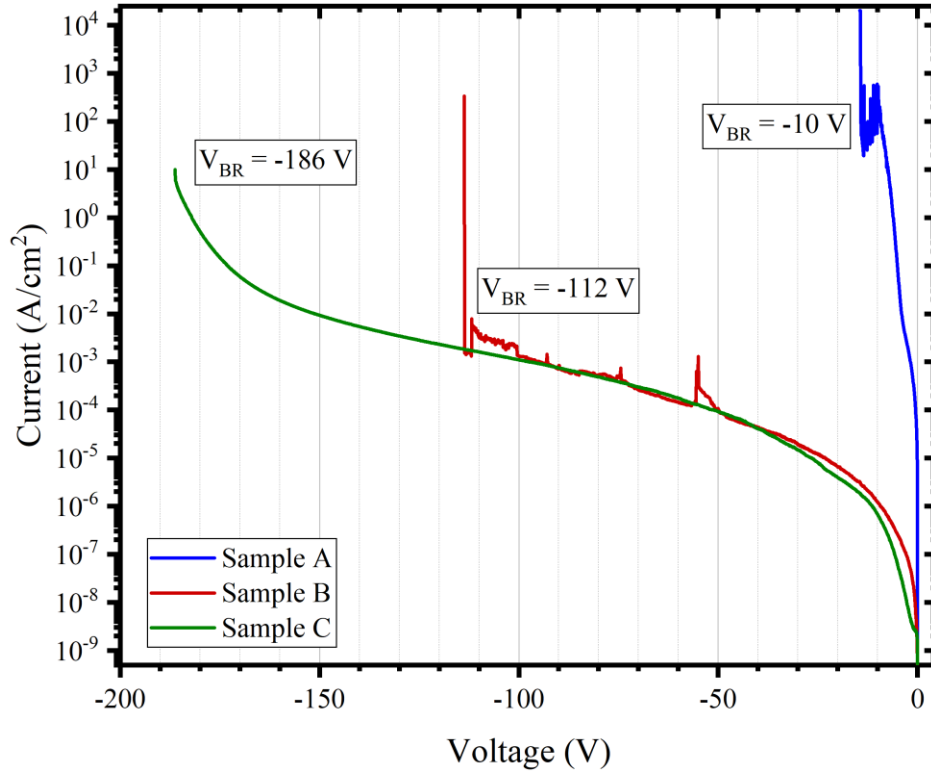


Figure 8.7 Reverse breakdown voltage measurements for the three samples.

$$q\Delta\phi_B = \sqrt{\frac{qE_M}{4\pi\epsilon}} \quad (8.16)$$

$$E_M = \sqrt{\frac{2qN_D}{\epsilon} (V_R + V_{bi})} \quad (8.17)$$

$$J_L = -A^*T^2 e^{-\frac{q}{kT}(\Phi_B - \Delta\Phi_B)} = -J_S e^{\frac{q}{kT}\Delta\Phi_B} \quad (8.18)$$

The Schottky barrier lowering estimated here does not fully account for the amount of leakage current present in the devices. The rapidly increasing leakage current is like due to field

emission, or Schottky barrier tunneling, which must also be considered for a more accurate representation of the devices. Incorporating the effects of tunneling results in the relationship of **Equation 8.19**, where C_T is the tunneling coefficient with units of cm^2/V^2 [10]. Solving this equation for C_T yields **Equation 8.20**. C_T values of $9.0 \times 10^{-13} \text{ cm}^2/\text{V}^2$, $2.50 \times 10^{-13} \text{ cm}^2/\text{V}^2$, and $3.0 \times 10^{-12} \text{ cm}^2/\text{V}^2$ were extracted for sample A, B, and C, respectively. The measured leakage current (J_{Meas}) of the three samples was modeled using these equations and the resulting fits are shown in **Figure 8.8 (b), (c), and (d)**. The fits shown for each sample include the leakage current due to reverse saturation (J_s), the leakage current due to reverse saturation and barrier lowering (J_{s+BL}), and the leakage current due to reverse saturation, barrier lowering, and tunneling (J_{s+BL+T}).

$$J_L = \underbrace{-A^*T^2 e^{-\frac{q}{kT}(\Phi_B)}}_{J_s} \underbrace{e^{\frac{q}{kT}(\Delta\Phi_B)}}_{J_{BL}} \underbrace{e^{C_T E_M^2}}_{J_T} \quad (8.19)$$

$$C_T = \frac{\varepsilon \ln\left(\frac{J_L}{J_s J_{BL}}\right)}{2qN_D(V_R + V_{bi})} \quad (8.20)$$

It can be seen that incorporating tunneling current increases the leakage current by more than six orders of magnitude for device A at a reverse bias of only -10 V. This is likely because of the Ni/Au Schottky contact having a relatively low Schottky barrier height in comparison to that of Pt/Ti/Au. The curve fits obtained within the voltage range of -4 to -7 V did not agree well with the experimental data. It is thought that this is due to the onset of tunneling. The increasing reverse bias voltage reduces the barrier width at the Ni/Ga₂O₃ interface. Once the voltage reaches -7 V, the distance required for carriers to achieve tunneling is reduced to such that the leakage current is equivalent to theoretical levels. For devices B and C, the leakage current increased by three orders of magnitude and six orders of magnitude near the breakdown voltage when accounting for tunneling, respectively. However, the model does not fully account for the current increase seen observed in device C at the onset of breakdown. At a $V_A = -160 \text{ V}$ the leakage current

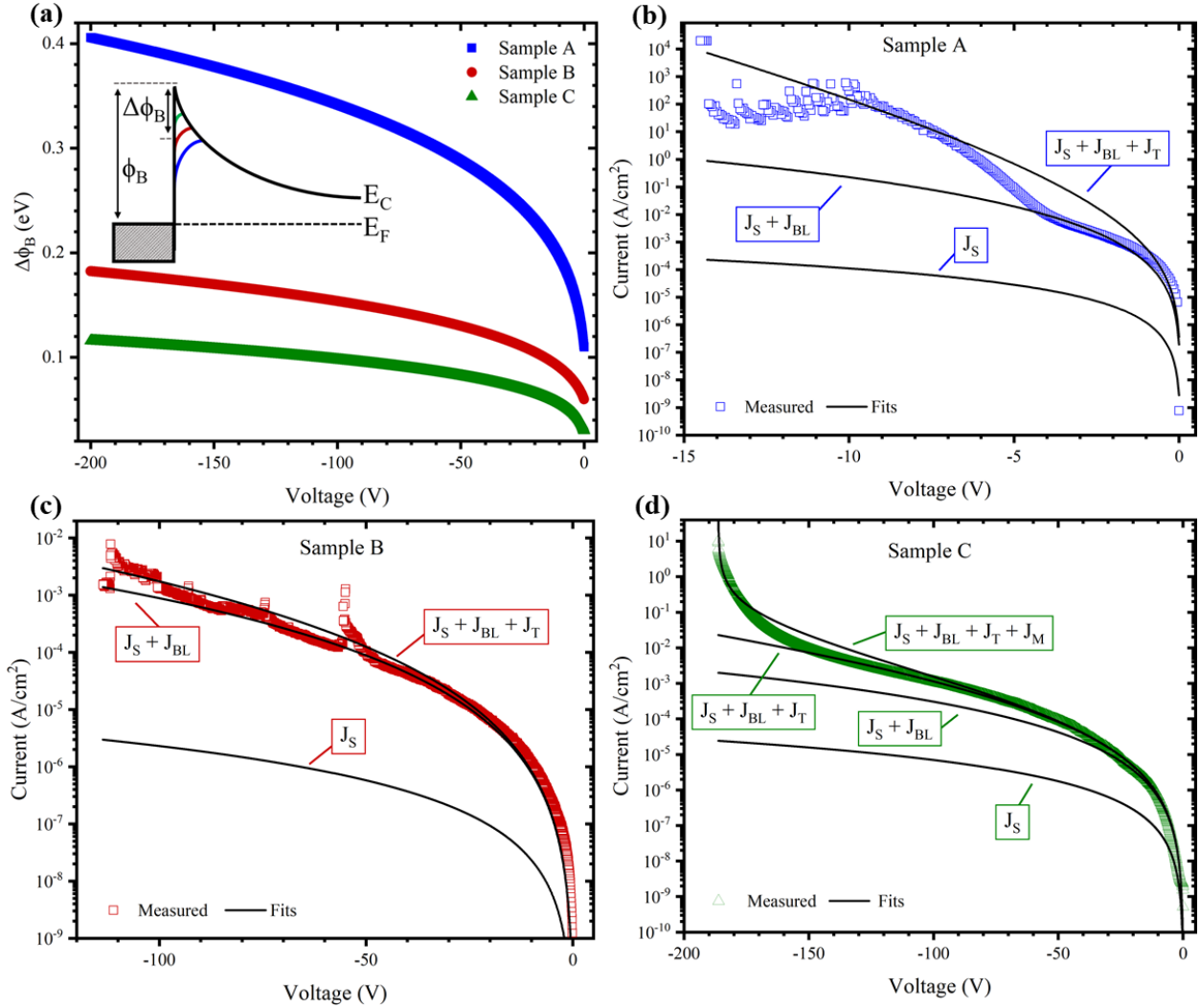


Figure 8.8 (a) Calculated amplitude of image force barrier lowering at the Schottky-Ga₂O₃ interface. The effect of barrier lowering shown in the inset band diagram sketch is not drawn to scale. (b – d) Leakage current model accounting for reverse saturation, barrier lowering, tunneling, and pre-avalanche multiplication processes.

begins to increase beyond what the tunneling model predicts, which could be explained by pre-avalanche multiplication. This phenomenon occurs when a large number of free carriers are transported through the structure at high reverse bias voltages nearing the breakdown voltage [10]. Quantification of the pre-avalanche multiplication process has yet to be reported for Ga₂O₃ Schottky barrier diodes, but for Si devices the multiplication coefficient (M_n) can be acquired using **Equation 8.21**. The leakage current of device C with an added pre-avalanche multiplication

contribution is shown in **Figure 8.8(d)**. The best fit was obtained when using a c coefficient value of 4.627.

$$M_n = \frac{1}{1 - 1.52 \left[1 - e^{-7.22 \times 10^{-25} E_M^c W_D} \right]} \quad (8.21)$$

8.3.2 Trap Characterization

One common way to quickly analyze trapping effects is through transient measurements. **Figure 8.9** shows the measured transient voltage while forcing a stress current (I_{Stress}) for 300 seconds, followed by a release current ($I_{Release}$) for 300 seconds. The amplitude of I_{Stress} and $I_{Release}$ used for each sample was varied such that the device was operating in saturation during I_{Stress} and operating below the turn-on voltage during $I_{Release}$. The forced I_{Stress} and $I_{Release}$ current amplitudes used for samples A, B, and C were 10 mA and 10 nA, 10 mA and 100 nA, and 10 nA and 1 pA, respectively. It can be seen that samples A and B showed no signs of trapping, as the transient voltage remained nearly constant during the five minute tests. For sample C the voltage ΔV_1 increased by 280 mV (+19.86%) over the 300 second I_{Stress} duration and the voltage ΔV_2 decreased by 16 mV (-10.88%) during the 300 second $I_{Release}$ duration. It is possible that the ΔV_1 increase is caused by electrons being captured at interface states and increasing the barrier height at the Schottky contact, which would require an increased voltage to force I_{Stress} . Likewise, the decrease in ΔV_2 is likely due to a reduced barrier height caused by the release of carriers from the interface trap states [12].

In 1963 Lehovec *et al.* showed field-effect capacitance analysis can be used to study surface states in semiconductor materials when the surface state admittance (Y_{ss}) was first calculated. The calculation was performed by integrating admittance (Y_s) across the bandgap continuum with respect to energy as shown in **Equation 8.22** where D_{it} is the density of interface

states, c_n is the electron capture probability, n_s is the electron density at the semiconductor surface, and f_0 is the fermi function established by the bias conditions [13]. Taking the real part of the integral solution and substitution of the trap time constant ($\tau_T = c_n \cdot n_s$) yields the continuum conductance of **Equation 8.23**.

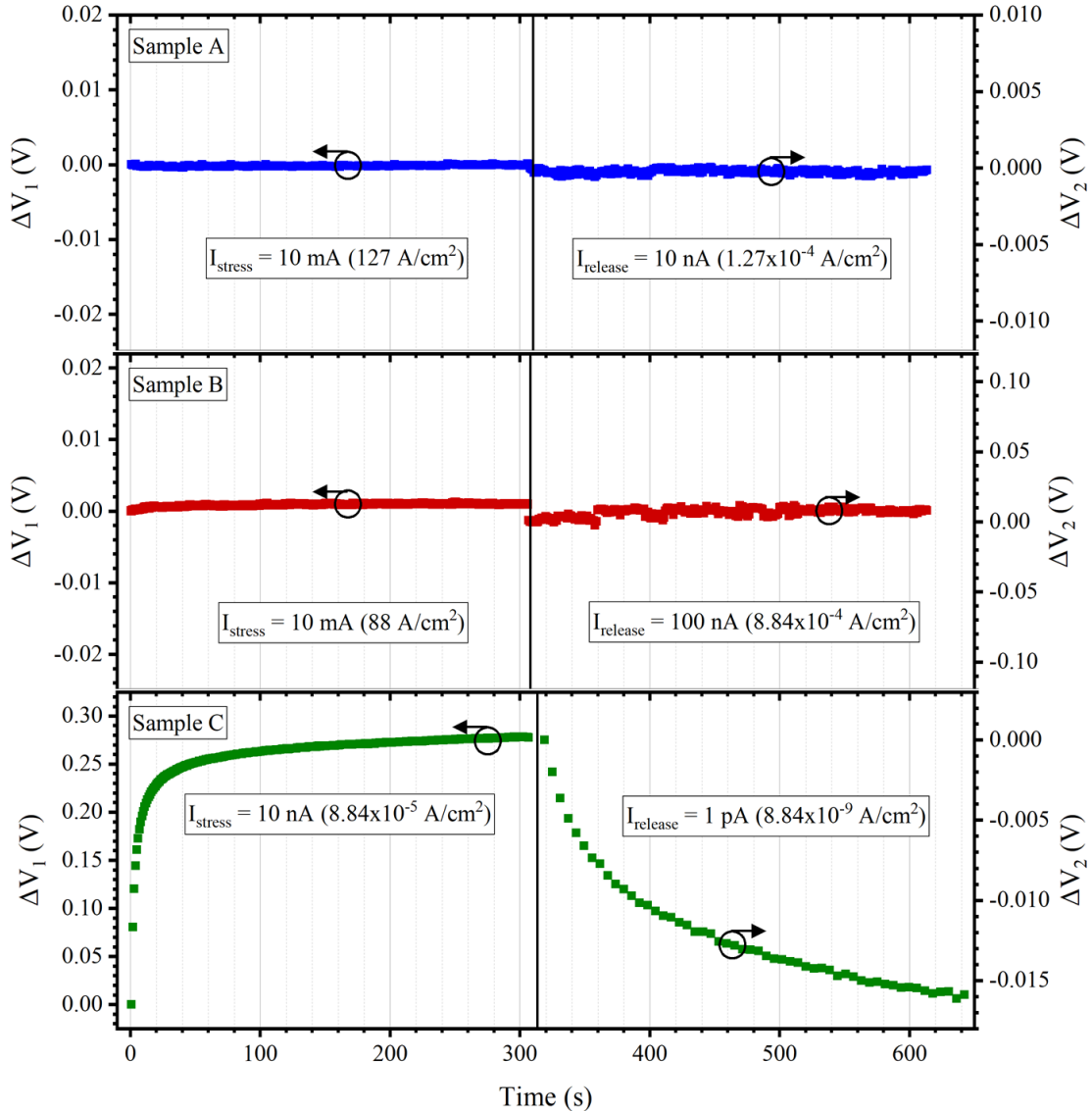


Figure 8.9 Transient voltage measured while forcing constant stress and release currents for approximately 300 seconds each.

$$Y_{SS} = j\omega \left(\frac{q^2}{kT} \right) \int \frac{D_{it} f_0 (1-f_0)}{\left(1 + \frac{j\omega f_0}{c_n n_s} \right)} d\psi \quad (8.22a)$$

$$Y_{SS} = \frac{qD_{it}c_n n_s}{2} \ln \left[1 + \left(\frac{\omega}{c_n n_s} \right)^2 \right] + jqD_{it}c_n n_s \tan^{-1}[\omega c_n n_s] \quad (8.22b)$$

$$\frac{G}{\omega} = \frac{qD_{it}}{2\omega\tau_T} \ln[1 + (\omega\tau_T)^2] \quad (8.23)$$

Since the time of this continuum conductance derivation there have many reports using the relationship to solve for Schottky barrier diode interface traps in a wide variety of semiconductor materials, including silicon, gallium nitride, and gallium oxide [12], [14]–[16]. This methodology has been adapted for characterizing trap levels in the sample C devices. **Figure 8.10 (a)** shows C-V measurements for sample C while varying the frequency from 2 to 200 kHz. At the lower frequencies of 2 to 5 kHz the profiles do contain a fair amount of capacitance fluctuation, but the overall frequency trend does still remain intact. **Figure 8.10 (b)** shows the equivalent parallel conductance G/ω - ω profiles for sample C which were measured while varying the bias voltage from 0.3 to 0.8 volts. Excellent curve fitting was acquired using **Equation 8.23** where ω ($2\pi f$) is frequency. The data points are shown with markers, while the curve fits are shown using lines. The trap time constants extracted using this fitting exercise are shown in **Figure 8.10 (c)**, where the trap lifetimes ranges from 0.2 to 1.3 ms. Furthermore, the interface trap energy levels were calculated using **Equation 8.24**, where σ_T is the capture cross-section of the trap state equal to $1 \times 10^{-15} \text{ cm}^{-2}$, N_C is the density of states in the conduction band, and v_t is the carrier average thermal velocity described by $[3kT/m^*]^{1/2}$ [12]. **Figure 8.10 (d)** shows the interface trap density as a function of trap energy level.

$$E_T = kT \ln[\sigma_T N_C v_t \tau_T] \quad (8.24)$$

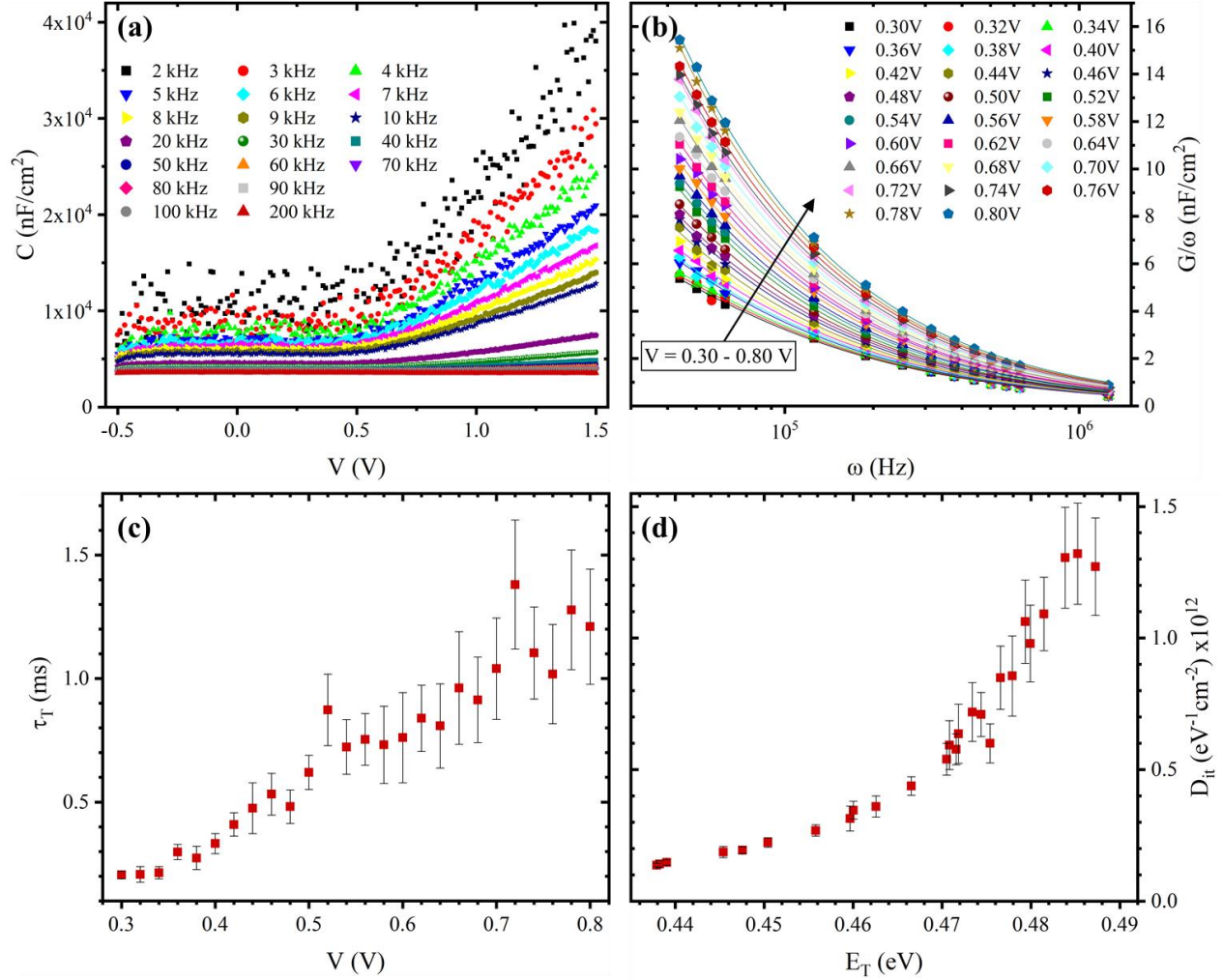


Figure 8.10 (a) C - V profiles measured while varying frequency from 2 – 200 kHz. (b) G/ω - ω profiles measured while varying bias voltage from 0.3 – 0.8 V. Measured data points are shown using markers and fitted curves are shown with lines. (c) Trap time constants extracted from the G/ω - ω profiles. (d) Interface trap density plotted versus trap energy level.

The calculations used here show that the interface trap density increases from the bottom of E_C towards and midgap and appears to maximize at a D_{it} of 1.3×10^{12} eV⁻¹cm⁻² around an $E_C - E_T$ of 0.485 eV. Ghadi *et al.* reported on defect states across the entire bandgap of Ga₂O₃ using a combination of deep-level transient spectroscopy and deep-level optical spectroscopy [17]. It was found that a trap state with point-defect source behavior was present at $E_C - E_T$ of 0.4 eV with a trap density of 3×10^{13} cm⁻³. However, it is also possible that the trap observed here has not been fully-revealed, meaning that the trap density could continue increasing deeper into the bandgap.

Other reports have shown the presence of a trap state located 0.62 eV below the Ga₂O₃ conduction band [18], [19]. Additional information on the trap state observed in this work would require further data acquisition using deep-level transient spectroscopy.

8.3.3 Electric Field Simulations

The breakdown voltage of sample C (-186 V) exceeds that of previously reported Ga₂O₃ Schottky barrier diodes (-150 V) which used similar device structures where Pt/Ti/Au Schottky contacts were implemented [5]. This is likely because of the low drift layer doping concentration of $1.2 \times 10^{16} \text{ cm}^{-3}$. However, there have been other reports demonstrating breakdown voltages of up to 2300 V [4], [7]. Achieving high breakdown voltages on this order of magnitude require edge termination, such as a field-plate or guard ring. Edge termination allows the device to reach higher voltages by lowering the electric field at the Schottky contact edge. As shown in **Equation 8.16** and **8.19**, the leakage current contributions from J_{BL} and J_T both depend heavily on E_M , so implementation of these edge termination strategies is also highly beneficial for reducing leakage. **Figure 8.11 (a)** and **(b)** show electric field simulations of the Ga₂O₃ Schottky barrier diodes for a device which is absent of field-plating and a devices containing a 200 nm SiO₂ layer which surrounded a Schottky metal stack of Pt (35 nm), Ti (15 nm), and Au (250 nm). The simulations occurred while applying a reverse bias voltage of -186 volts. **Figure 8.11 (c)** shows the extracted electric field profiles located at the Schottky-Ga₂O₃ interface. Sentaurus TCAD was used for generating the electric field profiles, and the associated code can be seen in the Appendices. Also shown in **Figure 8.11 (c)** is the simulated electric field profile for the device containing a field-plate when a -240 volt bias is applied. It was found that the electric field amplitude of 2.4 MV/cm is equivalent to that of the device without a field-plate for a -186 volt reverse bias.

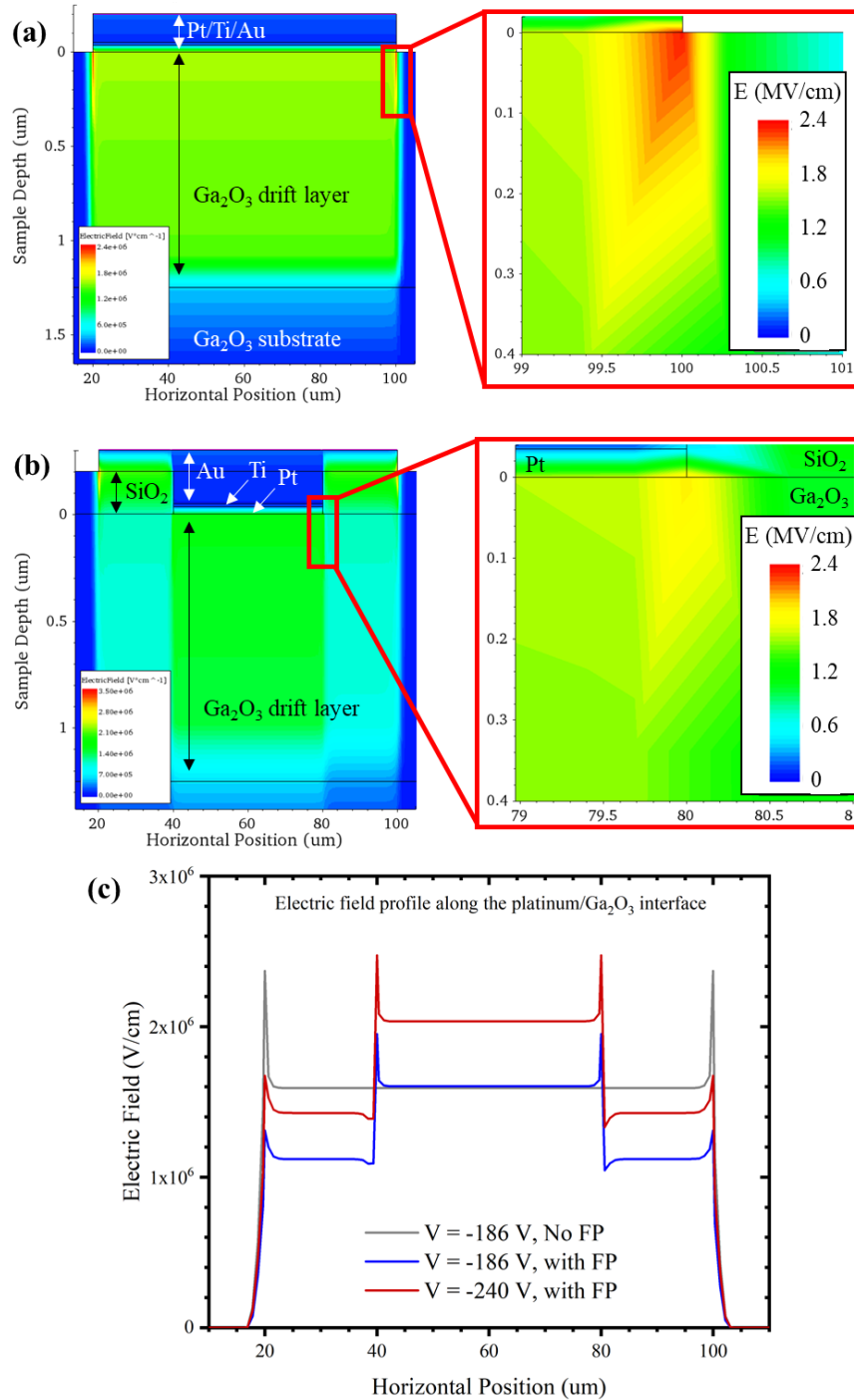


Figure 8.11 (a) Electric field simulations of the Ga₂O₃ Schottky barrier diode of sample C at a reverse bias voltage of -186 V. (b) Electric field simulations of a Ga₂O₃ Schottky barrier diode with a field-plate using a 200 nm SiO₂ layer at a reverse bias voltage of -186 V. (c) Electric field profiles at the Pt/Ga₂O₃ interface when applying a reverse bias voltage of -186 V. Also shown is the profile while biasing at -240 V, which has an equivalent electric field amplitude to the device without a field plate when biased at -186 V.

Increasing the drift layer thickness would also provide improve the device performance. As shown with **Equation 8.2**, the depletion width of the Schottky barrier diode increases with applied voltage. Increasing the bias voltage sufficiently high will eventually result in a depletion region width that is equal to that of the drift layer thickness. The fully-depleted drift layer results in a phenomenon known as punch-through where the electric field profile in the layer takes a trapezoidal shape rather than a triangular one [10]. Once punch-through occurs, the diode will undergo avalanche breakdown due to the maximum electric field becoming equal to the critical electric field causing breakdown. For the case of device B, the punch through voltage is estimated to be -90 volts due to the low drift layer doping concentration and 1200 nm thickness. Increasing the drift layer thickness to 5 μm would result in an increased punch-through voltage of 1580 V.

8.4 Conclusions

Schottky barrier diodes were fabricated using undoped and Sn-doped n^- Ga_2O_3 drift layers on Sn-doped n^+ Ga_2O_3 substrates. Schottky contacts were formed using Ni/Au and Pt/Ti/Au metal layers. Ti/Au metal layers were used for back-side ohmic contacts. The Schottky barrier diodes had excellent forward characteristics with high current amplitudes of more than 100 A/cm². The reverse leakage current of the devices was greatly improved by reducing the drift layer doping concentration from $1.8 \times 10^{18} \text{ cm}^{-3}$ to $1.2 \times 10^{16} \text{ cm}^{-3}$. Incorporating a Pt/Ti/Au Schottky metal stack on the undoped and n- Sn-doped drift layers resulted in increased Schottky barrier heights of 1.17 and 2.47 eV, respectively. These device improvements greatly benefited the reverse breakdown voltage, of which a maximum of -186 V was obtained. Transient measurements were performed to analyze trapping effects in the devices. A trap was identified at $E_C - E_T = 0.485 \text{ eV}$ with an interfacial trap density of $1.3 \times 10^{12} \text{ eV}^{-1} \text{ cm}^{-2}$ and candidate traps from the literature were discussed.

Electric field simulations were performed to demonstrate further device improvements that could be made to enhance the breakdown voltage.

8.5 References

- [1] M. A. Mastro, "Power MOSFETs and Diodes," in *Gallium Oxide - Technology, Devices and Applications*, 2019, pp. 401–418.
- [2] K. C. Kundeti, "The Properties of SiC Barrier Diodes Fabricated with Ti Schottky Contacts," Youngstown State University, 2017.
- [3] J. H. Klootwijk and C. E. Timmering, "Merits and limitations of circular TLM structures for contact resistance determination for novel III-V HBTs," *IEEE Int. Conf. Microelectron. Test Struct.*, vol. 17, no. March, pp. 247–252, 2004.
- [4] K. Konishi, K. Goto, H. Murakami, A. Kuramata, S. Yamakoshi, and M. Higashiwaki, "1-kV vertical Ga₂O₃ field-plated Schottky barrier diodes," *Appl. Phys. Lett.*, vol. 111, no. 22, p. 222104, 2017.
- [5] K. Sasaki, M. Higashiwaki, A. Kuramata, T. Masui, and S. Yamakoshi, "Ga₂O₃ Schottky Barrier Diodes Fabricated by Using Single-Crystal B-Ga₂O₃ (010) Substrates," *IEEE Electron Device Lett.*, vol. 34, no. 4, pp. 493–495, 2013.
- [6] J. Yang *et al.*, "High reverse breakdown voltage Schottky rectifiers without edge termination on Ga₂O₃," *Appl. Phys. Lett.*, vol. 110, no. 19, 2017.
- [7] J. Yang, F. Ren, M. Tadjer, S. J. Pearton, and A. Kuramata, "2300V Reverse Breakdown Voltage Ga₂O₃ Schottky Rectifiers," *ECS J. Solid State Sci. Technol.*, vol. 7, no. 5, pp. Q92–Q96, 2018.
- [8] S. Oh, G. Yang, and J. Kim, "Electrical Characteristics of Vertical Ni/ β -Ga₂O₃ Schottky Barrier Diodes at High Temperatures," *ECS J. Solid State Sci. Technol.*, vol. 6, no. 2, pp. Q3022–Q3025, 2017.
- [9] H. He *et al.*, "First-principles study of the structural, electronic, and optical properties of Ga₂O₃ in its monoclinic and hexagonal phases," *Phys. Rev. B - Condens. Matter Mater. Phys.*, vol. 74, no. 19, pp. 1–8, 2006.
- [10] B. J. Baliga, *Fundamentals of Power Semiconductor Devices*. 2008.
- [11] M. Higashiwaki *et al.*, "Temperature-dependent capacitance-voltage and current-voltage characteristics of Pt/Ga₂O₃ (001) Schottky barrier diodes fabricated on n --Ga₂O₃ drift layers grown by halide vapor phase epitaxy," *Appl. Phys. Lett.*, vol. 108, no. 13, pp. 1–6, 2016.
- [12] Z. Hu *et al.*, "The Investigation of β -Ga₂O₃ Schottky Diode with Floating Field Ring Termination and the Interface States," *ECS J. Solid State Sci. Technol.*, vol. 9, no. 2, p. 025001, 2020.
- [13] K. Lehovec, A. Slobodskoy, and J. L. Sprague, "Field Effect-Capacitance Analysis of Surface States on Silicon," *Phys. Status Solidi*, vol. 3, no. 3, pp. 447–464, 1963.
- [14] J. W. Huang, T. F. Kuech, H. Lu, and I. Bhat, "Electrical characterization of Mg-doped GaN grown by metalorganic vapor phase epitaxy," *Appl. Phys. Lett.*, vol. 68, no. 17, p. 2392,

1996.

- [15] W. A. Hill and C. C. Coleman, "A Single-Frequency Approximation for Interface-State Density Determination," *Solid. State. Electron.*, vol. 23, no. 9, pp. 987–993, 1980.
- [16] P. Chattopadhyay and B. RayChaudhuri, "Frequency dependence of forward capacitance-voltage characteristics of Schottky barrier diodes," *Solid State Electron.*, vol. 36, no. 4, pp. 605–610, 1993.
- [17] H. Ghadi *et al.*, "Full bandgap defect state characterization of β -Ga₂O₃ grown by metal organic chemical vapor deposition," *APL Mater.*, vol. 8, no. 2, 2020.
- [18] Z. Zhang, E. Farzana, A. R. Arehart, and S. A. Ringel, "Deep level defects throughout the bandgap of (010) β -Ga₂O₃ detected by optically and thermally stimulated defect spectroscopy," *Appl. Phys. Lett.*, vol. 108, no. 5, pp. 2–7, 2016.
- [19] E. Farzana, "Defects and Schottky Contacts in β -Ga₂O₃ : Properties , Influence of Growth Method and Irradiation," Ohio State University, 2019.

CHAPTER 9 – SUMMARY AND CONCLUSIONS

Pulsed laser deposition was used to grow heteroepitaxial and homoepitaxial β -Ga₂O₃ thin films on c-plane sapphire and bulk β -Ga₂O₃ substrates, respectively. A variety of β -Ga₂O₃ substrates with different orientations and dopants were used for native growth. Substrate orientations included (001), (010), and (-201), and the substrate were either undoped, Sn-doped, or Fe-doped. Ga₂O₃ thin films were doped by mixing precise concentrations of SiO₂ or SnO₂ powders with Ga₂O₃ powder to form ablation targets. By varying the dopant species mol% in the targets, the conductivity and carrier concentration of the thin films was able to be controlled over a wide range of 1.4×10^{-2} to $1.6 \times 10^3 \Omega^{-1} \text{cm}^{-1}$ and 7×10^{16} to $2 \times 10^{20} \text{cm}^{-3}$. Mobility values of up to $56.7 \text{cm}^2/\text{V-s}$ were obtained. X-ray diffraction was used to study the crystalline quality of the thin films, and it was found that the highest quality homoepitaxial thin films grown had FWHM values as low as 22 arcseconds.

Bulk and thin film Ga₂O₃ samples were used to investigate the anisotropic thermal conductivity of the material using the 3ω technique. Anisotropy was observed in the bulk material, of which samples included undoped, Sn-doped, and Fe-doped with a (010) surface orientation, and undoped and Sn-doped with a (-201) surface orientation. Patterning 3ω devices along *a* and *b* directions on the sample surface allowed for transverse and lateral heat flow measurements. Measurements were acquired at temperatures ranging from 295 to 405 K, and it was found that the thermal conductivity obeyed the power law for α slopes ranging from 0.366 to 0.697. The thermal conductivity was highest along the [010] crystal direction, reaching a maximum of 29.5 W/m-K at room temperature for the Sn-doped material. Interestingly, along the other crystallographic directions, the Sn-doped Ga₂O₃ had a lower thermal conductivity at room temperature than the Fe-doped and undoped counterparts. The 3ω differential method was used to measure the thermal

conductivity of undoped and Sn-doped Ga₂O₃ thin films grown on c-plane sapphire. Films with thicknesses ranging from 100 nm to 1.15 μm were analyzed. The thermal conductivity of the undoped and Sn-doped Ga₂O₃ thin films ranged from 2.92 to 12.34 W/m-K and 1.75 to 3.12 W/m-K, respectively. It was found that the thermal conductivity of the Ga₂O₃ samples had a power law dependence with the film thickness. The thickness dependence was further investigated using transmission electron microscopy. It was speculated that the thermal conductivity increased with film thickness because a decreased quantity of structural defects present in the thicker films.

Time-domain terahertz spectroscopy was used to investigate the high-frequency dielectric properties of bulk and thin film Ga₂O₃. Measurements were performed in the temperature ranges of 4 to 80 K and 4 to 750 K for bulk and thin film samples, respectively. The frequency range used to investigate the samples was 0.2 to 2.5 THz. The high-frequency behavior observed in the samples was described using a dual harmonic oscillator model, which was found to be capable of predicting the conductivity and permittivity spectra with significantly less error than Drude and Drude-Smith models. A non-monotonic temperature dependence was observed in the dielectric spectra of the bulk Ga₂O₃ sample, which was accurately predicted using the dual oscillator model. It was speculated that this behavior was caused by charge carrier localization due to unintentional dopants supplying additional charge carriers that become thermally activated at 55 K. The dielectric spectra of the thin film sample showed much different behavior than the bulk counterpart. The thin film Ga₂O₃ was much less dependent on temperature and also had a more linear frequency dependence. The thin film spectra was fit using a revised version of the Drude-Smith model to include an oscillation term that described low-lying phonons. The temperature dependence was described using charge localization, charge carrier density, and carrier scattering time parameters present in the model. The localization parameter had an inversely proportional

dependence with temperature, indicating that the probability of charge carriers to reflect from Ga₂O₃ grain boundaries was reduced. Atomic force microscopy data was presented to investigate the spectral differences observed in bulk and thin film samples.

Undoped Ga₂O₃ thin films were grown on c-plane sapphire and used to fabricate deep-UV photodetectors. Photodetector performance was increased by optimizing the oxygen partial pressure used during thin film growth. The oxygen partial pressure ranged from 0.1 to 10 mT, and the films grown at 1 mT showed the best performance. Additional optimization was performed by varying the photodetector metal density. A Ga₂O₃:metal ratio of 0.75 was found to provide the best electrical performance. High $I_{\text{photo}}/I_{\text{dark}}$ ratio and spectral responsivity values of 90X and 30.45 A/W were obtained, respectively. Transient response measurements were performed and it was found that two separate relaxation processes were present during periods of rise and decay. The fast rise and decay times were associated with direct band-to-band transitions. The slow rise response was likely caused by transitions between defect and conduction bands. The slow decay response was a result of transitions from the conduction band to recombination centers. The response times increased with oxygen partial pressure, which was attributed to an increase in oxygen-based defects.

Self-heating effects of Ga₂O₃ thin-channel MOSFETs were investigated using a combination of pulsed I-V, Raman nanothermography, ANSYS simulations. The transistors had excellent DC electrical performance, with V_{off} , V_{th} , and peak g_m values of -17.5 V, -15.1 V, and 12.8 mS/mm, respectively. The demonstrated pulsed I-V method was capable of gathering P_D -dependent channel temperature data. Using pulsed I-V and Raman nanothermography it was found that the transistors had R_{TH} values of 73 °C-mm/W and 60 °C-mm/W, respectively. The maximum channel temperature deviance observed between the two measurements techniques was

less than 10 °C at a dissipated power of 1 W/mm. It was speculated that the temperature difference was caused by irregular distribution of TiO₂ nanoparticles. ANSYS thermal simulations predicated that the maximum channel temperature was located in the center, so increasing the TiO₂ density there would likely result in the R_{TH} value of the two methods to converge.

Schottky barrier diodes using undoped and Sn-doped Ga₂O₃ drift layers grown on Sn-doped Ga₂O₃ substrates. The drift layer film thickness of the samples ranged from 1000 to 1250 nm. Three samples were developed to analyze the effects of drift layer doping concentration. Samples A, B, and C had doping concentrations of 1.8x10¹⁸ cm⁻³, 7.0x10¹⁶ cm⁻³, and 1.2x10¹⁶ cm⁻³, respectively. Cylindrical Schottky contacts were formed using either Ni/Au or Pt/Ti/Au layers. Back-side ohmic contacts were formed using Ti/Au layers. Samples A, B, and C had R_{ON} values of 0.803 mΩ-cm², 0.105 Ω-cm², and 6.529 kΩ-cm², saturation current densities of 3.5x10⁻⁸ A/cm², 9.0x10⁻⁹ A/cm², and 7.0x10⁻¹⁰ A/cm², and Schottky barrier heights of 1.10 eV, 2.47 eV, and 1.17 eV, respectively. All three samples had ideality factors of around 1.5. Sample A had the most conductive forward characteristics due to its high doping and low on-resistance, showing a current density of more than 1 kA/cm² at a 2 V bias. Sample A also had the highest leakage current, which caused its catastrophic breakdown to occur at just -10 V. Lowering the drift layer doping concentration of devices B and C was significantly improved the leakage current and resulted in breakdown voltages of -112 V and -186 V, respectively. Electric field simulations were used to demonstrate how the devices could be further improved by implementing edge-termination such as field-plating. Trapping effects were evaluated using a combination of transient V-I and frequency-dependent equivalent parallel conductance measurements. A trap state with an interfacial trap density of 1.3x10¹² eV⁻¹cm⁻² was identified 0.485 eV below the conduction band.

APPENDICES

Appendix A – Sentaurus TCAD SDE Command File

The code shown below was used to generate a two-dimensional model of a Ga₂O₃ Schottky barrier diode using the Sentaurus Synopsys TCAD Structure Editor.

```
; *** DEFINITIONS ***
(define EpiDop @EpiDop@)
(define SubDop 3.5E18)
(define Lepi @EpiThick@)
(define Lsub @SubThick@)
(define Ltot (+ Lsub Lepi))

; *** MESH PARAMETERS ***
(define xmax 5)
(define xmin 1)
(define ymax 5)
(define ymin 1)

; *** MATERIAL REGIONS ***
; *GA2O3*
(sdegeo:create-rectangle (position 0 0 0) (position 120 Lepi 0) "Ga2O3" "Ga2O3_Epi")
(sdegeo:create-rectangle (position 0 Lepi 0) (position 120 Ltot 0) "Ga2O3" "Ga2O3_Sub")

; * OHMIC METALS *
(sdegeo:create-rectangle (position 0 Ltot 0) (position 120 (+ Ltot 0.05) 0) "Titanium"
" Ohmic_Ti")
(sdegeo:create-rectangle (position 0 (+ Ltot 0.05) 0) (position 120 (+ Ltot 0.2) 0) "Gold"
" Ohmic_Au")

; *SCHOTTKY METALS *
(sdegeo:create-rectangle (position 20 0 0) (position 100 -0.05 0) "Nickel" "Schottky_Ni")
(sdegeo:create-rectangle (position 20 -0.05 0) (position 100 -0.2 0) "Gold" "Schottky_Au")

; *** CONTACT DEFINITIONS ***
; * OHMIC *
(sdegeo:define-contact-set "OhmicContact" 4 (color:rgb 0 1 0) "###")
(sdegeo:set-current-contact-set "OhmicContact")
(sdegeo:define-2d-contact (find-edge-id (position 60 (+ Ltot 0.2) 0)) "OhmicContact")

; * SCHOTTKY *
(sdegeo:define-contact-set "SchottkyContact" 4 (color:rgb 1 0 0) "###")
(sdegeo:set-current-contact-set "SchottkyContact")
(sdegeo:define-2d-contact (find-edge-id (position 60 -0.2 0)) "SchottkyContact")
```

```

; *** DOPING PROFILES ***
(sdedr:define-constant-profile "Const.Ga2O3.Sub" "nTinConcentration" SubDop)
(sdedr:define-constant-profile-region "PlaceCD.Ga2O3.Sub" "Const.Ga2O3.Sub"
"Ga2O3_Sub")
(sdedr:define-constant-profile "Const.Ga2O3.Epi" "nTinConcentration" EpiDop)
(sdedr:define-constant-profile-region "PlaceCD.Ga2O3.Epi" "Const.Ga2O3.Epi" "Ga2O3_Epi")

; *** MESH ***
; * WHOLE DOMAIN *
(sdedr:define-refeval-window "RefWin.all" "Rectangle" (position 0 (+ Ltot 2.15) 0) (position
120 -2.15 0))
(sdedr:define-refinement-size "RefDef.all" xmax ymax xmin ymin)
(sdedr:define-refinement-placement "PlaceRF.all" "RefDef.all" "RefWin.all")
(sdedr:define-refinement-function "RefDef.all" "DopingConcentration" "MaxTransDiff" 1)

; * EPILAYER *
(sdedr:define-refeval-window "RefWin.epi" "Rectangle" (position 0 0 0) (position 120 Lepi 0))
(sdedr:define-refinement-size "RefDef.epi" (/ xmax 5) (/ ymax 5) (/ xmin 5) (/ ymin 5))
(sdedr:define-refinement-placement "PlaceRF.epi" "RefDef.epi" "RefWin.epi")

;* EPI/SCHOTTKY INTERFACE - Epi Side*
(sdedr:define-refeval-window "RefWin.MB1" "Rectangle" (position 20 0 0) (position 100 0.2 0))
(sdedr:define-multibox-size "RefDef.MB1" 0.5 0.1 0 0.1 0.005 0 1 1.4 0)
(sdedr:define-multibox-placement "PlaceRF.MB1" "RefDef.MB1" "RefWin.MB1")

;* EPI/SCHOTTKY INTERFACE - Schottky Side*
(sdedr:define-refeval-window "RefWin.MB2" "Rectangle" (position 20 0 0) (position 100 -0.2
0))
(sdedr:define-multibox-size "RefDef.MB2" 0.5 0.1 0 0.1 0.005 0 1 -1.4 0)
(sdedr:define-multibox-placement "PlaceRF.MB2" "RefDef.MB2" "RefWin.MB2")

; *** BUILD MESH ***
; (sde:set-meshing-command "snmesh -a -c boxmethod")
; (sdedr:append-cmd-file "")
(sde:build-mesh "snmesh" "-a -c boxmethod" "n@node@")

```

Appendix B – Sentaurus TCAD SDevice I-V Command File

The code shown below was used to simulate the forward bias I-V characteristic of a Ga₂O₃ Schottky barrier diode using the Sentaurus Synopsys TCAD Device Editor.

```
## Ga2O3 Schottky Barrier Diode Characteristics
## Forward bias characteristics
#setdep @node|sde@

## Electrical contact definitions
Electrode {
    { Name="OhmicContact" EqOhmic Voltage= 0.0}
    { Name="SchottkyContact" Schottky Barrier = @Barrier@ Voltage= 0.0}
}

Thermode {
    { Name="OhmicContact" Temperature=300 SurfaceResistance=2e-4}
    { Name="SchottkyContact" Temperature=300 SurfaceResistance=2e-4}
}

## Input/Output files
File {
    Grid= "@tdr@"
    Plot= "@tdrdat@"
    Current= "@plot@"
    Output= "@log@"
    Parameter= "GaO.par"
}

## Physics models
Physics {
    * Area of the device is 5.0e-5 cm^2
    AreaFactor = 62
    Recombination (
        SRH (DopingDependence TempDependence)
        Auger )
    Mobility (
        DopingDependence
        eHighFieldSaturation (CarrierTempDrive))
    IncompleteIonization
    EffectiveIntrinsicDensity ( Slotboom NoFermi )
    eBarrierTunneling "NLM" (Band2Band=none)
```

```

    HeatCapacity(TempDep)
    ThermalConductivity(TempDep Conductivity)
    Hydrodynamic(eTemperature)
    Thermodynamic
}

Physics(MaterialInterface ="Ga2O3/Nickel") {
    Schottky
    eThermionic
}

Physics(MaterialInterface ="Ga2O3/Platinum") {
    Schottky
    eThermionic
}

Physics(Electrode="SchottkyContact"){
    Schottky
    eThermionic
}

Plot {
    NonLocal
    eDensity
    eCurrent
    ElectricField
    eQuasiFermi
    eQuasiFermiEnergy
    hQuasiFermiEnergy
    egradQuasiFermi
    Potential Doping SpaceCharge
    SRH Auger
    AvalancheGeneration
    eAvalanche
    eMobility
    DonorConcentration
    AcceptorConcentration
    Doping
    eVelocity
    BarrierTunneling
    ConductionBandEnergy
    ValenceBandEnergy
    BandGap
    eTemperature
}

```

```

Math {
  NonLocal "NLM" (
    RegionInterface="Ga2O3_Epi/Schottky_Ni"
    Length= 1.0e-5
    Permeation= 1.0e-5
    Digits= 5
    EnergyResolution= 0.001
    Direction = (010) MaxAngle=5)
  -CheckUndefinedModels
  Digits= 7
  Extrapolate
  ErrEff(electron)= 1e4
  ErrEff(hole)= 1e4
  RHSmin= 1e-20
  RHSmax= 1e30
  RHSFactor= 1e30
  Notdamped= 20
  Iterations= 15
  ExitOnFailure
  eMobilityAveraging= ElementEdge
  hMobilityAveraging= ElementEdge
  ExtendedPrecision(128)
  BM_ExtendedPrecision
  TensorGridAniso(aniso)
  ComputeGradQuasiFermiAtContacts= UseQuasiFermi
  ComputeDopingConcentration
  NumberofThreads= 4
  WallClock
}

Solve {
  Coupled(Iterations=100 LineSearchDamping= 0.001) {Poisson}
  Coupled(Iterations=100 LineSearchDamping= 0.001) {Poisson Hole}
  Coupled(Iterations=100 LineSearchDamping= 0.001) {Poisson Electron Hole}
  Coupled(Iterations=100 LineSearchDamping= 0.001) {Poisson Electron Hole eTemperature}
  NewCurrentPrefix= "IV_"
  Quasistationary (
    Initialstep= 0.001 Increment= 1.5 Decrement= 2.0
    Maxstep= 0.05 Minstep= 1.e-10
    Goal { Name="SchottkyContact" Voltage= @Vfor@ }
  ) { Coupled { Poisson Electron Hole eTemperature }}
}

```

Appendix C – Sentaurus TCAD SDevice B-V Command File

The code shown below was used to simulate the reverse bias I-V characteristic of a Ga₂O₃ Schottky barrier diode using the Sentaurus Synopsys TCAD Device Editor.

```
## Ga2O3 Schottky Barrier Diode Characteristics
## Breakdown voltage characteristics
#setdep @node|sde@

## Stop BV simulation when the current reaches Imax
#define Imax 1.0e-1

## Electrical contact definitions
Electrode {
    {Name="OhmicContact" Voltage= 0.0}
    {Name="SchottkyContact" Schottky Voltage= 0.0 Barrier= @Barrier@}
}

Thermode {
    {Name="OhmicContact" Temperature=300 SurfaceResistance=2e-4}
    {Name="SchottkyContact" Temperature=300 SurfaceResistance=2e-4}
}

## Input/Output files
File {
    Grid= "@tdr@"
    Plot= "@tdrdat@"
    Current= "@plot@"
    Output= "@log@"
    Parameter= "GaO.par"
}

## Physics models
Physics {
    * Area of the device is 5.0e-5 cm^2
    AreaFactor = 62
    Recombination (
        SRH(DopingDependence)
        Auger
        Avalanche(vanOverstraetendeMan))
    Mobility (
        DopingDependence
```

```

        eHighFieldSaturation(CarrierTempDrive))
    IncompleteIonization
    EffectiveIntrinsicDensity(Slotboom NoFermi)
    eBarrierTunneling "NLM" (BarrierLowering)
    HeatCapacity(TempDep)
    ThermalConductivity(TempDep Conductivity)
    Hydrodynamic(eTemperature)
    Thermodynamic
}

Physics(MaterialInterface ="Ga2O3/Nickel") {
    Schottky
    BarrierLowering
    eThermionic
}

Physics(MaterialInterface ="Ga2O3/Platinum") {
    Schottky
    eThermionic
}

Plot {
    NonLocal
    eDensity
    eCurrent
    ElectricField
    eQuasiFermi
    eQuasiFermiEnergy
    hQuasiFermiEnergy
    egradQuasiFermi
    Potential Doping SpaceCharge
    SRH Auger
    AvalancheGeneration
    eAvalanche
    eMobility
    DonorConcentration
    AcceptorConcentration
    Doping
    eVelocity
    BarrierTunneling
    ConductionBandEnergy
    ValenceBandEnergy
    BandGap
    eTemperature
}

```

```

Math {
  NonLocal "NLM" (
    Electrode= "SchottkyContact"
    Length= 1.0e-5
    Digits= 5
    EnergyResolution= 0.001
    Permeation=1.0e-5)
  -CheckUndefinedModels
  Digits= 8
  Extrapolate
  Avalderivatives
  ErrEff(electron)= 1e2
  ErrEff(hole)= 1e2
  RHSmin= 1e-20
  RHSmax= 1e70
  RHSFactor= 1e70
  Notdamped= 20
  Iterations= 12
  ExitOnFailure
  ExtendedPrecision(128)
  BM_ExtendedPrecision
  ##TensorGridAniso(aniso)
  ##ComputeGradQuasiFermiAtContacts= UseQuasiFermi
  ComputeDopingConcentration
  Wallclock
  NumberofThreads= 4
  CdensityMin= 1e-25}

Solve {
  Coupled(Iterations=1000 LineSearchDamping= 0.001) {Poisson}
  Coupled(Iterations=1000 LineSearchDamping= 0.001) {Poisson Hole}
  Coupled(Iterations=1000 LineSearchDamping= 0.001) {Poisson Electron Hole}
  Coupled(Iterations=1000 LineSearchDamping= 0.001) {Poisson Electron Hole eTemperature}

  NewCurrentPrefix= "BV_"

  Quasistationary (
    Initialstep= 1e-3 Increment= 1.4
    Maxstep= 0.5 Minstep= 1e-12
    Goal { Name="SchottkyContact" Voltage= @Vrev@ }
    BreakCriteria { Current (Contact="SchottkyContact" absval= Imax)}
  ) {Coupled {Poisson Electron Hole eTemperature}}
}

```

Appendix D – Sentaurus TCAD Ga₂O₃ Parameter File

The code shown below is the material parameter file for Ga₂O₃, nickel, platinum, titanium, and gold. This file was used while simulating the forward and reverse bias I-V characteristic of a Ga₂O₃ Schottky barrier diode using the Sentaurus Synopsys TCAD Device Editor.

```
***** References *****  
*****
```

```
** [REF1] ECS J. Solid State Sci. and Tech., vol. 9, num. 035003, 2020  
** [REF2] J. Appl. Phys., vol. 124, num. 085707, 2018  
** [REF3] ECS J. Solid State Sci. and Tech., vol. 8, num. Q3116, 2019
```

```
Material = "Ga2O3" {
```

```
***** Dielectric Constant: *****  
*****
```

```
Epsilon{  
* Ratio of the permittivities of material and vacuum  
* epsilon() = epsilon  
epsilon = 10.0 # [1]  
}
```

```
Epsilon_aniso{  
* Ratio of the permittivities of material and vacuum  
* epsilon() = epsilon  
epsilon = 10.0 # [1]  
}
```

```
***** Lattice Heat Capacity: *****  
*****
```

```
LatticeHeatCapacity{  
* lumped electron-hole-lattice heat capacity  
* cv() = cv + cv_b * T + cv_c * T^2 + cv_d * T^3  
cv = 2.5 # [J/(K cm^3)]  
cv_b = 0.0000e+00 # [J/(K^2 cm^3)]  
cv_c = 0.0000e+00 # [J/(K^3 cm^3)]  
cv_d = 0.0000e+00 # [J/(K^4 cm^3)]  
}
```

***** Thermal Conductivity: *****

```
Kappa{
* Lattice thermal conductivity
Formula = 1
* Formula = 1:
* kappa() = kappa + kappa_b * T + kappa_c * T^2
kappa = 0.2 # [W/(cm K)]
kappa_b = 0.0000e+00 # [W/(cm K^2)]
kappa_c = 0.0000e+00 # [W/(cm K^3)]
}
```

***** Bandgap: *****

```
Bandgap{
* Eg = Eg0 + alpha Tpar2 / (beta + Tpar) - alpha T2 / (beta + T)
* Parameter 'Tpar' specifies the value of lattice temperature
* at which parameters below are defined
* Chi0 is electron affinity
Chi0 = 4.0 # [eV]
Eg0 = 4.9 # [eV]
alpha = 0.0000e+00 # [eV K^-1]
beta = 0.0000e+00 # [K]
Tpar = 3.0000e+02 # [K]
}
```

```
eDOSMass{
* For effective mass specification Formula1 (me approximation):
* or Formula2 (Nc300) can be used:
Formula = 2 # [1]
* Formula2:
* me/m0 = (Nc300/2.540e+19)2/3
* Nc(T) = Nc300 * (T/300)3/2
Nc300 = 5.02e+18 # [cm-3]
* mass = 0.27*m0
}
```

```
hDOSMass{
* For effective mass specification Formula1 (mh approximation):
* or Formula2 (Nv300) can be used:
Formula = 2 # [1]
* Formula2:
* mh/m0 = (Nv300/2.540e+19)2/3
```

```

* Nv(T) = Nv300 * (T/300)3/2
Nv300 = 1.00e+14 # [cm-3]
* mass = 1.00*m0
}

```

***** Mobility Models: *****

** Doping Dependence [REF3]

ConstantMobility:

```

{
* mu_const = 30 # [cm2/(Vs)]
}

```

DopingDependence:

```

{
* Formula2 uses approximation suggested by Arora
formula = 2, 2 # [1]
* mu_dop = muminA + mudA/(1.+(N/N00)AA)
* N is net doping
* where
* muminA = Ar_mumin * (T/T0)Ar_alm
* mudA = Ar_mud * (T/T0)Ar_ald
* N00 = Ar_N0 * (T/T0)Ar_alN
* AA = Ar_a * (T/T0)Ar_ala

```

```

Ar_mumin = 13, 0.016 # [cm2/(Vs)]
Ar_alm = -0.57, -0.57 # [1]
Ar_mud = 235, 0.2 # [cm2/(Vs)]
Ar_ald = 0.78, 0.78 # [1]
Ar_N0 = 1.10e+18, 1.25e+17 # [cm-3]
Ar_alN = 2.4, 2.4 # [1]
Ar_a = 0.78, 0.78 # [1]
Ar_ala = -0.146, -0.146 # [1]
}

```

HighFieldDependence:

```

{
vsat0 = 2.5e+7, 2.5e+7 # [cm/s]
vsatexp = 2.5e+7, 2.5e+7 # [cm/s]
}

```

***** Recombination/Generation Models: *****

```

** Variable = electron value, hole value # [unit]
** vanOverstraetendeMan Ionization [REF2]

```

```

Scharfetter * relation and trap level for SRH recombination:
{
* tau = taumin + (taumax - taumin) / ( 1 + ( N/Nref )^gamma
* tau(T) = tau * ( (T/300)^Talpha )      (TempDep)
* tau(T) = tau * exp( Tcoeff * ((T/300)-1) ) (ExpTempDep)
taumin = 0.0000e+00, 0.0000e+00 # [s]
taumax = 1.0000e-9, 1.0000e-9 # [s]
Nref = 1.0000e+16, 1.0000e+16 # [cm-3]
gamma = 1, 1 # [1]
Talpha = -1.5000e+00, -1.5000e+00 # [1]
tcoeff = 2.55, 2.55 # [1]
Etrap = 0.0000e+00 # [eV]
}

```

```

Auger * coefficients:
{
* R_Auger = (C_n n + C_p p) ( n p - ni_eff^2)
* with C_n,p = (A + B (T/T0) + C (T/T0)^2) (1 + H exp(-{n,p}/N0))
A = 1.0000e-30, 1.0000e-30 # [cm^6/s]
B = 0.0000e+00, 0.0000e+00 # [cm^6/s]
C = 0.0000e+00, 0.0000e+00 # [cm^6/s]
H = 0.0000e+00, 0.0000e+00 # [1]
N0 = 1.0000e+18, 1.0000e+18 # [cm-3]
}

```

```

OkutoCrowell {
a = 0.1, 4.828e6      # [V^-1]
b = 6.346e6, 1.334e7 # [V/cm]
c = 0.0, 0.0        # [K^-1]
d = 0.0, 0.0        # [K^-1]
gamma =      1, 0.0 # [1]
delta = 2,    1.0   # [1]
}

```

```

vanOverstraetendeMan {
a (low) = 7.9e+5, 7.9e+5 # [cm-1]
a (high) = 7.9e+5, 7.9e+5 # [cm-1]
b (low) = 2.92e+7, 2.92e+7 # [V/cm]
b (high) = 2.92e+7, 2.92e+7 # [V/cm]
}

```

```

***** Incomplete Ionization: *****
*****
** Variable = electron value, hole value # [unit]
** Incomplete Ionization [REF1]

```

```

Ionization {
Species("nTinActiveConcentration") {
E_0 = 0.0520 # [eV]
alpha = 3.3980e-8 # [eV cm]
g = 2.0 # [1]
Xsec = 1.0000e-12 # [cm^2]
}
Species("nTinConcentration") {
E_0 = 0.0520 # [eV]
alpha = 3.3980e-8 # [eV cm]
g = 2.0 # [1]
Xsec = 1.0000e-12 # [cm^2]
}}

```

```

***** Barrier Tunneling: *****
*****

```

```

BarrierTunneling "NLM" {
* Non Local Barrier Tunneling
*  $G(r) = g \cdot A \cdot T / k_B \cdot F(r) \cdot Pt(r) \cdot \ln[(1 + \exp((E(r) - E_s) / k_B / T)) / (1 + \exp((E(r) - E_m) / k_B / T))]$ 
* where:
* Pt(r) is WKB approximation for the tunneling probability
*  $g = A_s / A$ ,  $A_s$  is the Richardson constant for carriers in semiconductor
* A is the Richardson constant for free electrons
* F(r) is the electric field
* E(r) is carrier energy
*  $E_s$  is carrier quasi fermi energy in semiconductor
*  $E_m$  is carrier fermi energy in metal
g = 1.0 , 1.0 # [1]
mt = 0.3 , 1.0 # [1]
A = 1.0 , 1.0
}}

```

```

***** Ga2O3/Schottky Interface: *****
*****

```

```

MaterialInterface = "Ga2O3/Nickel" {
BarrierTunneling "NLM" {
mt = 0.5, 0.5 # [1]
g = 1.0, 1.0 # [1]
A = 1.0, 1.0 # [1]
}}

```

```

***** Gold Properties: *****
*****

```

```

Material = "Gold" {
Bandgap {
Workfunction = 5 # [eV]
}

```

```

Kappa {
* Lattice thermal conductivity
Formula = 1
* Formula = 1:
* kappa() = kappa + kappa_b * T + kappa_c * T^2
kappa = 3.0 # [W/(cm K)]
kappa_b = 0.0000e+00 # [W/(cm K^2)]
kappa_c = 0.0000e+00 # [W/(cm K^3)]
}}

```

```

***** Nickel Properties: *****
*****

```

```

Material = "Nickel" {
Bandgap {
Workfunction = 5.01 # [eV]
}

```

```

Kappa {
* Lattice thermal conductivity
Formula = 1
* Formula = 1:
* kappa() = kappa + kappa_b * T + kappa_c * T^2
kappa = 0.7 # [W/(cm K)]
kappa_b = 0.0000e+00 # [W/(cm K^2)]
kappa_c = 0.0000e+00 # [W/(cm K^3)]
}

```

```

BarrierTunneling "NLM" {
mt = 0.5, 0.5 # [1]
g = 1.0, 1.0 # [1]
A = 1.0, 1.0 # [1]
}}

```

```

***** Titanium Properties: *****
*****

```

```

Material = "Titanium" {
Bandgap {
Workfunction = 3.85 # [eV]
}

```

```
}
```

```
Kappa {  
* Lattice thermal conductivity  
Formula = 1  
* Formula = 1:  
* kappa() = kappa + kappa_b * T + kappa_c * T^2  
kappa = 0.2 # [W/(cm K)]  
kappa_b = 0.0000e+00 # [W/(cm K^2)]  
kappa_c = 0.0000e+00 # [W/(cm K^3)]  
}}
```

```
***** Platinum Properties: *****  
*****
```

```
Material = "Platinum" {  
Bandgap {  
Workfunction = 6.35 # [eV]  
}
```

```
Kappa {  
* Lattice thermal conductivity  
Formula = 1  
* Formula = 1:  
* kappa() = kappa + kappa_b * T + kappa_c * T^2  
kappa = 0.7 # [W/(cm K)]  
kappa_b = 0.0000e+00 # [W/(cm K^2)]  
kappa_c = 0.0000e+00 # [W/(cm K^3)]  
}}
```

LIST OF PUBLICATIONS

- [1] Nicholas A. Blumenschein, Christelle Kadlec, Oleksandr Romanyuk, Tania Paskova, John F. Muth, and Filip Kadlec, *Editor's Pick: "Dielectric and conducting properties of unintentionally and Sn-doped β -Ga₂O₃ studied by terahertz spectroscopy"*, *Journal of Applied Physics*, 127, 16, 165702 (2020)
- [2] Nicholas A. Blumenschein, Neil A. Moser, Eric R. Heller, Nicholas C. Miller, Andrew J. Green, Andreas Popp, Antonio Crespo, Kevin Leedy, Miles Lindquist, Taylor Moule, Stefano Dalcanale, Elisha Mercado, Manikant Singh, James W. Pomeroy, Martin Kuball, Guenter Wagner, Tania Paskova, John F. Muth, Kelson D. Chabak, and Gregg H. Jessen, *"Self-heating characterization of β -Ga₂O₃ thin-channel MOSFETs by pulsed I-V and Raman nanothermography"*, *IEEE Transactions Electron Devices*, 67, 1, 204-211 (2020)
- [3] Dat Q. Tran, Nicholas A. Blumenschein, Alyssa Mock, Pitsiri Sukkaew, Hengfang Zhang, John F. Muth, Tania Paskova, Plamen P. Paskov, and Vanya Darackchieva, *"Thermal conductivity of ultra-wide bandgap thin layers – High Al-content AlGa_N and β -Ga₂O₃"*, *Physica B: Condensed Matter*, 579, 411810 (2020)
- [4] Nicholas A. Blumenschein, Tania Paskova, and John F. Muth, *"Effect of growth pressure on PLD-deposited gallium oxide thin films for deep-UV photodetectors"*, *Physica Status Solidi A*, 216, 20, 1900098 (2019)
- [5] Nicholas A. Blumenschein, Mike Slomski, Felix Kaess, Matthew H. Breckenridge, Plamen P. Paskov, John F. Muth, and Tania Paskova, *"Thermal conductivity of bulk and thin film β -Ga₂O₃ measured by the 3 ω technique"*, *SPIE: Oxide-Based Materials and Devices IX*, 10533, 77 (2018)
- [6] Mike Slomski, Nicholas A. Blumenschein, Plamen P. Paskov, John F. Muth, and Tania Paskova, *"Anisotropic thermal conductivity of β -Ga₂O₃ at elevated temperatures: Effect of Sn and Fe dopants"*, *Journal of Applied Physics*, 121, 23, 235104 (2017)